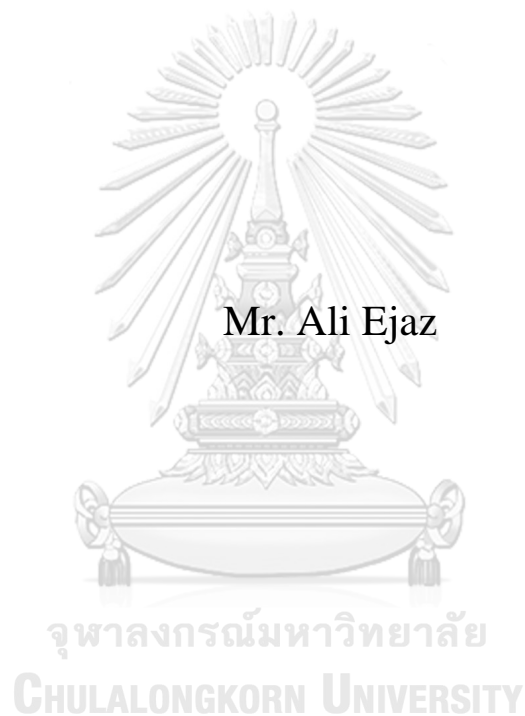# STRENGTHENING OF REINFORCED CONCRETE MEMBERS WITH LAP SPLICES USING STEEL COLLARS

Mr. Ali Ejaz

A Dissertation Submitted in Partial Fulfillment of the Requirements
for the Degree of Doctor of Philosophy in Civil Engineering
Department of Civil Engineering
FACULTY OF ENGINEERING
Chulalongkorn University
Academic Year 2022
Copyright of Chulalongkorn University

การเสริมกำลังองค์อาคารคอนกรีตเสริมเหล็กที่มีการต่อทาบโดยใช้ปลอกเหล็ก

นายอลี อีเจส

Thesis Title	STRENGTHENING OF REINFORCED CONCRETE MEMBERS WITH LAP SPLICES USING STEEL COLLARS
By	Mr. Ali Ejaz
Field of Study	Civil Engineering
Thesis Advisor	Professor Anat Ruangrassamee, Ph.D.

Accepted by the FACULTY OF ENGINEERING, Chulalongkorn University in Partial Fulfillment of the Requirement for the Doctor of Philosophy

.... Dean of the FACULTY OF ENGINEERING
(Professor SUPOT TEACHAVORASINSKUN, D.Eng.)

DISSERTATION COMMITTEE

.... Chairman
(Associate Professor Anil C. Wijeyewickrema, Ph.D.)

.... Thesis Advisor
(Professor Anat Ruangrassamee, Ph.D.)

.... Examiner
(Professor TOSPOL PINKAEW, D.Eng.)

.... Examiner
(Assistant Professor CHATPAN CHINTANAPAKDEE, Ph.D.)

.... Examiner
(Associate Professor PITCHA JONGVIVATSAKUL, Ph.D.)

จุฬาลงกรณ์มหาวิทยาลัย

CHULALONGKORN UNIVERSITY

อลี อีเจส : การเสริมกำลังองค์อาคารคอนกรีตเสริมเหล็กที่มีการต่อทาบโดยใช้ปลอกเหล็ก. (
STRENGTHENING OF REINFORCED CONCRETE MEMBERS WITH
LAP SPLICES USING STEEL COLLARS) อ.ที่ปรึกษาหลัก : ศ. ดร.อาณัติ เรืองรัศมี

การวิบัติจากแรงยึดเหนี่ยวที่จุดทาบเหล็กเป็นหนึ่งในความเสียหายในโครงสร้างที่เกิดขึ้นจากแผ่นดินไหว ได้มีการ
เสริมกำลังบริเวณที่มีการทาบเหล็กที่ไม่ได้มาตรฐานโดยใช้การโอบรัดด้วยปลอกหุ้ม วัสดุส่วนใหญ่มีสติฟเนสตามแนวแกนเป็น
หลัก แต่เนื่องจากคอนกรีตจะมีการขยายตัวออกด้านข้างจึงเกิดการดัดตัวของปลอกหุ้ม ส่งผลให้ประสิทธิภาพในการโอบรัด
ลดลง งานวิจัยนี้ได้ศึกษาปลอกเหล็กแบบหน้าตัดกลวงซึ่งมีสติฟเนสสูงทั้งแนวแกนและการดัดเพื่อช่วยป้องกันการวิบัติจากแรง
ยึดเหนี่ยวที่จุดทาบเหล็ก ในการศึกษาได้พิจารณาระยะทาบเท่ากับ 20, 28 และ 35 เท่าของเส้นผ่านศูนย์กลางของเหล็กเสริม
ได้ทดสอบคานจำนวน 19 ตัวอย่างโดยการให้แรง 4 จุดโดยที่จุดทาบเหล็กอยู่ตรงกลาง และได้มีการแปรเปลี่ยนค่าระยะทาบ
ระยะคอนกรีตหุ้ม และระยะห่างระหว่างปลอกเหล็ก จากการทดสอบพบว่าปลอกเหล็กช่วยป้องกันการวิบัติจากแรงยึดเหนี่ยวได้
อย่างมีประสิทธิภาพและยังทำให้จุดทาบเหล็กมีความเหนียวอีกด้วย ในการศึกษาได้ใช้หลักการพลังงานเพื่อใช้อธิบายพฤติกรรม
แทนการใช้กำลังยึดเหนี่ยว และได้เสนอสมการเพื่อทำนายพลังงานที่เพิ่มขึ้นจากการโอบรัดด้วยปลอกเหล็ก จากนั้นได้นำ
สมการที่เสนอไปใช้ในการคำนวณปริมาณการโอบรัดด้วยปลอกเหล็กที่เพียงพอสำหรับการทาบเหล็กที่ไม่ได้มาตรฐาน ในส่วน
สุดท้ายของการวิจัยได้ศึกษาแบบจำลองไฟเบอร์โดยใช้โปรแกรม OpenSees ในการทำนายพฤติกรรมของเสาและคานที่มี
การโอบรัดด้วยปลอกเหล็ก โดยได้เสนอแบบจำลองและพารามิเตอร์ที่เหมาะสมภายหลังจากการสอบเทียบข้อมูลกับผลการ
ทดสอบ

| สาขาวิชา | วิศวกรรมโยธา | ลายมือชื่อนิสิต .... |
| ปีการศึกษา | 2565 | ลายมือชื่อ อ.ที่ปรึกษาหลัก .... |

6278808121 : MAJOR CIVIL ENGINEERING
KEYWORD: HSS collar, bond strength, lap-splice, splitting, beam, column, OpenSees,
                interfacial fracture energy
        Ali Ejaz : STRENGTHENING OF REINFORCED CONCRETE MEMBERS WITH LAP
        SPLICES USING STEEL COLLARS. Advisor: Prof. Anat Ruangrassamee, Ph.D.

Bond splitting failure of substandard lap splices have caused extensive damage to many structures during earthquakes. Existing methods to strengthen substandard lap splices primarily involve wrapping the substandard lap spliced regions with jackets possessing mainly in-plane stiffness. Hence, the efficiency of such techniques is compromised due to the lateral bulging of concrete and flexural bending of jackets. This study investigated hollow steel section (HSS) collars which offer axial and flexural stiffness in mitigating splitting failures associated with lap splices not conforming to current design codes. Three lap splice lengths, mainly 20, 28, and 35 times the bar diameter (d_b) were studied. Experiments were conducted on 19 beams subjected to four-point bending, with substandard lap splices within the constant moment region. Test variables involved the lap splice length, concrete cover, and spacing of HSS collars. Results revealed that HSS collars successfully prevented splitting failures resulting in ductile behavior. It was found that the bond stress of the lap-spliced bars increased till the onset of their yielding. Beyond that, the bond stress was maintained close to their peak value in the beams sufficiently confined by HSS collars. By applying HSS collars, improvements in the bond strength for beams with $20d_b$ lap splices were evident. The control beams having longer lap splice lengths exhibited yielding, and the improvement in their bond strength was limited despite showing ductile behavior. In order to capture the contribution of HSS collars to the improvement from brittle behavior to ductile behavior, the interfacial fracture energy was also used instead of the bond strength alone. An equation for the increase in the interfacial fracture energy due to the confinement by HSS collars was obtained using nonlinear regression. This equation was utilized to determine the required confinement ratio of HSS collars for a given substandard lap splice. The required confinement ratios of HSS collars obtained from the proposed equation were found to agree with the experiment while overestimation was found in some cases. Nonlinear fiber modeling using *OpenSees* was performed to predict the experimental load-deflection curves of beams. Several existing approaches were compared to estimate the strength of substandard lap-splices, whereas the splice strength in the case of insufficiently confined beams was predicted by an analytical approach based on interfacial fracture energy dissipated by lap-splices. An existing approach was adopted to estimate the compressive stress-strain response of HSS collar confined concrete by considering the axial and flexural stiffness of HSS collars. The proposed modeling strategy for beams resulted in close agreement with the experimental results. The same modeling concept as that for beams was adopted to model HSS collar strengthened RC columns in combination with pinching and strength degradation rules. An energy-based calibration was adopted to calibrate the predicted hysteretic response of RC columns. The pinching and hysteretic damage parameters for sufficiently confined columns were proposed. A good agreement between the predicted and experimental hysteretic response was obtained.

Field of Study:	Civil Engineering	Student's Signature ....
Academic Year:	2022	Advisor's Signature ....

ACKNOWLEDGEMENTS

TABLE OF CONTENTS

List of Figures

List of Tables

Chapter 1 Introduction

1.1. Problem Statement

Some past earthquakes have resulted in severe damage to reinforced concrete (RC) structures with substandard lap splices [1-4]. Old buildings commonly used lap splices at the column-footing junctions. Further, those splices were designed considering only gravity loads and the lap splice length l_s was limited to $20d_b$, where d_b is the diameter of the bar [5]. This insufficient lap splice length, together with the poor confinement, resulted in the catastrophic failure of many existing structures [6, 7]. Recent seismic provisions [8] do not permit the use of tension lap splices within the plastic hinge zones of columns in special moment resisting frames [9].

In post-earthquake field inspections, extensive damage due to bond failures has been reported [10]. A premature bond failure undermines the design capacity of reinforced concrete structures. Two types of bond failures are commonly observed for steel bars in tension, namely pullout failure and splitting failure [11]. Ample confinement in the form of concrete cover results in direct pullout failure. On the contrary, poor concrete confinement results in concrete splitting in the vicinity of the bar called splitting failure. Key factors affecting the resistance to splitting failure include the bar diameter, spacing between bars, and transverse reinforcement [12-14]. A lapped bar transfers force to concrete that transfers the force to the other lapped bar [15]. This causes radially outward pressures resulting in splitting cracks that originate at the loaded end and propagate along the lapped bars [16]. The similarity in the failure modes of a single bar and lapped bars has led current design provisions to use similar or greater development lengths for lapped bars as that of a single anchored bar [17].

During the previous earthquakes, the failure of a lap splice has been proved to be fatal. Figure 1.1(a) shows bond failure at the pier base during the 1989 Loma Prieta earthquake [5], Figure 1.1(b) shows the collapse of the Hanshin expressway during the 1995 Kobe earthquake due to insufficient lap splice length [3], Figure 1.1(c) shows the failure of a column due to lap splice failure during the 2003 Bingöl

(Turkey) earthquake [18], and Figure 1.1(d) shows another lap splice failure in a residential building during the 2015 Gorkha earthquake Nepal [10].

(a) (b) (c)

(d)
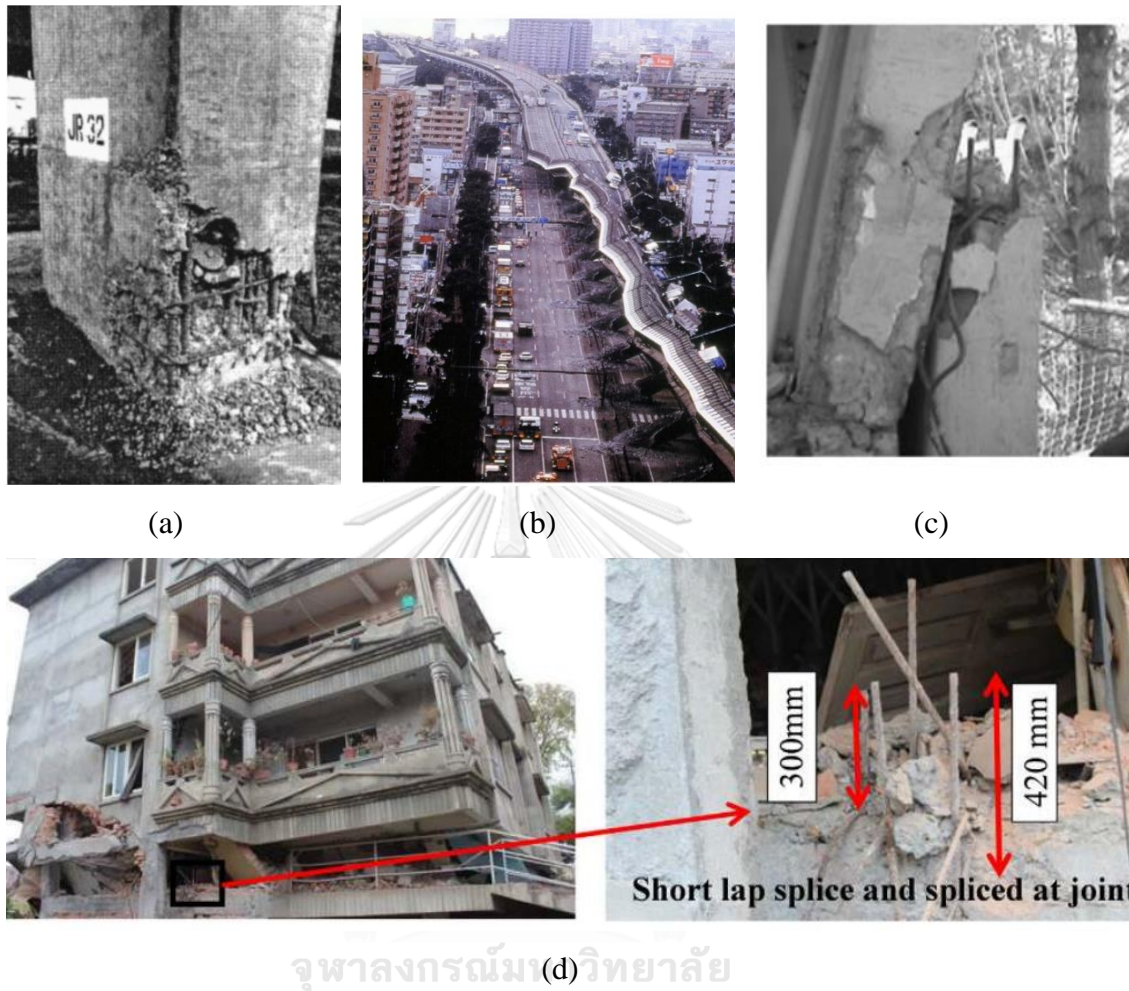
Figure 1.1 Lap splice failures observed in past earthquakes (a) 1989 Loma Prieta earthquake [5], (b) 1995 Kobe earthquake [3], (c) 2003 Bingöl (Turkey) earthquake [18], and (d) 2015 Gorkha earthquake Nepal [10].

Several techniques are available to strengthen the lap splices not conforming to the recent design guidelines. The mitigation was identified by jacketing the column surface externally in such a way that it keeps the concrete and transverse reinforcement from crushing and opening, respectively. This is achieved as the external jackets apply lateral confining pressures against the outward bursting forces from the concrete core. Conventional confinement techniques involve steel and reinforced concrete (RC) jackets covering critical bond regions. The steel and concrete jackets provide excellent strengthening solutions by restoring the strength

and ductility of RC members [19-28]. Despite possessing the potential to strengthen existing structures, the use of RC and steel jackets is limited, mainly attributed to the time of their application and by altering the stiffness of structures by enlarging the actual cross-sections [29, 30]. Fiber-reinforced polymer (FRP) jackets have gained interest over the last two decades, which is attributed to their noticeable strength-to-weight ratio, easy and rapid application, high resistance to corrosion, and high durability [31, 32]. In addition, FRP jackets do not change the look of the structure, and appreciably, the stiffness of the structure is not significantly altered [33]. In addition to the several advantages over the conventional strengthening techniques, FRP jackets have successfully eliminated splitting failures by providing adequate clamping pressures in the lap splice zones [34-38].

It is to be noted that existing jacketing techniques to strengthen substandard lap splices provide confinement through their in-plane stiffness mainly. This means that these jacketing techniques do not provide restraint to the out-of-plane bulging of concrete. This limitation has serious outcomes in the case of rectangular sections. Stress concentrations occur near sharp corners of rectangular sections and result in premature failure of these jackets [39]. To address this issue, the effectiveness of these jackets is improved by rounding off sharp corners [40-42]. It has been suggested that the degree of roundness is limited due to the presence of internal reinforcement [42]. As a result, another solution is to modify the rectangular cross-section to an oval or octagonal shape cross-section (see Figure 1.2) [20, 43].
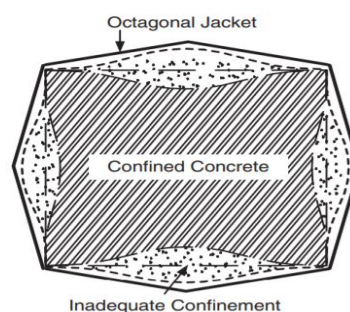
Figure 1.2 Modified cross-section to an octagonal shape [43].

Recognizing the issues related to the negligible flexural stiffness of jackets, Hussain and Driver [44] introduced flexural elements in the form of rectangular

hollow structural section collars, as shown in Figure 1.3. Hussain and Driver [44] strengthened RC columns with hollow structural section collars. A significant improvement in the peak compressive strength and ultimate strain of concrete was observed due to the confinement by hollow structural section collars.
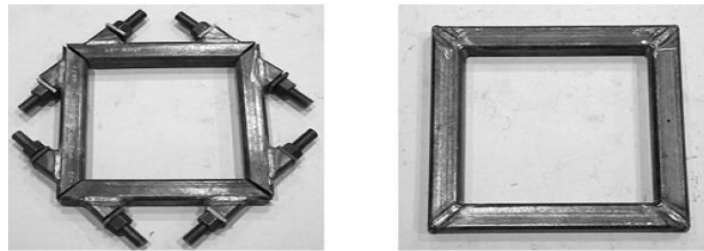
Figure 1.3 Hollow structural sections used by Hussain and Driver [44].

1.2. Objectives of the Study

Recognizing the benefits related to the flexural stiffness of hollow steel section (HSS) collars, it is evident that using steel collars to prevent bond splitting failures can be an effective solution. At present, no detailed studies are available to examine the effectiveness of steel collars in preventing splitting failure. The objectives of the present study are

- To investigate the efficiency of hollow steel section (HSS) collar confinement in preventing the brittle splitting failure associated with substandard lap splices

- To propose an expression from experimental results for the increase in interfacial fracture energy as a function of HSS collar parameters (spacings and cross-sectional area).

- To propose a design equation estimating the required confinement of HSS collars to strengthen substandard lap splices.

- Perform fiber-based non-linear analysis for HSS confined beams and columns and validate the correlation between analytical and experimental results.

1.3. Scope of the Study

The scope of the present study is

- The efficiency of HSS collars will be assessed in preventing splitting failures associated with substandard lap splices by using beam splice tests.
- The present study targets lap splices with concrete cover to diameter ratios ranging from 1.0 to 1.62 and lengths ranging from $20d_b$ to $35d_b$.
- Those columns and beams will be considered that are controlled by flexure.
- The fiber-based non-linear analysis will be performed for columns and beams with substandard lap splices confined with HSS collars using distributed plasticity methods only.

จุฬาลงกรณ์มหาวิทยาลัย

CHULALONGKORN UNIVERSITY

Chapter 2 Literature Review

Pre-1970 construction followed practices that involved the provision of substandard lap splices at critical locations in reinforced concrete members. For instance, lap splices provided at the base of bridge piers and columns to allow the continuity of the load-bearing mechanism were short. As a result, the capacity of the component was undermined due to the premature failure of lap splices. During past earthquakes, many instances of the premature failure of lap splices were reported leading to a partial or full collapse of the structure [3, 5, 10, 18] as discussed in Section 1.1. Subsequently, research works were initiated to counter premature lap splice failure by using external jacketing techniques. This chapter first presents research works that provide a comparison of the behavior of substandard lap splice columns with that of continuous longitudinal bars and demonstrate the strength and ductility degradation due to premature lap splice failure. Then, various existing jacketing techniques to strengthen substandard lap splices are discussed. This is followed by a discussion to highlight the shortcomings associated with existing jacketing techniques. Then, existing studies to strengthen RC columns by using hollow steel section (HSS) collars are discussed. Finally, non-linear fiber modeling of RC members is discussed, followed by a technique to model the concrete behavior confined by HSS collars.

2.1. Specimens to Study Bond Characteristics

Researchers have used different types of specimens to study bond characteristics between a steel bar and surrounding concrete. The specimens can be mainly divided into four categories: (1) pull-out specimens, (2) beam end specimens, (3) beams with anchored bars, and (4) beams with lap spliced bars.

Pull-out specimens were often used to study bond characteristics due to the ease of their fabrication, as shown in Figure 2.1. In the pull-out specimen, a single bar is anchored at the center of a concrete prism of known length. The bar is pulled out of the specimen, and the pull force and strain inside the bar are measured. Though this is the easiest way to study bond, it has a major drawback. The pull-out force is applied

at the expense of a compressive reaction on the concrete prism face. This compressive reaction results in compressive stress from the loading surface to the steel bar. As a result, the concrete surrounding the steel bar is placed in compression while the steel bar is in tension. This does not reflect the actual condition of steel bars in tension in RC members. Further, the compressive struts result in an increase in the bond strength [45].
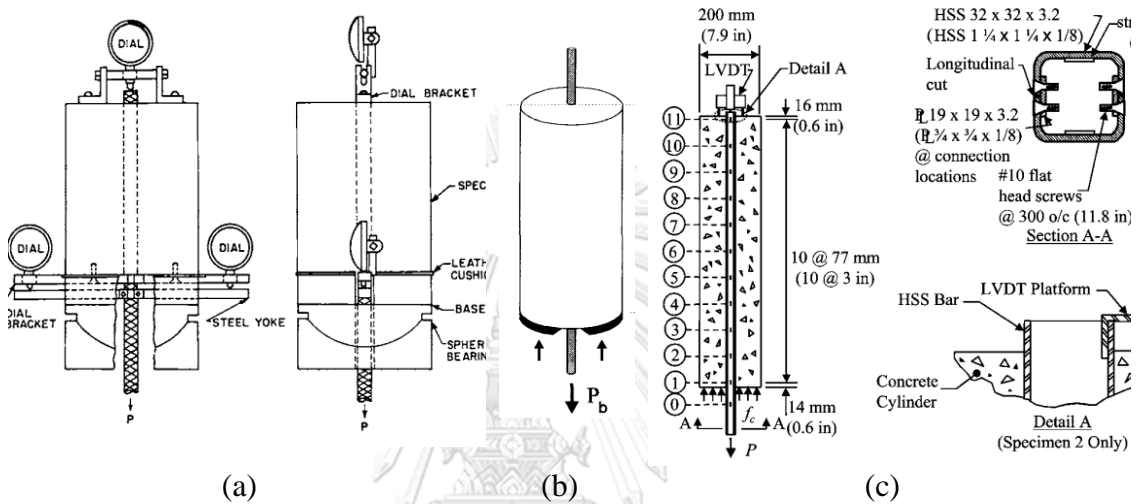
Figure 2.1 Pull-out specimens used by (a) Mathey and Watstein [46], (b) Abrishami and Mitchell [47], and (c) Feldman and Bartlett [48].

The second specimen type is beam-end specimens, as shown in Figure 2.2. This type of specimen can prevent the drawbacks associated with pull-out specimens. However, it requires a bond-free length near the surface to avoid conical failures.
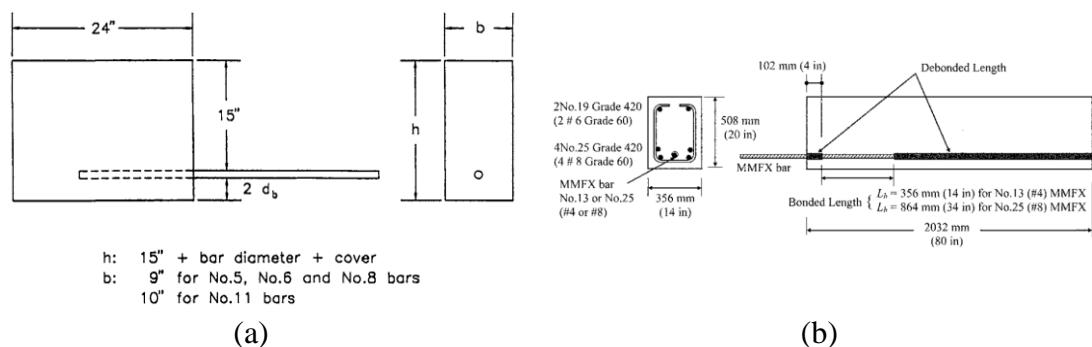
Figure 2.2 Beam-end specimens used by (a) McCabe et al. [49] and (b) Rizkalla et al. [50].

According to ACI 408R-03 [45], beam splice specimen provides accurate bond strength, and a bulk of data on bond has come from beam splice specimens. Given this, many researchers have adopted beam splice specimens to study the effect of external confinement on the bond strength between lap splices and surrounding concrete [51]. For instance, Figure 2.4 shows beam splice specimens used by researchers. ACI 408R-03 [45] recommends using either beam anchorage or beam splice specimens to study the bond, as shown in Figure 2.3.
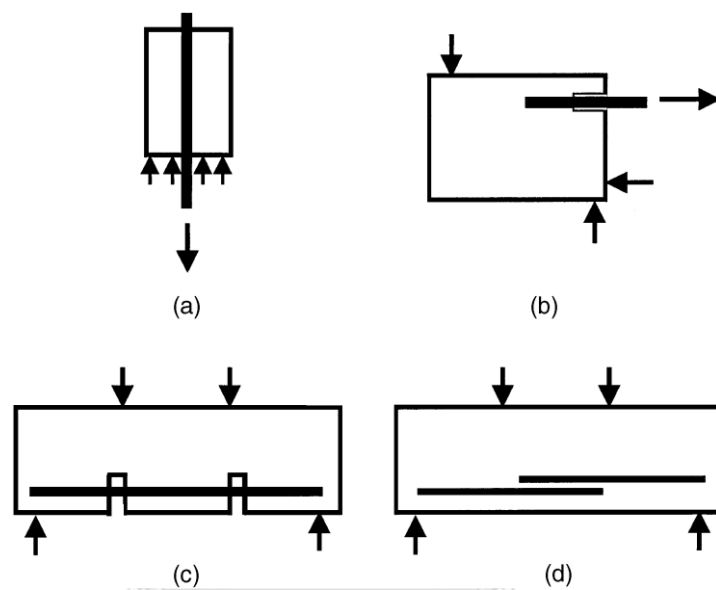
Figure 2.3 Types of specimens used to study bond between steel bars and concrete (a) pull-out specimen, (b) beam end specimen, (c) beam anchorage specimen, and (d) beam splice specimen [45].

(a)

(b)

(c)

(d)
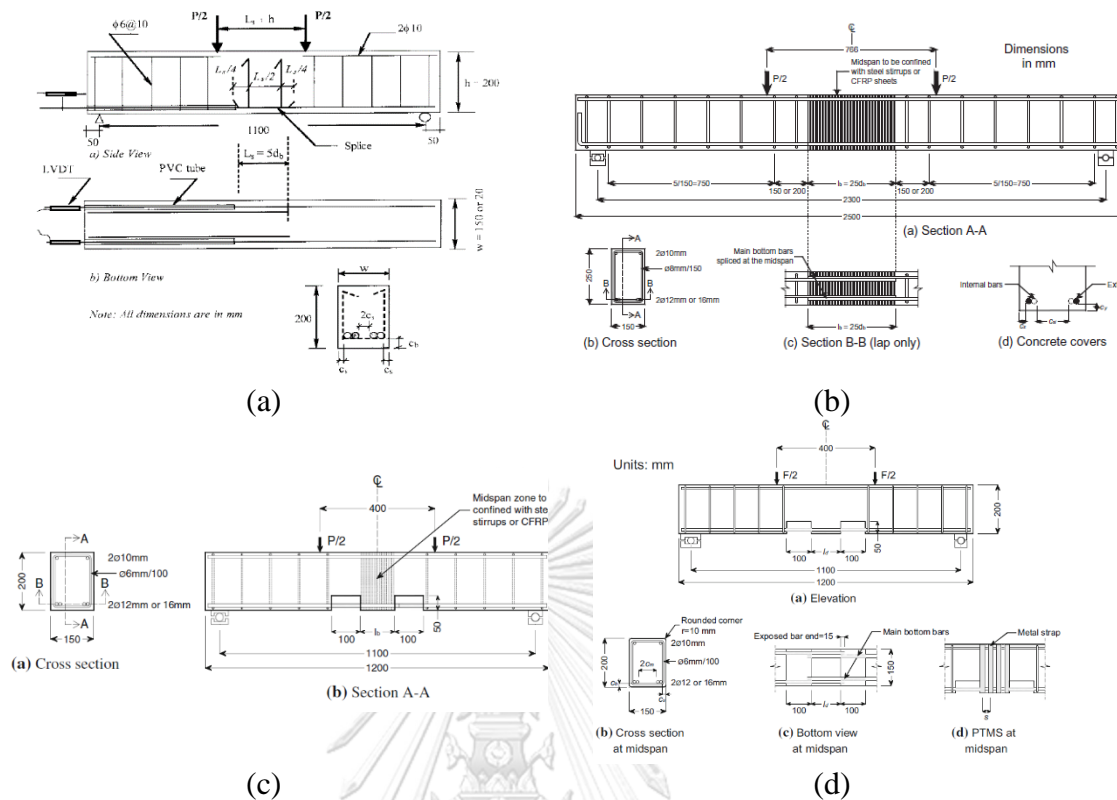
Figure 2.4 Beam splice specimens used by (a) Harajli et al. [51], (b) Garcia et al. [52], (c) Garcia et al. [53], and (d) Helal et al. [54].

2.2. Study of Bond Strength Using Beam Splice Tests

Esfahani and Rangan [55] tested 22 simply supported beams subjected to four-point bending. Each beam furnished a short lap splice within the constant moment region, as shown in Figure 2.5. Strain gages were installed at the ends of lap splices to record strains. The measured strains were converted to stresses, and by taking the equilibrium between the steel stress and bond strength, the bond strength values were determined. The study determined that the bond strength reduced as the length of the lap splice increased.
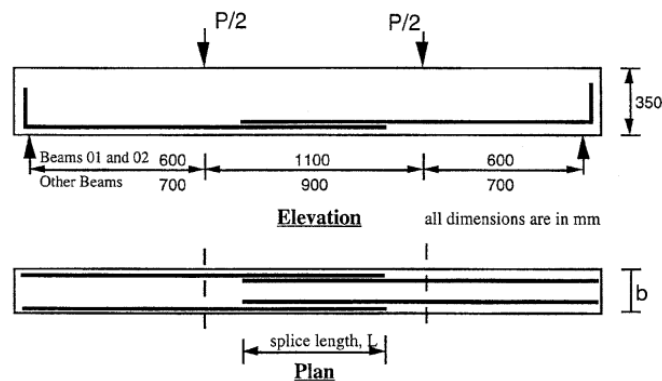
Figure 2.5 Beam splice specimens tested by Esfahani and Rangan [55].

Hamad [56] tested 13 simply supported beams with constant moment regions in the middle, as shown in Figure 2.6. All beams furnished a substandard lap splice of 305 mm corresponding to lap splice length to steel bar diameter ratio of 15. This splice length was selected to ensure the splitting mode of failure before attaining the yield stress in lap spliced bars. The bond strengths were calculated from experimental results, and it was found the rib face angle on lap spliced bars affected the behavior of lap spliced beams. A beam with lap splices having a rib face angle of 60° performed better than the beam with lap splices having a rib face angle of either 45° or 90°.
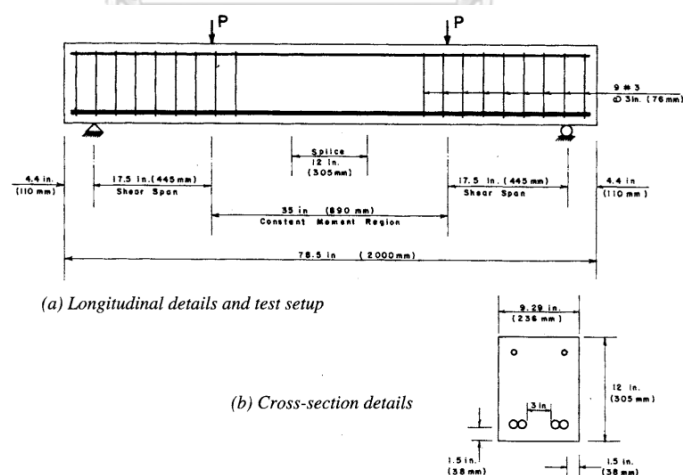
Figure 2.6 Beam splice specimens tested by Hamad [56].

Harajli et al. [57] investigated the bond-slip response of lap splices in unstrengthened concrete and concrete strengthened with internal steel fibers. Thirty-two lap spliced beams were tested, and the influence of concrete cover, bar diameter,

and the volume of steel fibers on bond strength was evaluated. Typical specimen details are shown in Figure 2.7. The study revealed that the bond strength of lap spliced bars increased with the concrete cover-to-diameter ratio and by increasing the volume fraction of internal steel fibers.
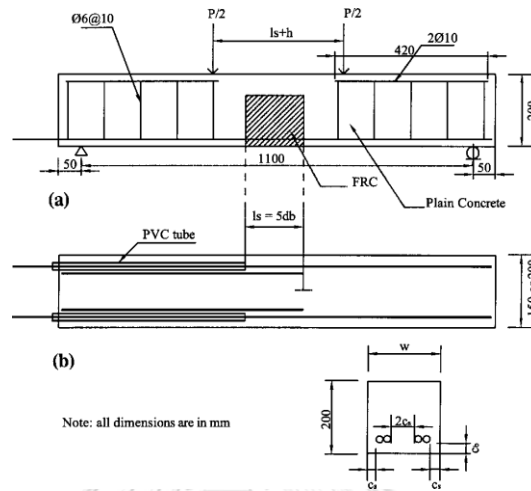
Figure 2.7 Beam splice specimen tested by Harajli et al. [57].

Based on the shape of the bond stress-slip response, Harajli et al. [57] proposed a bond stress-slip law, as shown in Figure 2.8. For each point on the bond stress-slip curve, separate equations were proposed by performing nonlinear regression analysis on test data. Harajli et al. [57] proposed Eq. 2.1 for the bond strength in unstrengthened concrete and Eq. 2.2 for bond strength in internal steel fiber reinforced concrete.

$$u_{max} = 0.75\sqrt{f_c'}\left(\frac{c}{d_b}\right)^{2/3} \qquad\qquad 2.1$$

$$u_{\max(FRC)} = c_f u_{\max(unstrengthened)} \qquad\qquad 2.2$$

where c is the concrete cover, d_b is the diameter of the lap spliced bar, and $c_f = 1.00$ for $\frac{V_f L}{d_f} \leq 0.25$; and $c_f = 1 + 0.34\sqrt{\frac{V_f L}{d_f} - 0.25}$ for $\frac{V_f L}{d_f} > 0.25$, where V_f is the volumetric ratio of steel fibers. L is the length of steel fibers, and d_f is the diameter of steel fibers.
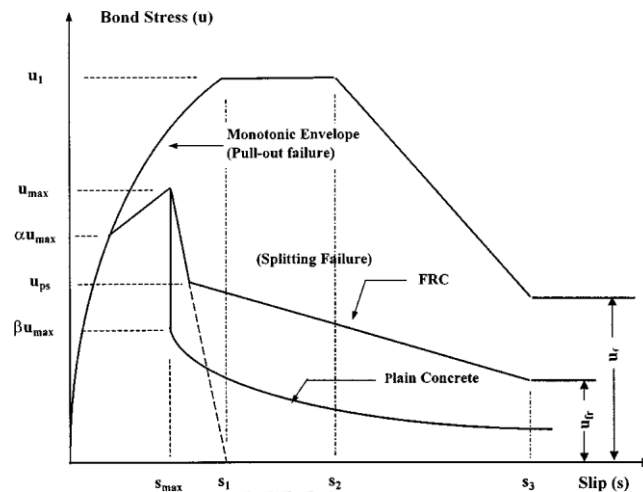
Figure 2.8 Bond stress-slip law proposed by Harajli et al. [57].

Hamad et al. [58] investigated the improvement in the bond strength of lap spliced bars due to the confinement by FRP wraps. For this purpose, simply supported beams were tested under four-point bending with a lap splice within the constant moment region, as shown in Figure 2.9. A total of ten beams were tested with a lap splice length of $15d_b$. The type (glass or carbon), configuration (one strip, two strips, or continuous), and the number of FRP wraps were taken as the main parameters. It was found that both glass and carbon FRP wraps were effective in improving the bond strength ductile behavior of substandard lap spliced beams.
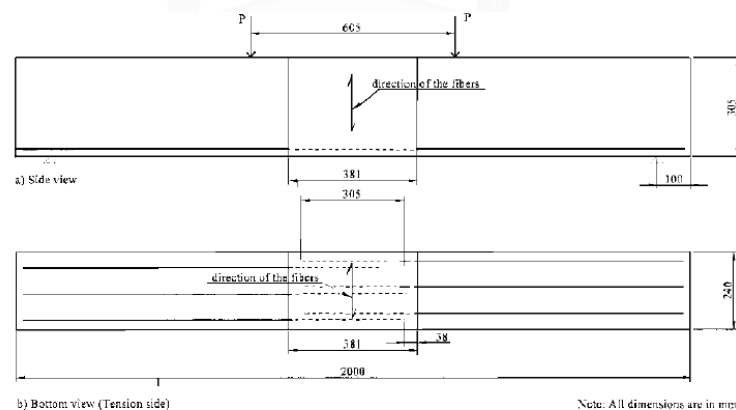
Figure 2.9 Beam splice specimens tested by Hamad et al. [58].

Harajli [59] tested 14 beams in two groups depending on the size of the bottom longitudinal bars. Each beam was simply supported, as shown in Figure 2.10,

with a short lap splice length of $5d_b$. Confinement in the form of internal steel ties or external CFRP wraps was provided, and the resulting improvement in the bond strength of lap spliced bars was evaluated. Nonlinear regression analysis was performed to propose Eq. 2.3 for the prediction of improvement in bond strength due to internal or external confinements.

$$u_{max} = 0.78\sqrt{f_c'}\left(\frac{c + k_c}{d_b}\right)^{\frac{2}{3}} \qquad\qquad 2.3$$

$$k_c = \frac{7.0A_{tr}}{sn_s}; \quad for\ internal\ steel\ confinement \qquad 2.4$$

$$k_c = \frac{56.0r_e n_f t_f}{n_s}; \quad for\ CFRP\ confinement \qquad 2.5$$

where A_{tr} is the area of internal reinforcement, n_s is the number of lap spliced pairs, s is the center-to-center spacing of internal reinforcement, r_e is the ratio of elastic modulus of CFRP material to the elastic modulus of steel, n_f is the number of CFRP wraps, and t_f is the thickness of a single CFRP wrap.
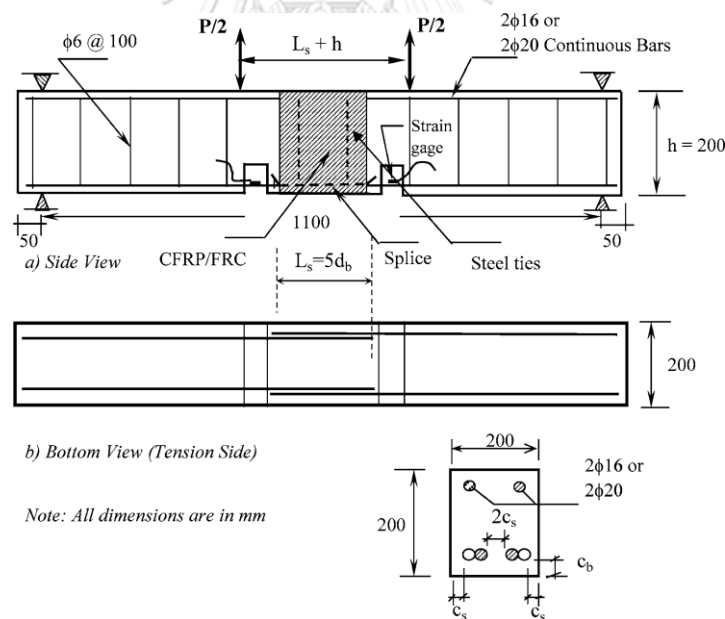
Figure 2.10 Beam splice specimens tested by Hrajli [59].

Garcia et al. [53] explored the bond behavior of lapped bars using fifteen RC beams tested in flexure. Twelve of the beams were designed in a way to fail by bond splitting at midspan, where the main flexural reinforcement was spliced at $10d_b$. The parameters examined involve the amount and type of confinement at midspan (no

confinement, internal steel stirrups, or externally bonded carbon FRP), concrete cover, and bar size. The geometry of specimens tested in this study is shown in Figure 2.11. To inspect the effects of concrete to diameter ratio (c/d_b), concrete covers of 10 mm and 20 mm were selected for the beams reinforced with 12 mm bars, whereas 27 mm was used for the beams reinforced with 16 mm bars. For each beam, the side and bottom covers were chosen to be approximately equal. The average bond stress along the lapped bars was found by assuming a uniform bond stress distribution along the lap length using the following equation:

$$\tau = \frac{f_s d_b}{4l_s} \qquad\qquad 2.6$$

where f_s is the stress in lap spliced bars, d_b is the diameter of lap spliced bars, and l_s is the lap splice length. To quantify the effects of CFRP confinement in enhancing the bond strength between the steel bar and concrete, a strain control approach was adopted. Confinement force applied by CFRP over its length (splice length in this case) is:

$$f_l = area \times effective\ stress = 2nt_f l_b f_{fe} = 2nt_f l_b \times \left(\epsilon_{fe} \times E_f\right) \qquad 2.7$$

where n=number of layers of CFRP, t_f=thickness of single CFRP sheet, ϵ_{fe}=effective strain in CFRP sheet, E_f=modulus of elasticity of CFRP, l_b=length of CFRP sheet (equal to splice length in this study), and ϵ_{fe} was taken equal to strain in concrete at splitting strength. The confinement force per splice is then given by:

$$confined\ force\ per\ splice = \frac{f_l}{n_b} = \frac{2nt_f l_b \,\epsilon_{ctm}\, E_f}{n_b} \qquad 2.8$$

Correspondingly, confinement stress is obtained by dividing the confinement force by the area of split as

$$confinement\ stress\ per\ splice = f_o = \frac{2nt_f l_b \,\epsilon_{ctm}\, E_f}{n_b A_{spl}}$$
$$= \frac{2nt_f l_b \,\epsilon_{ctm}\, E_f}{(n_b \times 2(c_{min} + d_b))l_b} \qquad 2.9$$

To quantify the effect of external CFRP jacket on bond strength enhancement $\Delta\tau_{spl}$, the following equation was proposed based on regression analysis.

$$\frac{\Delta\tau_{spl}}{\sqrt{f_c'}} = 1.15 \times \sqrt{f_o} \le 0.4 \qquad\qquad 2.10$$
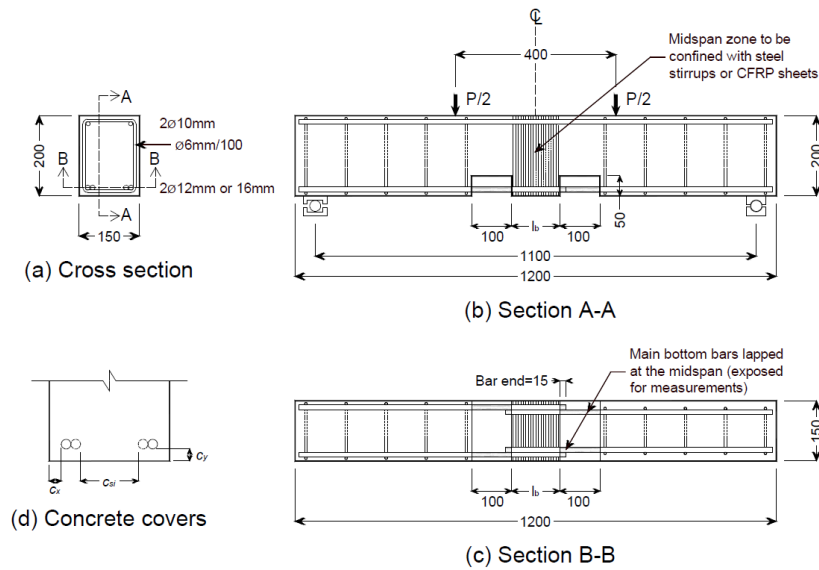
Figure 2.11 Beam splice specimen tested by Garcia et al. [53].

Helal et al. [54] tested 12 simply supported beams under four-point bending with a lap splice length of $10d_b$. In this study, post-tensioned metal straps were used to strengthen the substandard lap splices as shown in Figure 2.12. The results revealed that post-tensioned metal straps resulted in an increase of up to 60% in bond strength. Nonlinear regression analysis was performed to propose equations for the enhancement in bond strength due to post-tensioned metal straps confinement τ_{PTMS} as

$$\frac{\tau_{PTMS}}{\sqrt{f_c'}} = \frac{Nf_p t}{456n(c_{min}+d_b)}\left[1+\frac{\left(\frac{150d_b}{l_s}-12.6\right)c_{min}}{d_b}+\frac{2}{3}\left(\frac{l_s}{d_b}\right)\right] \qquad 2.11$$

where N is the number of metal straps, f_p is the post-tension force, and t is the thickness of metal straps.
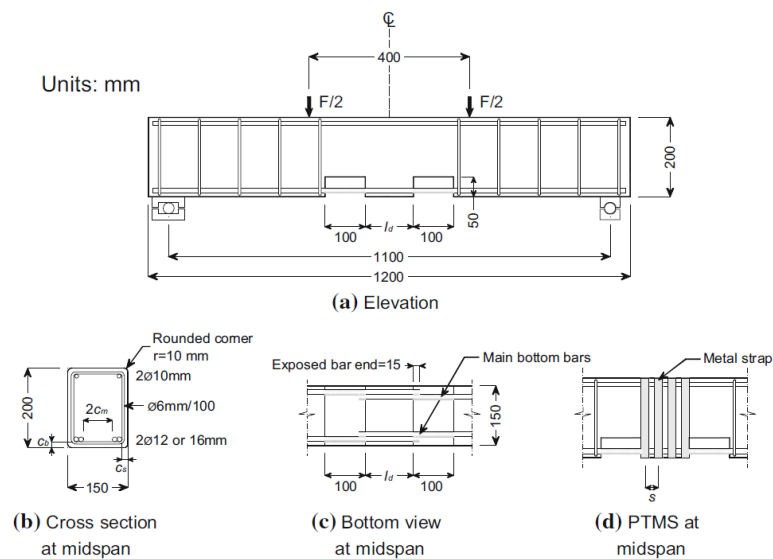
Figure 2.12 Beam splice specimens tested by Helal et al.[54].

2.3. Behavior of Columns with Substandard Lap splices

In this section, existing studies that tested RC columns with substandard lap splices and without strengthening are discussed. Experimental results related to unstrengthened substandard lap spliced columns and their corresponding columns with continuous reinforcement are discussed.

Chai et al. [19] tested circular RC columns with a 610 mm diameter and 3657 mm height, as shown in Figure 2.13(a). The columns were scaled down by a factor of 0.4 of the actual 1524 mm diameter column. Columns were subjected to an axial load corresponding to 18% of the weight of the column. The hysteretic load-deflection responses of the column with continuous reinforcement and with a substandard lap splice are shown in Figure 2.13(b) and Figure 2.13(c), respectively. The substandard lap splice column failed at a lateral load capacity of 218 kN and achieved a ductility of 1.5. In comparison, the column with continuous longitudinal reinforcement achieved a lateral load capacity that exceeded the theoretical capacity by 6%. In addition, a lateral load was maintained till a ductility of 5.0.
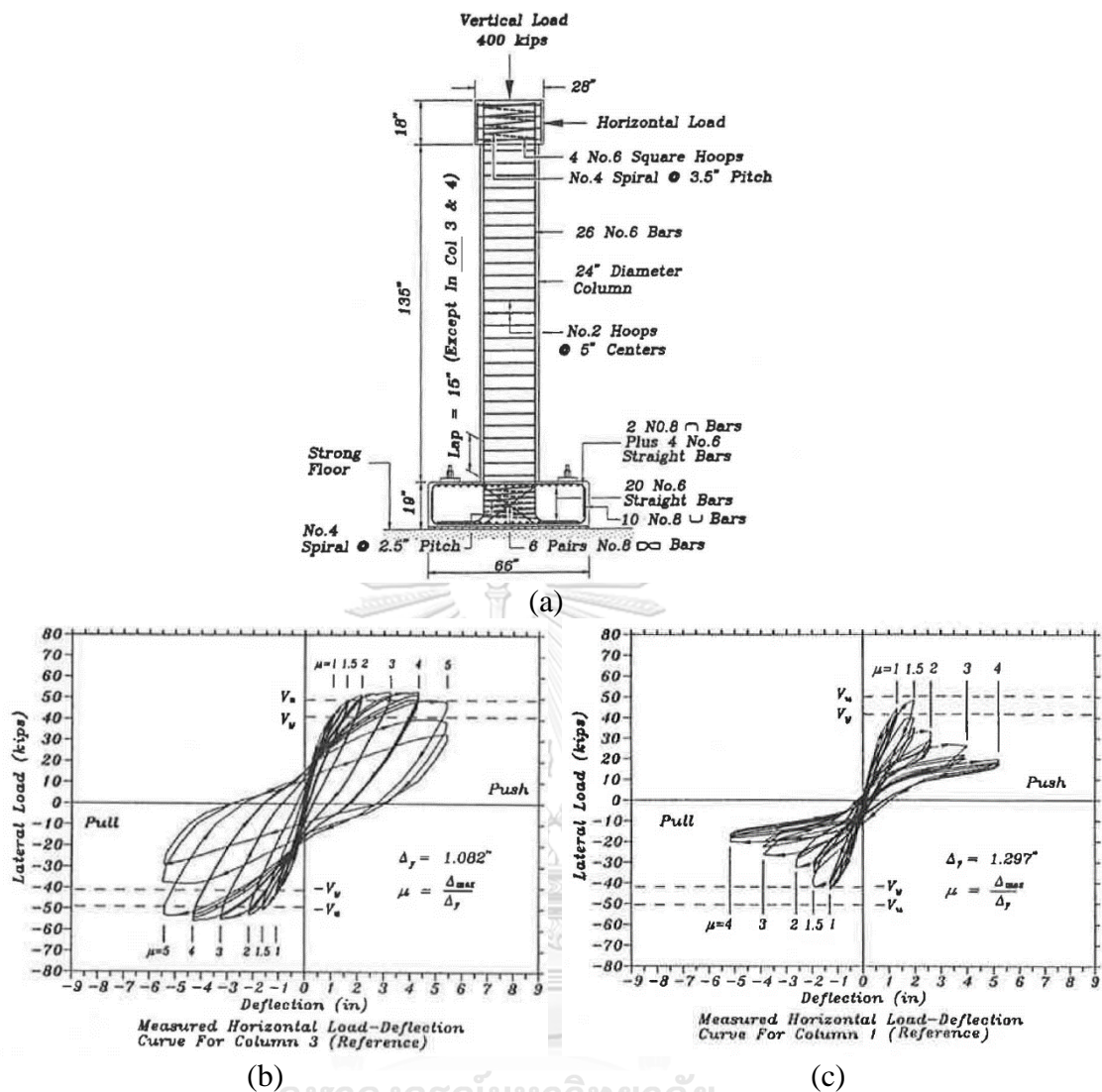
Figure 2.13 RC columns tested by Chai et al. [19] (a) details, (b) with continuous reinforcement into the footing, and (c) with a substandard lap splice.

Lynn et al. [60] tested square RC columns with and without a substandard lap splice of $20d_b$ at the junction with footing. Figure 2.14(a) presents structural details of tested specimens. Figure 2.14(b) presents the hysteretic response of Specimen 2CLH18, i.e., with continuous reinforcement, whereas the hysteretic response of Specimen 2SLH18, i.e., with $20d_b$ lap splice, is presented in Figure 2.14(c). Specimen 2CLH18 exhibited more cyclic strength degradation as compared to Specimen 2SLH18. The ductility achieved by Specimen 2CLH18 was 4.0 as compared to the ductility of 3.5 of Specimen 2SLH18.
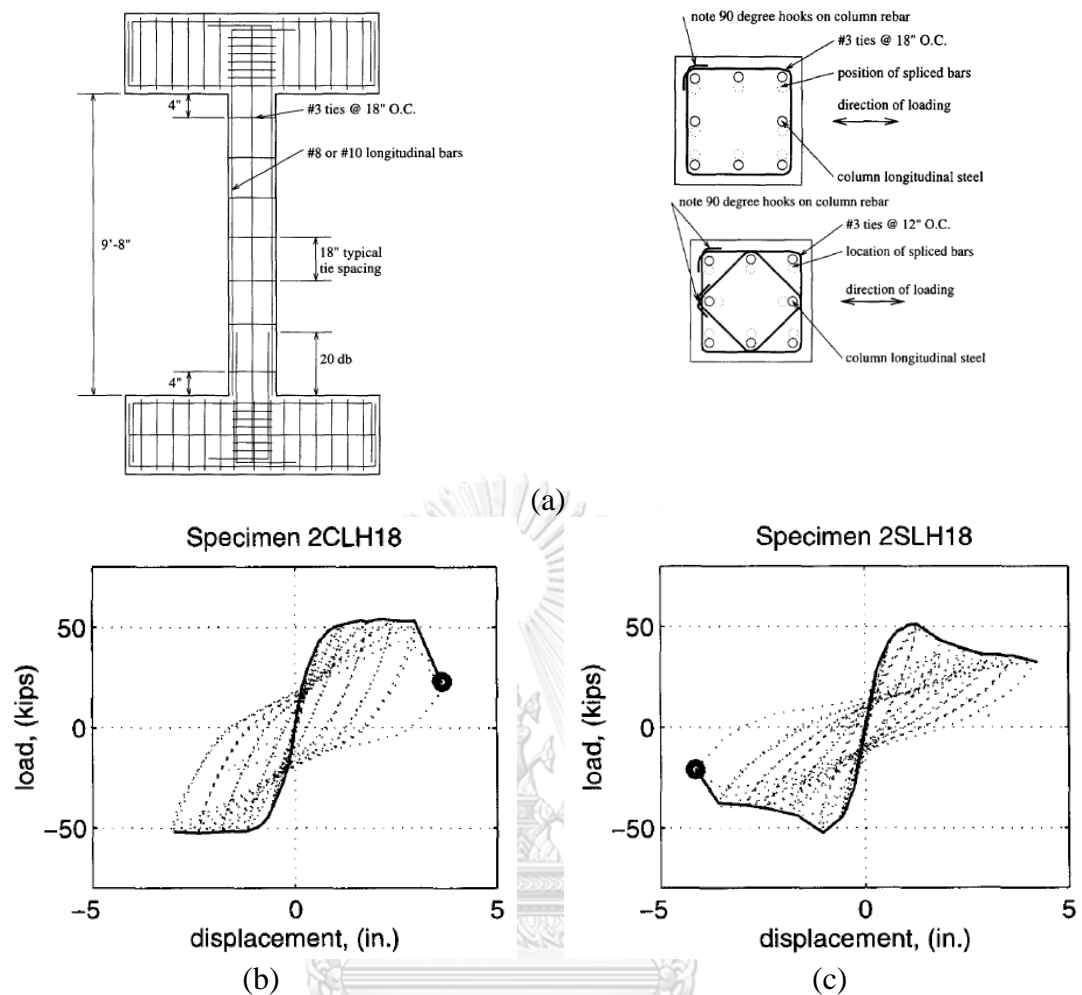
Figure 2.14 RC columns tested by Lynn et al. [60] (a) details, (b) with continuous reinforcement into the footing, and (c) with a substandard lap splice.

Ghobarah et al. [61] tested rectangular RC columns with a $40d_b$ lap splice. The tested column was representatives of ground story columns in an existing two-story building. The structural details of the tested lap spliced column are shown in Figure 2.15(a). Another column with structural details conforming to the earthquake-resistant design was also tested as a reference. An axial load of 8.0% of the column weight was applied at the top of each column. For the lap spliced column, rapid degradation of the lateral load capacity was observed near the ductility of 4.0, whereas the code conforming column did not exhibit a considerable drop in lateral load capacity till a ductility of 10.0.
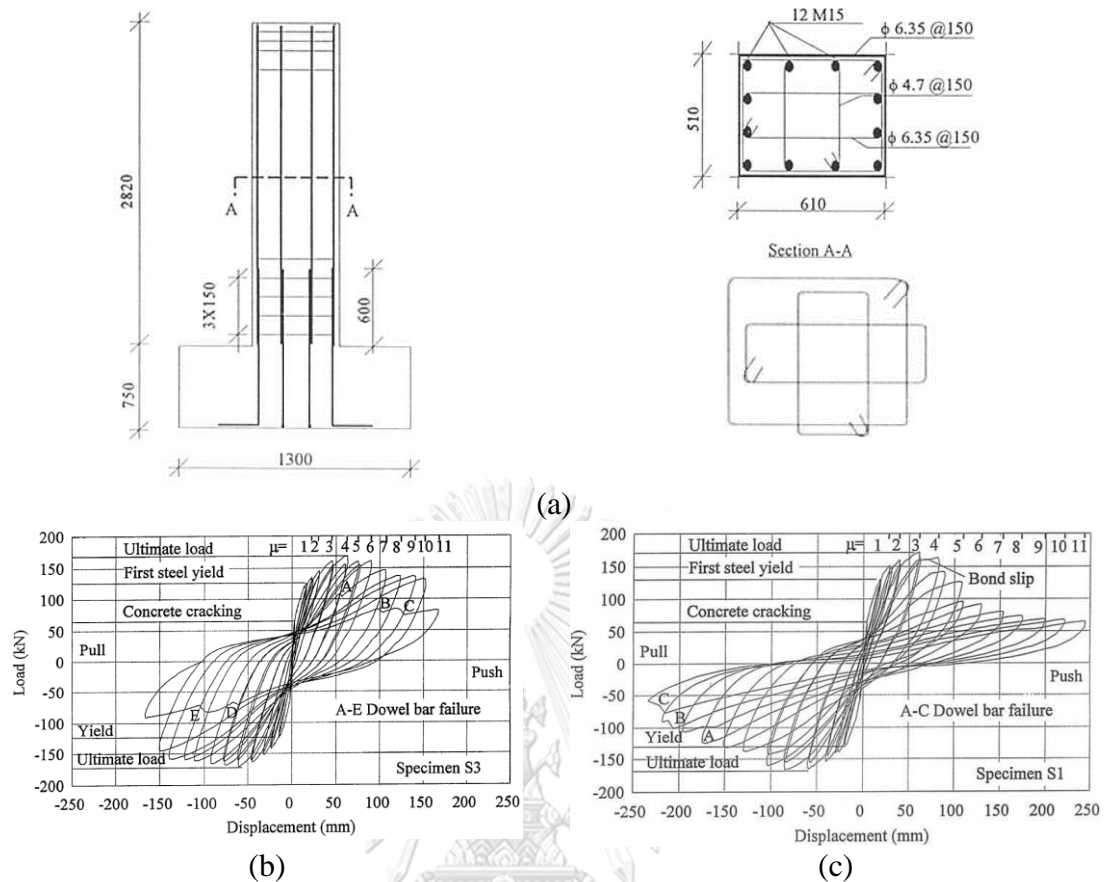
Figure 2.15 RC columns tested by Ghobarah et al. [61] (a) details, (b) with earthquake resistant design, and (c) with a substandard lap splice.

Harries et al. [35] performed cyclic tests on square RC columns with and without a $22d_b$ lap splice. An axial load of about 22% of the column self-weight was applied to each column. Reverse cyclic load was applied at the height of 2440 mm to produce a large shear span-to-depth ratio. In this study, the specimen with continuous reinforcement F0 was also poorly detailed by the transverse reinforcement. As shown in Figure 2.16(b), Specimen F0 achieved its nominal capacity but failed due to the crushing of concrete and buckling of longitudinal reinforcement. Specimen L0 was provided with a $22d_b$ lap splice, which was about 42% of the lap splice length required by ACI 318-19 [62]. The lap spliced specimen failed by exhibiting splitting cracks along the height of the column and was unable to achieve its theoretical flexural capacity.
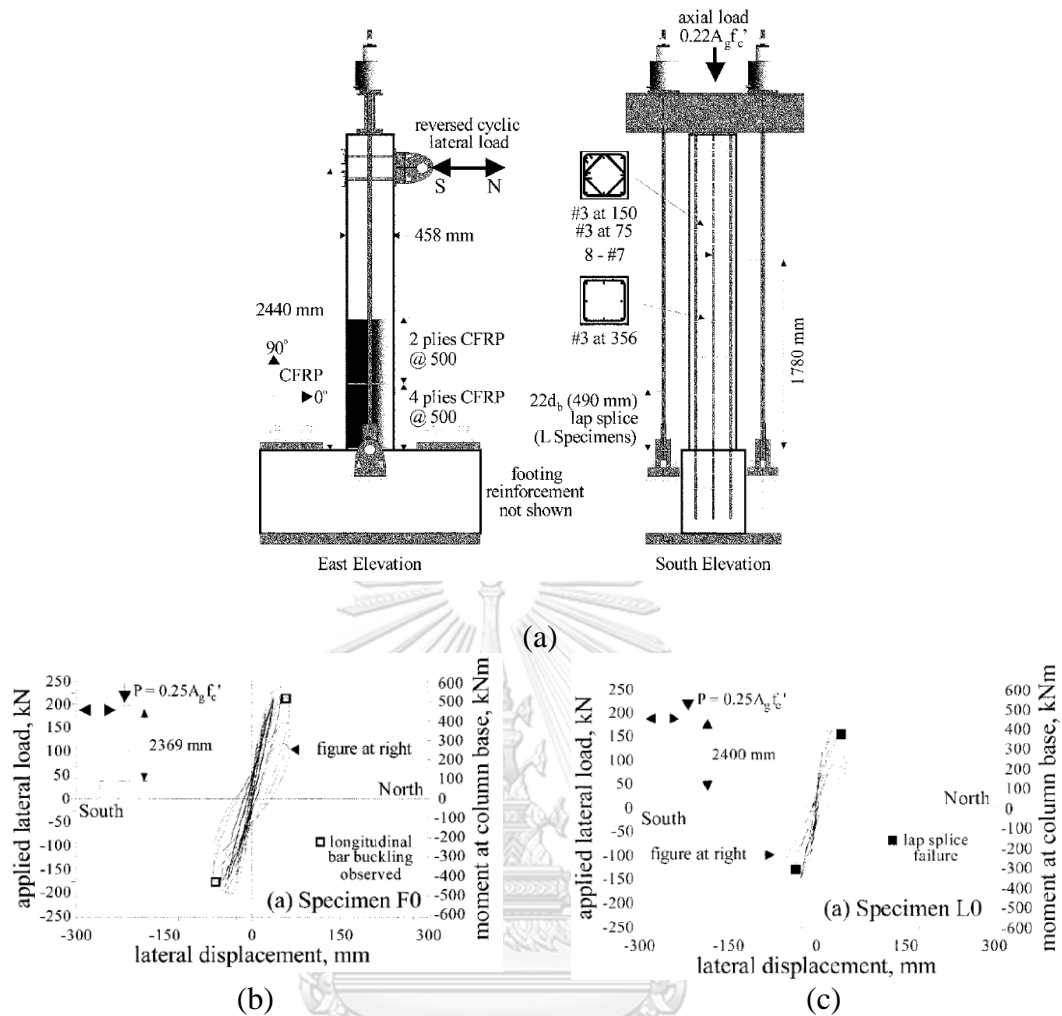
Figure 2.16 RC columns tested by Herries et al. [35] (a) details, (b) with continuous reinforcement, and (b) with a substandard lap splice.

Harajli [63] tested rectangular RC columns with geometry as shown in Figure 2.17(a) in three groups I, II, and III. In each group, one specimen was tested in as-built condition with a substandard lap splice of $30d_b$, whereas another specimen was constructed with earthquake resistant design (Type E). The details of other retrofitted specimens are not given here. The peak load sustained by Specimen C20E was 143.3 kN, whereas Specimen C20 failed at the maximum load of 87.3 kN. From the measured strains along the lap spliced bars, it was found that the maximum strain recorded in Specimen C20 was well below the yield strain. As a result, Specimen C20 did not exhibit ductile response.
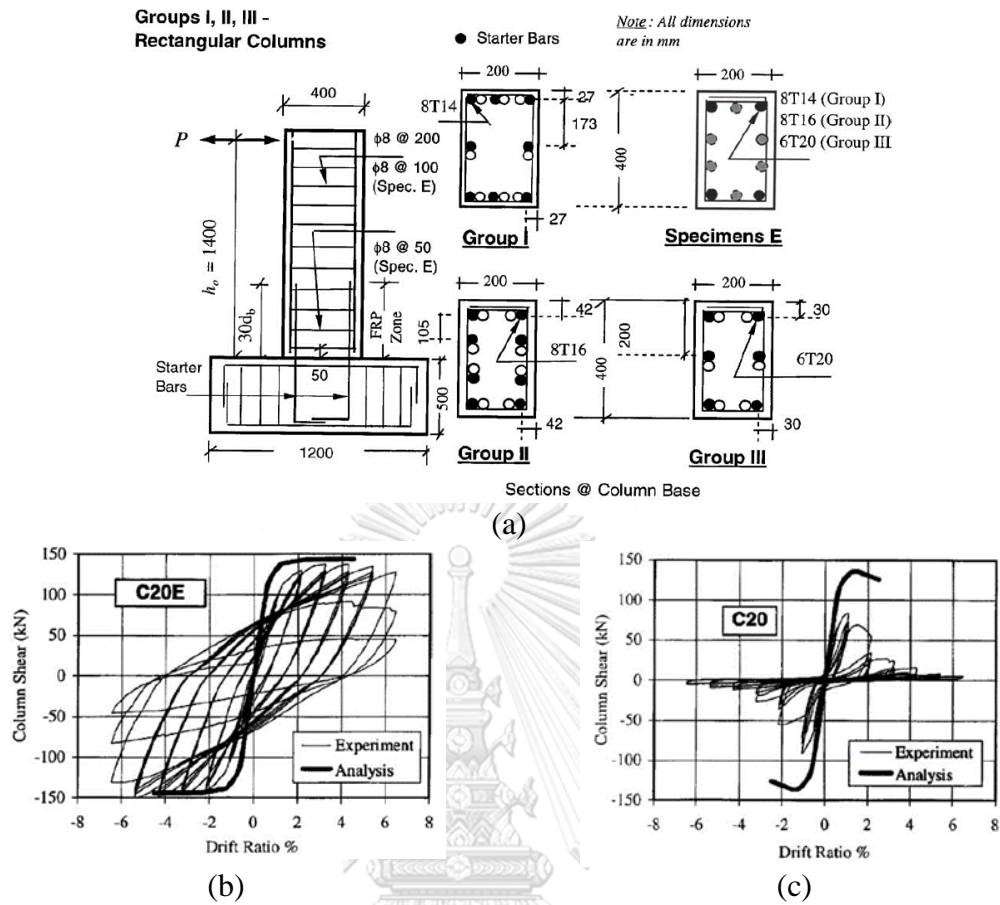
Figure 2.17 RC columns tested by Harajli [63] (a) details, (b) with earthquake resistant design, and (b) with a substandard lap splice.

Choi et al. [64] tested circular RC columns with structural details, as shown in Figure 2.18(a). The diameter of the columns was 400 mm, and a height of 1400 mm. Specimen SP50-N corresponds to a specimen with 50% of the longitudinal bars spliced at the base with starter bars. Specimen SP00-N was similar to Specimen SP50-N, except no bar splicing was performed at its base. Figure 2.18(b) shows the hysteretic response of Specimen SP00-N, whereas the hysteretic response of Specimen SP50-N is shown in Figure 2.18(c). The maximum load sustained by Specimen SP00-N was 132.2 kN as compared to the value of 107.8 kN for Specimen SP50-N. Moreover, Specimen SP00-N demonstrated a displacement ductility of 6.97, whereas Specimen SP50-N could only demonstrate a displacement ductility of 3.19 and failed in a brittle manner due to bond failure.
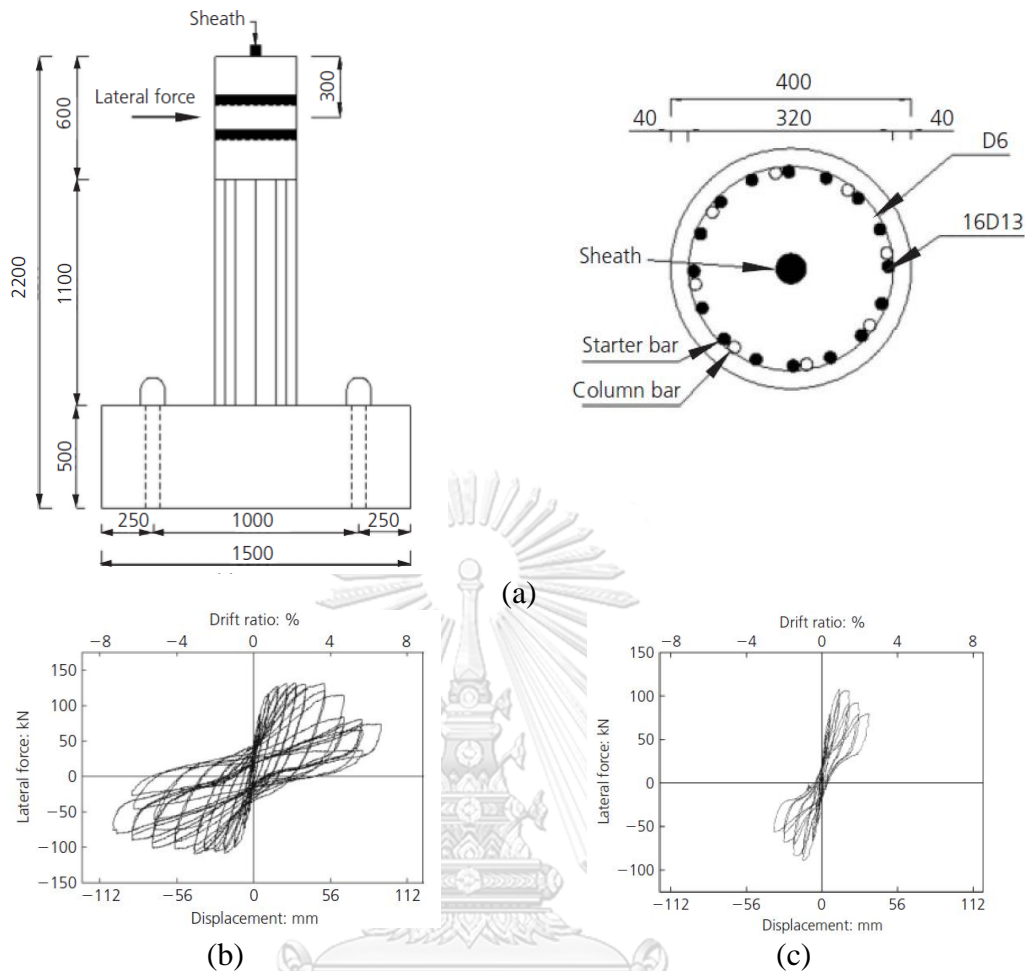
Figure 2.18 RC columns tested by Choi et al. [64] (a) details, (b) with earthquake resistant design, and (b) with a substandard lap splice.

Several other studies have also reported premature lap splice failure in RC columns. A summary of research works conducted on testing RC columns with substandard lap splices is shown in Table 1. Table 1 provides the provided lap splice length l_s and lap splice length required by ACI 318-19 $l_{s,ACI}$ [62] given as

$$\frac{l_{s,ACI}}{d_b} = \frac{9}{10}\frac{f_y}{\sqrt{f_c'}\left(\frac{(c+k_{tr})}{d_b}\right)} \qquad 2.12$$

where c is concrete cover taken as the smallest of bottom concrete cover, side concrete cover, or half the clear spacing between consecutive pairs of lap splices; f_y is the yield strength of steel bars; f_c' is the compressive strength of concrete; d_b is the diameter of steel bars; and k_{tr} is a parameter that accounts for the effect of transverse reinforcement. The last column reports a parameter R_{ls} which is the ratio of provided

lap splice length l_s to that required by ACI 318-19 [62] $l_{s,ACI}$. The R_{ls} values ranged from 0.16 to 0.78 in previous studies as shown in Table 2.1. It is to be noted that l_s values in the literature were based on old construction practices. Further, all the columns of studies in Table 2.1 failed in a brittle manner due to bond failure. Therefore, it can be established that a lap splice failure is expected for R_{ls} ranging from 0.16 to 0.78.

Table 2.1 Summary of R_{ls} values in existing studies.

Study	l_s (d_b)	$l_{s,ACI}$ (d_b)	R_{ls}
Chai et al. [19]	20	48	0.41
Aboutaha et al. [21]	24	70	0.35
Lynn et al. [60]	20	57	0.34
Xiao et al. [65]	20	31	0.64
Daudey et al. [24]	25	45	0.56
Malek et al. [7]	20	77	0.26
Haroun et al. [5]	20	46	0.44
Harries et al. [35]	22	49	0.45
Harajli [63]	30	99	0.31
ElGawady et al. [37]	35	45	0.78
Kim et al. [38]	24	47	0.51
Bournas and Triantafillou [66]	20	125	0.16
Juntanalikit et al. [29]	25	58	0.43

2.4. Literature on Strengthening of Substandard Lap splices

In literature, the strengthening of substandard lap splices in existing reinforced concrete members has been performed by using steel, concrete, or FRP jackets. This section summarizes a summary of existing jacketing techniques.

2.4.1. Steel jackets

Steel jacketing comes under the category of conventional jacketing methods along with RC jacketing. Chai et al. [19] tested six circular RC columns and strengthened them using steel jackets in two groups. Group 1 specimens incorporated a lap splice length of 20db, while Group 2 specimens had continuous longitudinal reinforcement. Figure 2.13(a) shows the typical specimen details. In each group, one

specimen was tested as-built while other specimens were tested after strengthening by steel jacketing. Table 2.2 presents the details of the tested specimens. The steel jacket consisted of a 12.7 mm thick A36 steel sheet. To avoid accidental strength enhancement due to the bearing of the jacket against footing at large lateral displacements, a gap of 50 mm was provided between the jacket and the top of the footing.

Table 2.2 Summary of tested specimens by Chai et al. [19].

Test Unit	Column & Footing Details		Remarks
1	20d$_b$ Lap For Long. Bars Without Steel Casing	Weak Footing	Reference
2	20d$_b$ Lap For Long. Bars With Steel Casing	Weak Footing	Full Retrofit
3	Continuous Column Bars Without Steel Casing	Strong Footing	Reference
4	Continuous Column Bars With Steel Casing	Strong Footing	Full Retrofit
5	20d$_b$ Lap For Long. Bars 1/4" Styrofoam Wrap	Strong Footing	Partial Retrofit
6	20d$_b$ Lap For Long. Bars With Steel Casing	Strong Footing	Full Retrofit
1 - R	20d$_b$ Lap For Long. Bars Repaired By Steel Casing	Weak Footing 300 kips Prestress	Repair

Each specimen was subjected to controlled lateral deflections. Figure 2.19 compares the responses of Specimen 3 and Specimen 6. Specimen 3 was the reference and did not incorporate a lap splice, while Specimen 6 incorporated a substandard lap splice and strengthened with a steel jacket. The responses of both specimens were comparable both in terms of ductility and strength achieved. The steel jacket strengthened specimen did not exhibit a strength degradation up to ductility of 7.0, whereas the reference specimen with continuous reinforcement exhibited a drop in its capacity near the ductility of 5.0. The substandard hysteretic response of the reference lap spliced specimen is already shown in Figure 2.13.

(a)   (b)
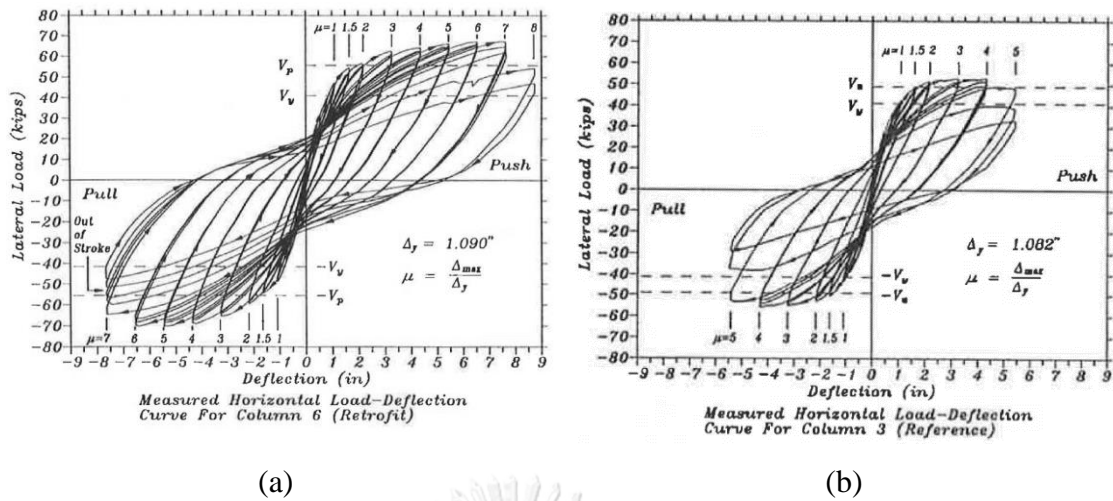
Figure 2.19 Comparison of the hysteretic response of columns tested by Chai et al. [19] (a) Specimen 6 with substandard lap splice and strengthened using a steel jacket and (b) Specimen 3 with continuous longitudinal reinforcement.

Aboutaha et al. [21] tested eleven rectangular RC columns were tested under controlled cyclic deflections. Seven out of eleven columns were strengthened using steel jackets of different configurations, while four columns were tested as built. Figure 2.20 provides details of tested specimens.
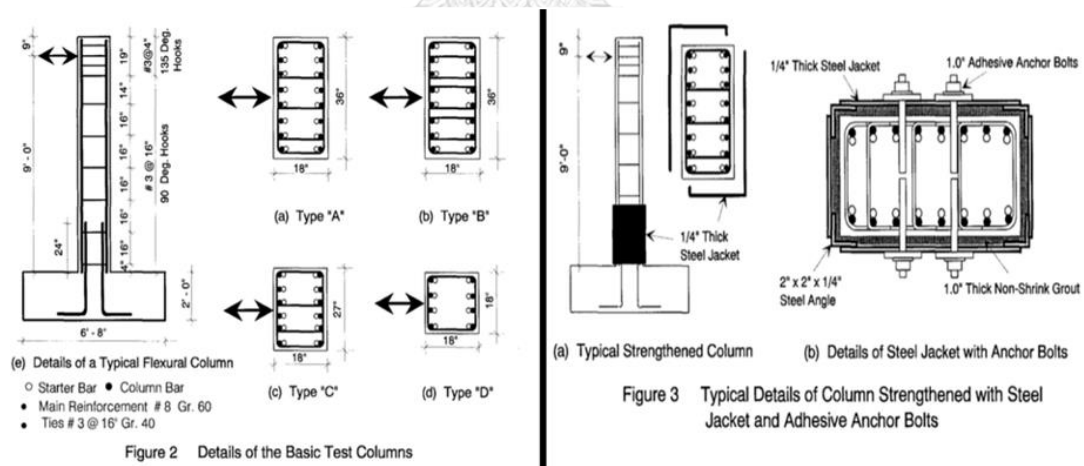
Figure 2.20 Details of specimens tested by Aboutaha et al. [21].

For strengthened specimens, two different lengths of steel jackets were used, termed as Long Steel Jacket (LSJ, 34.5" high) and Short Steel Jacket (SSJ, 27" high). Different configurations of anchor bolts were used on steel jackets. A summary of tested specimens and strengthening details are given in Table 2.3.

Table 2.3 Summary of specimens tested by Aboutaha et al. [21].

Summary of the Test Columns

Col. #	Type	Size	X-Sec.	Retrofit	Bolts	Bolts	Ref.
FC1	Basic	36"x18"	B	N/A	N/A	N/A	N/A
FC2	Strengthened	36"x18"	B	LSJ/B	1L5B	None	FC1
FC4	Basic	36"x18"	A	N/A	N/A	N/A	N/A
FC8	Strengthened	36"x18"	A	Collars	1L3B	None	FC4
FC9	Strengthened	36"x18"	A	LSJ/B	1L5B	None	FC4
FC11	Strengthened	36"x18"	A	SSJ/B	2L4B	2L3B	FC4
FC12	Strengthened	36"x18"	A	LSJ/B	2L3B	2L2B	FC4
FC14	Basic	27"x18"	C	N/A	N/A	N/A	N/A
FC15	Basic	18"x18"	D	N/A	N/A	N/A	N/A
FC16	Strengthened	27"x18"	C	LSJ/B	1L2B	None	FC14
FC17*	Strengthened	18"x18"	D	LSJ/B	1L2B	None	FC15

LSJ = Long Steel Jacket (34.5" high), SSJ = Short Steel Jacket (27" high), /B = with Adhesive Anchor Bolts.
L = Vertical Line, B = Adhesive anchor bolt, 2L3B indicates 2 vertical lines of bolts, with 3 bolts in each line.
* The steel jacket had an additional four extra corner angles.

Figure 2.21 compares the responses of rectangular sections. It can be seen that the unstrengthened specimen in Figure 2.21(a) exhibited a brittle response, and reinforcing bars could not achieve their yield strength. Figure 2.21(b) shows the hysteretic response of a rectangular section with LSJ anchored with bolts on one side only. Figure 2.21(c) signifies the hysteretic response of the rectangular section strengthened with SSJ and anchored with bolts on both sides. The short height of the steel jacket could not achieve the same ductility as was achieved with LSJ, even in the presence of anchor bolts on both sides. However, anchoring LSJ on both sides was the optimum solution among all strengthening schemes, as shown in Figure 2.21(d).
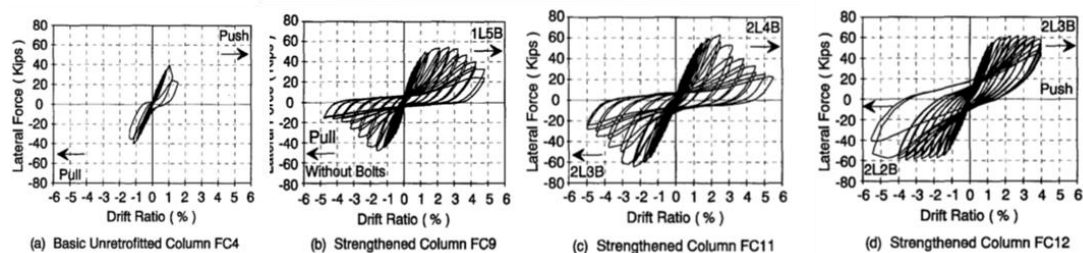
Figure 2.21 Comparison of the hysteretic response of rectangular specimens tested by Aboutaha et al. [21].

Square columns showed a similar response as that of the as-built specimen showing almost no ductility. However, strengthening with LSJ anchored with bolts on one side showed a similar response to that of the side without anchor bolts Figure 2.22. The conclusion drawn was the better confinement of steel jackets on square sections than on rectangular sections.

(e) Basic Unretrofitted Column FC15   (f) Strengthened Column FC17
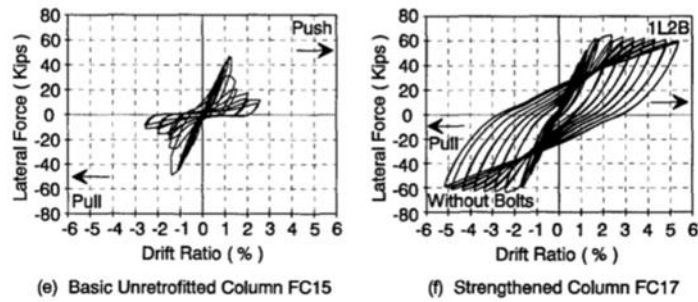
Figure 2.22 Comparison of the hysteretic response of square unstrengthened and steel jacket strengthened tested by Aboutaha et al. [21].

Ghobarah et al. [67] tested three columns, and the structural details are already shown in Figure 2.15(a). Two specimens were constructed with a lap splice length of $40d_b$, whereas one specimen was tested with continuous longitudinal reinforcement into the footing. It can be seen that the unstrengthened specimen with $40d_b$ did not exceed the ductility of 4.0, whereas the steel jacketed column was able to achieve ductility of 10.0. Ghobarah et al. [67] also presented a theoretical procedure to determine the steel jacket height and its thickness to clamp a substandard lap splice.

(a)   (b)
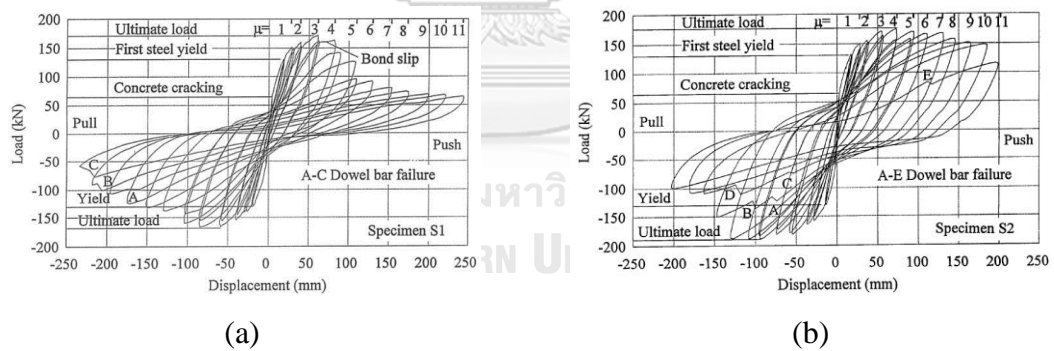
Figure 2.23 Comparison of the hysteretic response of (a) unstrengthened and (b) steel jacket strengthened column tested by Ghobarah et al. [67].

Daudey et al. [24] performed tests on five RC columns representatives of bridge piers in Canada. The size of bridge piers was scaled down to 1/3.65 scale. The test parameters included jacket geometry, the size of the vertical gap between the jacket and the top of the footing, and the properties of the fill material between the jacket and column surface. Specimen S0 was tested in as-built condition, Specimen S1 was strengthened with an elliptical steel jacket by modifying the original cross-

section to an oval shape with a 15 mm vertical gap between the jacket and the top of the footing, Specimen S2 was similar to Specimen S1 with an increase vertical gap of 40 mm between the jacket and the top of the footing, Specimen S3 was similar to Specimen S2 but with a circular steel jacket, and the last Specimen S4 was also similar to Specimen S2 but with a cement-based expansive grout was used to fill the gap between the jacket and column. The height of jackets in all columns was extended to the full height of the column to avoid the possibility of shear failure with a thickness of 3.2 mm. Figure 2.24 shows the structural details of a typical test specimen.
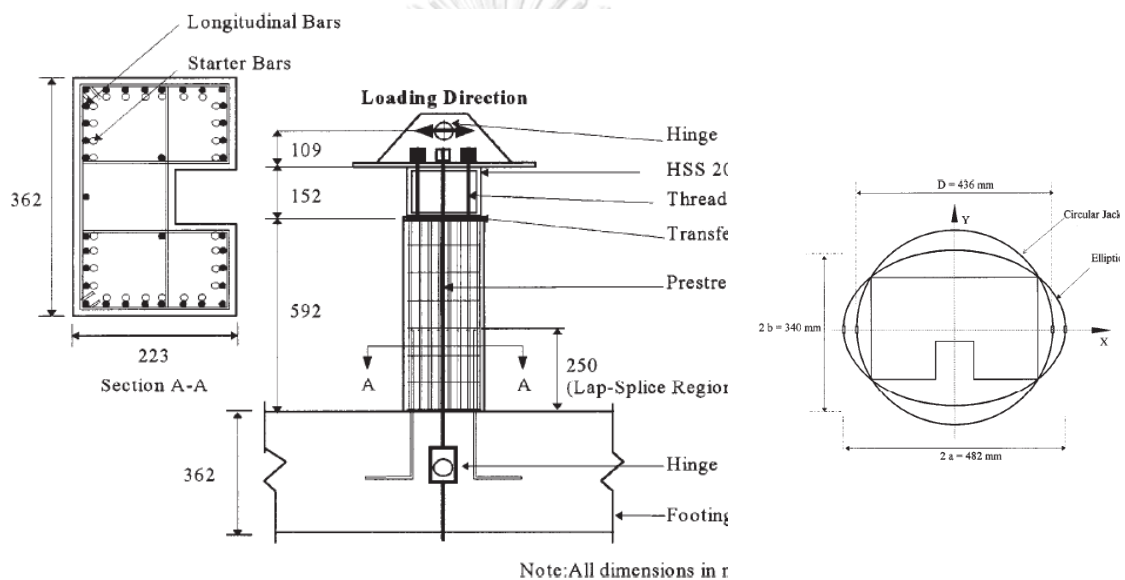
Figure 2.24 Test specimen of Daudey et al. [24].

The hysteretic response of all specimens tested by Daudey et al. [24] is shown in Figure 2.25. It can be seen that Specimen S0 failed suddenly at a ductility level of 2.0. All strengthened specimens exhibited compression buckling of longitudinal bars beyond ductility of 4.0. It was found that the geometry of the steel jacket played no important role. A minimum gap of 50 mm between the steel jacket and the top of the footing was suggested to avoid stress concentrations in longitudinal bars.
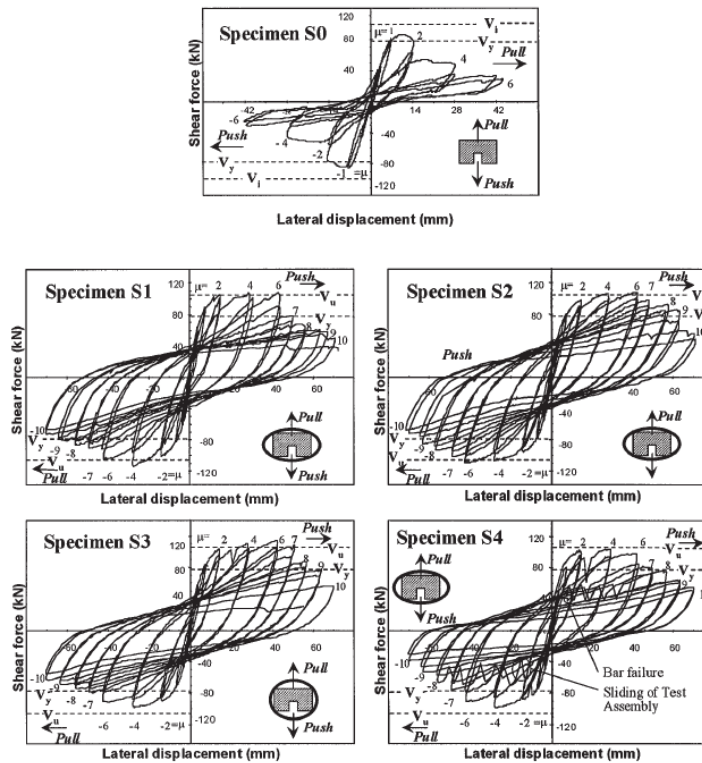
Figure 2.25 Hysteretic response of RC columns tested by Daudey et al. [24].

Lin et al. [43] assessed the efficiency of steel jackets in preventing brittle failures associated with substandard lap splices of $40d_b$. Three RC columns of 1.2.5 scale were tested under cyclic loads. An octagonal steel jacket and an elliptical steel jacket was applied to two RC columns, whereas one column was tested in as-built condition. An analytical procedure was proposed to design octagonal shaped steel jacket. The shape of the jackets was modified to avoid the out-of-plane bulging of the jackets in between the sharp corners. Typical specimen details of specimens tested by Lin et al. [43] are shown in Figure 2.26. A steel jacket of 2800 mm height was used. The thickness of the steel jacket was 6.0 mm and 3.0 mm for the octagonal shape and elliptical shape, respectively. A vertical gap of 30 mm was provided between the jacket toe and the top of the footing. The control column failed in a brittle manner due to premature lap splice failure, as shown in Figure 2.27(a). The displacement ductility factors for both octagonal and elliptical-shaped steel jacketed columns were above 6.0 and achieved their theoretical lateral load capacities. The use of an octagonal shape jacket was suggested for cost-effectiveness and spacing saving.
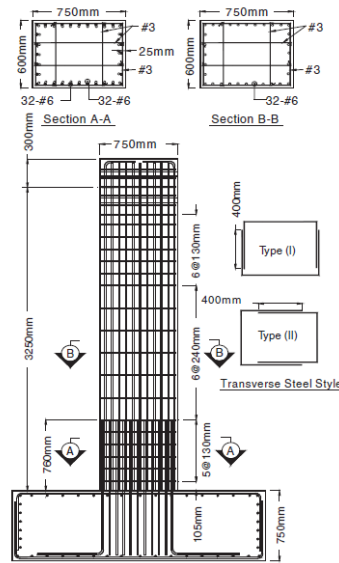
Figure 2.26 Specimen details by Lin et al. [32].
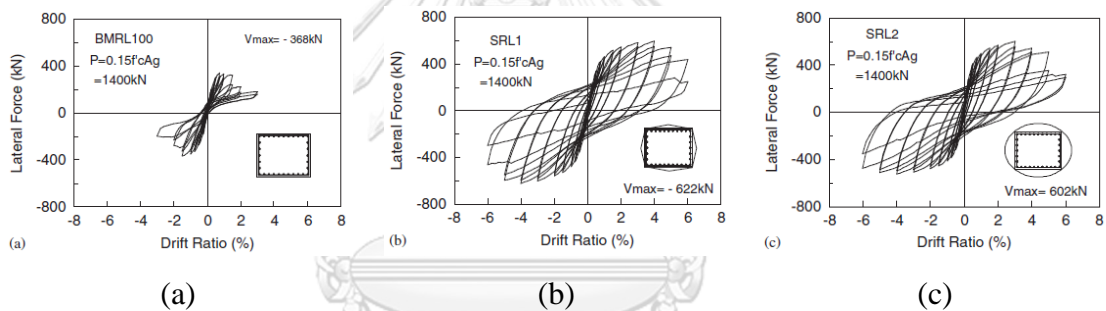
Figure 2.27 Hysteretic response of columns tested by Lin et al. [43] (a) unstrengthened lap splice column, (b) column strengthened with an octagonal jacket, and (c) column strengthened with an elliptical jacket.

Choi et al. [64] investigated the role of the newly proposed steel jacketing technique in improving the performance of circular RC columns with substandard lap splices. The structural details of specimens tested by Choi et al. [64] are shown in Figure 2.18(a). Four circular columns were tested. One column was tested in as-built condition, whereas three columns were strengthened by using a steel jacket of 1.0 mm thickness. Instead of using grout to fill the gap between steel jackets and columns, steel clamps were used to clamp steel jackets to RC columns. Figure 2.28 presents the comparison of the hysteretic response of Specimen SP50-NSJ (i.e., control specimen) and Specimen SP50-SJ1 (i.e., specimen strengthened with steel jacket). The maximum lateral load sustained by Specimen SP50-NSJ was 79.7 kN, whereas the

maximum load sustained by Specimen SP50-SJ1 was 95.2 kN. The control column SP50-NSJ failed at a displacement ductility of 3.19, whereas a displacement ductility of 8.40 was achieved by column SP50-SJ1. The lap spliced bars in Specimen SP50-SJ1 were able to achieve 51% higher stresses than the stresses achieved by lap spliced bars in Specimen SP50-NSJ. The peak bond stress achieved by the lap spliced bars in Specimen SP50-SJ1 was 6.5 MPa as compared to the bond stress of 4.29 MPa achieved by the lap spliced bars in Specimen SP50-NSJ. The peak bond stress (bond strength) in Specimen SP50-NSJ was suddenly dropped at a drift ratio of 1.78%, whereas the peak bond stress in Specimen SP50-SJ1 was maintained till large drift ratios.
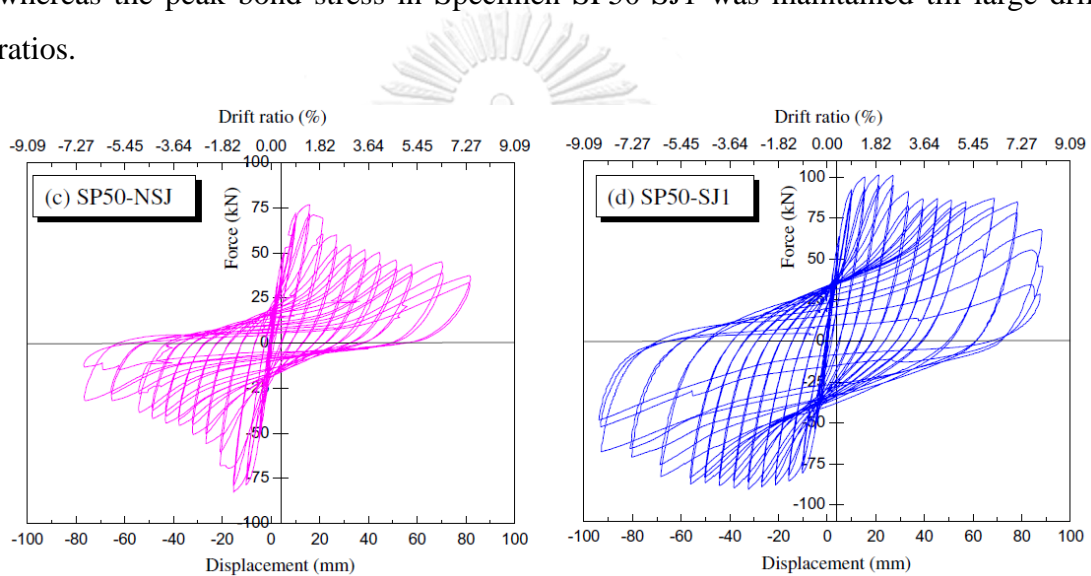
Figure 2.28 Comparison of the hysteretic response of unstrengthened specimen with substandard lap splice (SP50-NSJ) with the hysteretic response of steel jacket strengthened specimen (SP50-SJ1).

2.4.2. Concrete Jackets

Bousias et al. [68] experimentally investigated the effectiveness of RC jackets in strengthening substandard lap splices of plain bars. The idea was that FRP jackets do not extend beyond the joint and, therefore, cannot increase flexural resistance and stiffness. Two control specimens with lap splice lengths of $15d_b$ and $25d_b$ were tested, whereas two columns were retrofitted with RC jackets before testing as shown in Figure 2.29. The hysteretic response of all four columns is presented in Figure 2.30. No clear difference between the response of specimens with lap splice lengths of $15d_b$ and $25d_b$ was observed and both the columns failed in brittle manner. The same

columns strengthened with RC jackets demonstrated stable hysteretic loops, and deformation capacity was enhanced three times the reference control specimens. A significant improvement in the lateral load resistance was also observed.

(a)   (b)
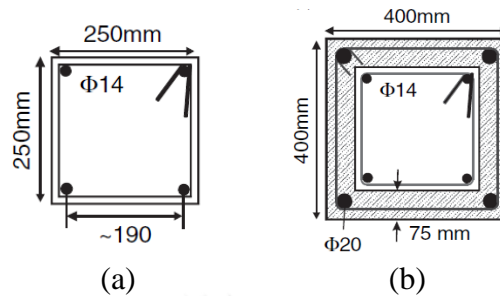
Figure 2.29 Cross-sectional details of specimen tested by Bousias et al. [68] (a) without jacket and (b) with RC jacket.

(a)   (b)

(c)   (d)
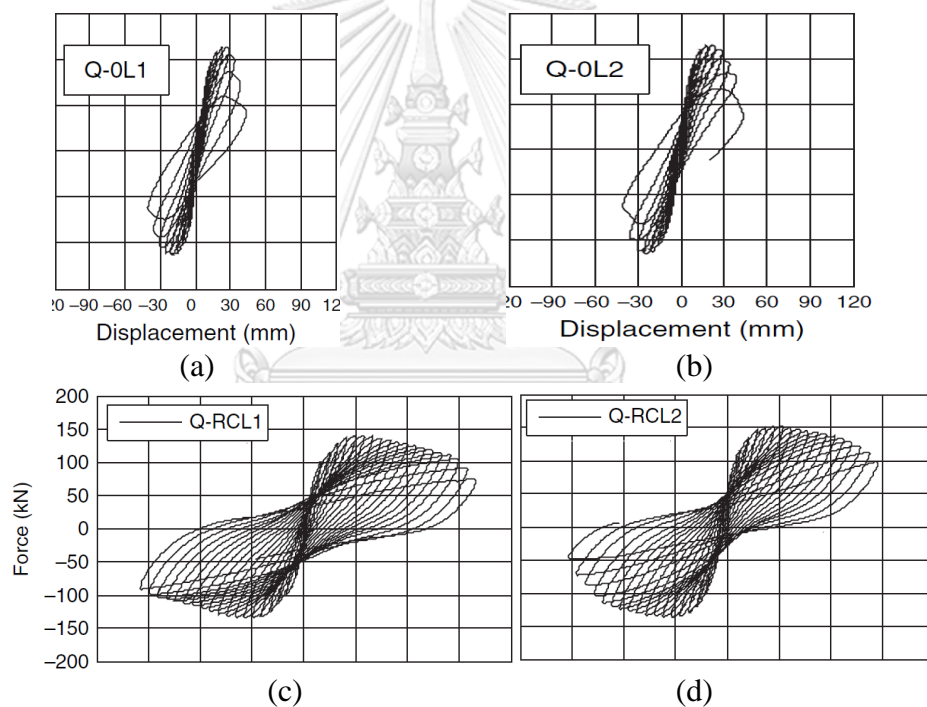
Figure 2.30 Hysteretic response of specimens tested by Bousias et al. [68] (a) unstrengthened specimen with $15d_b$ lap splice, (b) unstrengthened specimen with $25d_b$ lap splice, (c) RC jacket strengthened specimen with $15d_b$ lap splice, and (d) RC jacket strengthened specimen with $25d_b$ lap splice.

Kalogeropoulos and Tsonos [69] performed experiments on five columns. Two columns were tested in as-built condition with lap splice of $20d_b$ (O_1) and $24d_b$ (O_2). One column with similar structural details but with continuous longitudinal reinforcement into the footing was tested (C_1). Two columns similar to O_1 and O_2 but

strengthened with RC jackets were tested, denoted as *RWO₁* and *RWO₂*. A typical process for installing RC jackets is shown in Figure 2.31. The height of each column was 980 mm, whereas the square dimension of the cross-section was 200 mm.

(a)   (b)   (c)
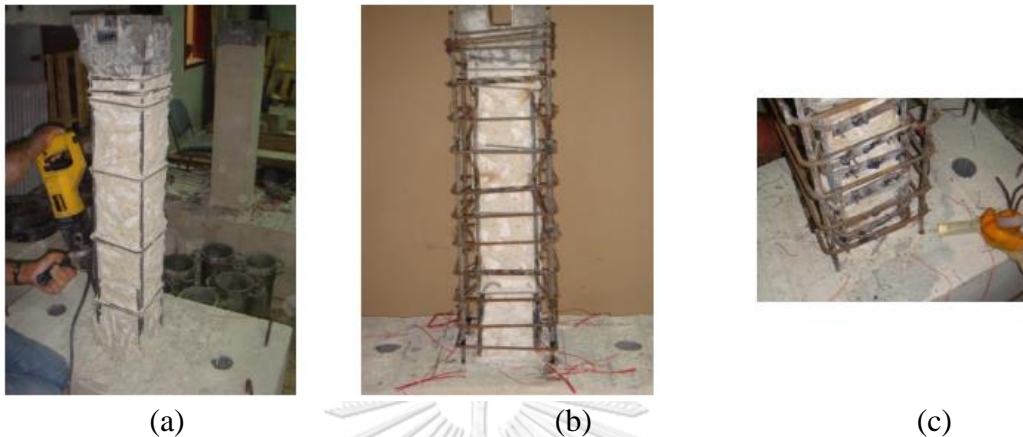
Figure 2.31 Steps taken to install external RC jackets by Kalogeropoulos and Tsonos [69] (a) cover is removed in original column, (b) lap splices in original and RC jackets are welded, and (c) epoxy is inserted into the holes.

Figure 2.32 presents the hysteretic response of specimens tested by Kalogeropoulos and Tsonos [69]. In addition to imparting significant ductility, RC jackets improved the lateral load resistance of both the lap spliced columns substantially.

(a) Hysteretic loops of specimens O_1 and RWL_1 (b) Hysteretic loops of specimens O_2 and RWL_2
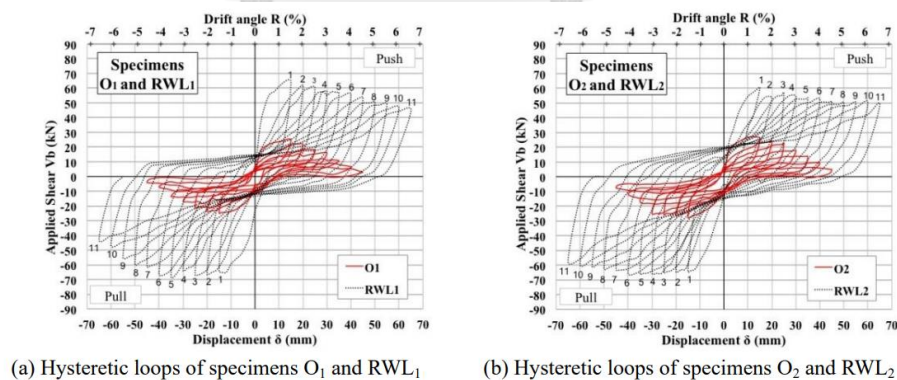
Figure 2.32 Hysteretic response of specimens tested by Kalogeropoulos and Tsonos [69].

2.4.3. Fiber Reinforced Polymers (FRP) Jackets

Within the last two decades, the use of composite jackets such as carbon fiber-reinforced polymer (CFRP) jackets or glass fiber-reinforced polymer (GFRP) jackets has gained significant interest. This can be attributed to their noticeable strength-to-weight ratio, easy and rapid application, high resistance to corrosion, and high durability [31, 70]. In addition, FRP jackets do not change the look of the structure, and appreciably, the stiffness of the structure is not significantly altered [33]. Several experimental works exist in the literature on the strengthening of substandard lap splices using composite jackets. A summary of a few of those studies is given below.

Xiao and Ma [65] carried out an experimental program to investigate the effectiveness of prefabricated composite jackets in enhancing the flexural ductility of bridge piers with substandard lap splices. The experimental program involved three 1:2 scale circular columns. Typical specimen details are shown in Figure 2.33(a), whereas the strengthening schemes deployed are shown in Figure 2.33(b-d). One column was tested in as-built condition. After testing the as-built column, it was repaired by cleaning the damaged concrete from within the plastic hinge zone, followed by the application of a 4-layer composite jacket (see Figure 2.33(d)). The other two columns were retrofitted with composite jackets with different schemes, as shown in Figure 2.33(b) and Figure 2.33(d). The composite jackets used for retrofitting were made of E-glass fiber-reinforced composite cylindrical shells with slits.
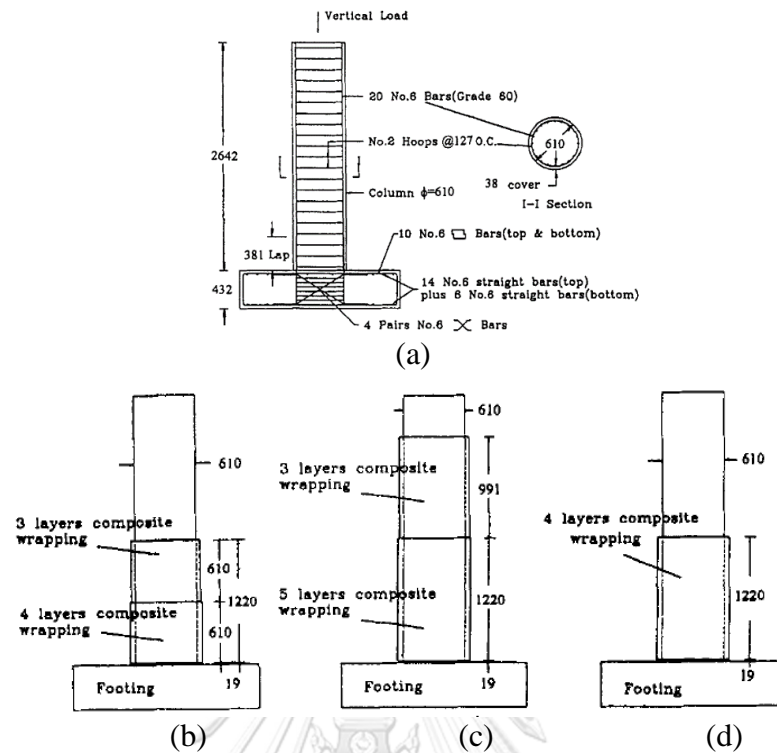
Figure 2.33 (a) Typical specimen details, (b) retrofitted column C2-RT4, (c) retrofitted column C3-R35, and (d) repaired column C4-RP4 tested by Xiao and Ma [65].

The hysteretic response of all columns tested by Xiao and Ma [65] is shown in Figure 2.34. The as-built column C1-A suffered a brittle loss in its lateral load capacity due to the splice failure. This was identified by longitudinal cracks along the lap splice at a lateral displacement of 41 mm. The retrofitted columns exhibited stable hysteretic response till a displacement ductility of 6.0 and demonstrated a loss of up to 20% of peak lateral load capacity at a displacement ductility of 8.0.
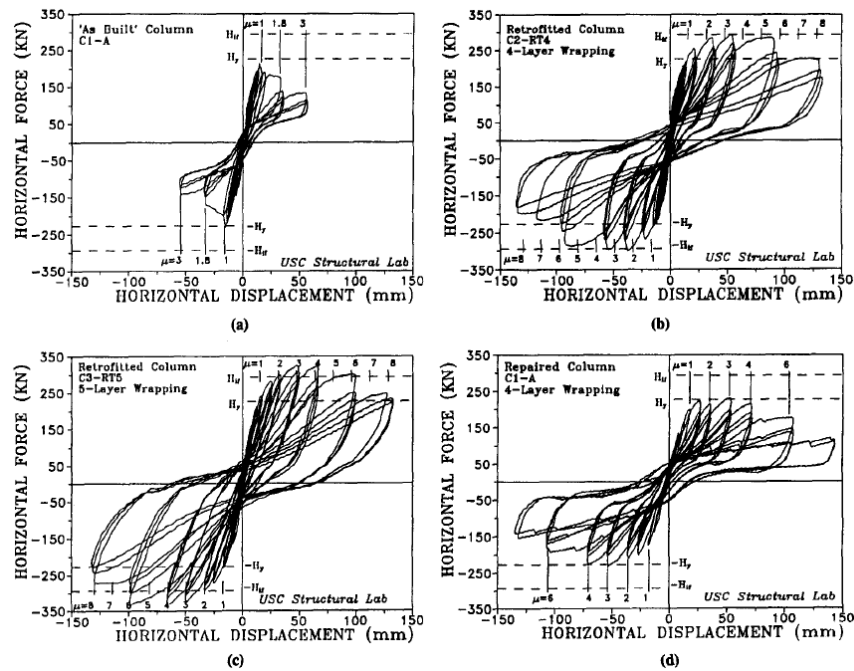
Figure 2.34 Hysteretic response of columns tested by Xiao and Ma [65] (a) as-built column C1-A, (b) retrofitted column C2-RT4, (c) retrofitted column C3-R35, and (d) repaired column C4-RP4.

Haroun et al. [5] aimed to investigate the effectiveness of FRP jacketing on circular and rectilinear columns. A total of 13 columns comprising eight circular and 5 square sections were tested under cyclic loadings. A substandard lap splice length of $20d_b$ was adopted in this study to mimic the construction practices prior to 1971. Figure 2.35 shows the column details tested in this study. Different combinations of FRP and adhesives were used. The summary of tested specimens and strengthening schemes is given in Table 2.4.
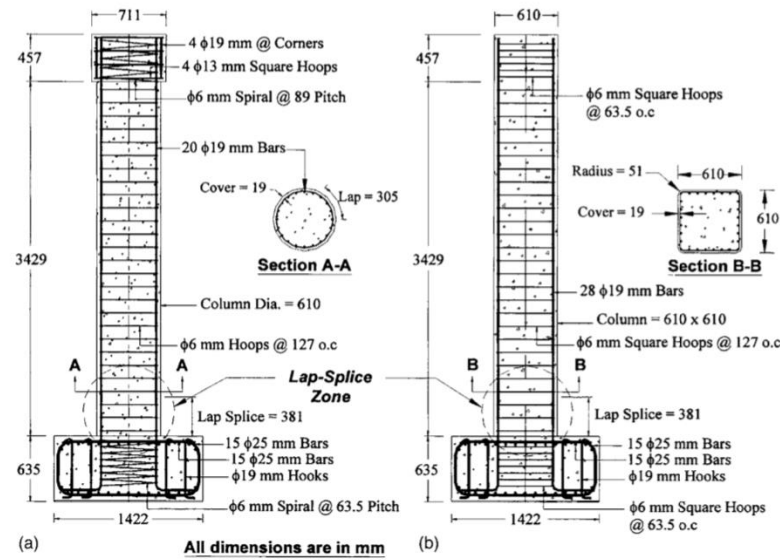
Figure 2.35 Column details tested by Haroun et al. [5].

Table 2.4 Summary of test specimens tested by Haroun et al. [5].

Test sample	Concrete strength (MPa)	Yield stress of main steel (MPa)	Composite jacket properties			
			Type	Thickness within lap-splice zone (mm)	Tensile strength (MPa)	Tensile modulus (GPa)
CF-A1	35.7	299.1	As-built circular column			
CF-A2	38.7	299.1	As-built circular column			
CF-R1	36.0	299.1	Carbon/epoxy[a]	0.7	4,168	231.5
CF-R2	36.9	299.1	Carbon/epoxy[a]	0.7	4,430	230.1
CF-R3	32.8	299.1	E-glass/vinyl ester[b]	11.4	744	36.5
CF-R4	37.7	299.1	Carbon/epoxy[a]	1.7	4,382	226.0
CF-R5	39.7	299.1	E-glass/polyester[b]	12.7	641	36.4
CF-R6	33.1	299.1	Carbon/epoxy[c]	8.3	937	63.0
RF-A1	41.4	443.4	As-built square column			
RF-R1	35.4	443.4	Carbon/epoxy[a]	4.0	4,168	231.5
RF-R2	41.9	443.4	Carbon/epoxy[a]	4.0	4,430	230.1
RF-R3	42.2	443.4	Carbon/epoxy[a]	2.5	4,382	226.0
RF-R4	42.2	443.4	E-glass/vinyl ester[b]	22.9	744	36.5

[a]Properties are based on net-fiber area.
[b]Precured shells.
[c]Low-modulus carbon/epoxy composite system with properties based on net-fiber area.

As-built circular specimens were able to achieve their ideal flexural capacities. However, lap splice failure rendered them to achieve a higher level of ductility. On the contrary, circular specimens strengthened with FRP jackets did not only achieve their ideal flexural strengths but were also able to maintain them up to ductility of 6.0. A comparison of the hysteretic responses of as-built and strengthened circular specimens is presented in Figure 2.36.
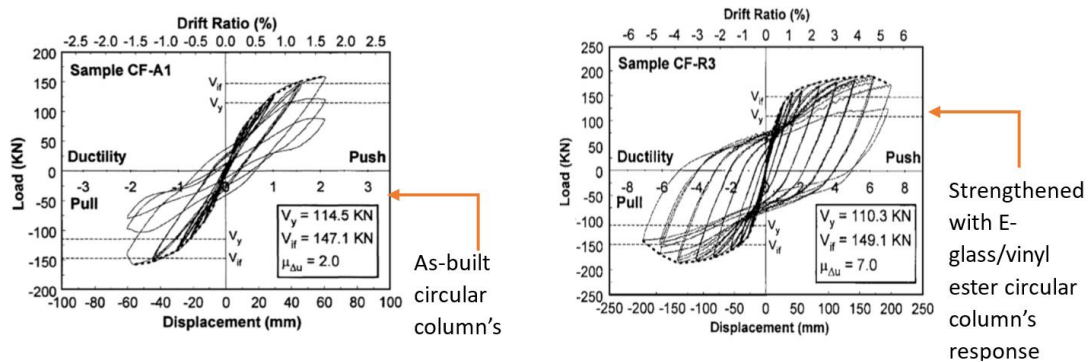
Figure 2.36 Comparison of as-built and strengthened circular columns tested by Haroun et al. [5].

Comparing the hysteretic responses of the square as-built and strengthened specimens Figure 2.37, it was found that the as-built square specimen was not able to achieve its ideal flexural strength and failed in a very brittle manner owing to the premature failure of lap splice. Strengthening it with FRP jackets did ameliorate the situation by achieving its ideal flexural capacity. Nonetheless, the improvement was inferior to the one obtained from the circular specimen. Haroun et al. [5] concluded that composite jackets on square columns could only induce confining pressures near corners. Therefore, lap spliced bars near the corners are effectively confined only.
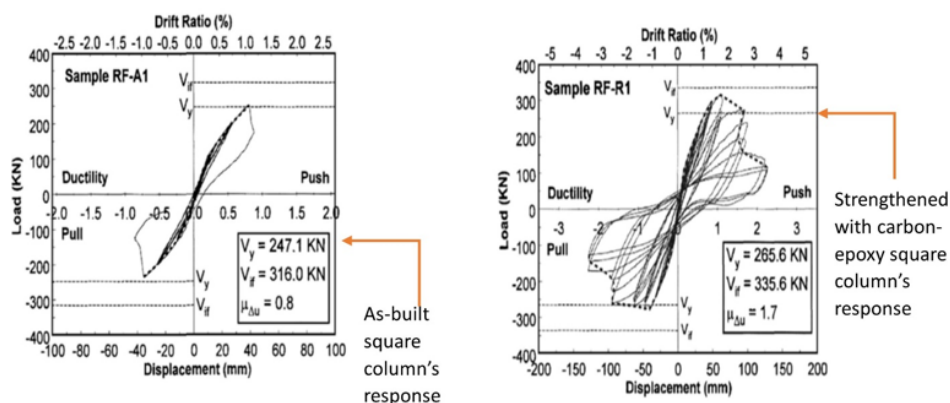
Figure 2.37 Comparison of as-built and strengthened square columns tested by Haroun et al. [5].

Harries et al. [35] investigated the effectiveness of CFRP wraps in strengthening substandard lap splices in square building columns. Five columns were tested, comprising two columns, L0 and L1, with continuous reinforcement into the

footing and three columns, F0, F1, and F2, with a $22d_b$ lap splice at the column-footing junction. Columns L0 and L1 were control columns. Columns F1 and L2 were identically strengthened using four plies of CFRP at the bottom 500 mm, whereas two plies of CFRP were applied for another 500 mm above the bottom 500 mm, as shown in Figure 2.38. To cover the stress concentrations near sharp corners, a corner radius of 38 mm was provided in all specimens.
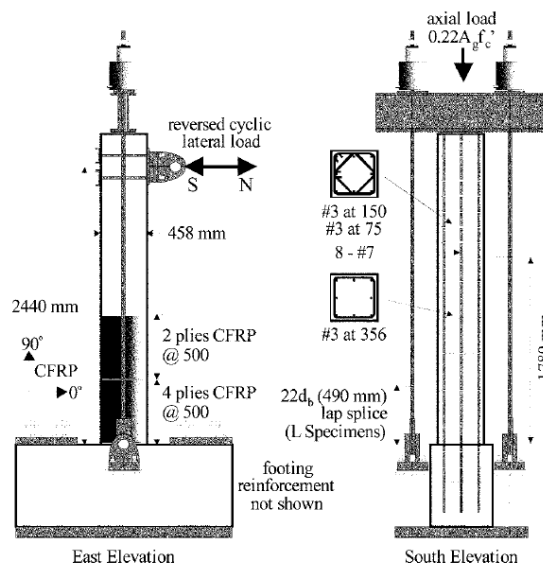
Figure 2.38 Specimen details tested by Harries et al. [35].

The hysteretic response of the lap spliced columns tested by Harries et al. [35] is shown in Figure 2.39. Column L0 failed by exhibiting large vertical splitting cracks along lap splices at a displacement ductility of 1.5. Columns L1 and L2 maintained their flexural capacity till a displacement ductility of 5.0. It was concluded that the jacket did not contribute to flexural capacity after the onset of bar slip and splitting.
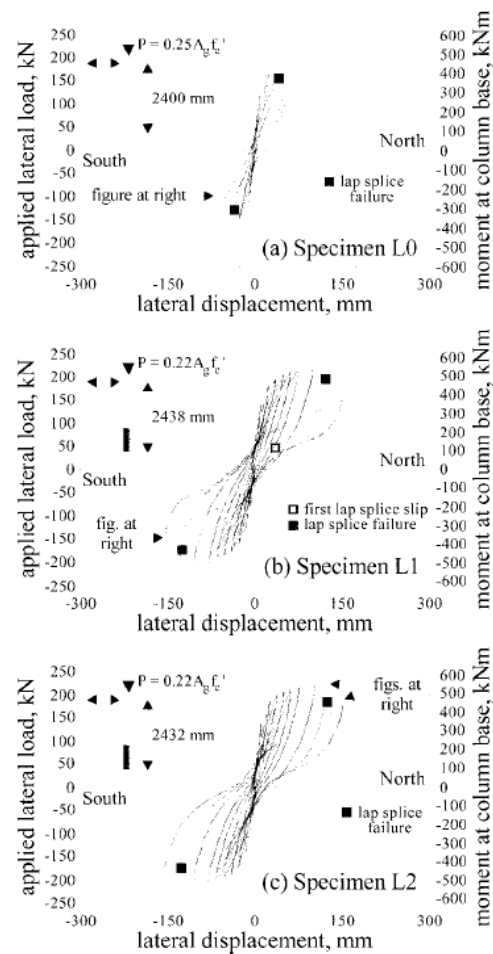
Figure 2.39 Comparison of the hysteretic response of lap spliced columns tested by Harries et al. [35].

Harajli [63] tested circular and rectangular columns to assess the performance of CFRP jackets with the thickness estimated by their proposed equation. The primary test variables included steel bar diameter, cover-to-diameter ratios, and thickness of CFRP jackets. Columns were tested into four groups, as shown in Table 2.5. Each group comprised one control column, two columns tested with one or two CFRP sheets, and one column detailed to be earthquake resistant conforming to modern design codes. The lap splice length provided at the base of columns was $30d_b$.

Table 2.5 Summary of columns tested by Harajli [63].

Column	Column reinforcement	c/d_b	f'_c	f_y	Number of FRP layers
(a) Group I (rectangular section)					
C14	8T14	1.4	39	550	None
C14FP1	8T14	1.4	39	550	1
C14FP2	8T14	1.4	39	550	2
C14[a]	8T14	—	32	550	None
(b) Group II (rectangular section)					
C16	8T16	2.1	40	528	None
C16FP1	8T16	2.1	40	528	1
C16FP2	8T16	2.1	40	528	2
C16E[a]	8T16	—	32	528	None
(c) Group III (rectangular section)					
C20	6T20	1.0	32	617	None
C20FP1	6T20	1.0	32	617	1
C20FP2	6T20	1.0	32	617	2
C20E[a]	6T20	—	32	617	None
(d) Group IV (circular section)					
CrU	5T14	1.6	39	539	None
CrFP1	5T14	1.6	39	539	1
CrFP2	5T14	1.6	39	539	2

[a]Earthquake-resistant specimens (Specimens E).

As shown in Figure 2.40, all control columns exhibited a brittle loss in lateral strength attributed to the failure of substandard lap splices. The lap splice failure became more noticeable as the ratio of concrete cover to bar diameter decreased. The increase in the lateral strength of CFRP confined columns ranged between 5% to 60%. It was found that the improvement in the bond strength and lateral strength of strengthened columns was dependent on the bond strength and flexural capacity of the corresponding control columns. Control columns with the bond strength and maximum splice stress close to the respective yield values exhibited a lower increase and vice versa. As a result, columns with higher concrete cover-to-diameter ratios exhibited a lower increase in their bond strengths and flexural capacity than the columns with lower concrete cover-to-diameter ratios.
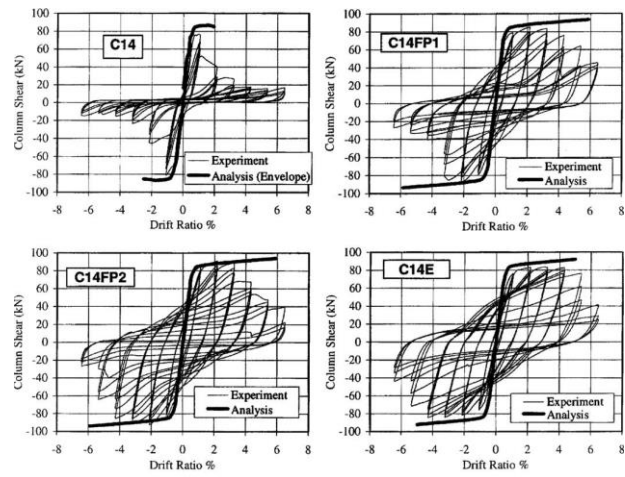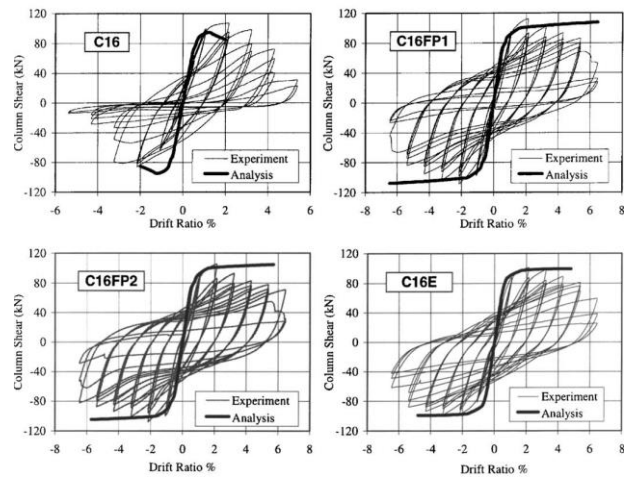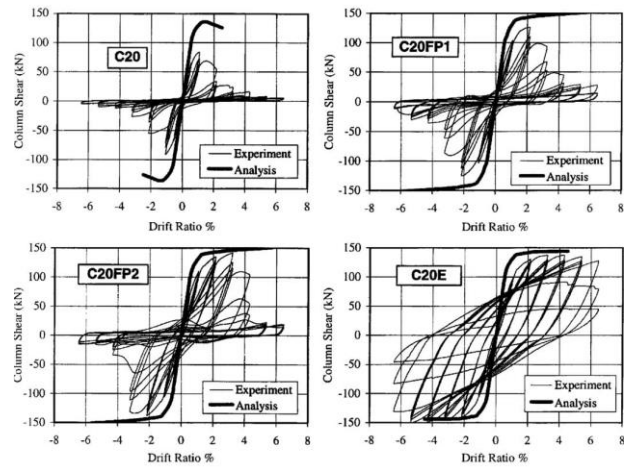
Figure 2.40 Comparison of the hysteretic response of columns tested by Harajli [63] with (a) 14 mm diameter bars, (b) 16 mm diameter bars, and (c) 20 mm diameter bars.

Elgawady et al. [37] aimed to investigate the effects of the number of CFRP jackets, their configuration, and strengthening materials on improvement in the seismic behavior of RC columns. A relatively longer length of $35d_b$ was employed in the lap splice. Eight 0.4 scale columns were tested: seven with rectangular sections while one section was square. Specimen details are given in Figure 2.41, and a summary of tested specimens is given in Table 2.6.
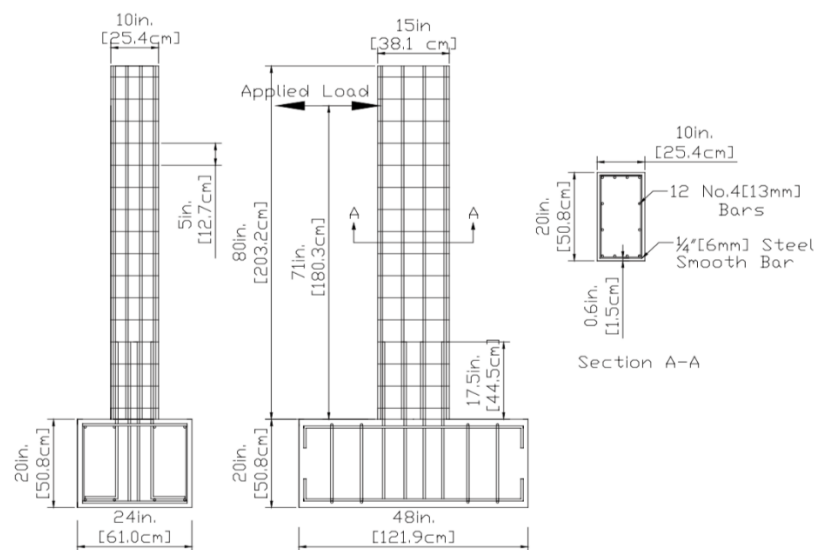
Figure 2.41 Details of specimens tested by Elgawady et al. [37].

Table 2.6 Summary of test specimens by Elgawady et al. [37].

Specimen	Test parameter	Retrofitting configuration	No. of FRP layers	Retrofit
AB-1	Control	NA	NA	None
AB-2	Control	NA	NA	None
FRP-MS	Retrofitting configuration	Oval	2	CFRP jacket
FRP-4	Retrofitting configuration	Rectangular	4	CFRP jacket
FRP-6	Retrofitting reinforcement ratio	Rectangular	6	CFRP jacket
FRP-8	Retrofitting reinforcement ratio	Rectangular	8	CFRP jacket
AR-2	Aspect ratio	Rectangular	5	CFRP jacket
SJ	Retrofitting material	Oval	NA	Steel jacket

Note: NA=not applicable.

Specimen with rectangular jackets were found to have the highest lateral strengths, whereas the specimen strengthened with steel jacket exhibited the least improvement in lateral strength. It was observed that RC columns with substandard lap splice of length $35d_b$ perform better than the columns with shorter lap splices. Both the steel and CFRP jackets altered the failure from brittle lap splice failure to ductile flexural failure. It was also observed that the damage localizes within the

vertical gap between the bottom of the jacket and the top of the footing. Further, the jacketing techniques did not influence the initial stiffness. The increase in the lateral strength was not found to be proportional to the number of CFRP jackets.

Bournas and Triantafillou [66] tested six columns in two groups. The first group of columns employed a $20d_b$ of lap splice, whereas a $40d_b$ lap splice was provided in the second group. The structural details of the tested columns are shown in Figure 2.42. To replicate the substandard details in old columns, a cover diameter ratio of 0.70 was provided in all columns. One column in each group was tested in as-built condition, one column was retrofitted with two layers of CFRP jacket, and one column was retrofitted with four textile reinforced mortar (TRM) jackets. A corner radius of 25 mm was provided to round off the sharp corners in the strengthened specimens.
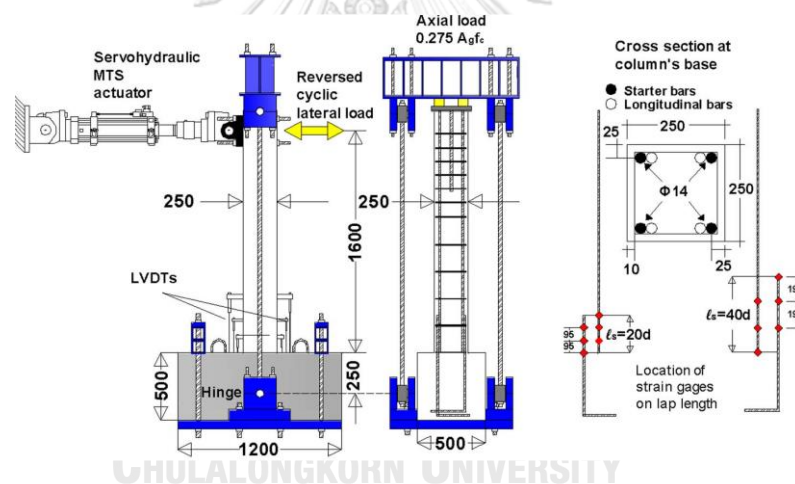
Figure 2.42 Structural details of columns tested by Bournas and Triantafillou [66].

The control column L20d_C performed slightly inferior to the control column L40d_C. From strain gage measurements along lap spliced bars, it was observed that the lap spliced bars in Specimen L40d_C achieved yielding in the push direction, whereas the maximum stress developed in lap spliced bars of Specimen L20d_C was 83% of the yield stress in the push direction. After strengthening by CFRP and TRM jackets, lap spliced bars in all columns achieved yielding. Further, a stable load-deflection response was observed for strengthened columns. The retrofit scheme was found more pronounced in the case of $40d_b$ lap spliced specimens.
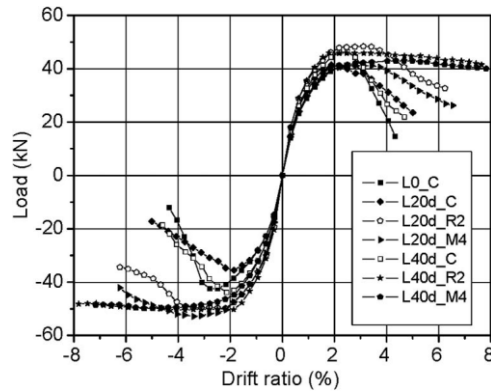
Figure 2.43 Load-deflection envelopes of the columns tested by Bournas and Triantafillou [66].

Kim et al. [38] examined the effectiveness of CFRP jackets on square and rectangular substandard lap spliced columns with a focus on the strengthening of rectangular columns. Three square and three rectangular columns were tested with structural details shown in Figure 2.44. A lap splice length of $24d_b$ was provided in all columns. Before the application of CFRP jackets, the corners were rounded to a radius of 50 mm. As shown in Figure 2.44, Type A, B, and C sections had 8, 10, and 20 lap splices, respectively. Two columns belonged to section Type A, one column belonged to section Type B, and three columns belonged to section Type C. All columns were strengthened by using a single CFRP sheet. To improve the effectiveness of CFRP sheets, CFRP anchors were used in all columns except in one column of section Type A. The test results concluded that a combination of CFRP jackets and anchors provided more improvement in the structural behavior of lap splices than that provided by CFRP jackets alone. The rehabilitated square columns performed better than rehabilitated rectangular columns. It was observed that the reduction in the number of anchors did not result in the reduction of the lap splice capacity. However, a larger number of anchors imparted a larger displacement capacity.
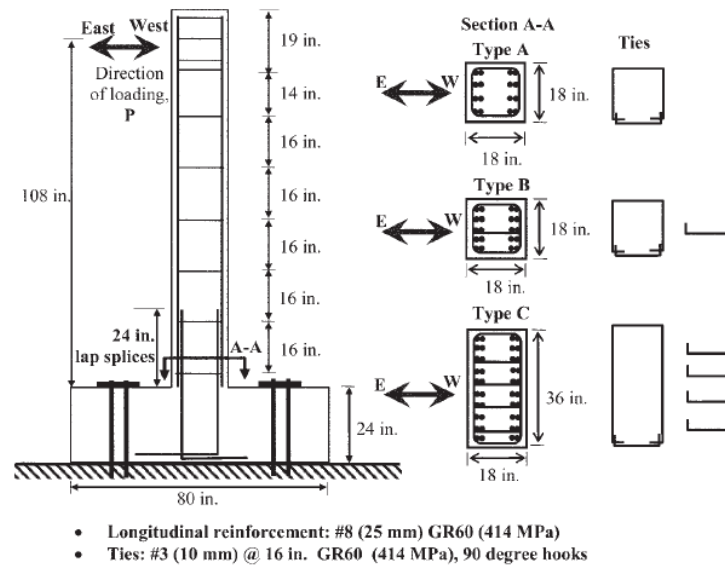
Figure 2.44 Structural details of columns tested by Kim et al. [38].

2.4.4. Summary of Existing Lap splice Strengthening Techniques

Three types of strengthening solutions for substandard lap splices in existing RC members are identified from the literature. The conventional solutions involve wrapping the lap spliced regions by using RC or steel jackets. The primary issue involved with these jackets is that these jackets significantly modify the weight of the structure. As a result, the dynamic characteristics of the member are altered. Further, these jackets require skilled labor for their application [29, 30]. RC jackets, in particular, are time-consuming and require the removal of existing concrete cover [68]. The use of FRP jackets instead of conventional jackets can solve these issues. However, the efficiency of FRP jackets is maximum in the case of circular cross-sections. This is because the sharp corners in rectangular/square sections induce stress concentrations, and the confinement of FRP jackets is mainly concentrated near the corners [35]. This issue, if not dealt with properly, can result in the premature rupture of FRP jackets near the corners [71]. As a result, the efficiency of the whole confining system is compromised. The efficiency of FRP jackets is improved by rounding off the sharp corners to provide continuity in the confining system [39, 72]. The degree of roundness is limited due to the presence of transverse reinforcement inside the members [42]. Hence, the deterioration caused by the sharp corners can only be partially removed.

2.5. Strengthening Using Flexural Elements

2.5.1. Strengthening RC Members without Lap splices

To address the problems related to the flexural stiffness of jackets, Hussain and Driver [44] proposed a relatively simple scheme to strengthen the concrete by the use of steel elements having considerable flexural stiffness in the form of hollow rectangular sections. It was stated that the collars used were able to prevent concrete spalling due to their significant bending capacity. Steel collars were assembled either by using welds or bolts, as shown in Figure 2.45. For bolted corner connections, 25.4 mm diameter high strength threaded rods were utilized.
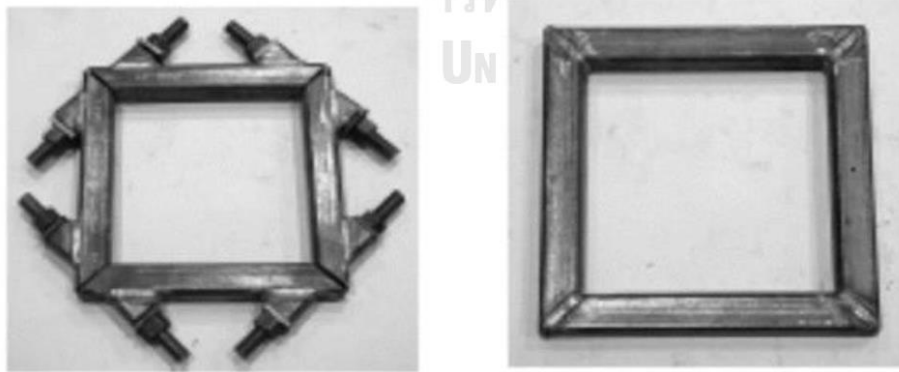
Figure 2.45 Hollow structural section collars used by Hussain and Driver [44].

In the case of the collars with a welded corner connection, a partial penetration single- V groove weld was placed all around the corner joints and then welded. A total of 11 columns were tested in this study, including two columns with conventional reinforcement, the control columns, and the remaining columns had external steel collars. For the columns that had external steel collars, no tie reinforcement was provided in the test region to study the effect of external confinement exclusively. Column reinforcement details and typical test specimen with welded collars in the test region are shown in Figure 2.46.
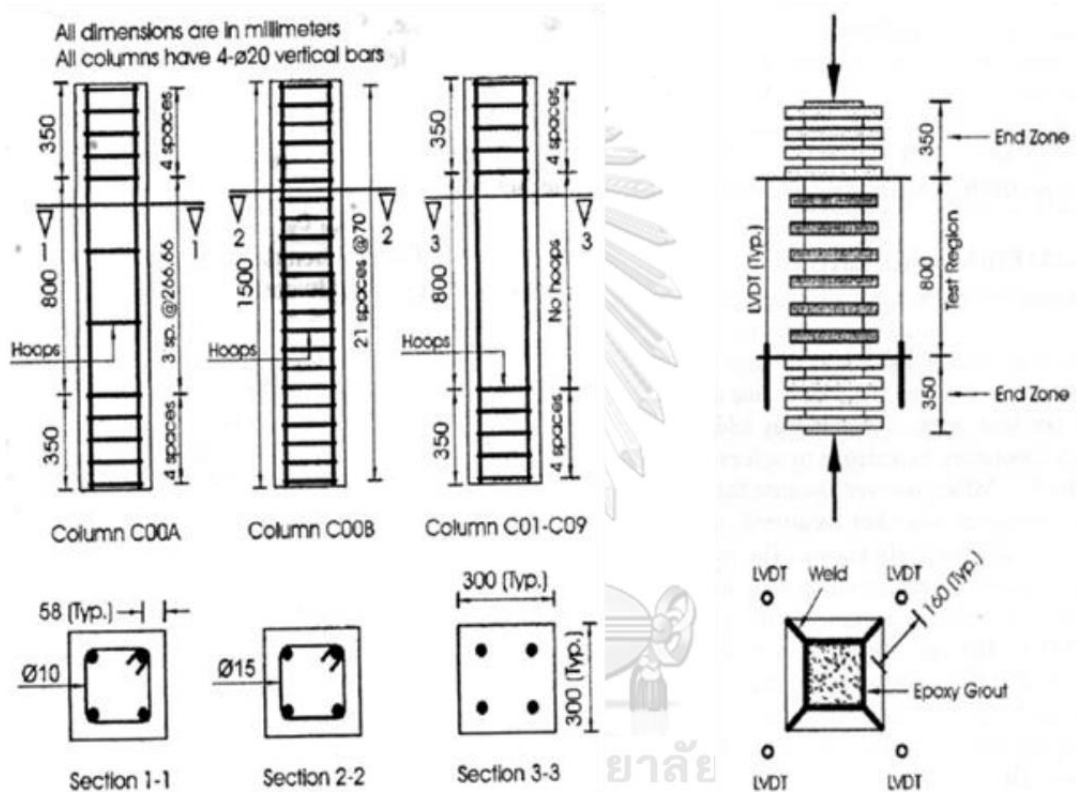
Figure 2.46 Typical test specimen and strengthening adopted by Hussain and Driver [44].

The control column C00A showed brittle failure mainly due to the wide spacing of ties, and a similar behavior was observed in the other control columns. On the contrary, ductile behavior was observed in the strengthened columns with the degree of ductility associated with the spacing of HSS collars Figure 2.47. It was concluded that the efficiency of the collars with welded connections in improving the peak axial load was better than that of the collars with bolted connections. However, due to the insufficient depth of the groove welds, the ultimate failure strain of the columns in the case of welded collars was lower due to the premature failure of the welds. It was suggested that a deeper weld would have avoided this premature failure, and a higher concrete ultimate strain would have been achieved. The effect of collar spacing was found predominant on the peak axial load. It was found that a 60% higher collar spacing would reduce the axial load capacity by half.
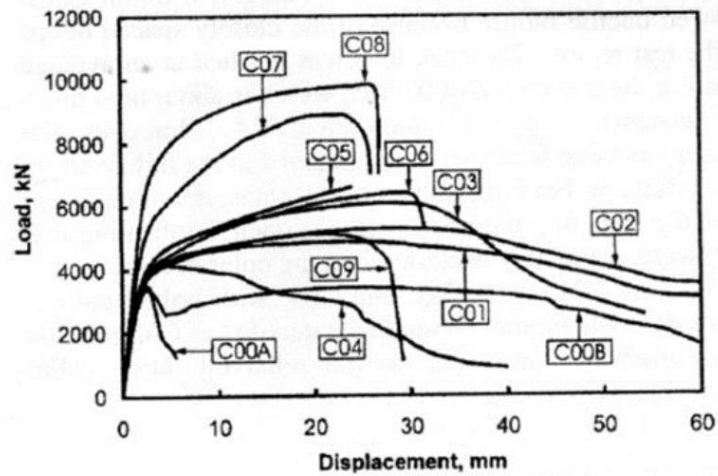
Figure 2.47 Axial load vs. displacement curves of columns tested by Hussain and Driver [44].

Liu et al. [73] assessed the role of hollow structural section collars in increasing the shear capacity of RC columns. The collars were assembled by using two L-shaped components, which were obtained by cutting a 50 mm thick steel plate. The purpose of this technique was to confine the concrete with significant flexural and axial stiffness. A total of ten columns were tested under constant axial and reverse cyclic loading. Two columns were tested in as-built condition, whereas the remaining eight columns were strengthened by using steel collars. Specimen reinforcement details are shown in Figure 2.48. Fabrication and assembled view of the steel collar are shown in Figure 2.49.
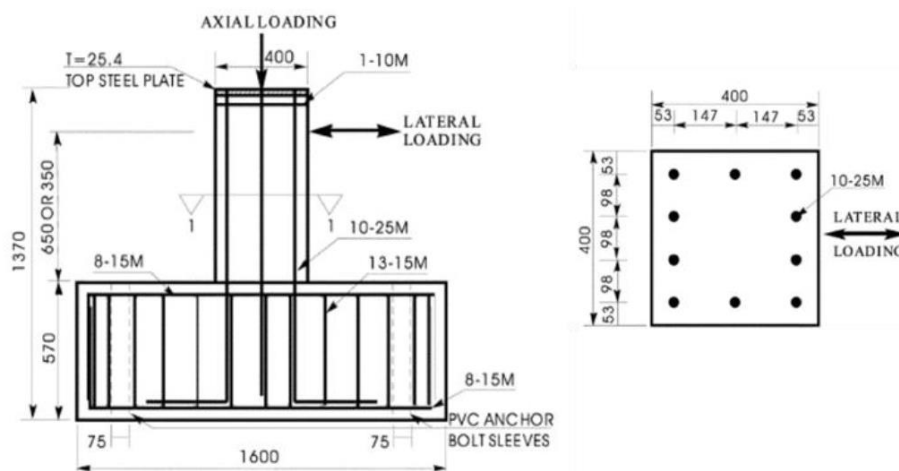
Figure 2.48 Specimen details tested by Liu et al. [73].
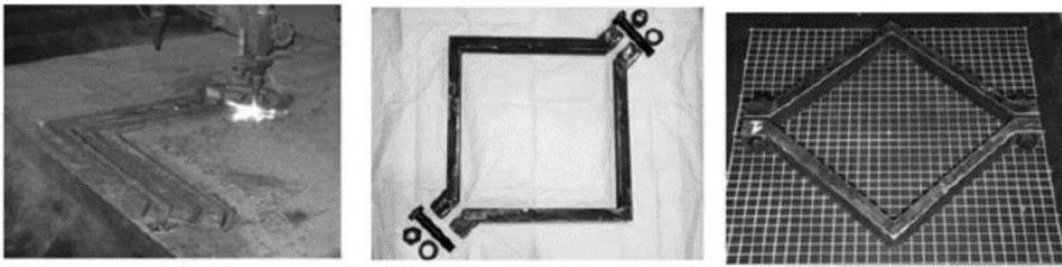
Figure 2.49 Steel collar assembling by Liu et al. [73].

It was concluded that all columns exhibited flexural failure except the specimen without axial load. In general, substantial improvement was observed in the behavior of strengthened columns in terms of lateral ductility and energy dissipation. Collars were rigidly fixed to the column throughout the loading without any slip. However, lateral bending of the collars was observed as expected. As a result, concrete spalling was prevented. The experiments showed that the collar columns had stable hysteresis behavior. Force displacement envelopes for retrofitted test specimens are shown in Figure 2.50.
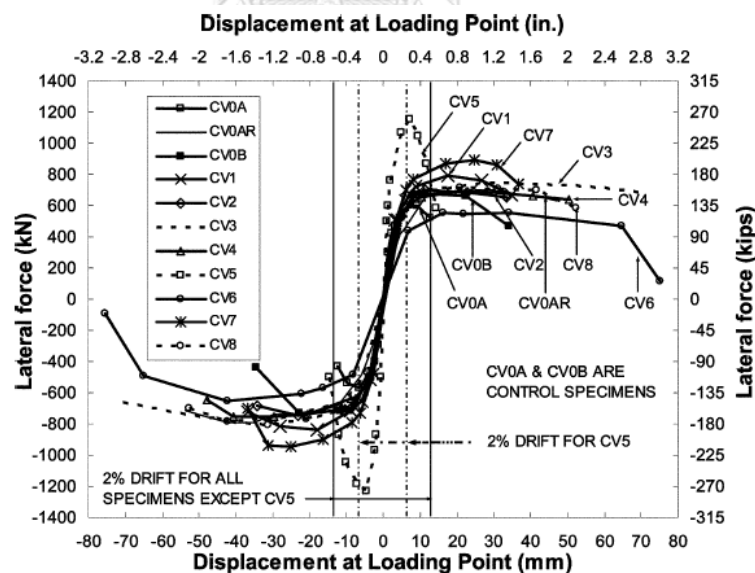
Figure 2.50 Lateral load-deflection envelopes of columns tested by Liu et al. [73].

Pudjisuryadi et al. [74] tested five columns comprising two control columns (CS1-1 and CS1-2) with conventional stirrups, and three columns strengthened with steel angle collars (S1-3, S1-4, and S1-5). The size of the steel angle collar was 40

mm × 40 mm × 4 mm. The spacing of steel angle collars in columns S1-3, S1-4, and S1-5 was 180 mm, 120 mm, and 90 mm, respectively. Typical control and collar specimens are shown in Figure 2.51. All columns were subjected to an axial load equal to 30% of the self-weight of the column. A displacement-controlled cyclic load was applied to the column tip. The basic difference between the collar application by Pudjisuryadi et al. [74] and by Hussain and Driver [44] was that no grouting between the collar and concrete face was provided by Pudjisuryadi et al. [74].
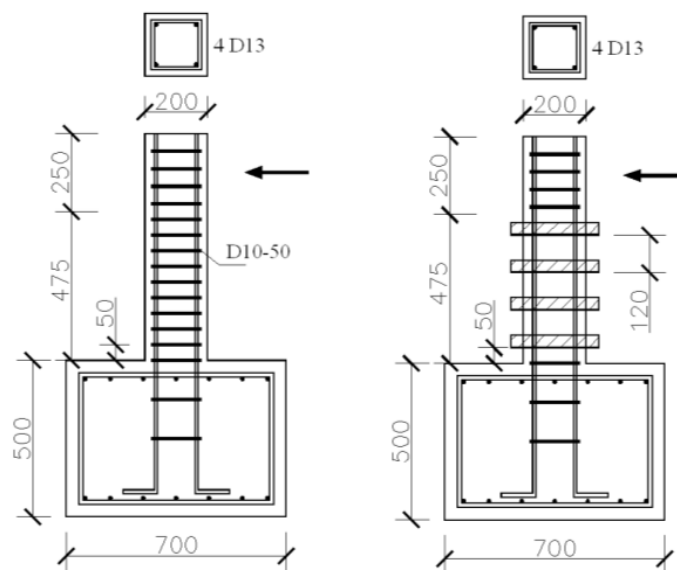
Figure 2.51 Typical control and collar specimen tested by Pudjisuryadi et al. [74].

The measured hysteretic response of all columns tested by Pudjisuryadi et al. [74] is shown in Figure 2.52. The internal confinement ratio (ties) was 0.78% and 2.36% in the control columns CS1-1 and CS1-2, respectively. The resulting improvement due to the increase in the number of ties is depicted in Figure 2.52(a) and Figure 2.52(b). It can be seen in Figure 2.52(d) that a collar spacing of 120 mm resulted in a similar ductile response as that of column CS1-2. All the strengthened columns demonstrated a ductility of 4.5, whereas the ductility of the control column CS1-1 was 3.5.
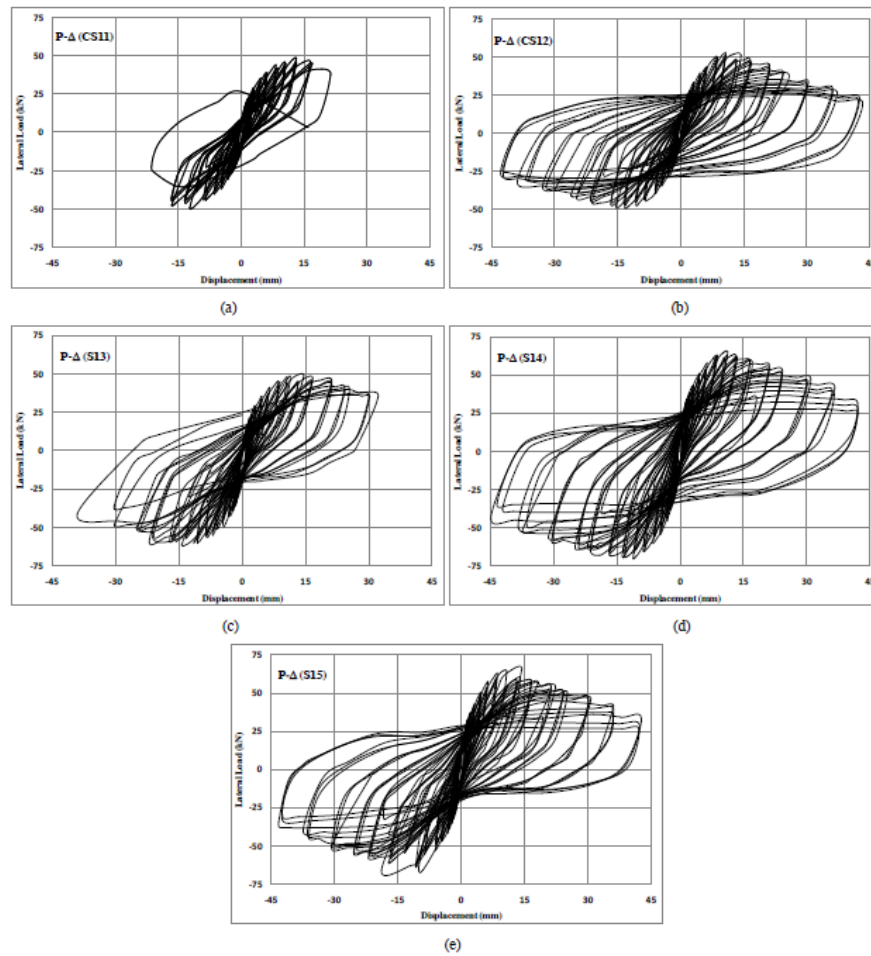
Figure 2.52 Lateral load-deflection hysteretic response of columns tested by Pudjisuryadi et al. [74] (a) CS1-1, (b) CS1-2, (c) S1-3, (d) S1-4, and (e) S1-5.

Dirikgil [75] tested nine columns in three groups depending on the cross-sectional area. Table 2.7 presents the details of all specimens and strengthening schemes applied. In this study, the performance of CFRP jackets and steel collars was compared in mitigating the shear failure in short columns.

Table 2.7 Details of test specimens tested by Dirikgil [75].

Series	Column	Long. Reinf.	Stirrup	Strengthening
300 × 400	SC300 × 400-Ref	8Ø16	Ø10/100	–
	SC300 × 400-CFRP	8Ø16	Ø10/150	200 mm CFRP full wrap + 50 mm wide 50 mm spaced strip
	SC300 × 400-C	8Ø16	Ø10/150	Two combined Collar + 50 mm wide 50 mm spaced collar
300 × 550	SC300 × 550-Ref	10Ø16	Ø10/100	–
	SC300 × 550-CFRP	10Ø16	Ø10/150	200 mm CFRP full wrap + 50 mm wide 50 mm spaced strip
	SC300 × 550-C	10Ø16	Ø10/150	Two combined Collar + 50 mm wide 50 mm spaced collar
300 × 700	SC300 × 700-Ref	12Ø16	Ø10/100	–
	SC300 × 700-CFRP	12Ø16	Ø10/150	200 mm CFRP full wrap + 50 mm wide 50 mm spaced strip
	SC300 × 700-C	12Ø16	Ø10/150	Two combined Collar + 50 mm wide 50 mm spaced collar

Collars were provided at a clear spacing of 50 mm. The typical collar used by Dirikgil [75] is shown in Figure 2.53. The width and thickness of the collar were 50 mm and 10 mm, respectively. All the columns were subjected to lateral cyclic loading in addition to an imposed axial load.
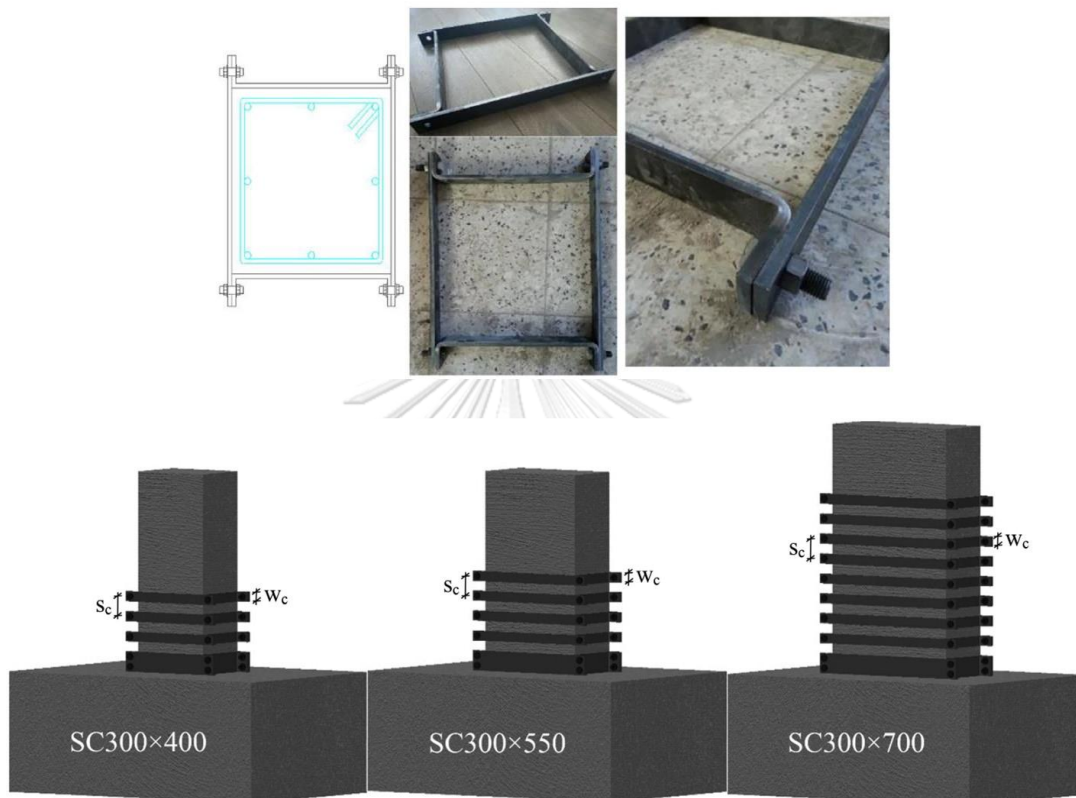
Figure 2.53 Details of the collars used by Dirikgil [75].

The lateral load-deflection envelopes of all three groups are shown in Figure 2.54. It is evident that the performance of CFRP and steel collar strengthened columns was superior to the performance of reference columns. In addition, the performance of CFRP and steel collar strengthened columns was comparable in group 2 columns. In group 1 and group 3, steel collar strengthened columns demonstrated slightly better performance than CFRP columns in terms of the peak lateral load and lateral displacement ductility. It was concluded that the performance of steel collars increased as the cross-section of the column increased. For instance, the lateral displacement ductility of the column SC(300×700)-CFRP was 6.61, whereas the

same column strengthened with steel collars demonstrated a lateral displacement ductility of 7.81.

(a)

(b)

(c)
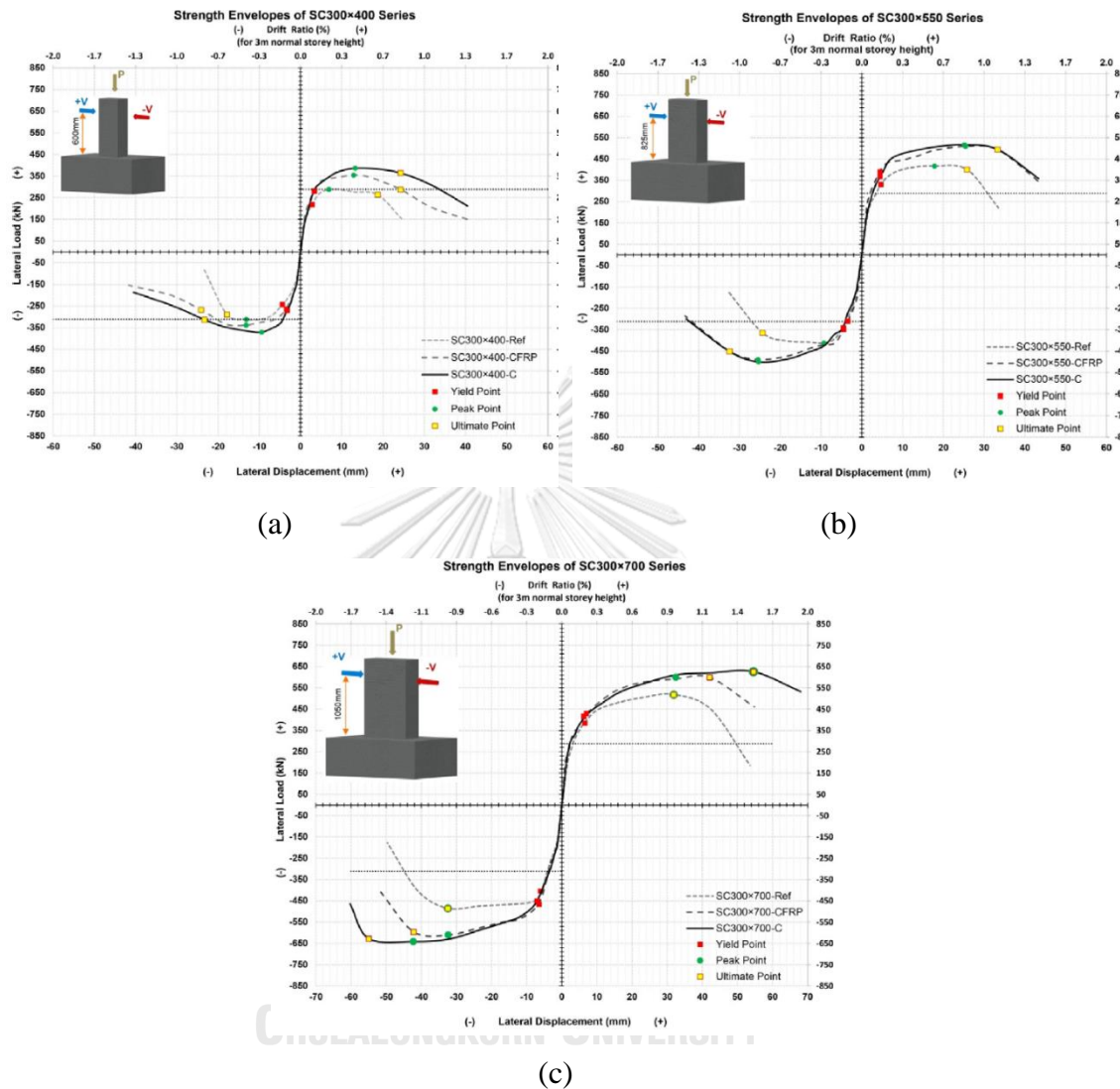
Figure 2.54 Lateral load-deflection envelopes of columns tested by Dirikgil [75] (a) group 1, (b) group 2, and (c) group 3.

2.5.2. Strengthening RC Members with Lap splices

Kruavit [76] tested a total of 7 RC columns. All the columns were flexure controlled with a shear span-to-depth ratio of 5.5. One column was provided with no lap splice, and one column was incorporated with a splice length of $28d_b$ and kept as control. Two columns incorporated mechanical splices, while three columns with $28d_b$ splice length were strengthened using steel collars at different spacings. All the

columns were subjected to a constant axial load and cyclic lateral loading. The cross-section and geometry of the tested specimens are shown in Figure 2.55.
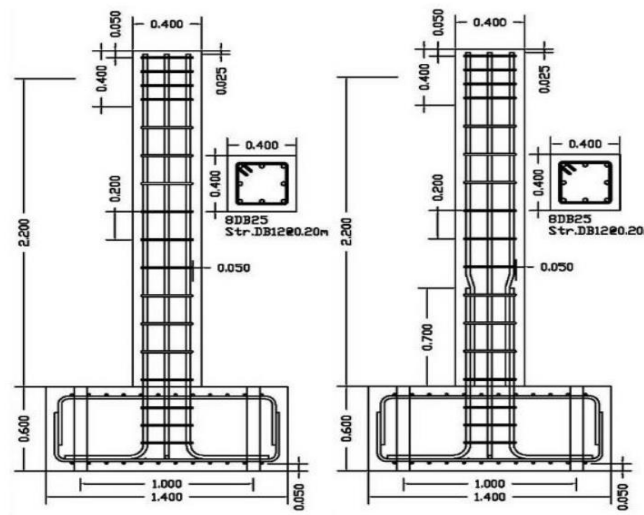
Figure 2.55 Typical column details tested by Kruavit [76].

Comparing the hysteretic envelopes of non-spliced NS and control column LS (having a lap splice length of $28d_b$), the column with continuous reinforcement showed a relatively stable hysteretic response, while the column with lap splice showed rapid degradation after reaching the peak strength. Column LS failed in a brittle manner due to lap splice failure and under-achieved its capacity as well as ductility. As shown in Table 2.8, column LS achieved a ductility of 1.58 as compared to the ductility of 3.69 for the NS column.

Table 2.8 Summary of experimental results of unstrengthened columns tested by Kruavit [76].

Specimen	P_{max}	Disp@ P_{max}	0.8 P_{max}	Displ@ 0.8P_{max}	Disp@75% secant	Ductility	Initial stiffness (kN-mm)
NS	143	60.7	114	109.0	29.5	3.69	8.76
LS	122	41.9	98	55.8	35.3	1.58	6.10

The design of the collar section was conducted by using the equation of Richart et al. [77] as

$$f_{cc} = f'_{co} + 4.1\sigma_2 \qquad\qquad 2.13$$

where f_{co}' is the unconfined concrete strength, σ_2 is the lateral confining pressure on concrete, and f_{cc} is the confined concrete strength. It was assumed that the splitting failure might be prevented by increasing the concrete strength as large as that in an unconfined state. From this assumption, the lateral confining pressure σ_2 was estimated to be 5.75 MPa. Among various cross-sectional shapes, a rectangular hollow steel section (HSS) was chosen as it provided the lowest weight for the same section modulus, as shown in Figure 2.56.
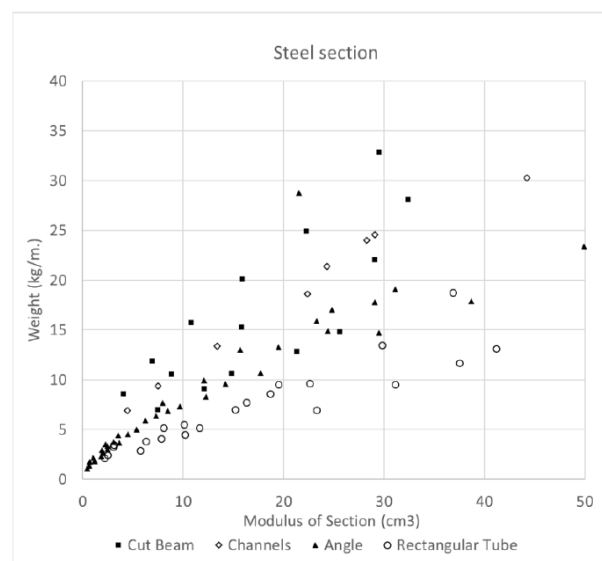
Figure 2.56 Weight vs. section modulus from various steel sections calculated by Kruavit [76].

An HSS size of $50 \times 50 \times 2.3$ was chosen from analysis on SAP2000. Then, the designed steel collars were used at three different spacings up to a height of 1100 mm, inclusive of which is 700 mm length of lap splice as shown in Figure 2.57. Collars were provided at 100 mm (column SC1), 200 mm (column SC2), and 333 mm (column SC3), respectively. The envelopes of lateral hysteretic load-displacement curves are shown in Figure 2.58. It can be seen that all the strengthened columns demonstrated better performance than the corresponding control column LS. The performance of columns SC1 and SC2 was better than the rest of the columns in terms of ductility and peak lateral load. Further, the ductility of specimen SC1 was found comparable to the ductility of the column without lap splices, i.e., the column NS1.
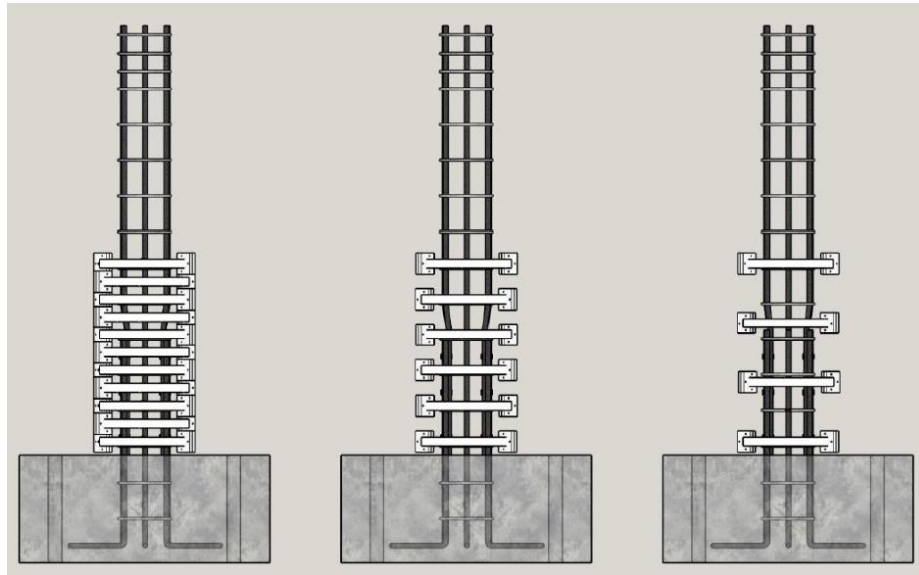
Figure 2.57 Different HSS collar arrangements to strengthen substandard lap splices by Kruavit [76].
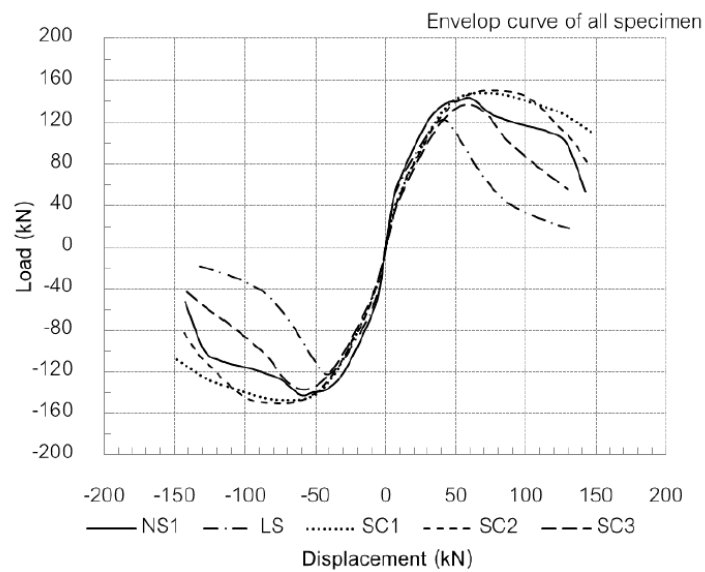
Figure 2.58 Envelope curves of the lateral load-displacement hysteretic curves of specimens tested by Kruavit [76].

2.5.3. Summary of Strengthening Using Steel Collars

In recent years, the axial, shear, and flexural performance of columns has been assessed by using steel collars. Steel collars have proved to be an effective solution to strengthen axial, shear, and flexural behavior. It is seen that the performance of steel

collars was comparable to or better than the performance of widely used FRP jackets, and the performance of steel collars was not affected by the cross-sectional size of the member [75] [49]. The study by Kruavit [76] demonstrated that hollow steel section (HSS) collars could prevent lap splice failures. It was found that a spacing of 100 mm of HSS collar with a cross-section of 50 mm × 50 mm × 2.3 mm was sufficient to mitigate the splitting failure of a $28d_b$ lap splice. The design of HSS collars by Kruavit [76] was vaguely based on the assumption that the splitting failure may be prevented by increasing the concrete strength twice as large as in an unstrengthened state. Further, no design guidelines were established to estimate the size and spacing of HSS collars for lap splices other than $28d_b$ in length.

2.6. Non-Linear Fiber Modelling of Substandard Lap spliced Reinforced Concrete Columns

In this section, a few approaches are discussed to analyze a column with substandard lap splice. The approaches consist of modeling based on distributed plasticity and concentrated plasticity.

2.6.1. Models Based on Distributed Plasticity

Tariverdilo et al. [78] recognized that a deficient lap spliced column at the base might not be able to develop its full capacity due to the premature splitting failure limiting steel stress within the lap splice below the yield strength. To obtain maximum developable stress within lap splice, the formulations of Priestley et al. [79] were used. It was assumed that maximum developable stress is proportional to the tensile strength of concrete. A failure surface around each lap spliced pair was assumed of height equal to the splice length and perimeter p given as

$$p = \frac{s}{2} + 2(d_b + c) \leq 2\sqrt{2}(d_b + c) \qquad 2.14$$

where s is the clear spacing between spliced pairs. It was further supposed that slip resistance is provided by a 45° truss mechanism between spliced bars or between a bar and surrounding concrete. From this, Eq. 2.15 was formulated as

$$T_b = A_s f_s = F_t p l_s \qquad 2.15$$

where f_s is maximum developable splice stress and F_t is the tensile strength of concrete given as $0.33\sqrt{f_c'}$ (MPa). After reaching f_s, stress drops until a stress f_r that corresponds to a constant residual stress zone. This residual stress was assumed to be supported by transverse reinforcement passing the splitting plane and providing frictional resistance corresponding to frictional coefficient μ (see Figure 2.59). Eq. 2.16 was proposed to estimate the residual stress f_r.

$$n_l n_t \mu A_h f_h = n A_b f_r \qquad\qquad 2.16$$

where n_l, n_t, A_h, f_h, n, and A_b are the number of legs of transverse reinforcement, the total number of transverse reinforcements within splice length, area of transverse reinforcement, yield strength of transverse reinforcement, number of longitudinal spliced bars, and area of a single longitudinal bar, respectively.
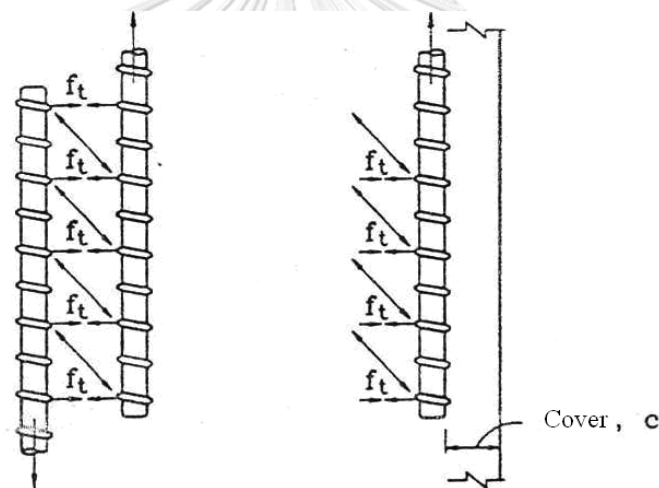
Figure 2.59 Force transfer in lap splice (Priestley et al. [79]).

Acknowledging the contribution of slip to total deformation, Eq. 2.17 and Eq. 2.18 were proposed to estimate strain at f_s and f_r, respectively.

$$\epsilon_s = \frac{f_s}{E_s} + \frac{1}{b} \qquad\qquad 2.17$$

$$\epsilon_r = \frac{10}{b} \qquad\qquad 2.18$$

where b and E_s are the width of the section and elastic modulus of steel, respectively. Factors 1.0 and 10.0 correspond to the slip of 1 mm and 10 mm, respectively. It was suggested to use *Hysteretic* material for steel within the lap splice zone. To account for pinching in x- and y-directions, values of 0.8 and 0.3 were suggested for *pinchX*

and *pinchY* parameters. Further, 0.0 and 0.02 values were suggested for *damage*2 and *damage*1 parameters, respectively, to account for displacement and energy degradation. The modeling strategy adopted by Tariverdilo et al. is shown in Figure 2.60.
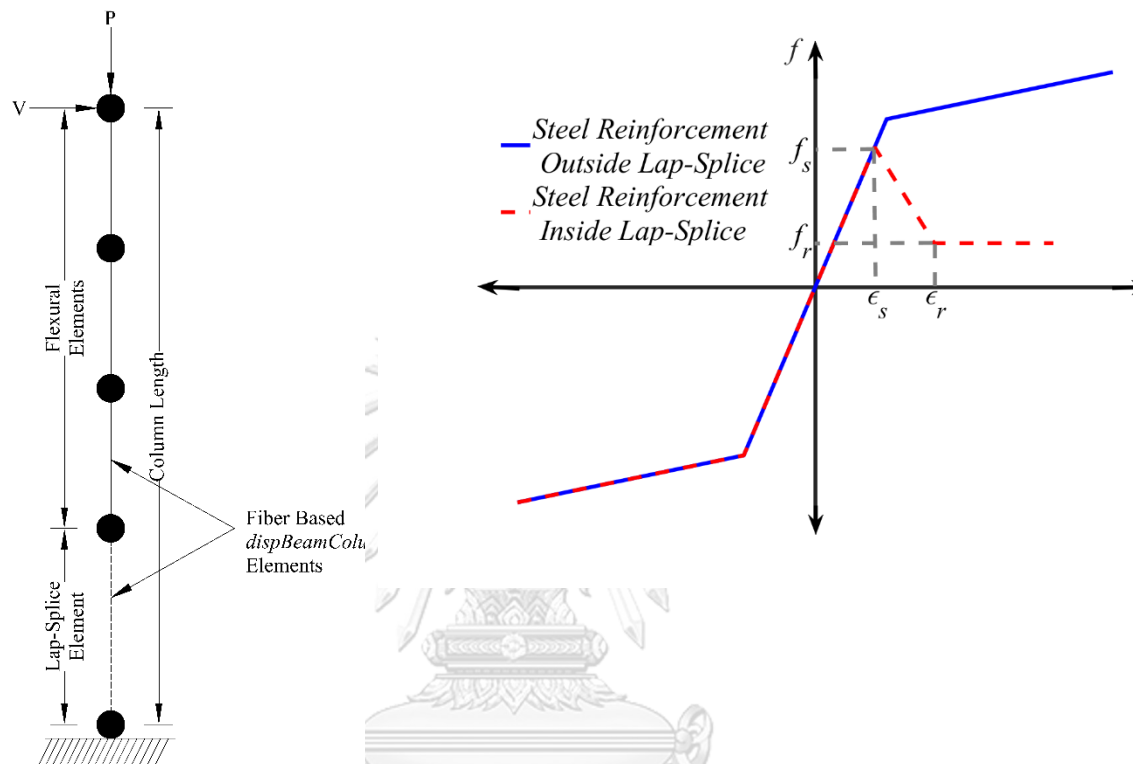
Figure 2.60 Column discretization and definition of steel bar stress-strain relationship by Tariverdilo et al. [78].

Concrete within cover and core was modeled using *Concrete02* material. Properties of core concrete were modified using the recommendations of Mander et al. [80]. Five integration points were used within each element.

Choi et al. [81] used a similar numerical model as that of Tariverdilo et al. [78] to predict the hysteretic load-deformation response of deficient lap spliced columns. *Hysteretic* material was used to model the stress-strain relation of lap spliced bars. However, the concrete was modeled using *Pinching4* material. The benefit of *Pinching4* material over *Hysteretic* material is that it offers more options to control cyclic strength and stiffness degradation as well as the pinching behavior. Mainly, points on the envelope correspond to define unloading stiffness, reloading

stiffness, and strength degradation under cyclic loading. As shown in Figure 2.61 Pinching4 material backbone curve in OpenSees, the point *rDispP* defines the ratio of the deformation at which reloading occurs to the maximum historic deformation demand, *rForceP* defines the ratio of the force at which reloading begins to force corresponding to the maximum historic deformation demand, and *uForceP* defines the ratio of strength developed upon unloading from negative load to the maximum strength developed under monotonic loading. This material was proposed by Lowes and Mitra [82], who implemented the damage rules of Park and Ang [83] for unloading stiffness, reloading stiffness, and strength degradation under cyclic loading. If the damage indices are assumed to be functions of displacement history and energy accumulation, the unloading stiffness damage index δk_i is defined as

$$\delta k_i = \left(gk_1 (\widetilde{d_{max}})^{gk_3} + gk_2 \left(\frac{E_i}{E_{monotonic}} \right)^{gk_4} \right) \leq gk_{lim} \qquad 2.19$$

$$\widetilde{d_{max}} = \max \left(\frac{d_{max,i}}{def_{(max)}}, \frac{d_{min,i}}{def_{(min)}} \right) \qquad 2.20$$

$$E_i = \int_0^{loadhistory} dE \qquad 2.21$$

$$E_{monotonic} = gE \left(\int_0^{monotonicloadhistory} dE \right) \qquad 2.22$$

where *i* refers to the current displacement increment, δ_i is the damage index (δ_i equal to 0 represents a state of no damage and δ_i equal to 1.0 represents the case of maximum damage), $gk's$ are parameters used to fit the damage rule to the experimental data, E is hysteretic energy with $E_{monotonic}$ equal to the energy required to achieve under monotonic loading the deformation that defines failure, def_{max} and def_{min} are, respectively, the positive and negative deformations that define failure, and $d_{max,i}$ and $d_{min,i}$ are, respectively, the maximum historic and minimum historic deformation demands. Finally, for the case of unloading stiffness, current unloading stiffness is evaluated from Eq. 2.23. A similar form of damage rule is adopted for reloading stiffness and strength degradation as well.

$$k_i = k_0 (1 - \delta k_i) \qquad 2.23$$

where k_0 is the initial unloading stiffness for no damage case. Choi et al. [81] calibrated their experimental results of the lap spliced column under hysteretic loading and by using *Pinching4* material. The calibrated parameters of *Pinching4* material are shown in Table 2.9. It must be mentioned that the same parameters were used for positive and negative loading directions.
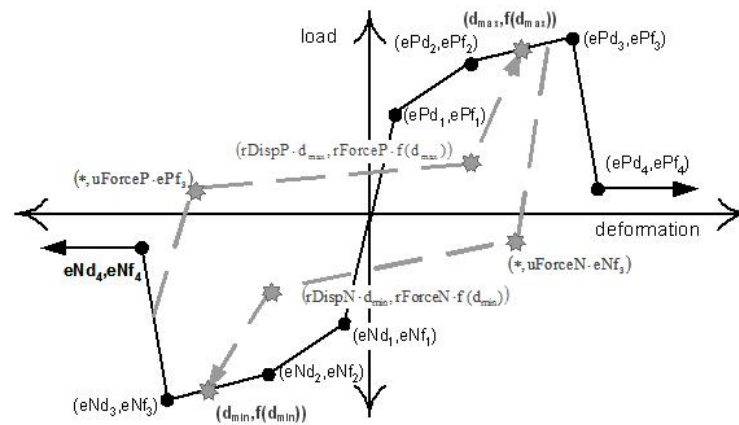
Figure 2.61 Pinching4 material backbone curve in OpenSees [84].

Table 2.9 Calibrated parameters for Pinching4 material by Choi et al. [81].

Parameter	Value	Parameter	Value
rDispP	0.01	*gD3*	0.1
RForceP	0.3	*gD4*	0.1
uForceP	0.4	*gDLim*	1
gK1	-0.4	*gF1*	0.2
gK2	-0.4	*gF2*	0.2
gK3	-0.4	*gF3*	1
gK4	-0.4	*gF4*	1
gKLim	1	*gFLim*	1
gD1	0.1	*dmgType*	"energy"
gD2	0.1	-	-

Zhang et al. [85] used force-based beam-column elements in *OpenSees* to model the substandard lap splice behavior. The recommendations of Tariverdilo et al. [78] were used to estimate the modified stress-strain relation of lap spliced bars, as shown in Figure 2.62. In addition to the modeling strategy adopted by Tariverdilo et al. [78], two additional rotational bond-slip springs were attached at the top and

bottom of the column (since the column was in double curvature). The rotational bond-slip springs were modeled by using zero-length elements in *OpenSees,* and the properties were estimated by using the model by Zhao and Sritharan [86].
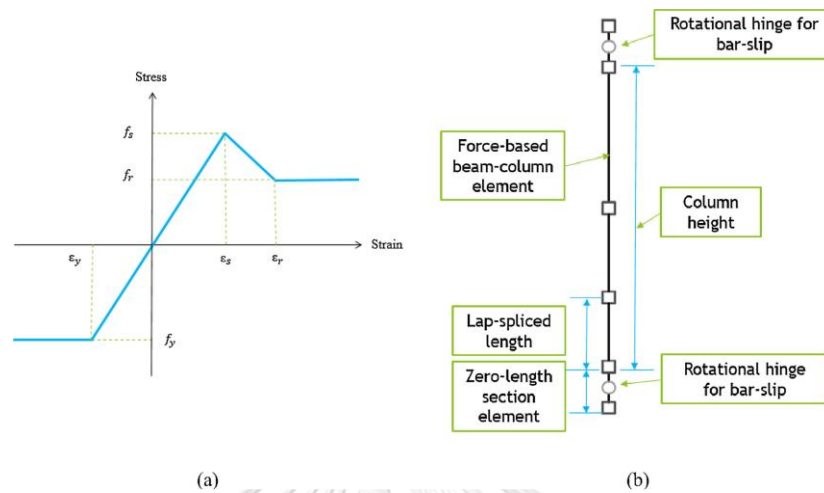
Figure 2.62 Modelling strategy for the lap spliced column by Zhang et al. [85] (a) stress-strain relation of lap spliced bars, and (b) analytical model of the column.

Zhang et al. [87] used force-based elements in OpenSees to model the lap spliced RC columns. The analytical model used by Zhang et al. [87] is shown in Figure 2.63. The model comprised two force-based elements connected in series. The length of the bottom element was taken equal to the lap splice length. The authors used the recommendations of Tariverdilo et al. [78] to model the stress-strain behavior of lap spliced bars. It has been known that strain-location occurs in force-based elements at the most-strained section, which is the column-to-footing junction in this case.
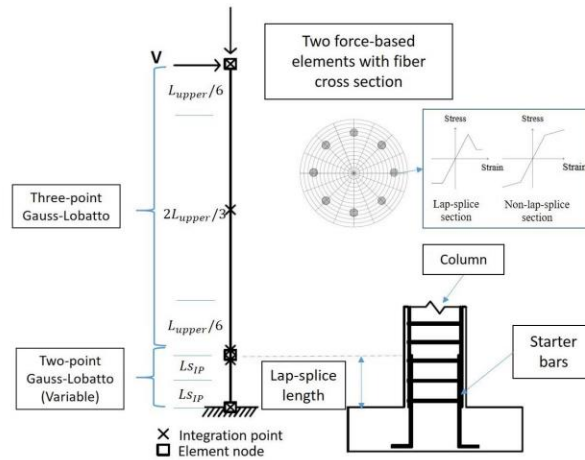
Figure 2.63 Analytical model of lap spliced RC column used by Zhang et al. [87].

The authors proposed a strain regularization scheme based on the concept of fracture energy [88]. According to Coleman and Spacone [88], the energy dissipated by using force-based elements depends upon the number of integration points. As the number of integration points increased, the energy dissipated by the most-strain integration points was reduced. Therefore, the concept of fracture energy was introduced to balance the energy dissipation and make it independent of the number of integration points. Coleman and Spacone [88] applied the concept of fracture energy regularization to the concrete material, as shown in Figure 2.64. By following this approach, the strain corresponding to the 80% reduction in peak strength was estimated as

$$\epsilon_{20u} = \frac{G_f^c}{0.6 f_c' L_{IP}} - \frac{0.8 f_c'}{E_c} + \epsilon_o \qquad 2.24$$

where G_f^c is the fracture energy obtained from experiments. A commonly used value of 25 N/mm was used for unconfined concrete, whereas a value of 150 N/mm was used for confined concrete. In Eq. (2.30), L_{IP} is the length of the most-strained integration point, and E_c is the elastic modulus of concrete.
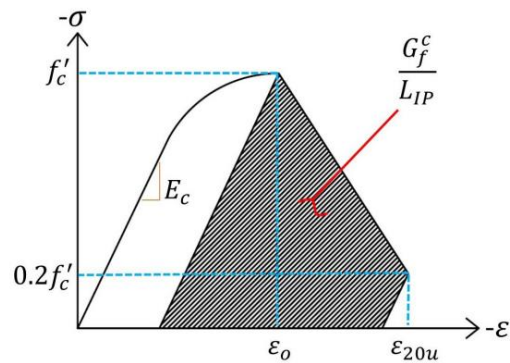
Figure 2.64 Post-peak fracture energy regularization of concrete material by Coleman and Spacone [88].

Zhang et al. [87] noticed that the fracture energy regularization of concrete material was insufficient to regularize the response of lap spliced columns. This is shown in Figure 2.65, where the static pushover curves of lap spliced columns are plotted. It can be seen that the softening behavior was dependent on the number of integration points.
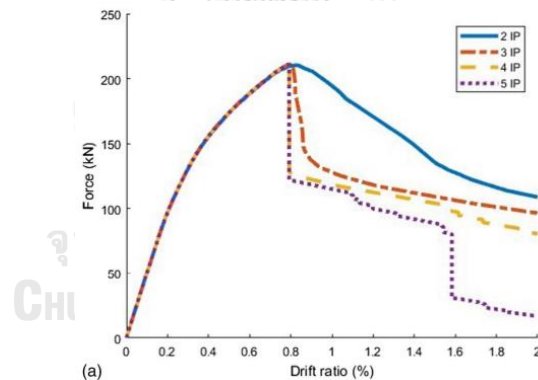
Figure 2.65 Non-regularized static pushover curves of lap spliced column by Zhang et al. [87].

Zhang et al. [87] applied the same regularization scheme to the stress-strain relation of substandard lap splices. The detailed derivation of the regularization process can be found in the paper by Zhang et al. [87]. In general, the point corresponding to the residual stress in the model of Tariverdilo et al. [78] was shifted depending upon the number of integration points used. For a greater number of integration points, the length of the most-strained integration point reduces. As a

result, it is required to increase the corresponding post-peak fracture energy to regularize the response, as shown in Figure 2.66. The resulting pushover curves are shown in Figure 2.67. It can be seen that the highly sensitive to the number of integration points response in Figure 2.65 is now insensitive to the number of integration points.
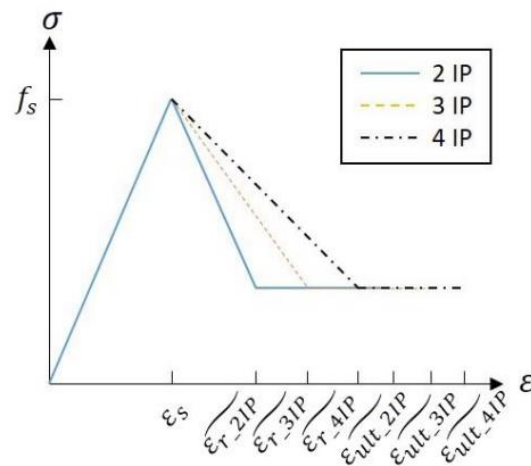
Figure 2.66 Effect of fracture energy regularization on the shape of stress-strain relation of lap spliced bar by Zhang et al. [87].
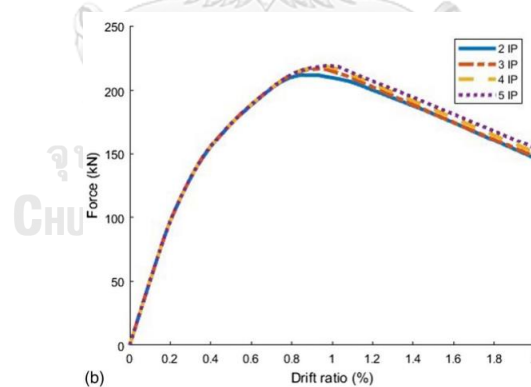
Figure 2.67 Regularized static pushover curves of lap spliced column by Zhang et al. [87].

Alvi et al. [89] performed regression analysis on experimental results of several RC columns failing in splitting. The idea was to link the parameters of *Hysteretic* material with various characteristics of columns. A similar approach to that of Tariverdilo et al. [78] was adopted. The need for an updated approach was recognized as the same strength and stiffness parameters proposed by Tariverdilo et

al. [78] did not result in good predictions of the hysteretic response of existing short lap spliced RC columns. A slight modification in the basic numerical model was suggested by adding an additional rotational spring at the base of the RC column. This was intended to simulate additional deformation components arising from the slip of lap spliced bars. The remaining numerical model remained the same as that of Tariverdilo et al. [78], as shown in Figure 2.68.
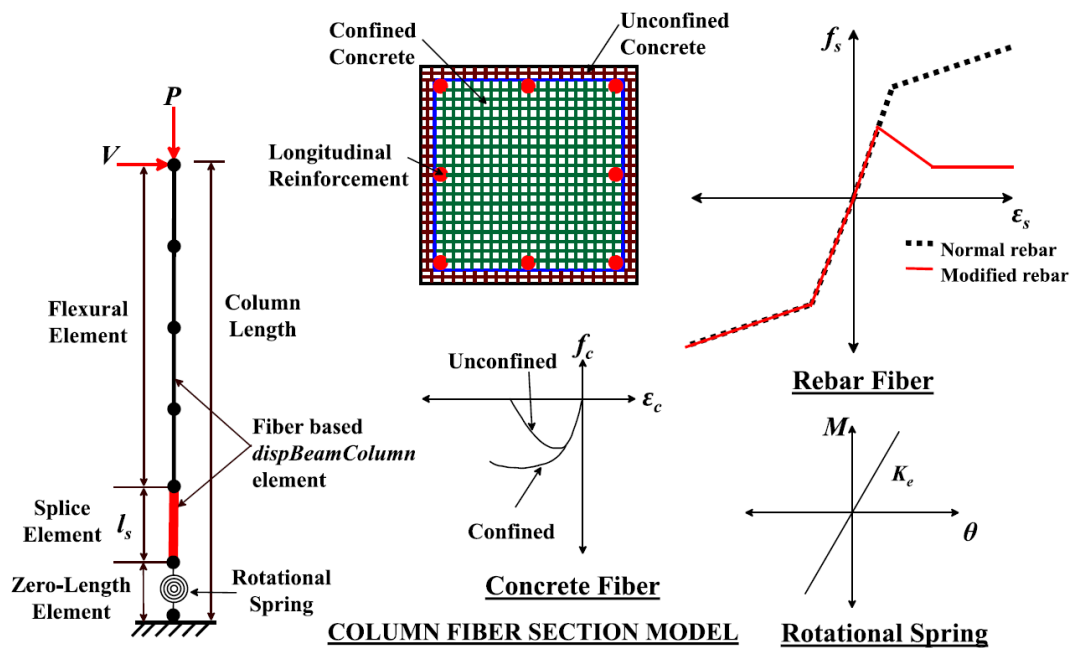
Figure 2.68 Analytical model proposed by Alvi et al. [89].

To modify the constitutional stress-strain relation of lap spliced bars in tension, parameters β, γ, and λ were suggested in Eq. 2.25, 2.26, and 2.27.

$$f_s = \beta f_y \qquad\qquad 2.25$$
$$f_r = \gamma f_y \qquad\qquad 2.26$$
$$\epsilon_r = \lambda \epsilon_y \qquad\qquad 2.27$$

where f_s is the maximum stress that can be transferred (on ascending branch), f_r is the residual stress, and ϵ_r is the strain corresponding to f_r. Further, the stiffness of the rotational spring was taken as a function of α.

$$k_e = \alpha \frac{E_c I_z}{L_c} \qquad\qquad 2.28$$

where E_c, I_z, L_c are elastic modulus of concrete, second moment of area of the cross-section, and length of the column, respectively. Pinching ($pinchX$ and $pinchY$) and damage ($damage1$ and $damage2$) parameters were taken as functions of various RC columns characteristics.

Considered characteristics for nonlinear regression included width of column cross-section B, the height of column cross-section H, effective depth d, shear span a, diameter of longitudinal reinforcement d_b, number of longitudinal reinforcement bars N, the diameter of transverse reinforcement d_h, the center-to-center spacing of transverse reinforcement s_h, longitudinal reinforcement ratio ρ_l, measured compressive strength of concrete f_c', measured yield strength of lap spliced bars f_y, measured yield strength of transverse reinforcement f_{yt}, length of lap splice l_s, and axial load on column P. The following equations were proposed for various parameters defining *Hysteretic* material in *OpenSees* for lap spliced bars.

$$\alpha = 9.096 - 245.12\left(\frac{A_s}{A_g}\right) - 25.667\left(\frac{P}{f_c'A_g}\right) + 1.13\left(\frac{a}{d}\right) - 0.07\left(\frac{f_{yt}}{f_c'}\right) - 0.580\left(\frac{s}{d_b}\right) -$$
$$42.739\left(\frac{A_s}{A_g}\frac{a}{d}\right) + 19.659\left(\frac{A_s}{A_g}\frac{s}{d_b}\right) + 7.758\left(\frac{P}{f_c'A_g}\frac{a}{d}\right) - 18.946\left(\frac{P}{f_c'A_g}\right)^2 \qquad 2.29$$

$$\beta = 2.457 - 0.022\left(\frac{a}{d}\right) - 4.247\left(\frac{s}{d}\right) + 27.387\left(\frac{A_{st}}{sb}\right) - 0.081\left(\frac{l_s}{d_b}\right) - 0.053\left(\frac{l_d}{d_b}\right) +$$
$$0.303\left(\frac{s}{d_b}\right) + 0.110\left(\frac{a}{d}\frac{s}{d}\right) + 0.056\left(\frac{s}{d}\frac{l_s}{d_b}\right) + 0.139\left(\frac{s}{d}\frac{s}{d_b}\right) + 0.001\left(\frac{l_s}{d_b}\frac{l_d}{d_b}\right) - 0.004\left(\frac{l_s}{d_b}\frac{s}{d_b}\right) \qquad 2.30$$
$$+0.001\left(\frac{l_s}{d_b}\right)^2 - 0.011\left(\frac{s}{d_b}\right)^2$$

$$\gamma = -1.952 - 120.46\left(\frac{A_s}{A_g}\right) + 0.222\left(\frac{P}{f_c'A_g}\right) + 0.789\left(\frac{a}{d}\right) + 129.93\left(\frac{A_{st}}{sb}\right) - 0.034\left(\frac{f_{yt}}{f_c'}\right) +$$
$$0.016\left(\frac{l_s}{d_b}\right) + 0.076\left(\frac{l_d}{d_b}\right) + 4271\left(\frac{A_s}{A_g}\frac{A_{st}}{sb}\right) + 3.003\left(\frac{A_s}{A_g}\frac{f_{yt}}{f_c'}\right) - 0.020\left(\frac{a}{d}\frac{l_d}{d_b}\right) - 6.043\left(\frac{A_{st}}{sb}\frac{l_s}{d_b}\right) \qquad 2.31$$
$$+1694.1\left(\frac{A_s}{A_g}\right)^2 - 8731\left(\frac{A_{st}}{sb}\right)^2$$

$$\lambda = -109.54 + 3742.6\left(\frac{A_s}{A_g}\right) + 6.569\left(\frac{P}{f_c'A_g}\right) + 2.755\left(\frac{a}{d}\right) + 63.365\left(\frac{s}{d}\right) + 34301\left(\frac{A_{st}}{sb}\right) +$$
$$0.354\left(\frac{l_s}{d_b}\right) + 0.583\left(\frac{l_d}{d_b}\right) - 238.57\left(\frac{A_s}{A_g}\frac{P}{f_c'A_g}\right) - 1693.4\left(\frac{A_s}{A_g}\frac{s}{d}\right) - 1.186\times10^6\left(\frac{A_s}{A_g}\frac{A_{st}}{sb}\right) - \qquad 2.32$$
$$13431\left(\frac{A_{st}}{sb}\frac{s}{d}\right) - 0.013\left(\frac{l_s}{d_b}\frac{l_d}{d_b}\right) - 26421\left(\frac{A_s}{A_g}\right)^2$$

$$pinchX = 4.021 - 191.21\left(\frac{A_s}{A_g}\right) - 7.521\left(\frac{P}{f_c'A_g}\right) + 0.463\left(\frac{a}{d}\right) - 0.057\left(\frac{f_{yt}}{f_c'}\right) - 3.806\left(\frac{l_s}{d_b}\right) +$$
$$298.86\left(\frac{A_s}{A_g}\frac{P}{f_c'A_g}\right) + 30.094\left(\frac{A_s}{A_g}\frac{a}{d}\right) + 0.536\left(\frac{P}{f_c'A_g}\frac{a}{d}\right) - 0.136\left(\frac{P}{f_c'A_g}\frac{f_{yt}}{f_c'}\right) + 0.218\left(\frac{f_{yt}}{f_c'}\frac{l_s}{d_b}\right) + \qquad 2.33$$
$$2.682\left(\frac{P}{f_c'A_g}\right)^2 - 0.112\left(\frac{a}{d}\right)^2 - 0.003\left(\frac{f_{yt}}{f_c'}\right)^2$$

$$pinchY = 1.857 + 0.008\left(\frac{A_g}{A_s}\right) - 2.19\left(\frac{P}{f_c'A_g}\right) - 0.103\left(\frac{a}{d}\right) - 693.91\left(\frac{A_{st}}{sb}\right) - 0.0008\left(\frac{f_{yt}}{f_c'}\right)$$

$$-0.172\left(\frac{A_{cc}}{A_g}\right) - 1.928\left(\frac{l_s}{d_b}\right) - 0.0006\left(\frac{A_g}{A_s}\frac{f_{yt}}{f_c'}\right) + 0.313\left(\frac{P}{f_c'A_g}\frac{a}{d}\right) + 21.47\left(\frac{A_{st}}{sb}\frac{f_{yt}}{f_c'}\right) + \qquad 2.34$$

$$466.18\left(\frac{A_{st}}{sb}\frac{l_s}{d_b}\right) + 4.338\left(\frac{P}{f_c'A_g}\right)^2 + 0.753\left(\frac{l_s}{d_b}\right)^2 \leq 1.0$$

$$damage1 = -1.041 + 0.369\left(\frac{A_s}{A_g}\right) - 0.002\left(\frac{f_y}{f_c'}\right) - 0.132\left(\frac{P}{f_c'A_g}\right) + 0.176\left(\frac{d}{a}\right) +$$

$$164.11\left(\frac{A_{st}}{sb}\right) + 2.558\left(\frac{A_{cc}}{A_g}\right) - 0.004\left(\frac{l_d}{d_b}\right) + 0.0009\left(\frac{s}{d_b}\right) + 7.903\left(\frac{A_s}{A_g}\frac{P}{f_c'A_g}\right) -$$

$$252.17\left(\frac{A_{st}}{sb}\frac{A_{cc}}{A_g}\right) + 0.007\left(\frac{A_{cc}}{A_g}\frac{l_d}{d_b}\right) - 52.214\left(\frac{A_s}{A_g}\right)^2 - 0.002\left(\frac{P}{f_c'A_g}\right)^2 + 3937.7\left(\frac{A_{st}}{sb}\right)^2 \qquad 2.35$$

$$-1.540\left(\frac{A_{cc}}{A_g}\right)^2 \geq 0.0$$

2.6.2.   Model Based on Concentrated Plasticity

The model for an RC column with a short lap splice considered by Cho and Pincheira [90] is shown in Figure 2.69. The model used a concentrated plasticity approach with three zero-length rotational springs to model the flexural, shear, and slip behavior of the column. The length of the column was modeled as an elastic element. The model was implemented in the program DRAIN2D.
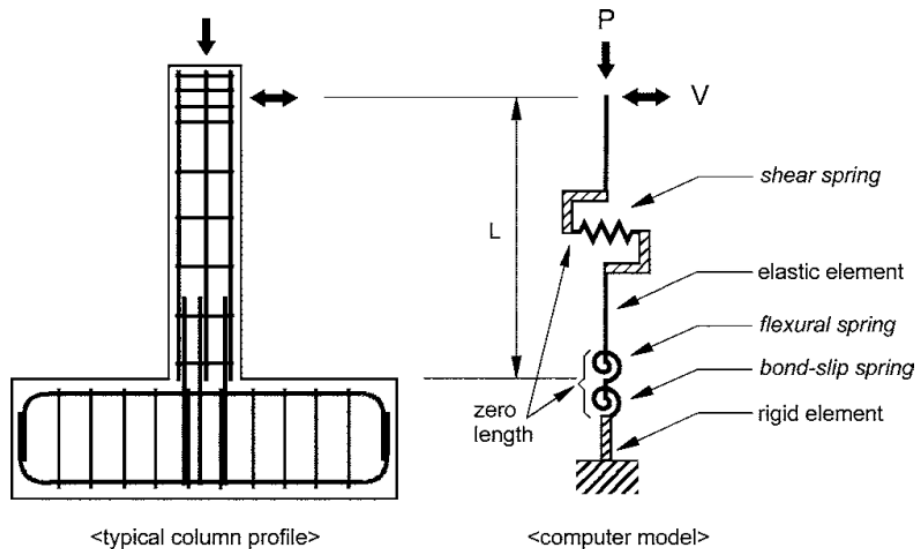
Figure 2.69 Analytical model of lap spliced column by Cho and Pincheira [90].

The bond-slip rotational spring was used to include the effect of a short lap splice. For this purpose, a 1-D model of the bar was considered, as shown in Figure 2.70. Non-linear springs were attached to the bar at various locations, and each spring

was assigned a bond stress-slip law proposed by Harajli [91]. In the first step, the bond force-slip relation was calculated from the 1-D model. From this, end rotations due to bar slip were calculated by following the recommendations of Razvi and Saatcioglu [92]. By using the end rotations and bar force, the moment rotation relation was estimated from the moment-curvature analysis.
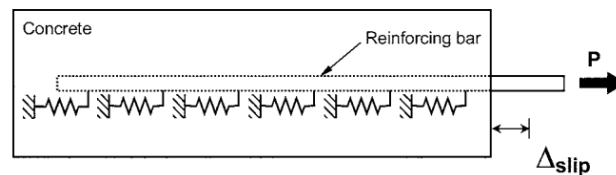
Figure 2.70 1-D model of anchored bar to populate the bond-slip rotational spring by Cho and Pincheira [90].

Juntanalikit et al. [29] modeled the RC column with substandard lap splice by using a concentrated plasticity model, as shown in Figure 2.71. The model consisted of an elastic limit with a length equal to the length of the column minus the length of the plastic hinge. At the column base, a zero-length element was used with nonlinear springs of concrete and steel material. A rigid link of length equal to the plastic hinge length was used to connect the elastic and zero-length elements. In addition, a zero-length shear spring was used at the column base to model the shear behavior of the column.
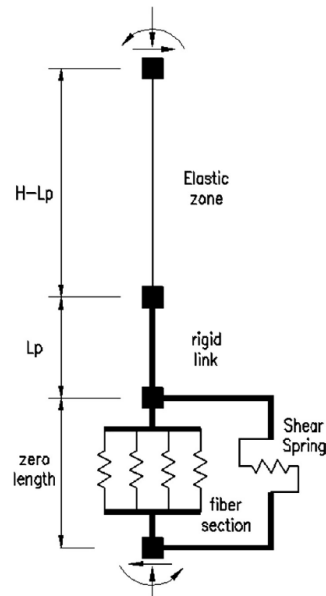
Figure 2.71 Concentrated plasticity model adopted by [29].

The zero-length element incorporating concrete and steel fibers is shown in Figure 2.72. A monotonic curve was used to simulate the behavior of unconfined and confined concrete, as shown in Figure 2.73.
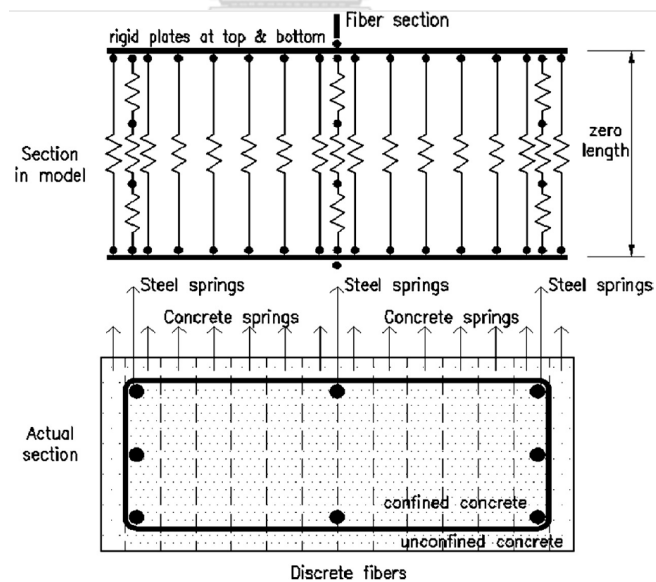
Figure 2.72 Zero-length element with nonlinear concrete and steel springs used by Juntanalikit et al. [29].
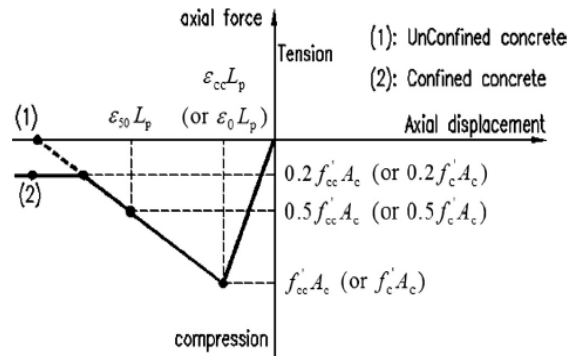
Figure 2.73 Monotonic curve to model the concrete behavior by Juntanalikit et al. [29].

The steel spring comprised three sub springs connected in series, as shown in Figure 2.74. The constitutive steel stress-strain relation was assigned to the steel bar sub-spring, whereas a modified stress-strain relation was assigned to the lap splice sub-spring to incorporate the effect of short lap splice length.
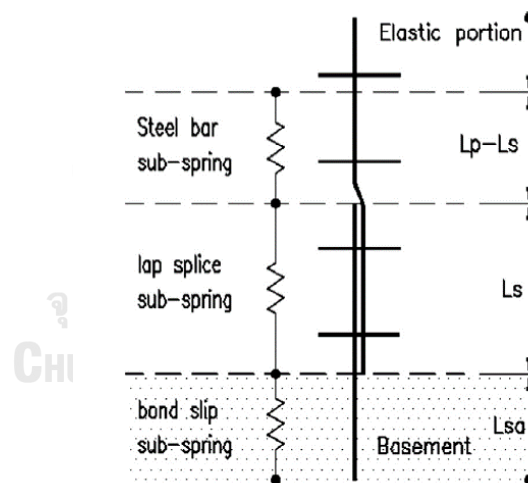
Figure 2.74 Three-spring model adopted by Juntanalikit et al. [29] to model the behavior of lap splices.

To model the lap splice sub-spring, a tri-uniform bond distribution along the lap splice was adopted, as shown in Figure 2.75. The bond stress distribution comprised three regions, including the post-splitting region, splitting region, and yielding region. Juntanalikit et al. [29] utilized the bond stress-slip law of Harajli [59] and derived equations for each part of the lap splice sub-spring. Depending upon the

equilibrium between the bond stress and lap splice stress, equations were derived to estimate the length of each zone within the lap splice sub-spring as

$$f_s = \left(u_{sp}L_{sp} + u_rL_r + u_yL_y\right)P \qquad\qquad 2.36$$

where u_{sp}, u_r, and u_y are bond strengths within the post-splitting zone, splitting zone, and yielding zone, respectively and L_{sp}, L_r, and L_y are the lengths of three zones, P is the perimeter around each lap splice bar. Depending on the magnitude of f_s, the failure was distinguished either by pre-yield or post-yield, as shown in Figure 2.76. Finally, the proposed model was implemented in Ruaumoko 2D.
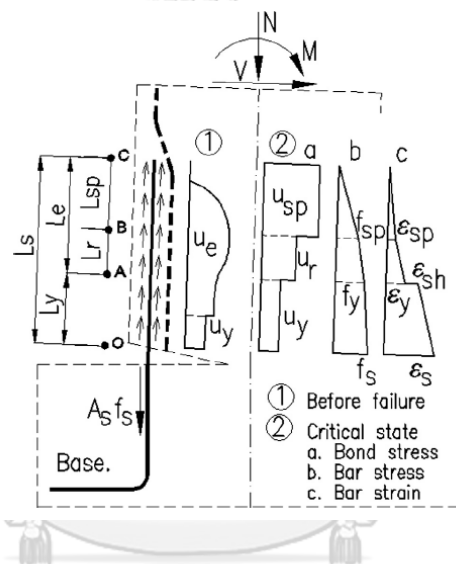
Figure 2.75 Tri-uniform bond stress distribution along the lap splice adopted by Juntanalikit et al. [29].
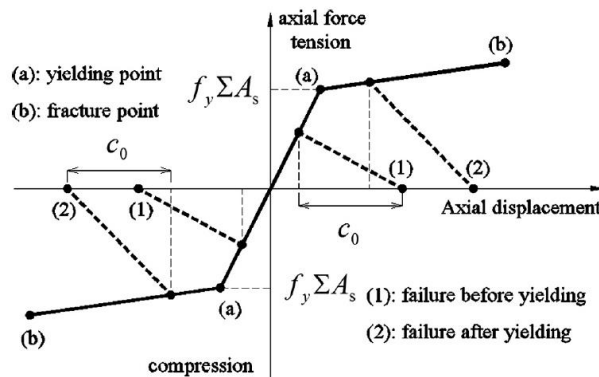
Figure 2.76 Modified stress-strain relation for lap spliced bars by Juntanalikit et al. [29].

Opabola et al. [93] adopted a phenomenological model (i.e., a macroscopic model) to model deficient lap spliced RC columns because up to 90% of deformation contribution in the case of lap spliced columns comes from the slip mechanism. A rotational spring was attached to the bottom of the RC column. Moment-rotation relation was assigned to *Modified Ibarra-Medina-Krawinkler Deterioration Model with Pinched Hysteretic Response* (*ModIMKPinching* material) in OpenSees. As shown in Figure 2.77, several parameters are needed to be defined for this material. To define the backbone curve of *ModIMKPinching* material, parameters θ_e, θ_p, θ_{pc} and M_b and M_{max} are required. These parameters correspond to elastic rotation capacity, pre-capping rotation capacity, post-capping rotation capacity, moment strength corresponding to the maximum stress that can be transferred, and peak moment strength, respectively. In this study, M_b and M_{max} were taken equal.
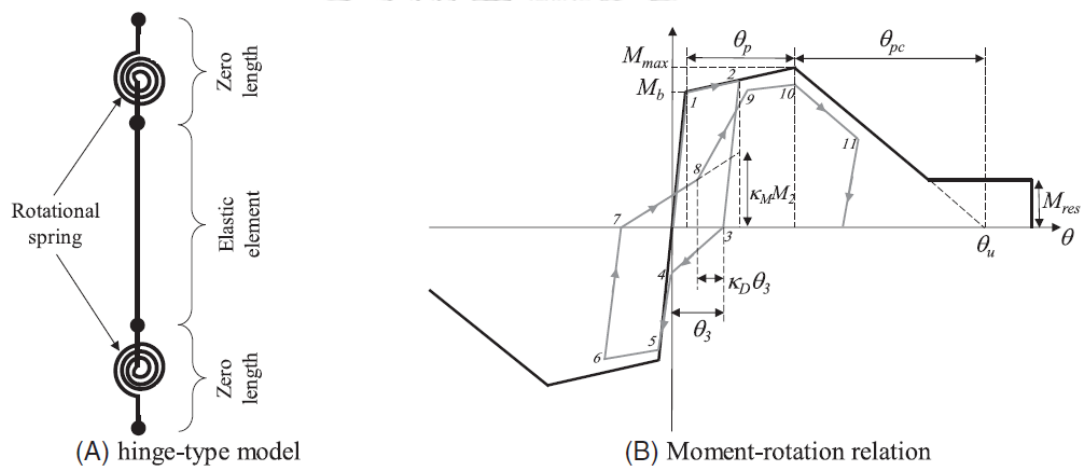
Figure 2.77 Macroscopic model of lap splice RC column (a) numerical model with zero length springs, and (b) moment rotation relation modeled by Ibarra-Medina-Krawinkler (*IMK*) material in OpenSees (Opabola et al. [93]).

The authors described various equations obtained from regression analysis for these parameters. Elastic rotation capacity θ_e was given as Eq. 2.37.

$$\theta_e = \frac{V_{max}a^2}{3EI_{eff}}$$

$$2.37$$

where V_{max} correspond to the lateral strength corresponding to M_b, a is shear span, and EI_{eff} is effective flexural rigidity. From the moment-curvature analysis of the cross-section, peak moment strength can be obtained. Knowing the maximum stress

that can be developed in lap splice, corresponding moment capacity M_b can be obtained, whereas EI_{eff} was obtained from the proposed Eq. 2.38.

$$EI_{eff} = \alpha \left[0.27 \left(\frac{a}{d} \right) - 0.07 \right] \qquad 2.38$$

The parameter α defines the reduction in flexural rigidity and is a function of the axial load ratio. It can be obtained from Table 10–5 of ASCE/SEI 41-17 [94]. The drift capacity at lateral failure $a_{nl,o}$ was given as in Eq. 2.39 and shown in Figure 2.78.

$$a_{nl,o} = 0.75\% \leq 3.9 - 0.9 \frac{A'_s f_s}{A_v f_{yt} \left(\frac{l_{s,prov}}{s} \right)} \leq 3\% \qquad 2.39$$

The effect of axial load ratio was accounted for by multiplying Eq. 2.39 with parameter λ.

$$a_{nl} = \lambda a_{nl,o} \leq 0.03 \qquad 2.40$$

where λ equals 1 for $N/A_g f'_c < 0.2$ and 0 for $N/A_g f'_c > 0.5$. Linear interpolation is required for $0.2 < N/A_g f'_c < 0.5$. Similarly, the drift at axial load failure b_{nl} is given in Eq. 2.41.

$$b_{nl} = 0.15K \frac{h}{a} \left[1 - \frac{N}{0.7 f'_c A_g} \right] \qquad 2.41$$

Here, K is defined in Eq. 2.42.

$$K = 0.5 \left(\frac{a}{d} \right) - 0.4 \qquad 2.42$$

Another parameter that is required to define the backbone of *ModIMKPinching* material is M_{res}. Eq. 2.43 was proposed to define a ratio of $\frac{M_{res}}{M_b} = c$.

$$c = \frac{M_{res}}{M_b} = 0.2 - 0.4 \frac{N}{f'_c A_g} \geq 0.0 \qquad 2.43$$

To account for cyclic strength and stiffness deterioration, a constant value of 0.4 for Λ was suggested where Eq. 2.44 was suggested to estimate the pinching parameter.

$$\kappa = 0.6 - \frac{0.0002}{\rho_t} \geq 0.0 \qquad 2.44$$

where ρ_t is transverse reinforcement ratio.
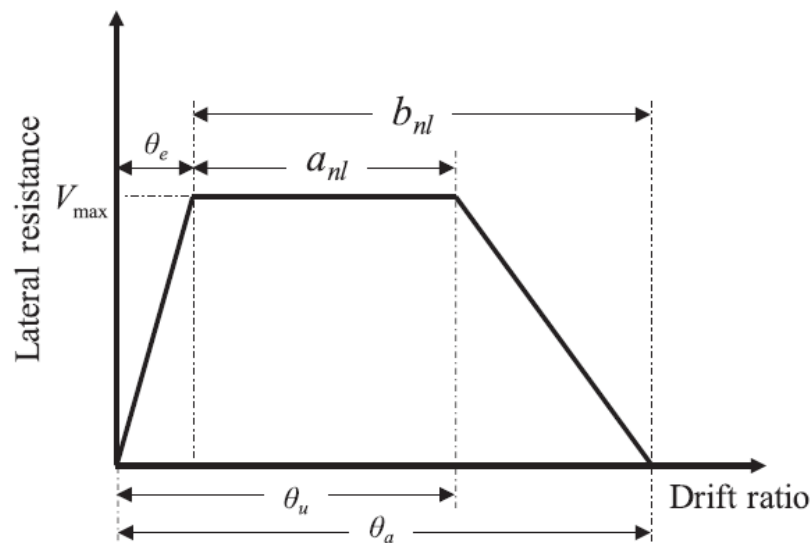
Figure 2.78 Definition of backbone parameters for *ModIMKPinching* material by Opabola et al. [93].

2.7. Modeling Hollow Structural Sections Confined Concrete

External confinement improves the compressive stress-strain response of the concrete. The following two approaches exist in the literature that consider the effect of steel collar confinement on the compressive stress-strain behavior of concrete.

2.7.1. Modeling Based on Steel Combined Failure Criteria Under Axial and Bending Loads

Pudjisuryadi et al. [95] proposed a new approach to determine the confining pressure generated by steel collars. The confinement effectiveness of steel collars was assumed to vary, as shown in Figure 2.79. The confinement pressure was assumed to vary in the form of 45° parabolas at collar level. From this, the expression for the unconfined area A_{par} is given as

$$A_{par} = \frac{2}{3}b^2 \qquad 2.45$$

where b is the dimension of the square section. By considering the unconfined areas in horizontal and vertical planes, an expression of the total unconfined area A_e was proposed by following the concept of Mander et al. [80] as

$$A_e = A_c \left(1 - \frac{A_{par}}{A_e}\right)\left(1 - \frac{s_c}{2b}\right)^2 \qquad \text{2.46}$$

where A_c is the core area and s_c is the clear spacing between two consecutive steel collars. Finally, the confinement effectiveness factor k_e can be expressed as

$$k_e = \frac{A_e}{A_{cc}} \qquad \text{2.47}$$

where A_{cc} is the core area, excluding the area of longitudinal reinforcement. Once k_e is known, the effective confinement pressure f_{le} can be calculated as

$$f_{le} = k_e f_l \qquad \text{2.48}$$

where f_l is the confinement pressure generated by steel collars without considering the ineffectively confined regions.
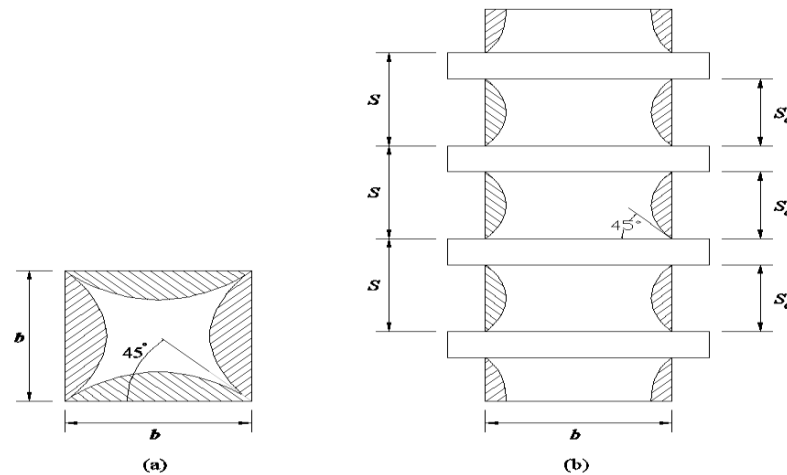
Figure 2.79 Idealization of the steel collar confinement (a) at collar level and (b) along the height of the member by Pudjisuryadi et al. [95].

Xiao and Wu [96] argued that, unlike conventional transverse reinforcement, steel collars utilize their combined axial and flexural capacities to resist the outward bursting pressures from the concrete core. As shown in Figure 2.80(a), it was assumed that the deflection of steel collars maintains the compatibility of the outward concrete bulging. It was further assumed that the failure of steel collars accompanies the formation of plastic hinges at corners and midway between the corners, as shown in Figure 2.80(b). From Figure 2.80(b), the axial force p and the bending moment m developed in the collar were given as

$$p = f_l \frac{b}{2} s \qquad\qquad 2.49$$

$$m = f_l \frac{b^2}{16} s \qquad\qquad 2.50$$

A combined failure criterion of steel under axial and bending loads was adopted as

$$\frac{p}{\phi p_n} + \frac{8}{9}\left(\frac{m}{\phi m_n}\right) = 1 \rightarrow for \ \frac{p}{\phi p_n} \geq 0.2 \qquad\qquad 2.51$$

$$\frac{p}{2\phi p_n} + \left(\frac{m}{\phi m_n}\right) = 1 \rightarrow for \ \frac{p}{\phi p_n} < 0.2 \qquad\qquad 2.52$$

where p_n and m_n are the nominal axial and flexural capacities of the collar section, respectively. By inserting Eq. 2.49 and Eq. 2.50 into Eq. 2.51 or Eq. 2.52, the value of the confinement pressure f_l can be estimated. Once f_l is known, the effective confinement pressure f_{le} can be estimated by using Eq. 2.48.
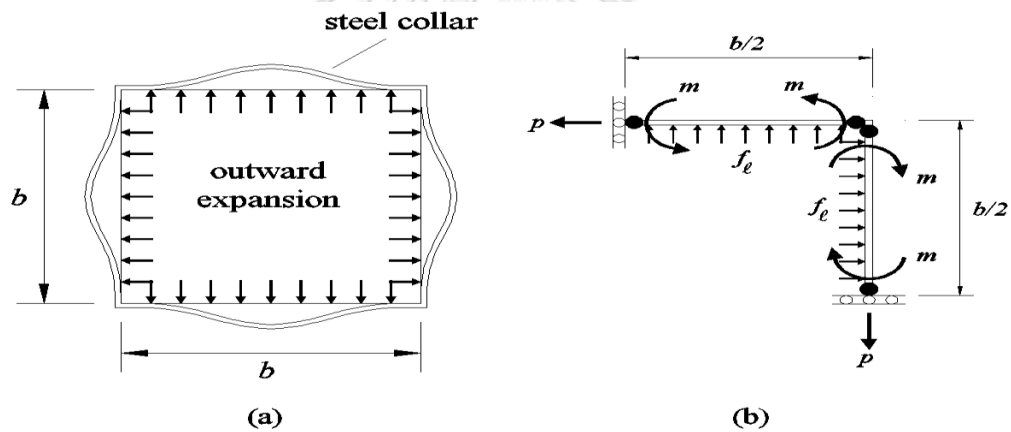
Figure 2.80 (a) Deflection of steel collars under outward concrete bulging and (b) equilibrium of forces at a quarter of the section by Pudjisuryadi et al. [95].

Pudjisuryadi et al. [95] compared the formulations of Mander et al. [80], Razvi and Saatcioglu [97], and Tabsh [98] to calculate the peak compressive strength and compressive stress-strain response. The results of these models were applied to the steel collar strengthened columns of Hussain and Driver [44]. Pudjisuryadi et al. [95] noticed that the strain corresponding to the peak compressive stress generated by the model of Tabsh [98] was quite large. Based on the experimental results of steel collar strengthened columns tested by Pudjisuryadi et al. [74], a new equation for the strain at peak compressive stress ϵ_{cc} was proposed. Figure 2.81 compares the analytical compressive stress-strain curves obtained by the approach of Pudjisuryadi et al. [95]

with the experimental stress-strain curves of steel collar confined columns tested by Hussain and Driver [44]. It can be seen that although the predicted peak compressive strength is comparable to the experimental results, the predicted compressive stress-strain curves do not exactly trace the experimental curves.

(a)

(b)

(c)
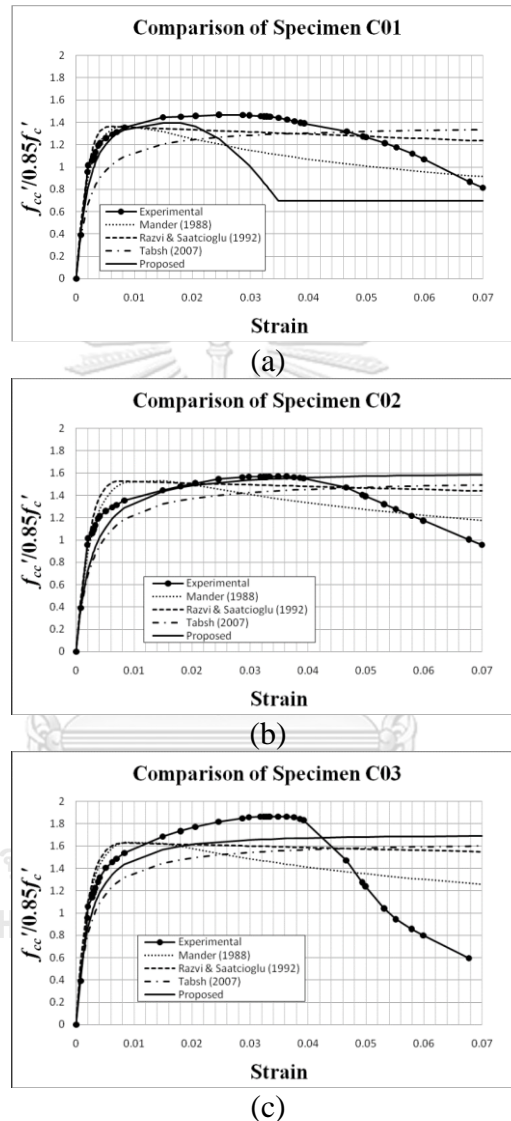
Figure 2.81 Comparison of predicted compressive stress-strain curves of steel collar confined concrete by the approach of Pudjisuryadi et al. [95] with experimental curves of Hussain and Driver [44] (a) Column C01, (b) Column C02, and (c) Column C03.

2.7.2. Modeling Based on Incremental Collar Pressure Under Lateral Strain

Chapman and Driver [99] recognized the deficiencies in existing analytical models for predicting the compressive stress-strain response of concrete strengthened

by steel collars. The main deficiencies highlighted by Chapman and Driver [99] were: (1) The effect of the flexural stiffness of steel collars cannot be modeled by existing models as none of the existing models contain a parameter to account for the flexural stiffness of the confining elements, (2) several existing models assume uniform confining pressure by the confinement throughout the load history. It was found from the experimental program conducted by Chapman and Driver [99] that steel collars do not yield at the start of the loading, and strains in steel collars are increased as the loading is progressed. Therefore, a uniform confining pressure corresponding to the yield of steel bars, such as assumed by Mander et al. [80] is not justified in the case of steel collars, and (3) existing models do not incorporate the effect of active confining pressure. With this background, a new analytical framework was proposed to trace the compressive stress-strain curve of steel collar confined concrete. The following sections discuss the analytical framework of Chapman and Driver [99] in detail.

Collar Behavior

The collars were modeled as elastic elements with lengths equal to the width of the column h. The ends and midspan of the collars were modeled as rigid plastic hinges. Under combined axial and flexural loads, a plastic hinge was assumed to occur once the following condition was met:

$$\left(\frac{F}{F_y}\right)^2 + \left(\frac{M}{M_p}\right) = 1.0$$

2.53

where F and M are the axial force and bending moment present in the collar, respectively and F_y and M_p are the yield strength and plastic moment capacity of the collar section, respectively. An incremental procedure was developed to approximate the collar pressure that would result in the formation of plastic hinges at collar ends and midspan. Under the incremental increase in the confining pressure in analysis step n, Eq. 2.54 takes the following form:

$$\left(\frac{F_{n,total}}{F_y}\right)^2 + \left(\frac{M_{n,total}}{M_p}\right) = 1.0$$

2.54

where $F_{n,total}$ and $M_{n,total}$ are the sum of axial force and bending moments till the analysis stage n, respectively. From Figure 2.82, the axial force F_n and bending moment M_n during a particular analysis stage n are found as:

$$F_n = \frac{\sigma_n \times t \times h}{2} \qquad 2.55$$

$$M_n = \frac{\sigma_n \times t \times h^2}{C} \qquad 2.56$$

$$F_{n,total} = \sum_{i=1}^{n-1} F_i + F_n \qquad 2.57$$

$$M_{n,total} = \sum_{i=1}^{n-1} M_i + M_n \qquad 2.58$$

where σ_n is the confining pressure during stage n, t is the collar dimension, and C is the coefficient related to the bending moment of the elastic curve. The value of C is 12.0 before the formation of the plastic hinge at collar ends and 8.0 afterward.
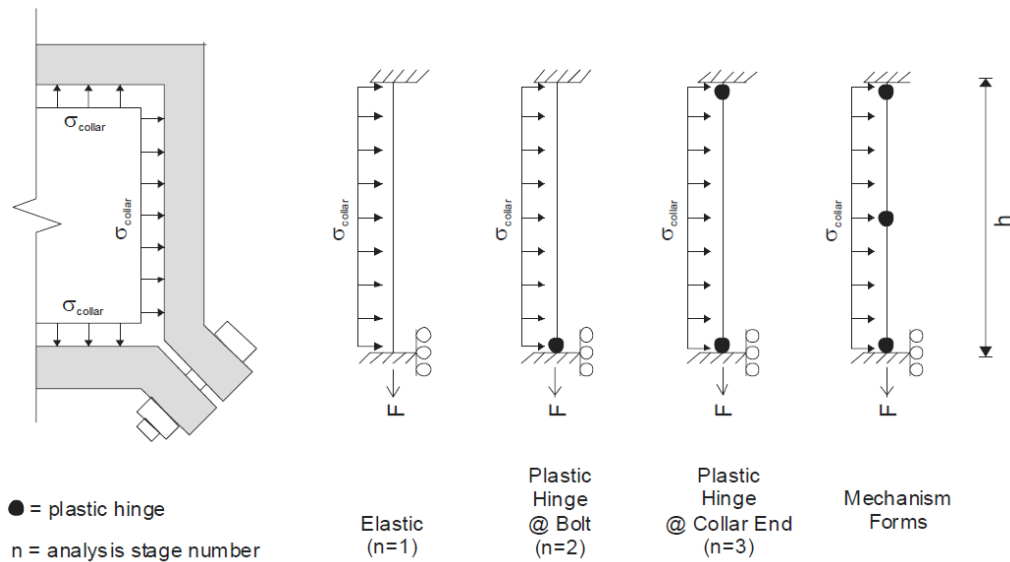
Figure 2.82 Collar failure mechanism based on plastic hinge formations proposed by Chapman and Driver [99].

Chapman and Driver [99] derived equations for the lateral collar deformation by considering the axial Δ_{axial} and bending $\Delta_{bending}$ components due to the confining pressure. For a particular analysis stage, the total lateral deformation $\Delta_{n,total}$ was given as

$$\Delta_{n,total} = \sum_{i=1}^{n-1} \Delta_i + \Delta_n \qquad 2.59$$

$$\Delta_n = \Delta_{axial} + \Delta_{bending} \qquad 2.60$$

The lateral strain in the collar at the end of each analysis stage $\epsilon_{lat,n}$ is given as

$$\epsilon_{lat,n} = \frac{2\Delta_{n,total}}{h} \qquad 2.61$$

Chapman and Driver [99] derived equations for different collar end restraints as given in Table 2.10.

Table 2.10 Lateral deflection of collar element derived by Chapman and Driver [99].

Analysis Stage * n	Beam End Condition	Elastic Deflection Curve $\Delta(x)$ **	Bending Deflection Δ_{bend}	Axial Deflection Δ_{axial}
1	fixed / fixed	$\dfrac{\sigma_n t x^2 (h-x)^2}{24 E_s I_{collar}}$	$\dfrac{\sigma_n t h^4}{720 E_s I_{collar}}$	$\dfrac{\sigma_n t h^2}{4 A_{collar} E_s}$
2	fixed / pinned	$\dfrac{\sigma_n t x (h^3 - 3hx^2 + 2x^3)}{48 E_s I_{collar}}$	$\dfrac{\sigma_n t h^4}{320 E_s I_{collar}}$	$\dfrac{\sigma_n t h^2}{4 A_{collar} E_s}$
3	pinned / pinned	$\dfrac{\sigma_n t x (h^3 - 2hx^2 + x^3)}{24 E_s I_{collar}}$	$\dfrac{\sigma_n t h^4}{120 E_s I_{collar}}$	$\dfrac{\sigma_n t h^2}{4 A_{collar} E_s}$

* These stages correspond to a collar with a mixed bolted/continuous end condition

** The quantity x represents the distance from the beam end (pinned end for stage 2)

Concrete Behavior

According to Chapman and Driver [99], the net lateral displacement of concrete can be found using the superposition of two conditions. In the case of no lateral restrain, the concrete is allowed to expand freely under an axial load, and the free lateral expansion Δ_{co} is given as

$$\Delta_{co} = \frac{\nu_c h \epsilon_{cc}}{2} \qquad 2.62$$

where ν_c is the secant Poisson's ratio corresponding to the applied axial strain ϵ_{cc}. Under the influence of a uniform confining pressure σ_h, the inward lateral contraction of concrete Δ_{ci} is given as

$$\Delta_{ci} = \frac{(1 - \nu_c) h \sigma_h}{2 E_c} \qquad 2.63$$

where E_c is the secant modulus of concrete stress-strain relation. The net lateral deflection of the concrete Δ_c is given as

$$\Delta_c = \Delta_{co} - \Delta_{ci} \qquad \qquad 2.64$$

Chapman and Driver [99] utilized the equation of Fam and Rizkalla [100] to estimate the secant Poisson's ratio of concrete which is given as

$$\nu_c = \nu_{co} \left[C_1 \left(\frac{\epsilon_{cc}}{\epsilon'_{cc}} \right) + 1 \right] \leq 0.50 \qquad \qquad 2.65$$

$$C_1 = 1.914 \left(\frac{\sigma_h}{f'_{co}} \right) + 0.719 \qquad \qquad 2.66$$

where ν_{co} is the initial secant ratio, ϵ'_{cc} is the strain at peak compressive stress, and f'_{co} is the compressive strength of unconfined concrete.

Confining Pressure

By following the lateral displacement compatibility, the following condition must be met.

$$\Delta_c = \Delta_{collar} \qquad \qquad 2.67$$

$$\Delta_{collar} = \frac{h\sigma_{collar}}{2E_{collar}} \qquad \qquad 2.68$$

where E_{collar} is the secant modulus of the collar confining pressure and lateral strain relationship that is already developed. Thus, the following equation for equilibrium passive confining pressure is obtained.

$$\sigma_{passive} = \frac{\nu_c \epsilon_{cc}}{\dfrac{1}{E_{collar}} + \dfrac{1 - \nu_c}{E_c}} \qquad \qquad 2.69$$

Confinement Efficiency

Chapman and Driver [99] proposed a two-part factor to include the effect of collar spacing and confinement effectiveness, as shown in Figure 2.83 and given as

$$K = K_{dist} K_{eff} \qquad \qquad 2.70$$

$$K_{dist} = \frac{t}{s'} \leq 1.0 \qquad \qquad 2.71$$

$$K_{eff} = \frac{(h - 0.5s')^2}{h^2} \qquad \qquad 2.72$$

Then, the effective confinement pressure $\sigma'_{passive}$ can be calculated as

$$\sigma'_{passive} = K\sigma_{passive} \qquad \qquad 2.73$$
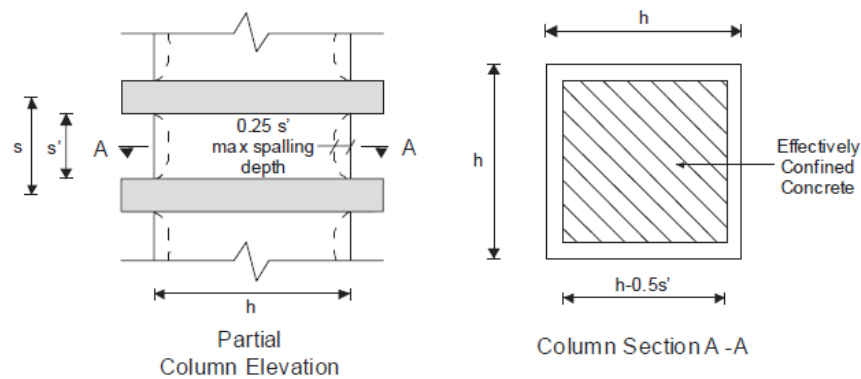
Figure 2.83 Calculation of confinement effectiveness factor by Chapman and Driver [99].

Confined Peak Concrete Strength and Corresponding Strain

Once $\sigma'_{passive}$ is estimated, Chapman and Driver [99] proposed to use the confined peak compressive strength equation of Mander et al. [80] as

$$f'_{cc} = f'_{co}\left[2.254\sqrt{1 + \frac{7.94\sigma'_{passive}}{f'_{co}}} - 2\frac{\sigma'_{passive}}{f'_{co}} - 1.254\right] \qquad 2.74$$

The strain at the peak stress f'_{cc} was computed by the model of Richart et al. [77] as

$$\epsilon'_{cc} = \epsilon'_{co}\left[1 + 5\left(\frac{f'_{cc}}{f'_{co}} - 1\right)\right] \qquad 2.75$$

where ϵ'_{co} is the strain at the peak stress in an unconfined state.

Concrete Stress-Strain Relationship

Chapman and Driver [99] utilized the model proposed by Popovics [101] to trace the full stress-strain relation of concrete as follows:

$$f_{cc} = \frac{f'_{cc}xr}{r - 1 + x^r} \qquad 2.76$$

$$r = \frac{E_{co}}{E_{co} - E'_c} \qquad 2.77$$

$$E'_c = \frac{f'_{cc}}{\epsilon'_{cc}} \qquad 2.78$$

$$x = \frac{\epsilon_{cc}}{\epsilon'_{cc}} \qquad 2.79$$

where f_{cc} is the general stress value corresponding to the general strain ϵ_{cc} and E_{co} is the initial secant concrete modulus that can be obtained as $E_{co} = 3900\sqrt{f'_{co}}$.

Solution Strategy

An iterative strategy is required to trace the full stress-strain response of steel collar confined concrete. The axial strain value is assumed initially. Twelve unknowns are encountered during a particular iteration, including the equilibrium confining pressure $(\sigma_h)_i$, the secant modulus of concrete $(E_c)_i$, the Poisson's ratio $(\nu_c)_i$, the constant $(C)_i$, the strain at peak compressive strength in a confined state $(\epsilon'_{cc})_i$, the secant slope of steel collar confining pressure-lateral strain relation $(E_{collar})_i$, the lateral strain $(\epsilon_l)_i$, the peak confined concrete stress $(f'_{cc})_i$, the stress corresponding to the assumed axial strain $(f_{cc})_i$, the parameters $(x)_i$ and $(r)_i$ for the Popovics [101] equation, and $(E_{sec})_i$. For each value of axial strain, the values of these twelve unknowns are assumed arbitrarily at the start of iterations. For each iteration, the values obtained in the previous iteration are used.

A comparison of experimental and predicted stress-strain response of axially loaded and steel collar confined columns tested by Hussain and Driver [44] is shown in Figure 2.84. It can be seen that the model by Chapman and Driver [99] is able to trace the experimental stress-strain response with reasonable accuracy. For the same columns, the model by Pudjisuryadi et al. [95] exhibited a significant deviation from the experimental response.
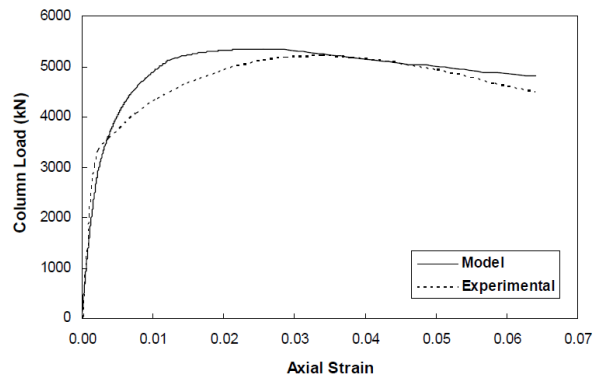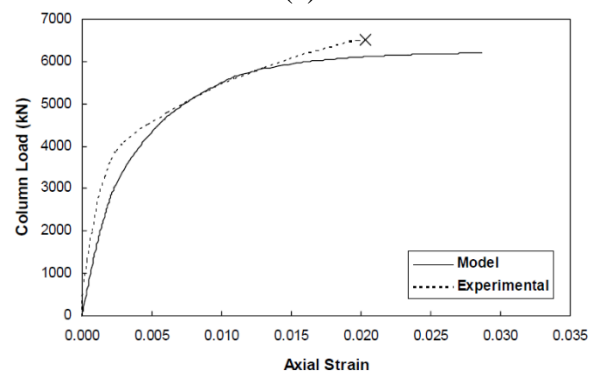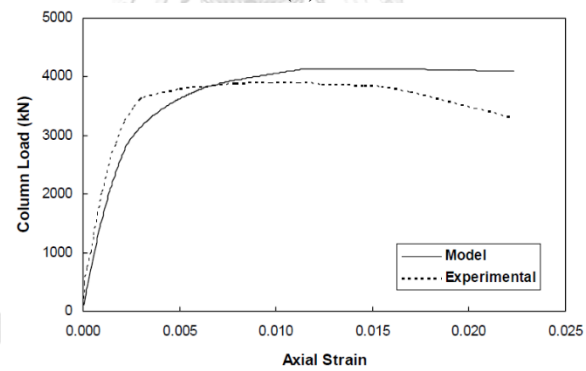
Figure 2.84 Comparison of experimental and predicted stress-strain response of axially loaded and steel collar confined columns tested by Hussain and Driver [44].

Chapter 3 Experimental Program

The first objective of this study was to investigate the role of HSS collars in improving the performance of substandard lap splices. It has been known that external confinement on lap splices improves the bond between lap splices and the surrounding concrete. Therefore, the bond strength between the lap splice and surrounding concrete has been used extensively to relate the improvement in the behavior of a substandard lap splice with external confinement. In the present work, beam specimens were chosen to study the effects of HSS collars on substandard lap splices.

3.1. Specimen Details

A total of nineteen beam splice specimens were tested in this study. Each beam furnished a substandard lap splice within its constant moment region. All beams were categorized into three groups depending on the lap splice length. Group 1 beams were constructed with a lap splice length of $20d_b$, beams in Group 2 were constructed with a lap splice length of $28d_b$, and a lap splice length of $35d_b$ was provided in Group 3 beams. This was equivalent to 20, 28, and 35 times the diameter $"d_b"$ of bottom longitudinal steel rebars, respectively. Table 3.1 describes the categorization of all beams into three groups. Seven beams were tested in the first group comprising four beams with a bottom concrete cover of 16 mm and three beams constructed with a 32 mm bottom concrete cover. Each of groups 2 and 3 comprised six beams in two subgroups. The first subgroup beams furnished a 16 mm bottom concrete cover, whereas a 32 mm cover was incorporated in the second subgroup. Further details on the strengthening scheme adopted for each beam are summarized in Table 3.1. The structural details of all beams are shown in Figure 3.1. Each beam had a cross-section of 200 mm × 250 mm and a length of 2200 mm. Each beam was simply supported at both ends with a clear span of 2000 mm. A 100 mm × 100 mm notch was provided on either side of the lap splice to measure bar slip. For each beam, the shear span was kept at 570 mm. Two 16 mm-diameter deformed bars were used as bottom reinforcement, whereas two 12 mm-diameter deformed bars were used as top

reinforcement. Stirrups with a diameter of 9 mm were arranged at a center-to-center spacing of 75 mm within each shear span to prevent shear failure.

A 3-part nomenclature was adopted for each beam comprising "LX", "CY", and "SZ". The first part, i.e., "LX" denoted lap splice length where "X" took values of $20, 28,$ and $35d_b$ for groups 1, 2, and 3, respectively. The second part, i.e., "CY" represented the controlling concrete cover where "Y" took values of 1 and 2 for 16 mm and 26 mm covers, respectively. Finally, the last part, "SZ" corresponded to the strengthening configuration of steel collars where "Z" took values of 75, 100, and 200 for collars provided at center to center spacing of 75 mm, 100 mm, and 200 mm, respectively.

Table 3.1 Parameters of test specimens.

Group	Beam ID	l_s (mm)	l_s /d_b	c (mm)	c/d_b	Spacing of Collars (mm)	f_c' (MPa)
	L20C1SC	320	20	16	1	-	48.0
	L20C1S200	320	20	16	1	200	27.4
	L20C1S100	320	20	16	1	100	29.5
1	L20C1S75	320	20	16	1	75	48.0
	L20C2SC	320	20	26	1.62	-	34.7
	L20C2S200	320	20	26	1.62	200	34.7
	L20C2S100	320	20	26	1.62	100	34.7
	L28C1SC	448	28	16	1	-	34.9
	L28C1S200	448	28	16	1	200	34.9
	L28C1S100	448	28	16	1	100	34.9
2	L28C2SC	448	28	26	1.62	-	34.9
	L28C2S200	448	28	26	1.62	200	34.9
	L28C2S100	448	28	26	1.62	100	34.9
	L35C1SC	560	35	16	1	-	48.0
	L35C1S200	560	35	16	1	200	34.9
	L35C1S75	560	35	16	1	75	48.0
3	L35C2SC	560	35	26	1.62	-	34.9
	L35C2S200	560	35	26	1.62	200	34.9
	L35C2S100	560	35	26	1.62	100	34.9

Note: l_s = lap splice length; d_b = bar diameter; c = controlling concrete cover; f_c' = cylinder compressive strength on test day.
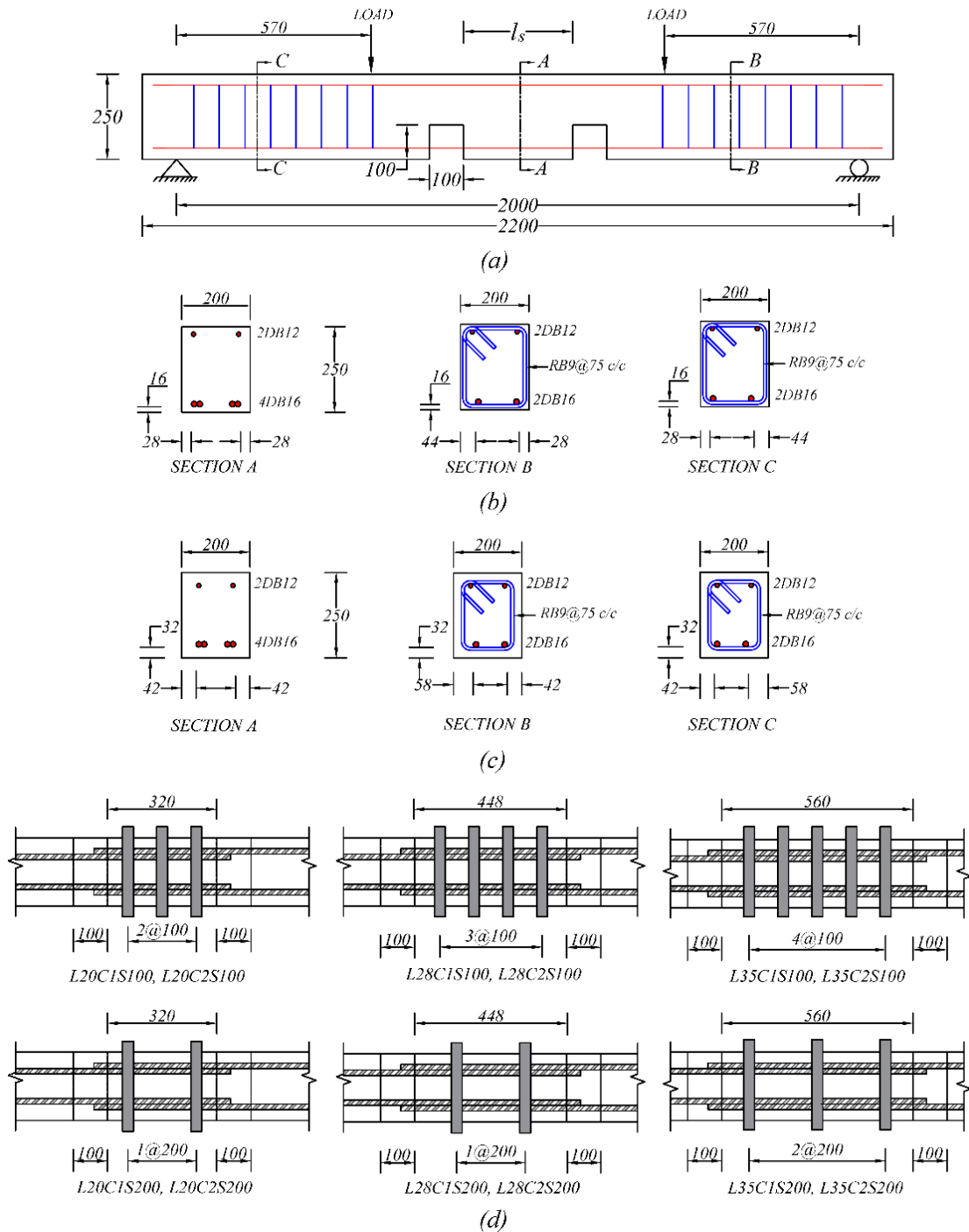
Figure 3.1 Typical test specimen (a) reinforcement along the beam, (b) sections with bottom concrete cover of 16 mm, (c) sections with bottom concrete cover of 32 mm, and (d) configuration of HSS collars along the lap splice (top view). Note: all dimensions are in "mm"; l_s=320 mm, 448 mm, and 560 mm for groups L20, L28, and L35, respectively; the diameter of the bottom steel bars d_b is 16 mm for all specimens; RB = round bar; and DB = deformed bar.

3.2. Preparation of Test Specimens

The panels of formwork were prepared in advance for all beams. The cutting of formwork was important, and special care was adopted. The panels for concrete cover with 32 mm bottom cover were cut accordingly. For each beam, seven types of panels were cut. Panels B1 and B2 were cut in a 4 mm larger dimension than the diameter of longitudinal bars d_b, i.e., 16 mm. The typical construction sequence is shown in Figure 3.2. In the first step, panels B1 and B2 were attached to the base panel A at the specified locations. In the second step, the bottom bars were placed to pass through the cut regions of panels B1 and B2. Then, panels B3 were attached to panels B1, and B2 with the help of panels G. The stirrups were then placed in the shear zones and tied with bottom and top longitudinal bars. Lifting hooks were tied at the specified locations. Then, panels C and D were attached. Finally, threaded rods were placed at the midspan, which were used for the instrumentation purpose. The practiced construction sequence is shown in Figure 3.3. After placing cages in formwork, concrete was poured in three equal layers. Compaction of the concrete was performed by using a mechanical vibrator.
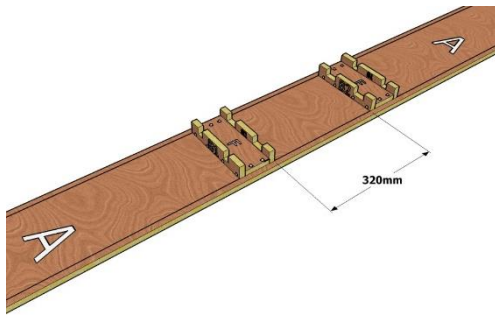
(a) Join panels B1, B2, and A
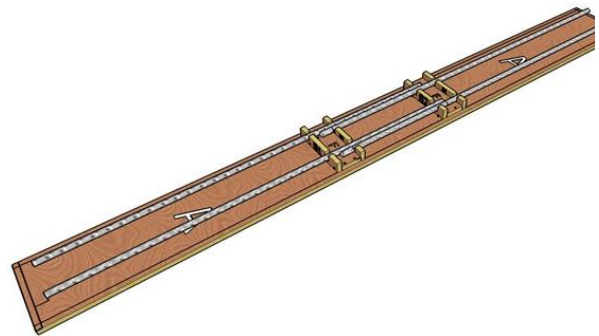
(b) Place bottom bars
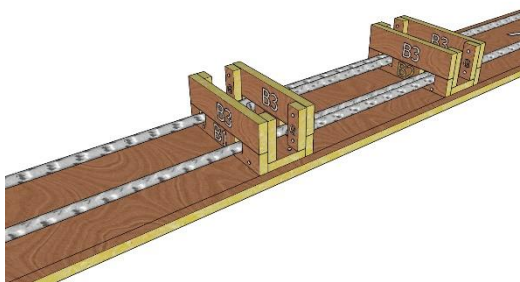
(c) Join panels B3 with panels B1 and B2 using panel G
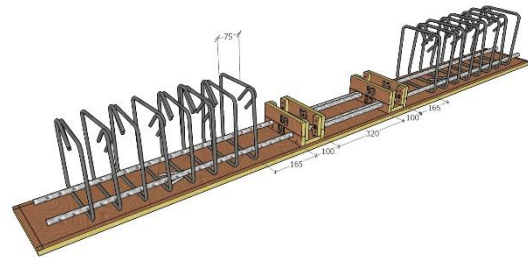
(d) Place stirrups
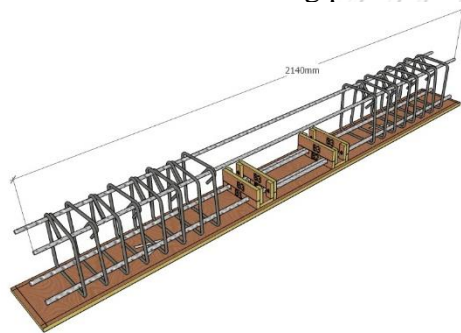
(e) Tie stirrups to top bars
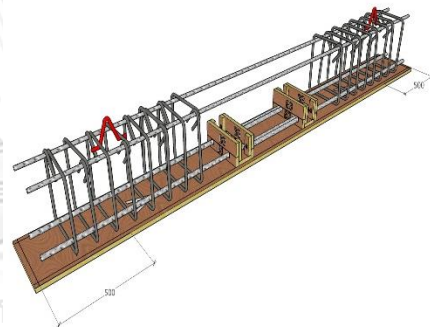
(f) Tie lifting hooks
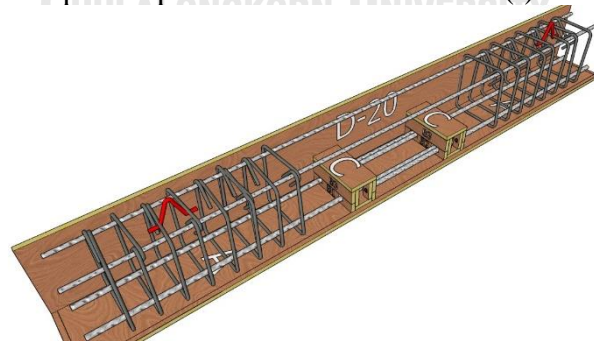
(g) Join panels D and C

Figure 3.2 Typical sequence of formwork construction for beams.
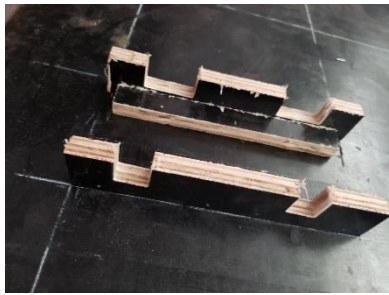
(a) Panels B1 and B2 joined
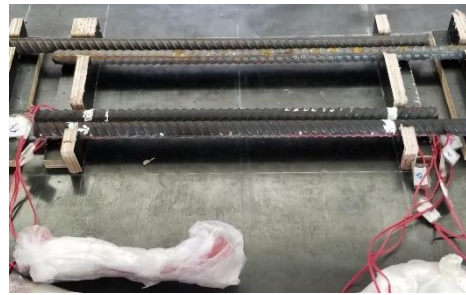
(b) Bottom bars placed

(c) Tying stirrups to bottom bars
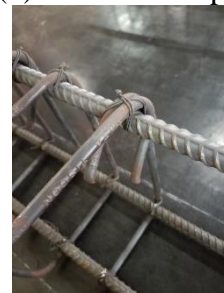
(d) Stirrups tied to top bars

(e) Prepared cage

(f) Prepared cage in formwork

(g) Placing and compacting

concrete

(h) Typical concrete-filled formworks

Figure 3.3 Typical process of constructing beams.

3.3. Selection of Hollow Steel Section (HSS) Collar

An estimate of the external confinement pressure required to hold lap splices intact, avoiding brittle splitting, was required. Priestley et al. [79] suggested Eq. 3.1 to calculate the magnitude of external confinement pressure.

$$f_{l,required} = \frac{A_b f_s}{\mu p l_s} \qquad 3.1$$

where f_s and μ were recommended to be $1.7 f_y$ and 1.4, respectively. The term p corresponded to the splitting plane perimeter associated with each pair of the lap splice and was suggested using Eq. 3.2.

$$p = \frac{s}{2} + 2(d_b + c) \leq 2\sqrt{2}(c + d_b) \qquad 3.2$$

where s is the clear spacing between consecutive lap splices and the term c stands for clear concrete cover. To estimate the confining pressure generated by HSS collars, an approach proposed by Xiao and Wu [96] was adopted. A detailed explanation of the collar design is presented in Appendix A1. Depending upon the equilibrium between the required collar pressure in Eq. 3.2 and estimated collar pressured by the approach of Xiao and Wu [96], a collar size of 32 mm×32 mm×2.3 mm was selected.

3.4. Material Properties

3.4.1. Concrete Properties

Standard cubes and cylinders were prepared, as shown in Figure 3.4, to estimate the cylindrical compressive strength f_c' of the concrete on the day of testing. In the present study, all the beams were constructed using ready-mix concrete. Table 3.2 presents the summary of concrete strength variation with age for two concrete batches. It was observed that the ratio of the cylinder to cube strength was around 0.87. Figure 3.5(a) presents the evolution of measured cube concrete strength with age for two batches. As shown in Table 3.2, the ratio of measured cube strength to measured cylindrical strength was 0.87. Hence, the cube strengths were reduced by a factor of 0.87. The resulting cylindrical strengths are shown in Figure 3.5(b). Finally, the measured cylindrical strengths of Batch 2 are shown in Figure 3.5(c).

(a)

(b)

Figure 3.4 Specimens for concrete strength testing (a) 150 mm×150 mm×150 mm cubes and (b) 150 mm× 300 mm cylinders.

(a)

(b)

(c)
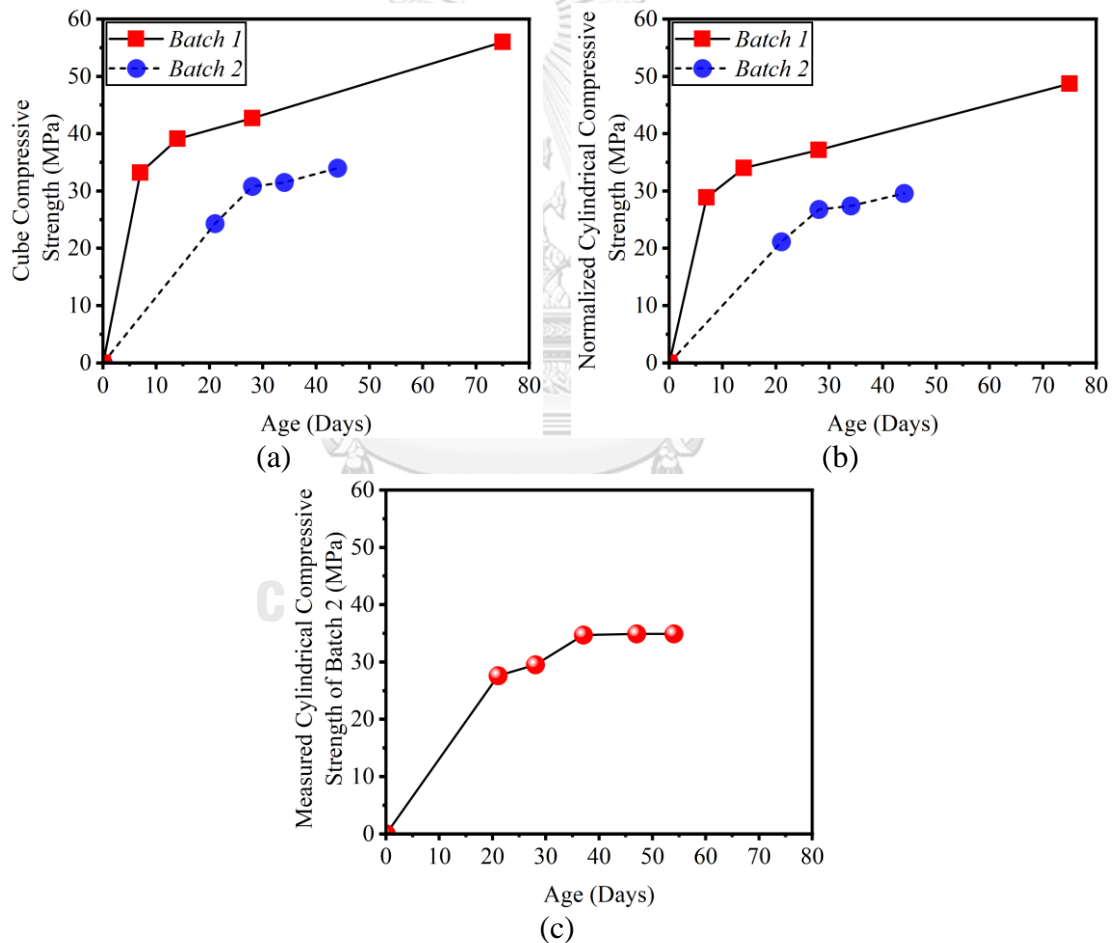
Figure 3.5 Evolution of cylindrical compressive strength with age (a) actual cube strength, (b) cube strength normalized by a factor of 0.87, and (c) measured cylindrical compressive strength in Batch 2.

Table 3.2 Evolution of concrete strength with age.

	Strength (MPa)	Age (Days)							
		7	14	21	28	37	47	54	75
Batch1	Cube	33.2	39.1	-	42.7	-	-	-	56.0
	Cylinder	-	-	-	-	-	-	-	-
	Beam Tested	-	-	-	-	-	-	-	L20C1SC L20C1S75 L35C1SC L35C1S75
Batch2	Cube	24.3	30.8	31.5	34.0	-	-	-	-
	Cylinder	-	-	27.6	29.5	34.7	34.9	34.9	-
	Beam Tested	-	-	L20C1S200	L20C1S100	L20C2SC L20C2S200 L20C2S100	L28C1SC L28C1S200 L28C1S100 L28C2SC L28C2S200 L28C2S100	L35C1S200 L35C2SC L35C2S200 L35C2S100	-
	Strength Ratio	-	-	0.87	0.87	-	-	-	-

3.4.2. Steel Properties

The bottom and top longitudinal bars were deformed bars with a diameter of 16 mm and 12 mm, respectively, whereas a 6 mm diameter round bar was used to provide shear strength in the shear zones. In the present study, the mechanical properties of the bottom bars were estimated by performing a uniaxial tensile test. The resulting stress-strain curve is shown in Figure 3.6. The yield strength of the bottom bars was estimated as 497 MPa at a strain of 0.0024, whereas the ultimate strength was 636 MPa at a strain of 0.073. The yield strength of DB6 bars was 300 MPa, as provided by the manufacturer.
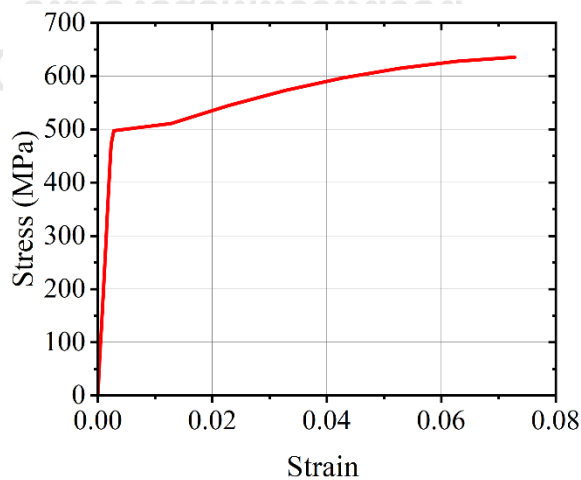
Figure 3.6 Stress-strain curve of bottom steel bars.

3.4.3. Hollow Steel Section (HSS) Collars

The yield strength of HSS collars was 408 MPa, as provided by the manufacturer. Steel collars were fabricated using two components, i.e., a U-shaped component joined to a straight component to facilitate the installation, as shown in Figure 3.7. The components were joined using E-70 electrode welds, forming miter joints for the U-shaped component. HSS sections were connected to 10 mm steel plates using closed square butt weld joints, whereas a 5 mm deep groove weld was applied at the inner connection of the HSS section with steel plates, as shown in Figure 3.7. The U-shaped component was connected to the straight component through bolted connections. Four Class 8.8 bolts were used for the bolted connection. It is noted that a gap of 10 mm − 15 mm was left between the inside face of the collars and concrete for ease of installation. A two-part epoxy (Sika Lanko 534) was mixed in a 2:1 ratio (2-part resin to 1-part hardener) to fill the gap between the collar and concrete. The epoxy was injected after tightening the bolts of steel collars.

(a)   (b)
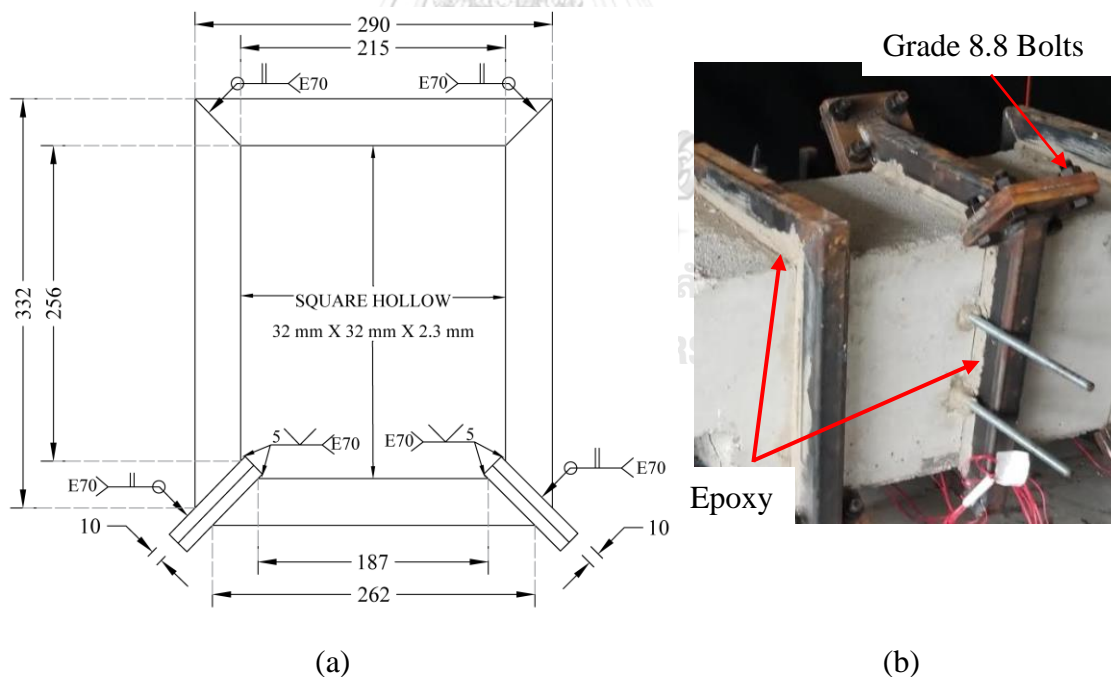
Figure 3.7 Details of HSS collar (a) dimensions and (b) HSS collar on beam. (Note: all dimensions are in "mm").

3.5. Instrumentation

3.5.1. Strain Gages

In the present study, several strain gages were attached along the lap spliced bars to measure the strain. The measured strains along the lap spliced bars were then used to estimate the bond stress distribution along the lap splice. The application of strain gage on the surface of the steel bar results in a disturbance in the continuity of the interactive surface between the steel bar and concrete. This has detrimental effects on the experimental bond strengths. The issue was first recognized by Mains [102], who stated that "bond is partially destroyed at the very points where strain is measured". The problem was overcome by attaching the strain gages inside the steel bars. Steel bars were cut in along the longitudinal sections first. The surfaces were milled to produce a smooth surface. Then, a groove was cut longitudinally in the larger cut section to accommodate strain gages and wires. After securing the strain gages with tapes, the two sections were joined together using a glue epoxy resin to form a complete bar identical to the original one. The process of making a test bar is pictorially depicted in Figure 3.8.
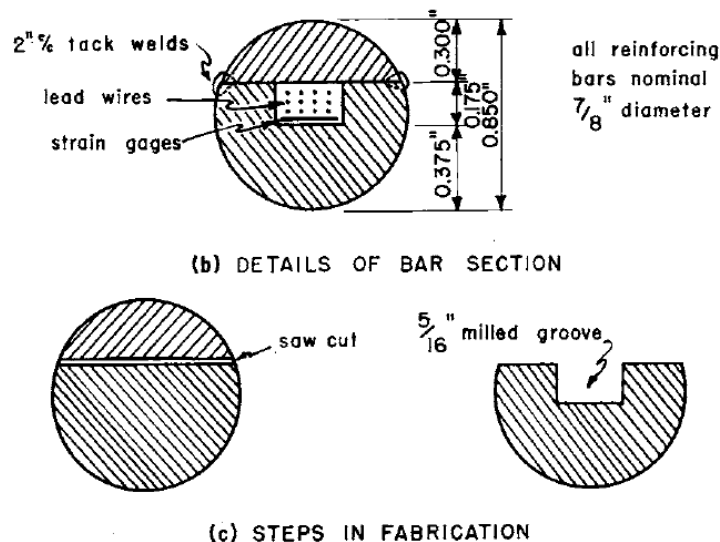
Figure 3.8 Process of attaching strain gages along the bars by Mains [102].

This technique was followed by many researchers later in a slightly modified form. Perry and Thompson [103] modified this technique. Instead of sawing the bars

in uneven sections, the bars were cut along the longitudinal rib, as shown in Figure 3.9.
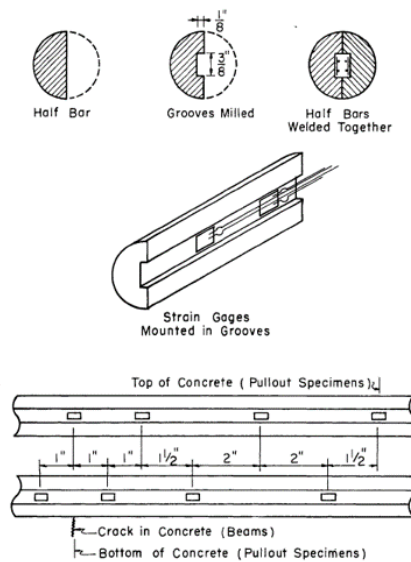
Figure 3.9 Process of attaching strain gages along the bars by Perry and Thompson [103].

To minimize the laborious work associated with the technique of cutting steel bars along their longitudinal axes, Viwathanatepa et al. [104] cut grooves along the longitudinal ribs of reinforcing bars. Bond strengths were computed from push-out and pull-push tests on concrete prisms. Bond strengths obtained from grooved and un-grooved steel bars were computed and compared. Figure 3.10 shows the application of this technique. The study compared the bond strengths of grooved and un-grooved bars, and it was concluded that the bond strengths obtained from grooved bars were about 10% higher than those obtained from un-grooved bars.
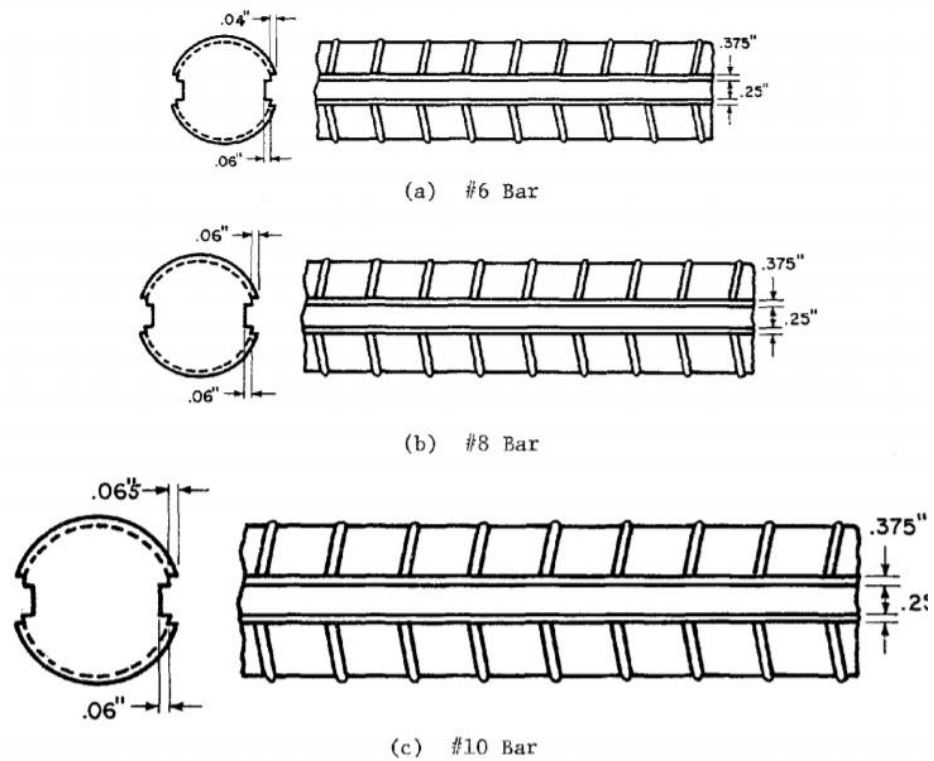
Figure 3.10 Process of attaching strain gages along the bars by Viwathanatepa et al. [104].

Table 3.3 summarizes a list of previous studies that mounted strain gages in the grooves cut along the longitudinal directions of bars. Table 3.3 presents groove sizes adopted in several studies. It can be observed that cross-sectional area loss ranged from 0.9% to 13.3%.

Table 3.3 Summary of existing works on mounting strain gages in grooves cut along the longitudinal direction of steel bars.

| Reference | Near-Surface Mounted Strain Gages | | | | Area Loss (%) |
	Bar Diameter (mm)	Groove (mm)	No. of Strain Gages	Gage Length (mm)	
Mains [102]	22	8x5	3 to 20	6	9.5
Perry and Thompson [103]	22	9x3	-	5	2.4
Viwathanatepa et al. [104]	19	6x1.5	11	-	6.3
Kankam [105]	25	6x3	12	3	3.7
Weathersby [106]	25	1.5x1	5	1.5	0.9
Lee and Mulheron [107]	16	4x3.2	4	7	5.9
Lagier et al. [108]	25	4x2	8	3	2.4
Lee et al. [109]	13	4.5x2.5	9	2	10.2
Kaklauskas et al. [110]	20	10x2	9	10	9.5
Kang et al. [111]	12 and 16	5x2.5	-	-	13.3
Long et al. [112]	12	4.5x2	-	-	11.9
This study	16	4x4	6, 7, 8	5	7.9

Strain gages were used to record the strain of the bottom bars within the lap splice zone. For each beam, strain gages were attached to one lap splice. As shown in Figure 3.11, each lap splice was instrumented with 6, 7, and 8 strain gages for Groups L20, L28, and L35, respectively. The strain gage model was KYOWA KFGS-5-120-C1-11L3M2R with a gage length of 5 mm. By minimizing the area loss and considering the dimensions of strain gages, a groove size of 4 mm × 4 mm was adopted. Strain gages were installed at the locations, as shown in Figure 3.12(a). Grooves were backfilled with silicone, and the surface was flushed to the level of the steel bar surface to minimize the risk of damage to strain gages during concrete placement (see Figure 3.12(b)).
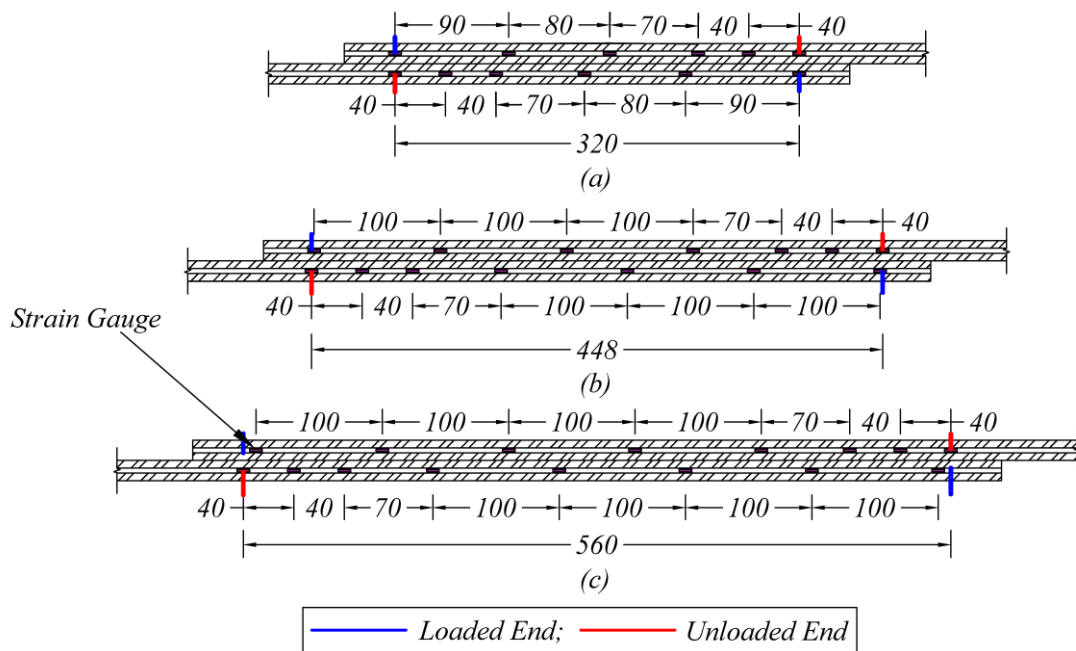
Figure 3.11 Locations of strain gages along lap splice (a) $20d_b$ lap splice, (b) $28d_b$ lap splice, and (c) $35d_b$ lap splice. (Note: all dimensions are in "mm").

(a)   (b)
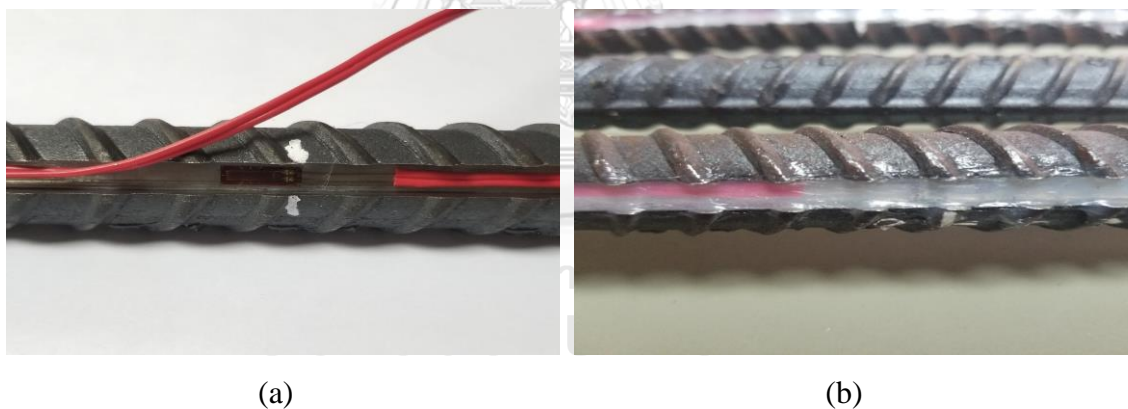
Figure 3.12 Strain gage installation (a) strain gage in the groove, and (b) groove flushed with silicone.

3.5.2. Displacement Transducers and Test Setup

A monotonic four-point bending setup was adopted for all beams using a hydraulic jack with a $500\,$kN capacity. The intensity of the applied load was measured using a load cell, as shown in Figure 3.13. Two displacement transducers were installed to measure the midspan vertical deflection, whereas four displacement transducers were used to measure the loaded end slip of lap spliced bars, as shown in

Figure 3.14. Data were recorded using a data logger with a sampling frequency of 60 Hz.
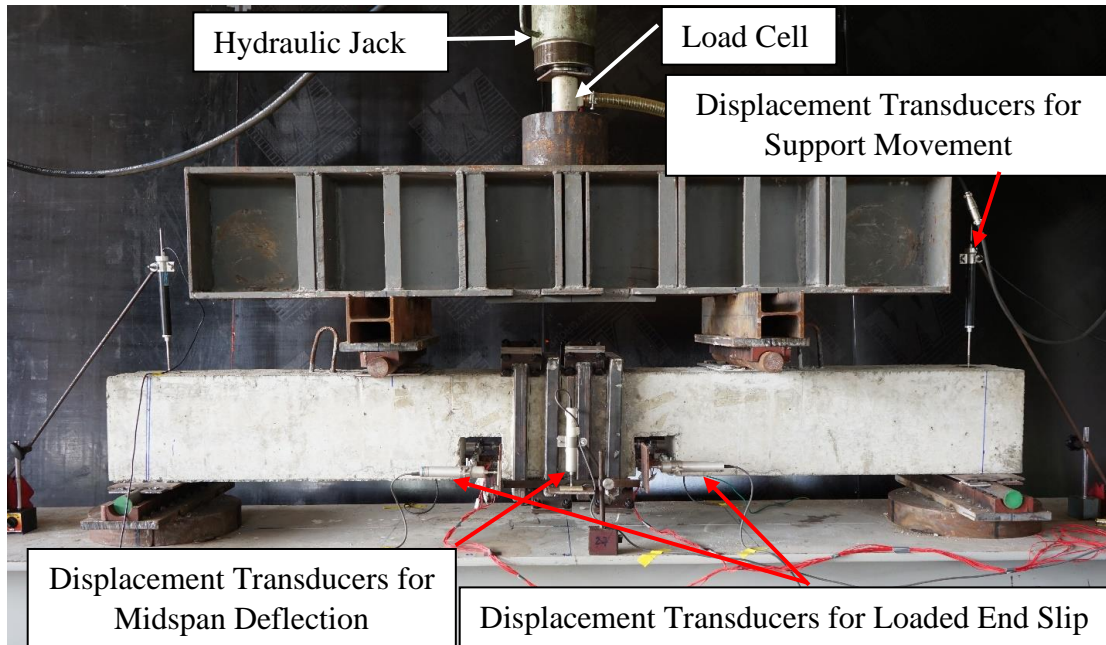
Figure 3.13 Instrumentation and test setup.

(a)   (b)
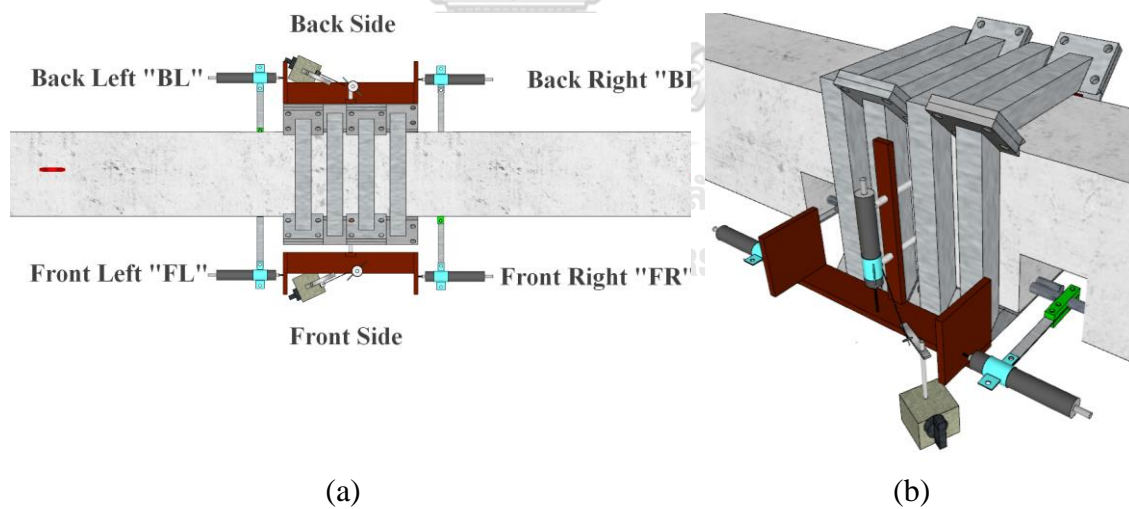
Figure 3.14 Positions of displacement transducers (a) top view and (b) side view.

No axial load was applied to the beams. The effect of axial load on bond strength has found to be beneficial. Malek et al. [113] carried out experimental investigations on bond strength by testing lap splice critical RC columns. The columns were subjected to axial loads of variable magnitudes. As shown in Figure

3.15, the bond strengths obtained from column tests were generally higher than those obtained from beam tests for similar confinement by concrete cover. Malek et al. [113] also found that by increasing the axial load ratio as 10%, 20%, and 30%, the corresponding bond strength of lap spliced bars increased as $0.99\sqrt{f_c'}$ MPa, $1.01\sqrt{f_c'}$ MPa, and $1.07\sqrt{f_c'}$ MPa, respectively. Mahrenholtz [114] did not apply axial load on their specimens for bond tests with argument that axial load enhances the bond strength and delays the strength degradation. Hence, the test of bond without axial load was termed as "conservative". Harajli [115] proposed expression for the increase in bond strength by testing beam splice specimens (without axial load). Later, Harajli [63] utilized this expression to develop design expression for estimating the requirement confinement of CFRP sheets to strengthen lap splices. The resulting confinement amounts were found sufficient to prevent splitting failures in RC columns. Garcia et al. [52] also proposed bond strength-based design criteria for CFRP confinement without considering axial loads. Moreover, the current design expression of ACI 318-19 [62] for development length of single bar or lap splices is based on the work of Orangun et al. [116] which did not incorporate the effect of axial load. Therefore, it can be concluded that the effect of axial load on bond strength is positive and design expressions obtained in the absence of axial load are conservative for the members subjected to axial load.
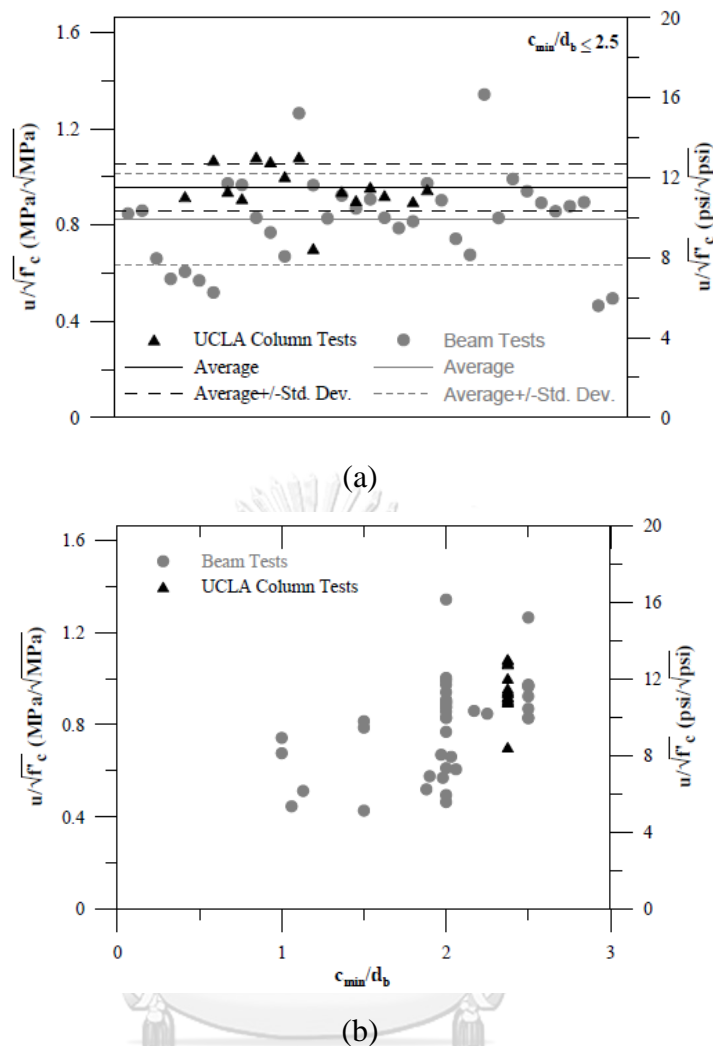
Figure 3.15 Comparison of bond strengths of beams and columns tested by Malek et al. [113] (a) bond strengths from existing literature and (b) bond strength measured by Malek et al. [113].

3.6. Experimental Results

It is recalled that all beams were designed to fail in splitting. This was ensured by furnishing lap splice lengths lower than those required by ACI 318-19 [62]. ACI 318-19 [62] proposes Eq. (3.7) for the calculation of lap splice length. Further, recognizing the amount of steel bar area being spliced at a single location, lap splices are categorized as Class-A and Class-B. Since 100% of steel bars were lapped at a single location in beams, required lap splice lengths were obtained using Eq. 3.3.

$$l_{s,req\,(ACI)} = \frac{f_y \psi_e \psi_e \psi_s}{1.1\lambda\sqrt{f_c'}\left(\dfrac{c + k_{tr}}{d_b}\right)} d_b \qquad\qquad 3.3$$

where f_y, f_c', d_b, and k_{tr} are yield strength of lapped bars, 28-day cylindrical strength of surrounding concrete, the diameter of lapped bars, and a factor accounting for the presence of transverse reinforcement (taken as 0 here). The term c refers to the minimum value of the side concrete cover c_s, bottom concrete cover c_b, and one-half the clear spacing between pairs of lapped bars c_{cs}. This is shown schematically in Figure 3.16.
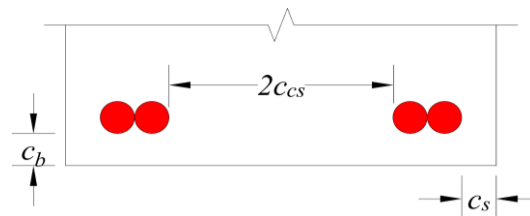
Figure 3.16 Definition of cover for calculation of splice length.

Table 3.4 provides the range of R_{ls} values for all the beams tested in this study, where R_{ls} is the ratio of provided lap splice length to the lap splice length required by ACI 318-19 [62]. It can be seen that R_{ls} ranged from 0.23 to 0.74. Hence, a brittle lap splice failure was predicted for all the control beams.

Table 3.4 Provided vs. required lap splice lengths as per ACI 318-19 [62].

Beam ID	f_c' (MPa)	f_y (MPa)	Cover (mm)			$\dfrac{c_{min}}{d_b}$	$l_{s,provided}$ (d_b)	$l_{s,req\,(ACI)}$ (d_b)	$\dfrac{l_{s,provided}}{l_{s,req\,(ACI)}}$
			c_s	c_b	c_{cs}				
L20C1S0	48.0	497	28	16	40	1	20	70	0.31
L20C1S75	48.0	497	28	16	40	1	20	70	0.31
L20C1S100	29.5	497	28	16	40	1	20	90	0.24
L20C1S200	27.4	497	28	16	40	1	20	93	0.23
L20C2S0	34.7	497	42	32	26	1.62	20	51	0.42
L20C2S100	34.7	497	42	32	26	1.62	20	51	0.42
L20C2S200	34.7	497	42	32	26	1.62	20	51	0.42
L28C1S0	34.9	497	28	16	40	1	28	82	0.36
L28C1S100	34.9	497	28	16	40	1	28	82	0.36
L28C1S200	34.9	497	28	16	40	1	28	82	0.36
L28C2S0	34.9	515	42	32	26	1.62	28	51	0.59
L28C2S100	34.9	497	42	32	26	1.62	28	51	0.59
L28C2S200	34.9	497	42	32	26	1.62	28	51	0.59
L35C1S0	48.0	497	28	16	40	1	35	70	0.53
L35C1S75	48.0	497	28	16	40	1	35	70	0.53
L35C1S200	34.9	497	28	16	40	1	35	82	0.46
L35C2S0	34.9	497	42	32	26	1.62	35	51	0.74
L35C2S100	34.9	497	42	32	26	1.62	35	51	0.74
L35C2S200	34.9	497	42	32	26	1.62	35	51	0.74

The bond stress between two consecutive strain gages $\tau_{i,i-1}$ can be evaluated as [104, 117, 118]

$$\tau_{i,i-1} = \frac{d_b}{4}\left(\frac{f_{s,i} - f_{s,i-1}}{x_i - x_{i-1}}\right) \qquad 3.4$$

where $i-1$ and i are indices of two consecutive points measured from the unloaded end of the lap splice, d_b is the bar diameter, and $f_{s,i}$ and $f_{s,i-1}$ are the estimated stresses in the bar at a distance x_i and x_{i-1} from the unloaded end, respectively. A bilinear idealization of the stress-strain curve was performed to approximate the stress in the bar, as shown in Figure 3.17. The stress f_s was calculated as

$$f_s = \begin{cases} \epsilon_s E_s & for\ \epsilon_s \leq \epsilon_y \\ f_y + (\epsilon_s - \epsilon_y)E_{sh} & for\ \epsilon_s > \epsilon_y \end{cases} \qquad 3.5$$

where f_s is the bar stress corresponding to the strain ϵ_s, f_y is the bar yield stress, E_s is Young's modulus of the bar, and E_{sh} is the post-yield modulus considered to be 1% of Young's modulus as obtained from the test.
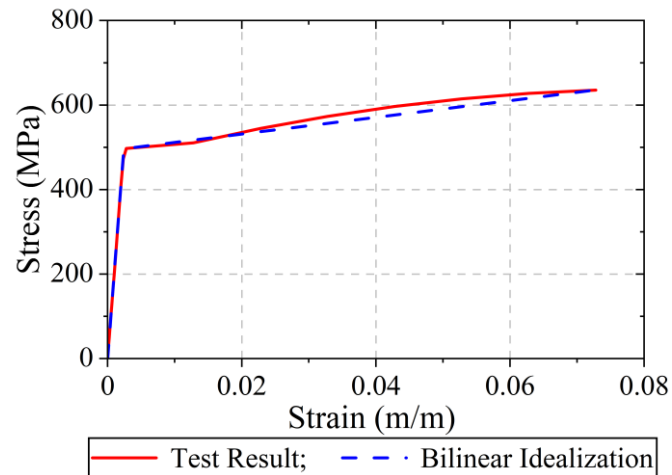
Figure 3.17 Stress-strain curve of bottom steel bars.

3.6.1. Group 1 Beams

i. Beam L20C1SC

Figure 3.18 shows experimental results for the beam L20C1SC. As seen in Figure 3.18(a), a linear load-deflection response was observed, followed by a sudden loss of capacity. The maximum sustained load was 102kN. High strains were observed near the loaded end (see Figure 3.18(b)), whereas steel strains were negligible towards the unloaded end. Nonetheless, the maximum recorded strain was 1620 microns which is 33% lower than the yield strain, i.e., 2400 microns. Since the bond stress is directly related to the first derivative of steel stress, higher bond stresses were observed near the loaded end. Maximum bond stress was 4.30 MPa observed at the loaded-end slip of 0.17 mm. Figure 3.19 shows visuals of beam L20C1SC during and after the test. As seen in Figure 3.19(c), beam L20C1SC failed suddenly due to the cover delamination accompanied by a loud sound. This type of failure was referred to as Type-I failure.

Figure 3.18 Experimental results for L20C1SC (a) load-deflection response (Type-I), (b) strain distribution along splice, (c) bond stress distribution along splice, and (d) bond stress-slip relation.
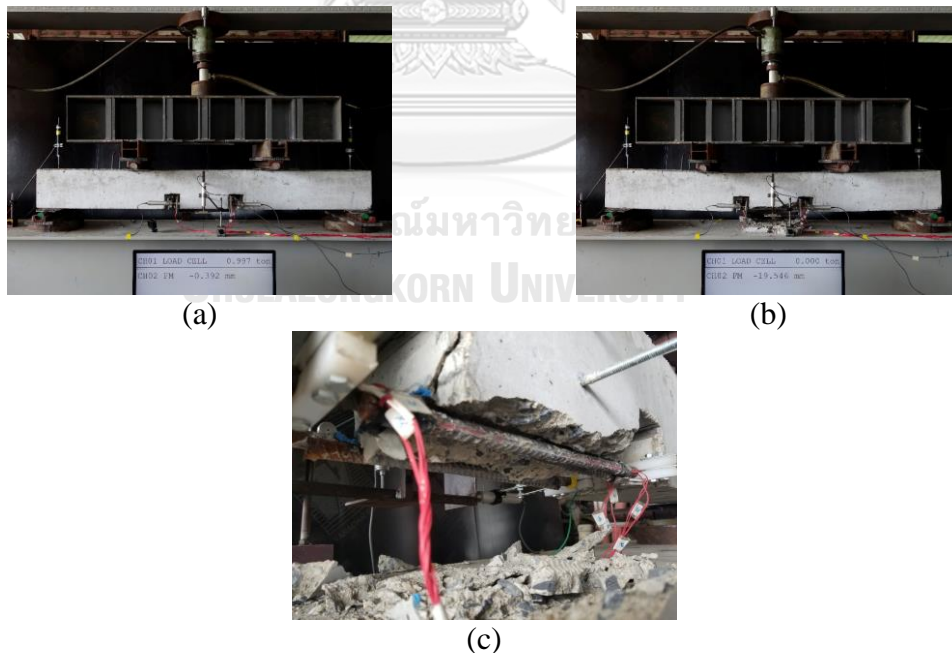
Figure 3.19 L20C1SC during test (a) start of test (b) at failure (c) cover delamination.

ii.   Beam L20C1S200

Figure 3.20 shows experimental results for the beam L20C1S200. As seen in Figure 3.20(a), a brittle load-deflection response was observed. The failure corresponding to insufficient confinement was referred to as Type-II. The maximum sustained load was 127 kN. Strain distribution along the lap splice is shown in Figure 3.20(c). The highest recorded strain was below the yield strain. Though the provision of HSS collars at 200 mm increased the maximum sustained load than that of the beam L20C1SC, it was unable to sustain this load as the deflections increased. This is also reflected in the bond stress-slip response showing a sharp reduction in the bond stress in the post-peak response (see Figure 3.20(d)). The maximum bond stress was 5.40 MPa at the loaded end slip of 0.80 mm. Figure 3.21 shows visuals of beam L20C1S200 during the test. Provisions of HSS collars at 200 mm could not inhibit brittle splitting failure (see Figure 3.21(c)), indicating insufficient clamping pressure. Sudden delamination of the side and the bottom concrete cover was observed at a load of 127 kN.
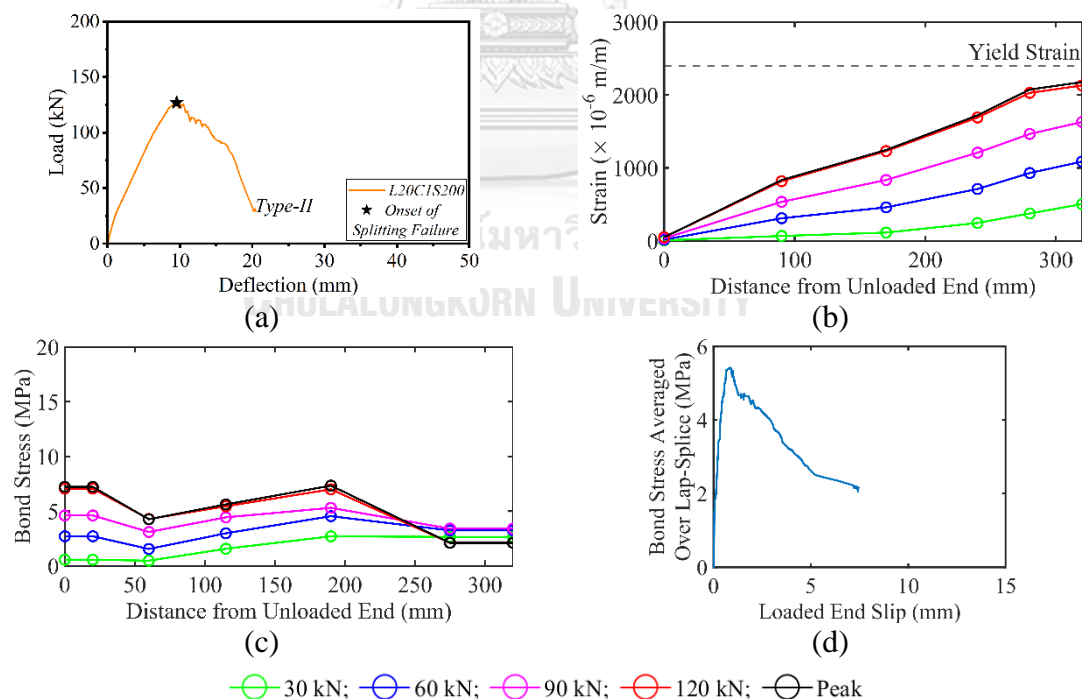
Figure 3.20 Experimental results for L20C1S200 (a) load-deflection response (Type-II), (b) strain distribution along splice, (c) bond stress distribution along splice, and (d) bond stress-slip relation.

(a)

(b)

(c)

Figure 3.21 L20C1S200 during test (a) start of test (b) at failure (c) splitting failure.

iii. Beam L20C1S100

Figure 3.22 shows experimental results for the beam L20C1S100. As seen in Figure 3.22(a), a brittle post-peak response was observed exhibiting Type-II failure. The maximum sustained load was 160.0 kN. High strains were observed near the loaded end (see Figure 3.22(b)). At peak load, approximately 22% of splice length at the loaded end exhibited yielding. Bond stress distribution tended to be uniform at peak load (see Figure 3.22(c)). Due to yielding, bond stress reduced near the loaded end. The bond stress-slip response showed an initial stiff branch followed by a drop in the bond stress. Beyond this initial drop, accurate bond stress could not be obtained as strain gages malfunctioned. The maximum bond stress was 6.20 MPa at the loaded-end slip of 0.98 mm. Figure 3.28 shows visuals of beam L20C1S100 during the test. As shown in Figure 3.23(c), this beam exhibited vertical and side-splitting cracks. At one end of the splice, a pull-out of the bar was observed, indicating that HSS collars provided at 100 c/c were not sufficient to clamp the lap splice. Consequently, peak load could not be sustained, and this beam did not demonstrate a ductile response.

Figure 3.22 Experimental results for L20C1S100 (a) load-deflection response, (b) strain distribution along splice, (c) bond stress distribution along splice, (d) bond stress-slip relation.
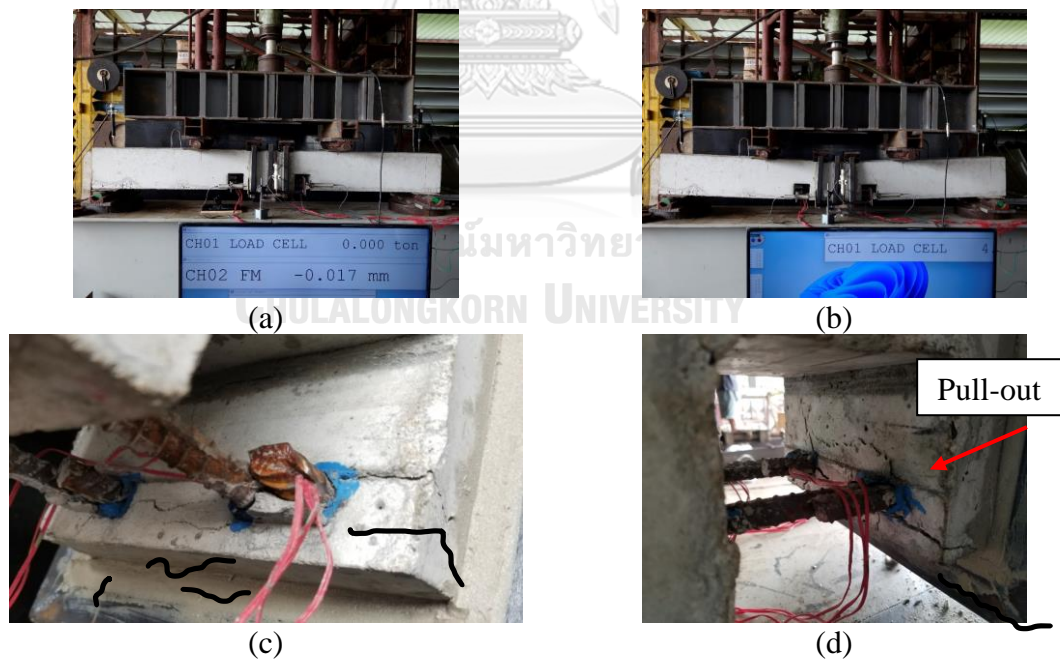
Figure 3.23 L20C1S100 during test (a) start of test, (b) at failure, (c) splitting cracks at loaded end, and (d) pull-out of the lap spliced bar.

iv.   Beam L20C1S75

Figure 3.24 shows experimental results for the beam L20C1S75. As seen in Figure 3.24(a), a ductile load-deflection response was observed without splitting failure, which is referred to as Type-III. High strains were observed near the loaded end (see Figure 3.24(b)). The lap splice strains exhibited a linear trend at all load levels. At peak load, approximately 27% of splice length at the loaded end showed yielding. Bond stress distribution tended to be uniform at peak load (see Figure 3.24(c)). Finally, the bond stress-slip response exhibited stable bond stress beyond the initial stiff branch. This suggests that the HSS collars provided at 75 mm c/c spacing were able to sustain peak load till large deflections, and subsequently, peak bond stress did not drop. Figure 3.25 shows visuals of beam L20C1S75 during the test. As shown in Figure 3.25(b), beam L20C1S75 sustained large deflections without demonstrating substantial damage. The onset of splitting cracks was observed along the bottom concrete cover. However, propagation of splitting cracks was inhibited by HSS collars at 75 mm c/c spacing.

Figure 3.24 Experimental results for L20C1S75 (a) load-deflection response, (b) strain distribution along splice, (c) bond stress distribution along splice, and (d) bond stress-slip relation.

(a)

(b)

(c)

Figure 3.25 L20C1S75 during test (a) start of test, (b) at failure, and (c) splitting cracks at loaded end.

v.   Beam L20C2S0

Figure 3.26 shows experimental results for the beam L20C2S0. As seen in Figure 3.26(a), a brittle load-deflection response of Type-I was observed. The maximum sustained load was 92 kN. High strains were observed near the loaded end (see Figure 3.26(b)). Steel strains exhibited a linear trend at all load levels. At peak load, no portion of the lap splice yielded. High bond stresses were observed near the loaded end, whereas bond stresses were nearly uniform away from the loaded end. Figure 3.26(d) shows the bond-slip relation of the beam L20C2S0. Bond stresses increased at low slip levels and reached the peak at about 0.034 mm slip. A sudden drop in the bond strength was observed analogous to the corresponding load-deflection response. Figure 3.27 shows visuals of beam L20C2SC during the test. As shown in Figure 3.27(c), complete delamination of the concrete below the lap splice was observed at the peak load leading to the sudden drop in load with a loud noise.

Figure 3.26 Experimental results for L20C2SC (a) load-deflection response, (b) strain distribution along splice, (c) bond stress distribution along splice, and (d) bond stress-slip relation.
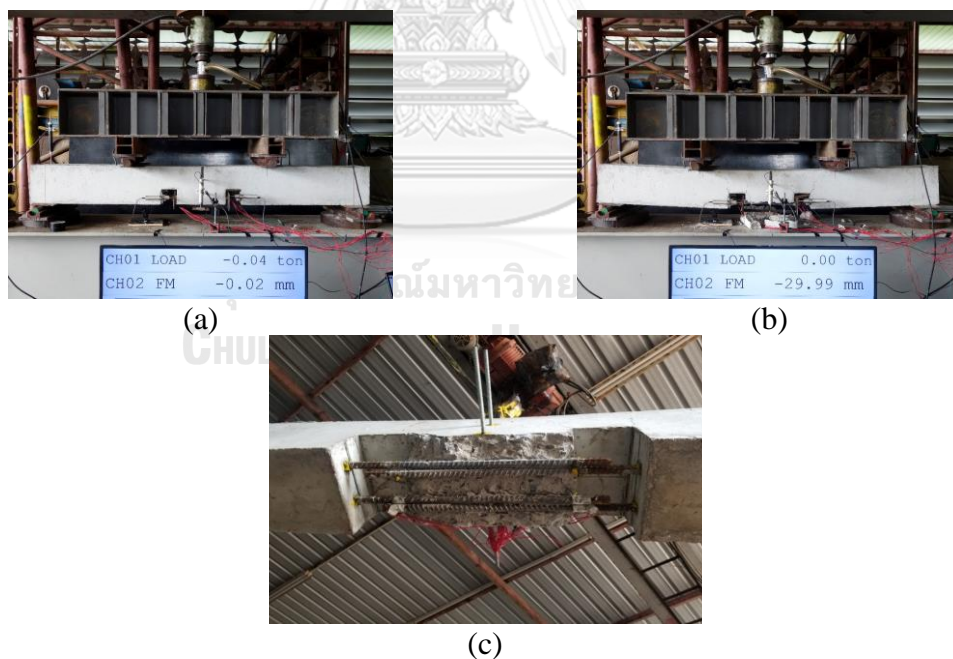
Figure 3.27 Beam L20C2SC during test (a) start of test, (b) at failure, and (c) splitting failure.

vi. Beam L20C2S200

Figure 3.28 shows experimental results for the beam L20C2S200. As seen in Figure 3.28(a), a brittle load-deflection response of Type-II was observed. The maximum sustained load was 119 kN. High strains were observed near the loaded end (see Figure 3.28(b)). Bond stress distribution along the lap splice is shown in Figure 3.28(c). Since no yielding occurred near the loaded end, higher bond stresses were observed there. Finally, analogous to the brittle load-deflection response, the bond stress-slip response also exhibited a brittle post-peak behavior. Maximum bond stress was 6.0 MPa at the loaded-end slip of 0.53 mm. Though the beam exhibited a brittle splitting behavior, the slip corresponding to the maximum bond stress was greater than its counterpart value for the control beams. Figure 3.29 shows visuals of beam L20C2S200 during the test. As observed from the load-deflection response, this beam initiated bottom and face splitting cracks near the loaded end. This beam had demonstrated brittle post-peak behavior indicating that the splitting failure had occurred. A careful post-failure observation indicated that, indeed, splitting cracks had propagated along the lap splice length, as shown in Figure 3.29(d).
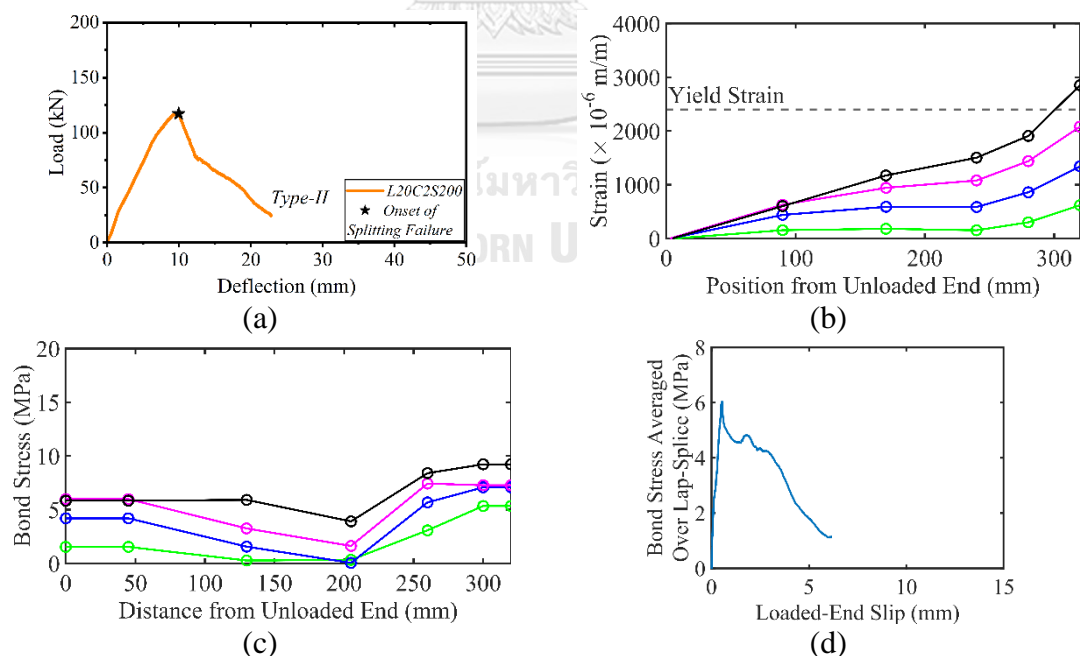
Figure 3.28 Experimental results for L20C2S200 (a) load-deflection response, (b) strain distribution along splice, (c) bond stress distribution along splice, and (d) bond stress-slip relation.
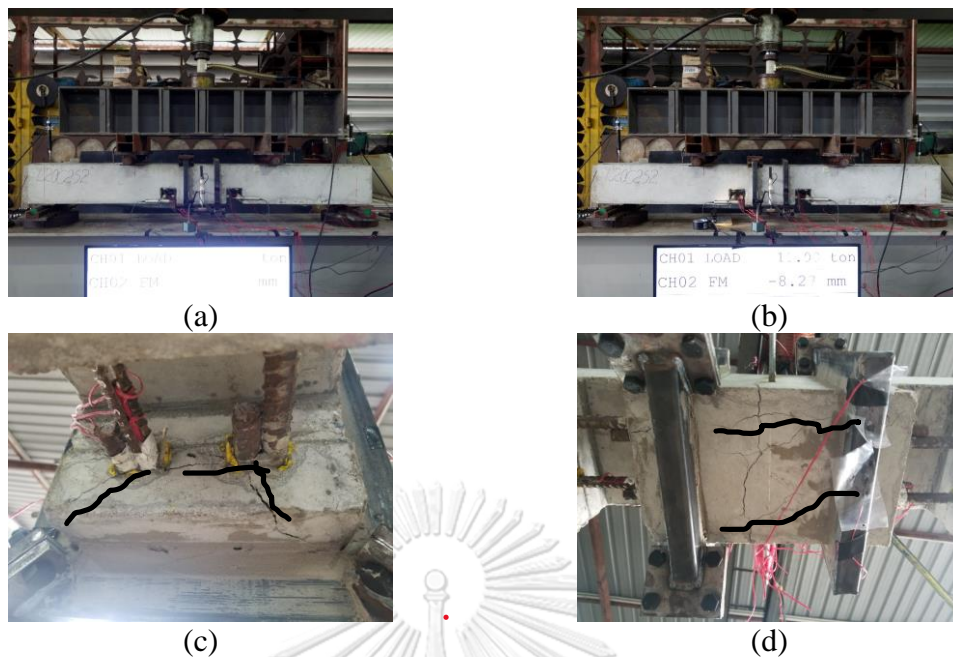
Figure 3.29 L20C2S200 during test (a) start of test, (b) at failure, (c) splitting cracks at loaded end, and (d) splitting cracks propagated along splice length.

vii.   Beam L20C2S100

Figure 3.30 shows experimental results for the Beam L20C2S100. As seen in Figure 3.30(a), a ductile load-deflection response of Type-III was observed. The maximum sustained load was 149.8 kN. Unlike Beam L20C1S100, HSS collars provided at 100 mm in the presence of c_{min}/d_b 1.62 proved to be sufficient in mitigating splitting failure. Towards the loaded end, a significant portion of the lap splice exhibited strains larger than the yield strain, whereas the circumferential contraction due to yielding near the loaded end resulted in the drop of bond stress, as shown in Figure 3.30(c). The bond stress distribution within the pre-yield zone of the lap splice was roughly uniform. Figure 3.30(d) shows the bond stress (averaged over the lap splice) vs. slip relation. After the initial stiff branch, a slight drop in the bond stress was observed. The bond stress was observed to be uniform as the load-end slip increased. Figure 3.31 shows visuals of beam L20C2S100 during the test. As shown in Figure 3.31(b), Beam L20C2S100 sustained large deflections without demonstrating substantial damage. As shown in Figure 3.31(c), splitting cracks initiated in the bottom cover and between the lapped bars. However, these splitting

cracks did not propagate along the splice, as shown in Figure 3.31(d), indicating that splitting failure was suppressed.

(a)

(b)

(c)

(d)

| 30 kN | 60 kN | 90 kN | 120 kN | 150 kN | Peak |
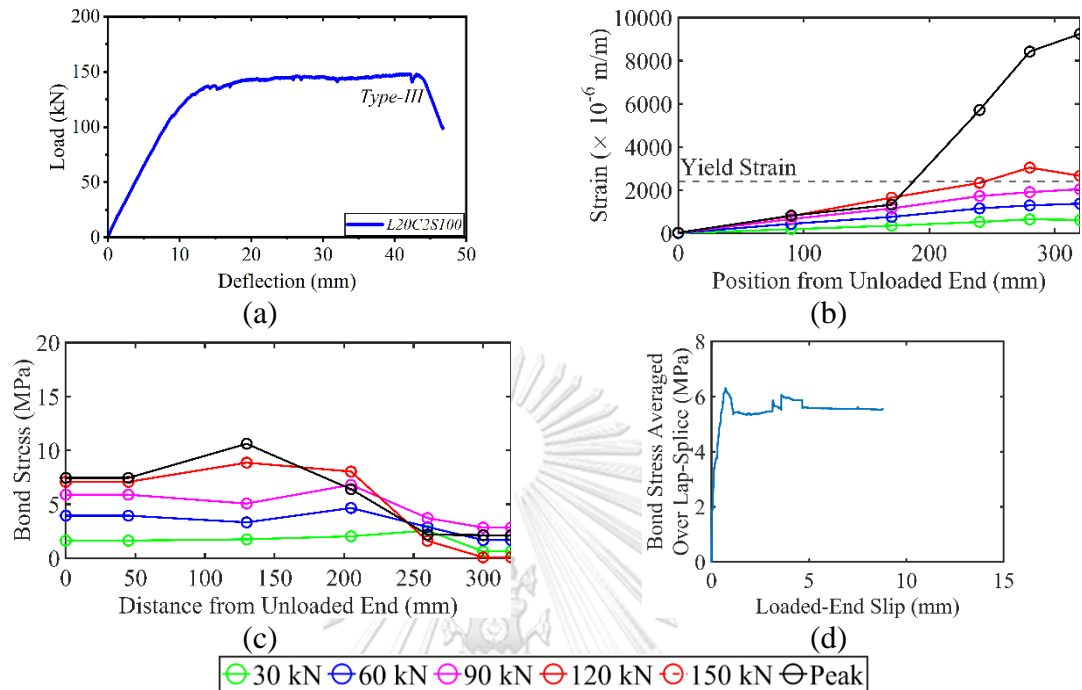
Figure 3.30 Experimental results for L20C2S100 (a) load-deflection response, (b) strain distribution along splice, (c) bond stress distribution along splice, and (d) bond stress-slip relation.

(a)

(b)

(c)

(d)
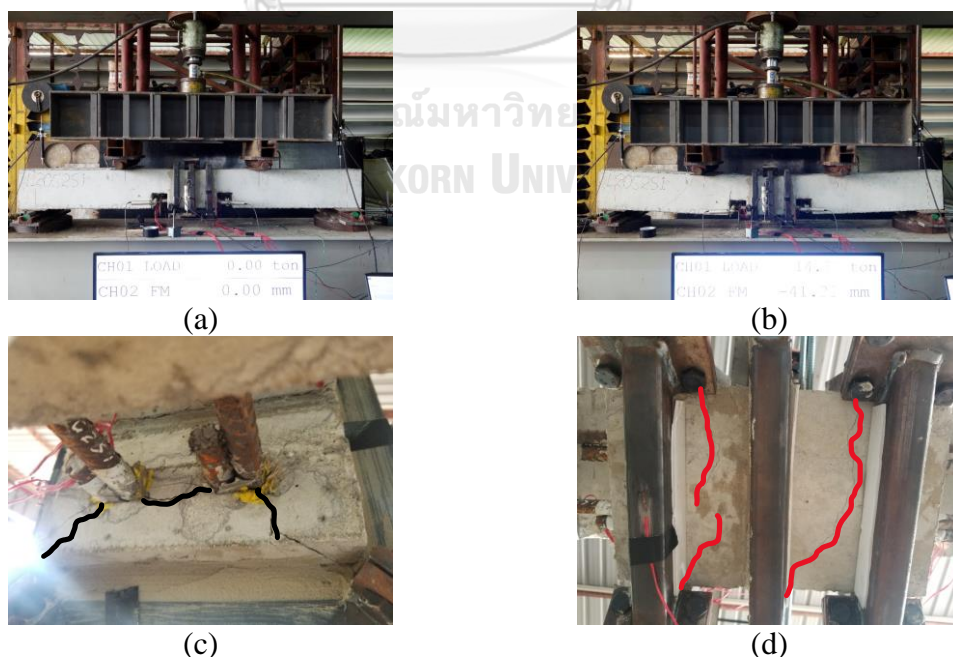
Figure 3.31 L20C2S100 during test (a) start of test, (b) at failure, (c) splitting cracks at loaded end, and (d) posttest bottom view with no splitting cracks (red lines showing flexural cracks).

viii.   Comparison of Group 1 Results

Figure 3.32 shows the experimental load versus deflection response of all seven beams of series L20. For clarity, responses are plotted separately for beams in Subgroups C1 and C2. Load-deflection response of control beams in both subgroups was characterized by a sudden drop before attaining peak capacities. For the sake of direct comparison, the load at each deflection of all beams was multiplied to $\left(f_c'\ of\ L20C1S200\right)\Big/ f_c'^{\,0.25}$ [14], where f_c' is the beam whose load is being normalized. A clear improvement in the ductility is observed as the collar spacing is reduced. For both subgroups, collar spacing at 200 mm did not bring significant improvement in ductility. However, the peak sustained load was higher than that of the corresponding control beam. For subgroup C1, a fully ductile response was observed at a collar spacing of 75 mm, whereas a similar response in Subgroup C2 was observed at a collar spacing of 100 mm. This difference is manifested in smaller concrete cover within beams of Subgroup C1, i.e., 16 mm, in comparison to the higher concrete cover in Subgroup C2, i.e., 32 mm.
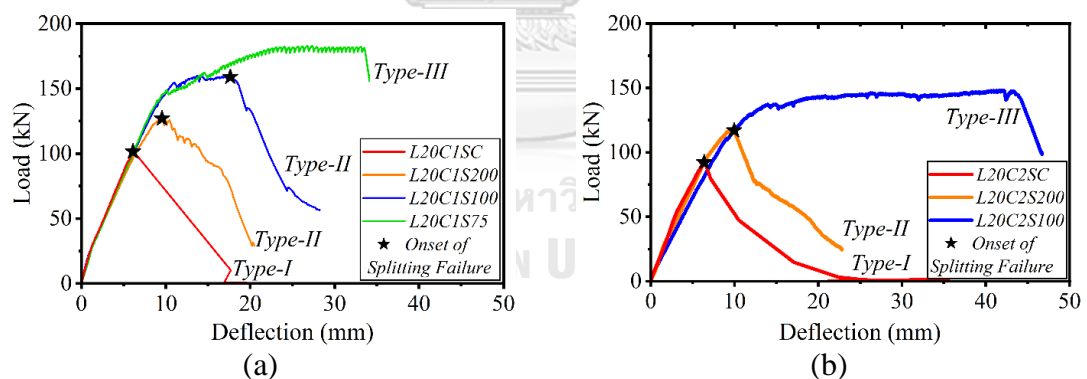
Figure 3.32 Comparison of load-deflection response of Group 1 beams (a) Subgroup C1 and (b) Subgroup C2.

Control beams in both subgroups failed in a sudden and explosive manner without any warning (Type-I). This was expected attributed to their substandard lengths of lap splices. Strengthening them using steel collars at 200 mm delayed splitting crack propagation along lap splices. However, the final failure mode was controlled by sudden splitting (Type-II). Decreasing collar spacing to 100 mm prevented splitting crack propagation along the lap splice. However, pull-out failure

dominated in beam L20C1S100, and a complete ductile response was not achieved. This is evident from its load-deflection response. On the contrary, 100 mm spacing of HSS collars in beam L20C2S100 resulted in a ductile response, and pull-out failure was inhibited. This discrimination may be attributed to the smaller concrete cover in beam L20C1S100 than that in beam L20C2S100, thereby demanding higher confining pressures. This observation seems true as reducing collar spacing to 75 mm inhibited pull-out for the case of 16 mm cover, i.e., see the response of L20C1S75 in Figure 3.32. Figure 3.33 and Figure 3.34 present splitting cracks observed at the loaded ends of lap splices for the C1 and C2 subgroups, respectively.

(a) Splitting failure (Type-I)   (b) Splitting cracks restrained (Type-III)

(c) Splitting cracks restrained but pull-out   (d) Splitting failure (Type-II)
(Type-II)
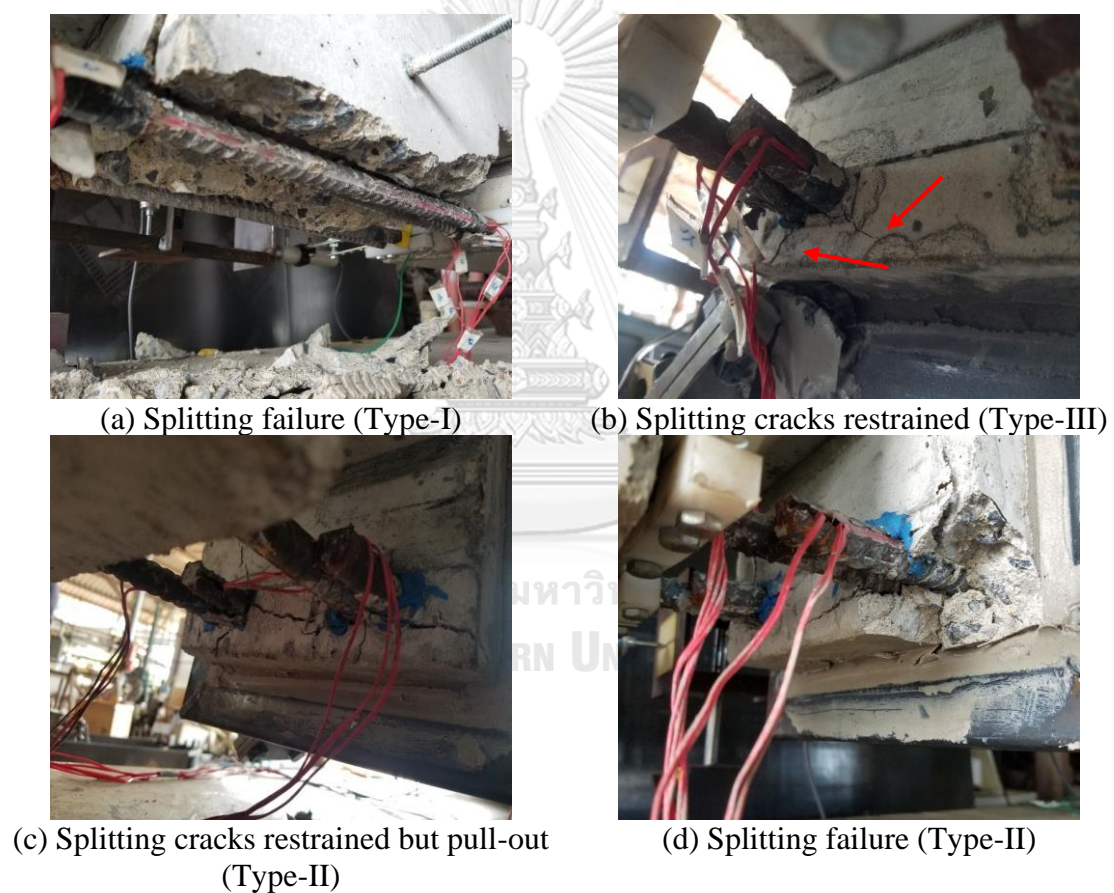
Figure 3.33 Splitting cracks and failure at loaded ends of beams (a) L20C1S0, (b) L20C1S75, (c) L20C1S100, and (d) L20C1S200.

(a) Splitting failure (Type-I)   (b) Splitting cracks restrained (Type-III)

(c) Splitting cracks initiated and propagated along lap splice (Type-II)

Figure 3.34 Splitting cracks and failure at loaded ends of beams (a) L20C2S0, (b) L20C2S100, and (c) L20C2S200.

Table 3.5 presents the comparison of maximum load sustained, bond strengths, and failure modes of series $20d_b$ beams. It can be seen that a large increase in bond strength was observed when the cover was 16 mm. Increasing the cover to 32 mm resulted in a better lap splice performance for the control beam. Since the bond strength enhancement is limited to the point where yield is achieved at the loaded end, the control beam with a 16 mm cover had a larger margin for the improvement in the maximum strain at its loaded end than that for the beam with a 32 mm cover. As a result, greater improvement in the bond strength was observed for the beams of Subgroup C1 after the application of HSS collars.

Table 3.5 Summary of peak loads and bond strengths of Group 1 beams.

Beam ID	Peak Load (kN)	Increase in Peak Load (%)	Mode of Failure	τ (MPa)	$\Delta\tau$ (MPa)
L20C1S0	100.1	-	Type-I	4.3	-
L20C1S200	127.4	27.4	Type-II	5.4	1.1
L20C1S100	160.0	60.0	Type-II	6.2	1.9
L20C1S75	182.8	82.8	Type-III	6.6	2.3
L20C2S0	93.9	-	Type-I	5.3	-
L20C2S200	119.2	26.9	Type-II	5.7	0.4
L20C2S100	149.8	59.5	Type-III	5.9	0.6

3.6.2. Group 2 Beams

i. Beam L28C1SC

Figure 3.35 shows experimental results for the beam L28C1SC. As seen in Figure 3.35(a), a linear load-deflection response was observed, followed by a sudden loss of capacity depicting Type-I failure. The maximum sustained load was 117 kN. High strains were observed near the loaded end (see Figure 3.35(b)). Nonetheless, the maximum recorded strain was 1819 microns which is 24% lower than the yield strain, i.e., 2400 microns. Since bond stress is directly related to the first derivative of steel stress, a uniform bond stress distribution was observed along the lap splice. Maximum bond stress was 4.4 MPa observed at the loaded-end slip of 0.60 mm. A sudden drop in the bond stress was observed after the peak value of 4.4 MPa due to the cover delamination. Figure 3.36 shows visuals of beam L28C1SC during and after the test. Since this beam was tested without HSS collar confinement, a sudden brittle splitting failure was expected. At about 117 kN load, bottom concrete cover delamination was observed within the lap splice region, followed by the complete loss of load-carrying capacity. Figure 3.36(c) shows the delamination of the bottom concrete cover.
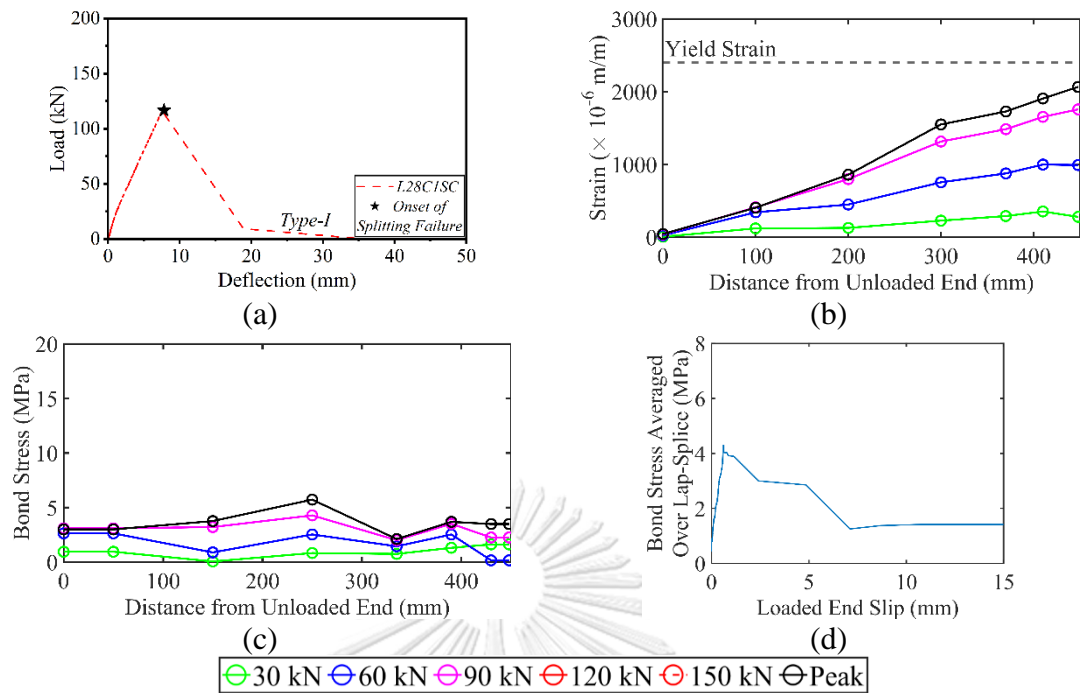
Figure 3.35 Experimental results for L28C1SC (a) load-deflection response, (b) strain distribution along splice, (c) bond stress distribution along splice, and (d) bond stress-slip relation.
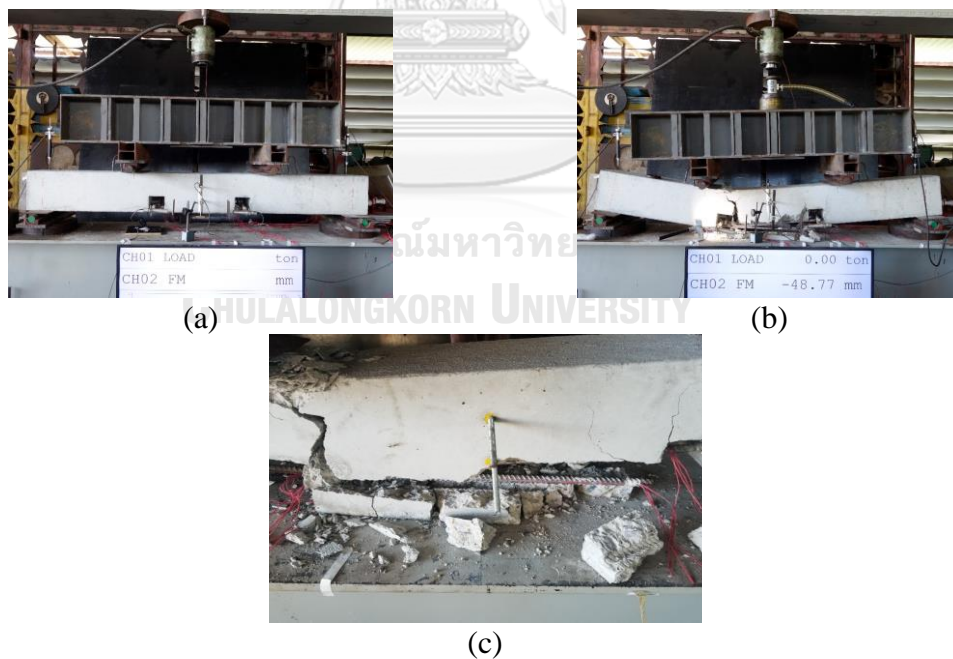
Figure 3.36 L28C1SC during test (a) start of test, (b) at failure, and (c) splitting failure and cover delamination.

ii. Beam L28C1S200

Experimental results of the beam L28C1S200 are shown in Figure 3.37. This beam was confined with HSS collars at a spacing of 200 mm. As shown in Figure 3.37(a), this beam attained a maximum load of 156.7 kN. However, this load could not be sustained beyond a vertical deflection of 20 mm, and a sudden failure of Type-II was observed. However, the maximum recorded strain was limited to 3600 microns only. Bond stress distribution was roughly uniform within the elastic zone of the lap splice. Since the steel bar yielded at the loaded end, a substantial drop in the bond stress was observed at the loaded end. The maximum bond stress was 4.6 MPa at the loaded-end slip of 0.31 mm. At this point, a sudden drop in the load capacity due to Type-II splitting failure occurred. Consequently, strain gage readings were not accurate, and the bond stress-slip response showed a spurious spike. Figure 3.38 presents the ultimate failure mode of the beam L28C1S200. Further inspection at the bottom of the beam at the end of the test revealed that splitting cracks had propagated along the lap splice. This suggests that HSS collars provided at 200 mm spacing were not sufficient to inhibit splitting failure.
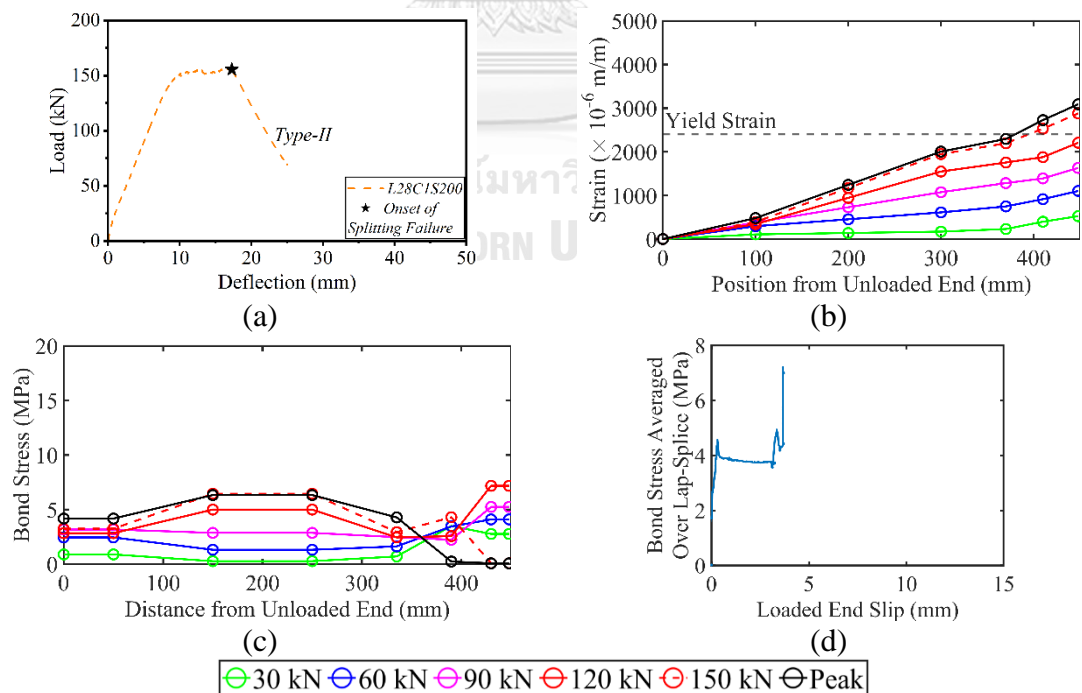
Figure 3.37 Experimental results for L28C1S200 (a) load-deflection response, (b) strain distribution along splice, (c) bond stress distribution along splice, and (d) bond stress-slip relation.

(a)   (b)

(c)   (d)
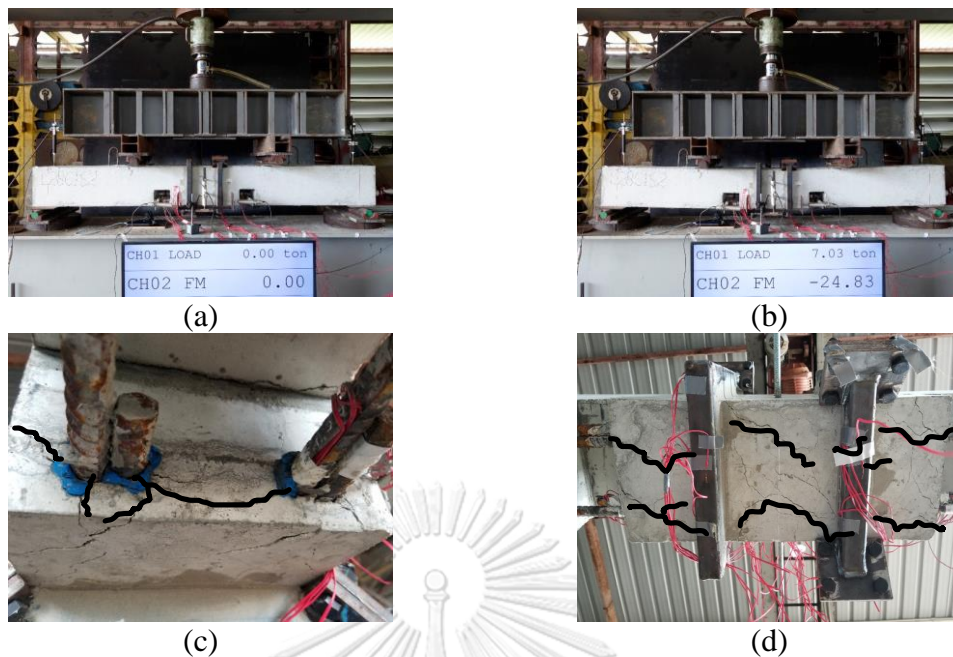
Figure 3.38 L28C1S200 during test (a) start of test, (b) at failure, (c) splitting cracks initiated at splice end, and (d) splitting cracks propagated along splice length.

iii.   Beam L28C1S100

Experimental results of the beam L28C1S100 are shown in Figure 3.39. This beam was confined with HSS collars spaced at 100 mm. From Figure 3.39(a), a fully ductile response of Type-III was observed till 40 mm deflection. The test was stopped at this point as displacement transducers attained their maximum stroke. As shown in Figure 3.39(b), approximately 23% of the loaded end experienced yielding. The bond stress-slip response included an initial stiff branch followed by a slight drop. This is attributed to the onset of yielding of steel bars at the loaded end. With the further increase in load, bond stress first remained constant as the slip increased. The maximum bond stress was observed as 4.7 MPa at the loaded-end slip of 0.91 mm. Figure 3.40 presents the visuals of beam L28C1S100 during and after the test. As seen in Figure 3.40(b), this beam was able to withstand large deflections without compromising on the sustained load. This is an indication that for the lap splice length of $28d_b$ and c_{min}/d_b of 1, HSS collars provided at 100 mm were sufficient to mitigate splitting failure. Figure 3.40(c) shows the onset of splitting cracks at one of the ends of the lap splice zone. The bottom view of the beam at the end of the test is

shown in Figure 3.40(d). Splitting cracks initiated at the ends of the lap splice zone were restricted in their origin.

(a)

(b)

(c)

(d)

| 30 kN | 60 kN | 90 kN | 120 kN | 150 kN | Peak |
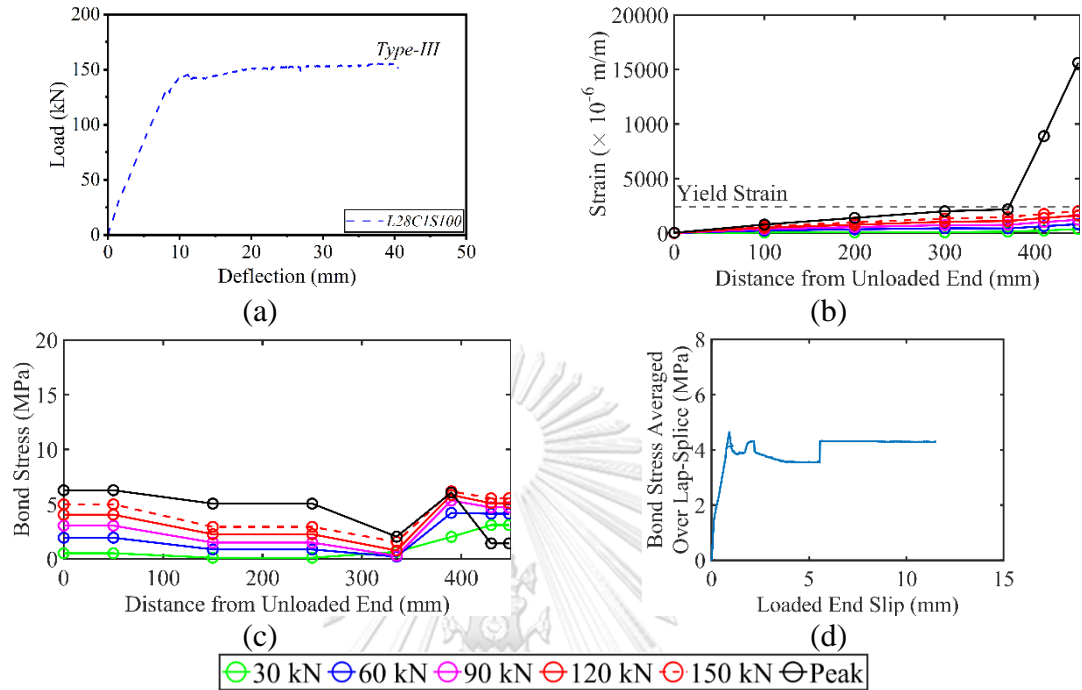
Figure 3.39 Experimental results for L28C1S100 (a) load-deflection response, (b) strain distribution along splice, (c) bond stress distribution along splice, and (d) bond stress-slip relation.

(a)

(b)

(c)

(d)
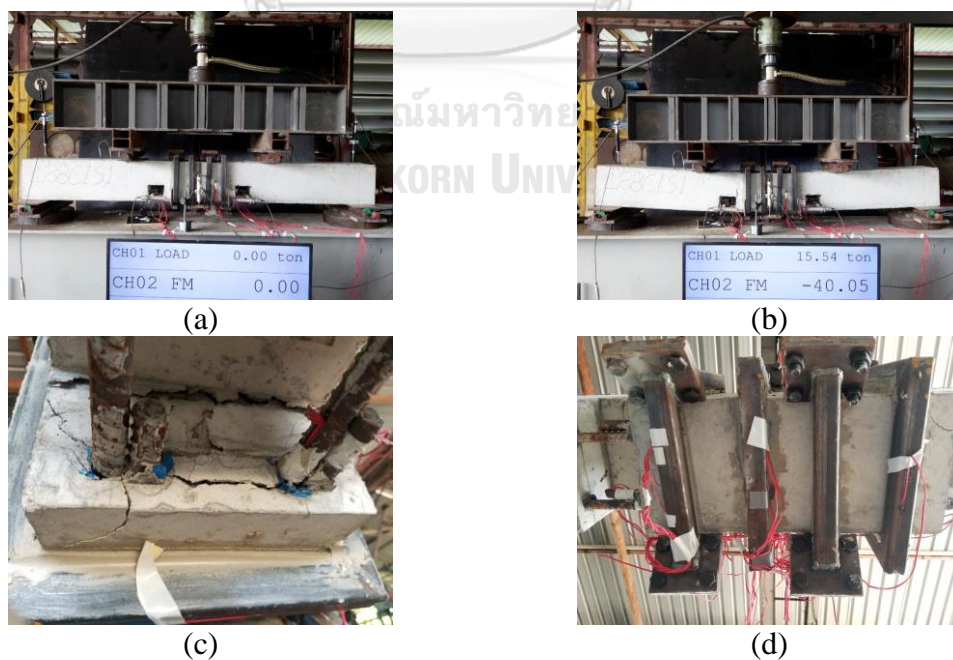
Figure 3.40 L28C1S100 during test (a) start of test, (b) at failure, (c) bottom and face splitting at splice end, and (d) no splitting cracks along splice length.

iv. Beam L28C2SC

L28C2SC was the control beam in this category. Since it was furnished with a deficient lap splice length, it demonstrated a sudden drop in its capacity (Type-I failure) before achieving its peak load, as shown in Figure 3.41(a). The maximum load attained was 124 kN. Near the loaded end, about 10% of splice length exhibited yielding. However, the maximum strain was limited to 2900 microns. At the peak load, a uniform bond-stress distribution was observed within the elastic zone of the lap splice (see Figure 3.41(c)). A sharp drop in the bond stress was observed near the loaded end due to yielding. Finally, the bond stress-slip relation is presented in Figure 3.41(d). It comprised a stiff ascending branch up to the peak bond stress of 4.5 MPa, corresponding to the loaded-end slip of 0.91 mm. Beyond this point, peak bond stress could not be sustained, and it vanished quickly as the slip increased. Since beam L28C2SC was a control beam and furnished a deficient lap splice length, it exhibited a brittle splitting failure at its peak load. Its failure accompanied complete delamination of the concrete cover within the splice zone, as shown in Figure 3.42c.
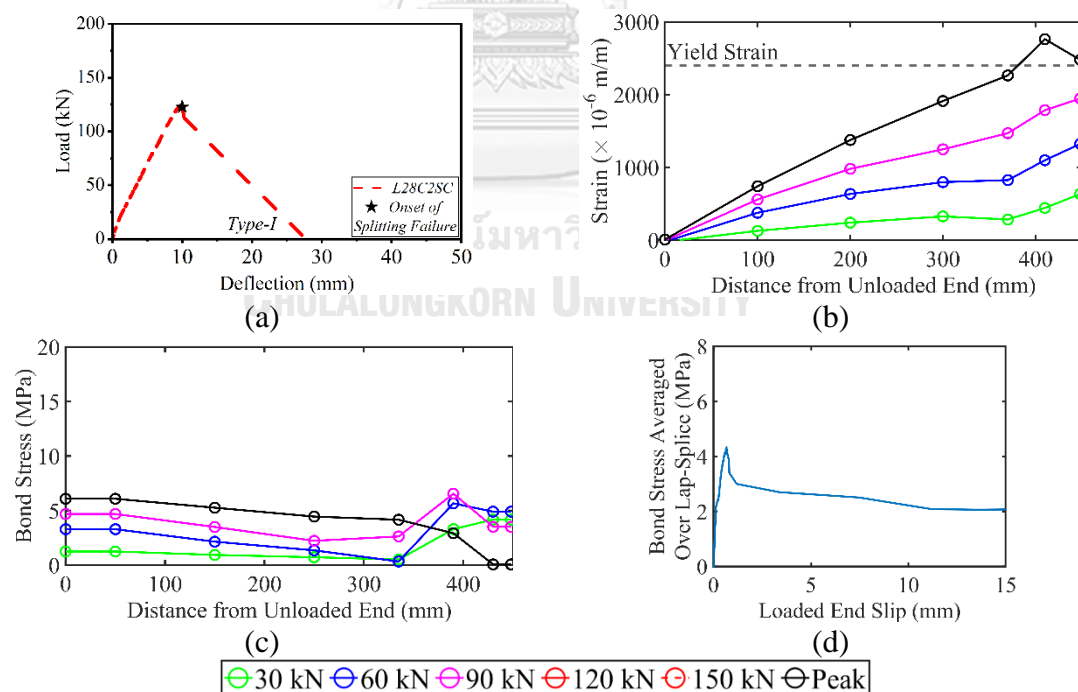
Figure 3.41 Experimental results for L28C2SC (a) load-deflection response, (b) strain distribution along splice, (c) bond stress distribution along splice, and (d) bond stress-slip relation.

(a)

(b)

(c)
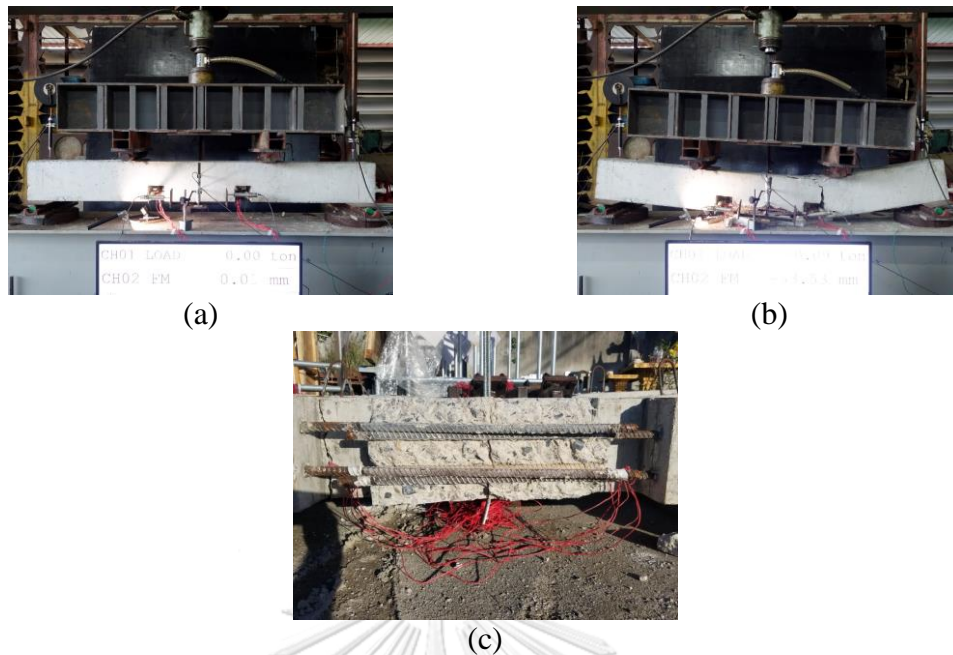
Figure 3.42 L28C2SC during test (a) start of test, (b) at failure, and (c) splitting failure and cover delamination.

v.   Beam L28C2S200

Beam L28C2S200 was strengthened with HSS collars at 200 mm spacing. Unlike beam L28C1S200, which suffered a splitting failure, this beam was able to inhibit splitting failure. This is ascribed to the larger concrete cover of 32 mm in this beam as compared to the 16 mm cover in Beam L28C1S200. Consequently, a ductile load-deflection response of Type-III was obtained, as shown in Figure 3.43(a). Strain distribution along the splice suggested that about 24% of its length experienced yielding. Bond stress distribution was roughly uniform within the elastic zone, whereas a sharp drop in bond strength was observed near the loaded end due to yielding (see Figure 3.43(c)). The bond stress-slip response is plotted in Figure 3.43(d). Analogous to other beams, the bond stress-slip response was characterized by an initial stiff branch till peak bond stress, followed by a slight drop. This drop in bond stress was attributed to the yielding at the loaded end. The peak bond stress was 4.7 MPa at the loaded-end slip of 0.92 mm. Further, the peak bond stress was maintained till large loaded-end slip values. Finally, post-test observations at the ends of splices revealed that bottom and face splitting cracks had initiated, as shown in Figure 3.44(c). However, further inspection along the splice length revealed that the

splitting cracks could not propagate along the splice length. Hence, the clamping pressure from HSS collars at 200 mm on this beam was sufficient to restrict the dilation of concrete around the lapped bars.
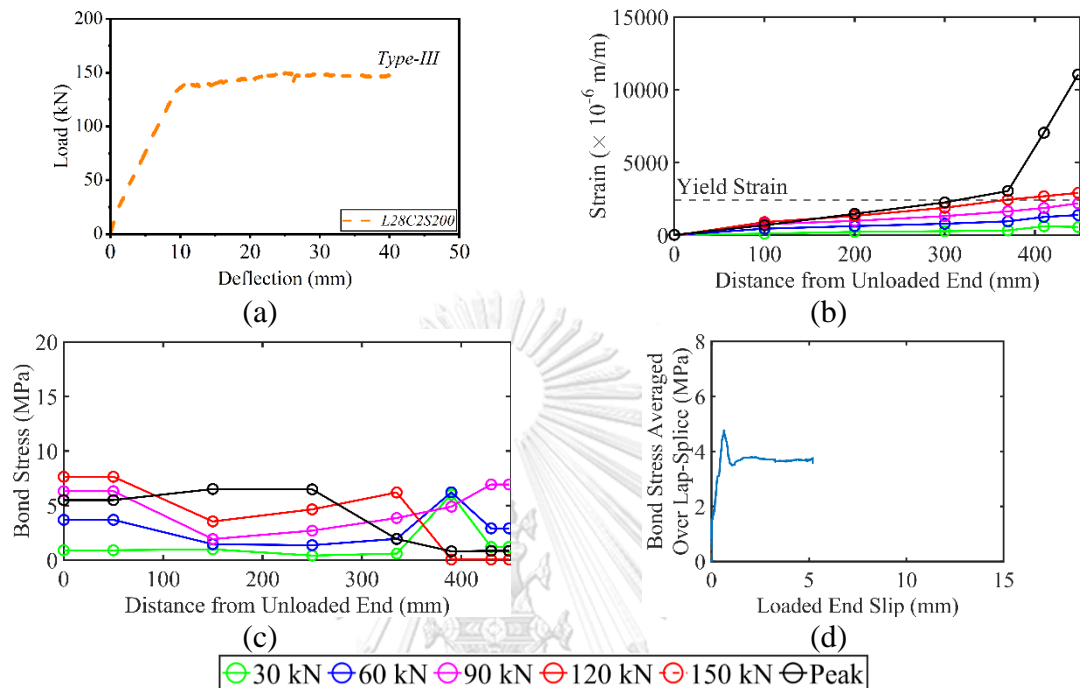
Figure 3.43 Experimental results for L28C2S200 (a) load-deflection response, (b) strain distribution along splice, (c) bond stress distribution along splice, and (d) bond stress-slip relation.

(a)

(b)

(c)

(d)
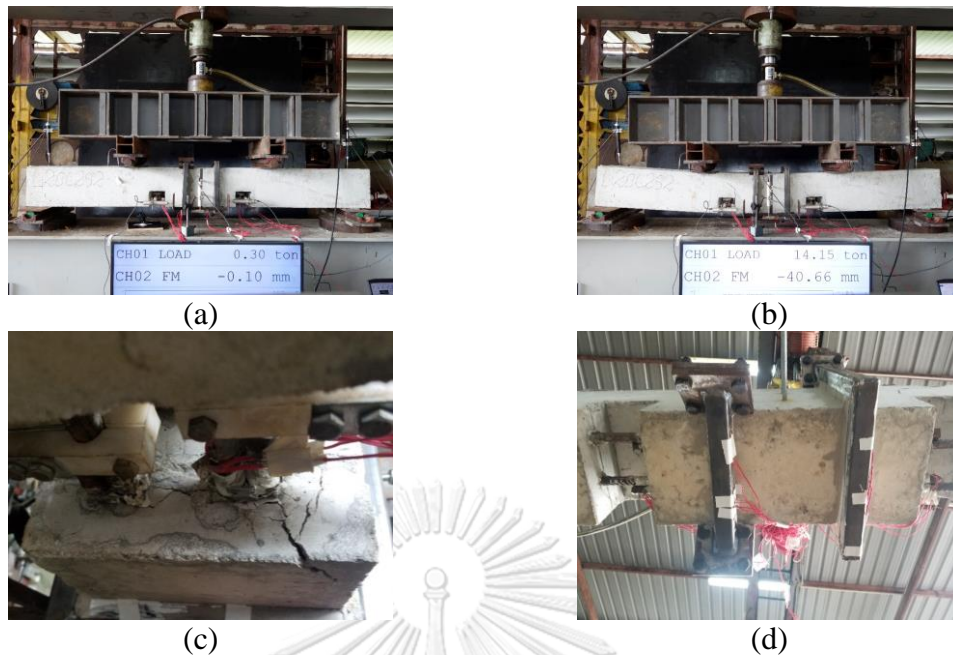
Figure 3.44 L28C2S200 during test (a) start of test, (b) at failure, (c) bottom and face splitting cracks at ends of splice, and (d) no propagation of splitting cracks along the splice length.

vi.   Beam L28C2S100

Beam L28C2S100 was confined with HSS collars at 100 mm spacing. As shown in Figure 3.45(a), a fully ductile load-deflection response of Type-III was obtained. The strain distribution of steel bars is presented in Figure 3.45((b), indicating a linear trend, and approximately 25% of the splice length at the loaded end experienced yielding. Consequently, bond stress reduced drastically towards the loaded end, as shown in Figure 3.45((c). The bond stress-slip response is shown in Figure 3.45(d), indicating maximum bond stress of 4.7 MPa at the corresponding loaded-end slip of 0.33 mm. Following the peak bond stress, a drop in bond stress was observed ascribed to the loaded end yielding. Figure 3.45(d) suggests that bond stress was maintained at large slip values. Load-deflection response of this beam did not show a decline in peak loads even at high deflections. This suggested that HSS collars provided sufficient clamping pressure to restrain the propagation of splitting cracks that initiated at splice ends (see Figure 3.46(c)). Posttest inspection underneath the beam revealed that splitting cracks were constrained near the splice ends. Hence, splitting failure was successfully inhibited.
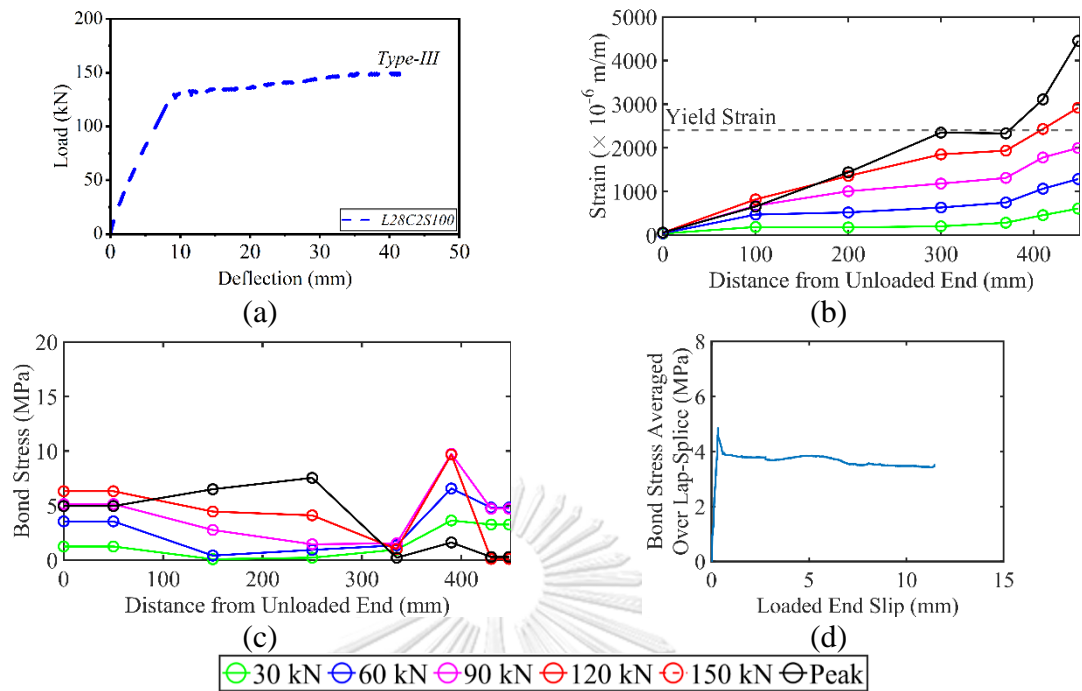
Figure 3.45 Experimental results for L28C2S200 (a) load-deflection response, (b) strain distribution along splice, (c) bond stress distribution along splice, and (d) bond stress-slip relation.
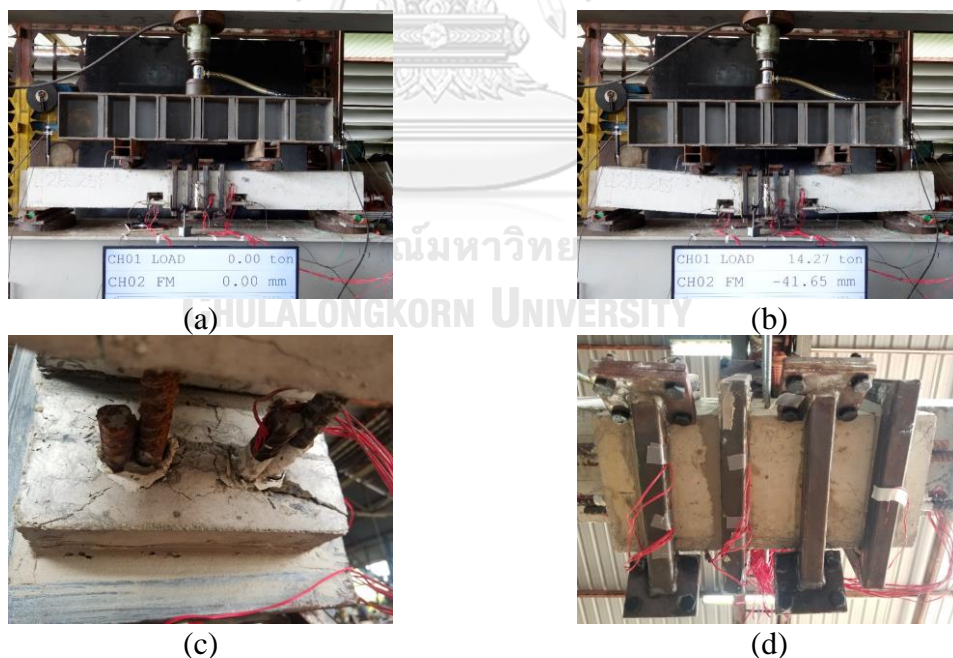
Figure 3.46 L28C2S100 during test (a) start of test, (b) at failure, (c) bottom and side splitting at splice ends, and (d) bottom view of the beam showing no splitting cracks along the splice length.

vii. Comparison of Group 2 Results

Figure 3.47 presents a comparison of the load-deflection response of the beams tested in series $28d_b$. Figure 3.47(a) corresponds to the subgroup of beams with 16 mm cover, whereas Figure 3.47(b) refers to the response of beams with 26 mm controlling cover. None of the control beams in both groups exhibited Type-III response, and a sudden drop in capacity was observed exhibiting Type-I response. Confining the beams with HSS collars at 200 mm spacing delayed the onset of splitting in beam L28C1S200. However, the beam failed in splitting, exhibiting a Type-II response at a deflection of 17 mm. On the contrary, similar confinement on beam L28C2C200 resulted in a ductile response of Type-III. This can be attributed to the larger concrete cover in the C2 series than that of the C1 series resulting in lower demand for external clamping pressure. Finally, HSS collars at 100 mm resulted in a Type-III response preventing splitting failure in the L28C1 series.
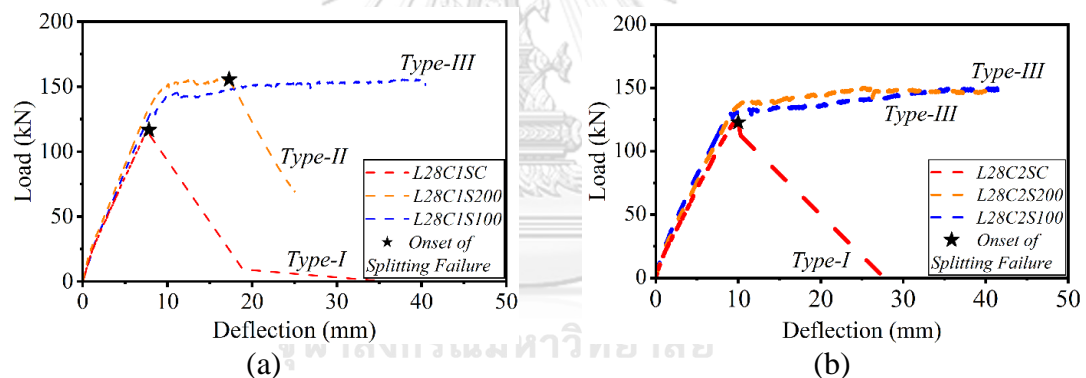
Figure 3.47 Comparison of load-deflection response of Group 2 beams (a) Subgroup C1 and (b) Subgroup C2.

Figure 3.48 presents a comparison of failure modes observed in the L28C1 series. In Figure 3.48(a), the control beam L28C1SC failed in a brittle splitting failure (Type-I) involving complete delamination of the bottom concrete cover along the lap splice. This type of failure was not observed after the beams were confined with HSS collars. However, as shown in Figure 3.48(d) and Figure 3.48©, the beam L28C1S200 allowed the onset of bottom and face-splitting cracks at splice ends. Post failure inspection revealed that splitting cracks had propagated along the splice length. On the contrary, HSS collars at 100 mm spacing successfully restrained the propagation of splitting cracks along the lap splice. As shown in Figure 3.48(b) and

Figure 3.48(c), splitting cracks initiated at splice ends were unable to propagate along the splice length. Figure 3.48(c) shows the bottom view of beam L28C1S100 where no longitudinal cracks occurred.

Figure 3.49 presents a comparison of failure modes observed in the L28C2 series. The control beam failed in a similar manner as that of the L28C1 series (Type-I failure). Complete delamination of the bottom concrete cover was observed. Again, this kind of brittle failure was not observed when the beam was confined with HSS collars at 100 mm and 200 mm spacing. Unlike beam L28C1S200 that failed in splitting, application of collars at 200 mm spacing in the L28C2 series resulted in a ductile response, and propagation of splitting cracks was restrained, indicating an adequate clamping pressure to inhibit concrete dilation around lapped bars.

(a)

Splitting cracks

Splitting crack initiated but restrained from

(b)

Splitting cracks

Splitting cracks propagated along

(c)
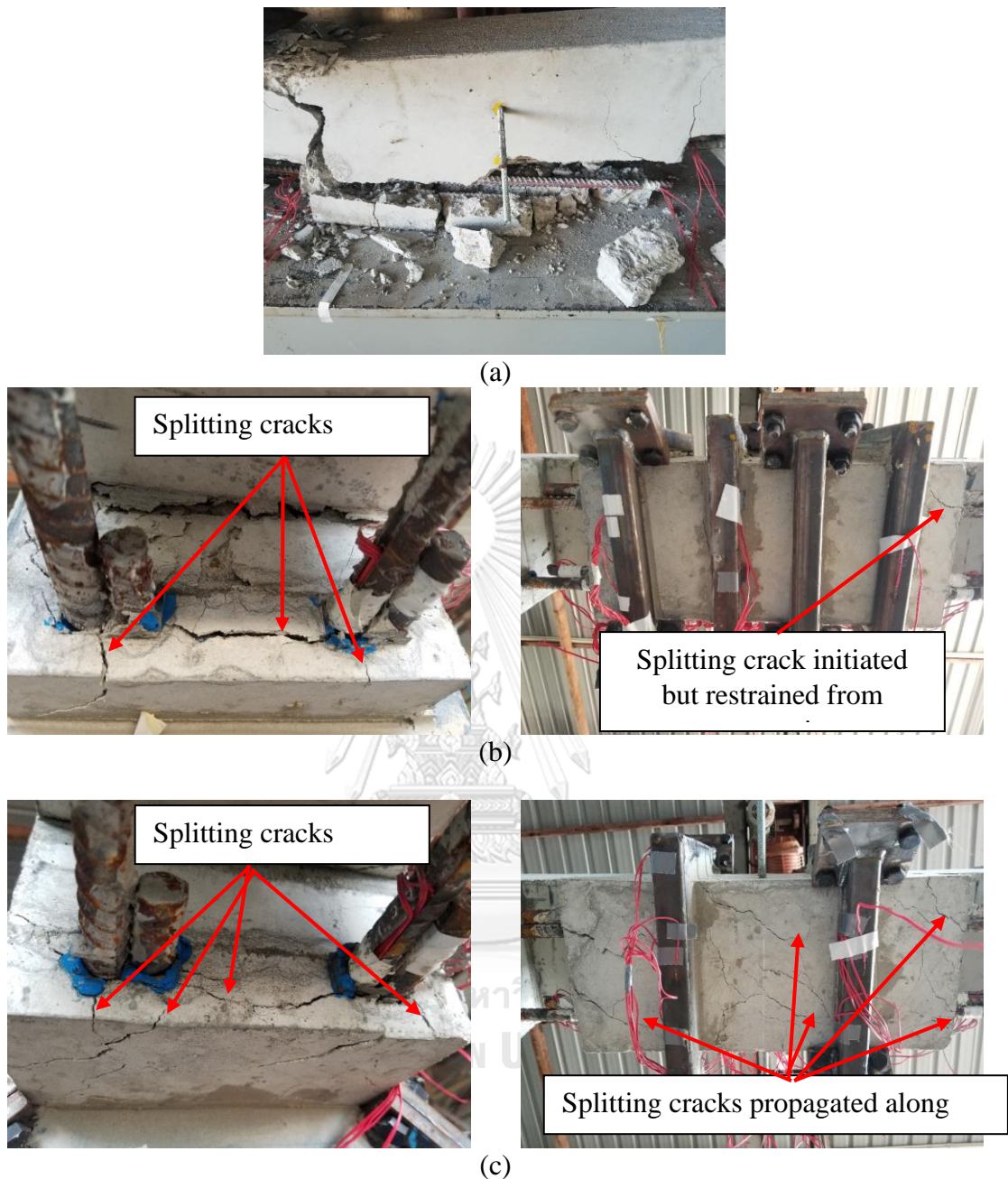
Figure 3.48 Comparison of failure modes of series L28C1 (a) L28C1SC, (b) L28C1S100, and (c) L28C1S200.

A summary of experimental results of series L28 beams is provided in Table 3.6, including average bond stress along the lap splice and increase in bond stress as a result of HSS collar confinement. As expected, Beam L28C1S100 demonstrated the highest increase in bond strength, i.e., 0.3 MPa. It is because the control beam L20C1SC was weaker than L20C2SC and confined with HSS collars at 100 mm, i.e., maximum confinement within this series.

(a)

Splitting cracks

Splitting crack initiated
but restrained from

(b)

Splitting cracks

Splitting crack initiated
but restrained from

(c)
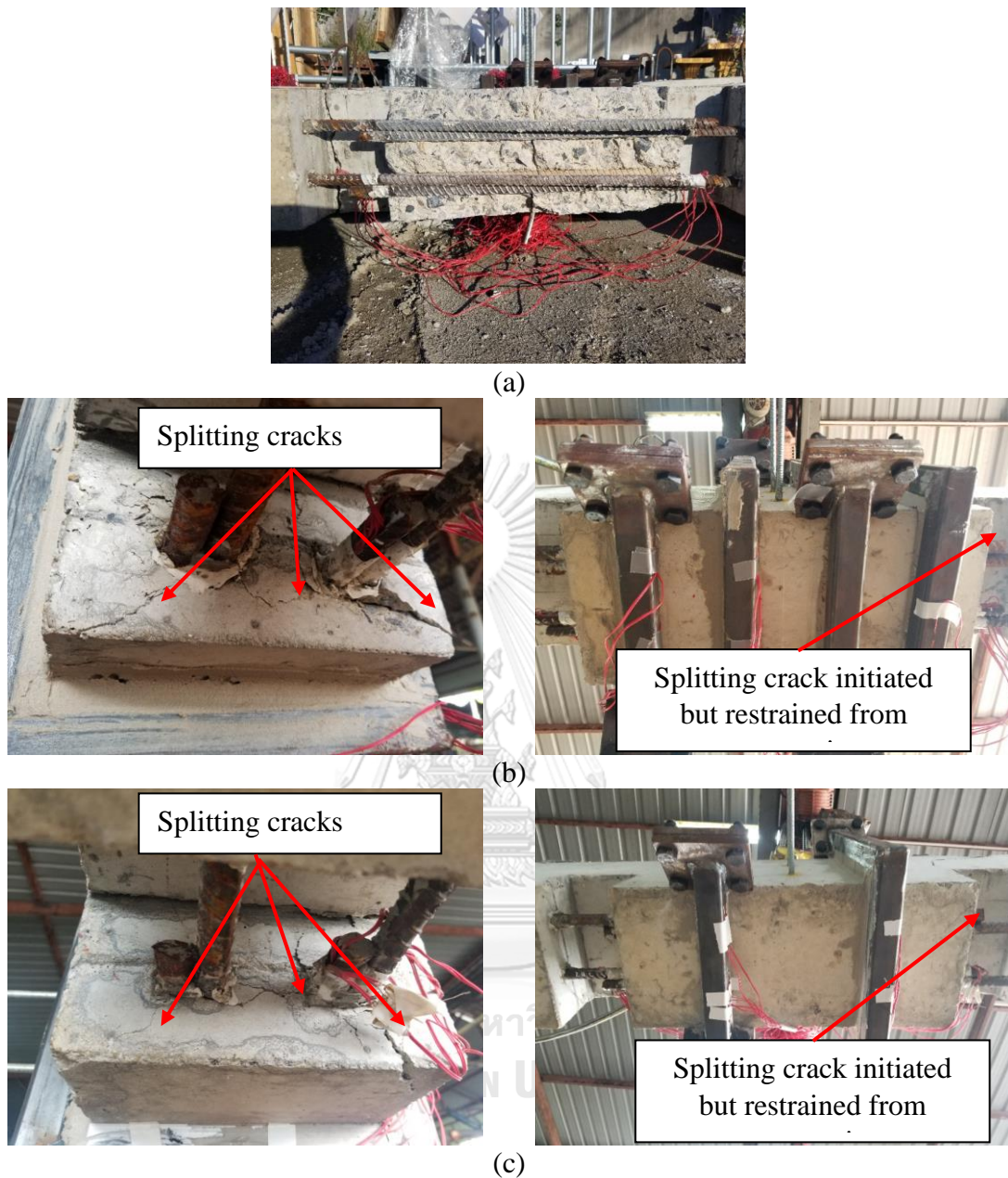
Figure 3.49 Comparison of failure modes of series L28C2 (a) L28C2SC, (b) L28C2S100, and (c) L28C2S200.

Table 3.6 Summary of peak loads and bond strengths of Group 2 beams.

Beam ID	Peak Load (kN)	Increase in Peak Load (%)	Mode of Failure	τ (MPa)	$\Delta\tau$ (MPa)
L28C1SC	117.1	-	Type-I	4.4	-
L28C1S200	156.7	33.8	Type-II	4.6	0.2
L28C1S100	155.1	32.4	Type-III	4.7	0.3
L28C2SC	124.4	-	Type-I	4.5	-
L28C2S200	149.4	20.1	Type-III	4.7	0.2
L28C2S100	149.6	20.2	Type-III	4.7	0.2

3.6.3. Group 3 Beams

i. Beam L35C1SC

Beam L35C1SC furnished a deficient splice length of $35d_b$. Therefore, it was unable to undergo a ductile response. The maximum sustained load was 155 kN, followed by a sudden drop to half of its capacity, as shown in Figure 3.50(a). The beam lost half of its capacity as the cover surrounding one pair of splices delaminated, whereas the other pair remained intact. Nonetheless, having lost half of its capacity at this point, the beam was considered to have failed. Figure 3.50(b) shows the strain distribution along its splice length. At the peak load, a small portion of the lap splice at its loaded end yielded, but large inelastic strains could not be achieved. Figure 3.50(c) presents the corresponding bond stress distribution. As seen in Figure 3.50(b), the strain slope increased towards the loaded end. Therefore, higher bond stresses were generated towards the loaded end. Figure 3.50(d) shows the bond stress-slip relation. A stiff ascending branch was observed initially, followed by a spurious constant plateau. This is because the lap splice pair that remained intact after failure was the one with strain gages. Therefore, strain values did not drop significantly. Plotted in the same figure is a dotted line that could have been obtained had this splice pair did not remain intact. This is the drop that was observed in other control beams. Figure 3.51 presents visuals of this beam during and after the test. As shown in Figure 3.51(c), the front side of the beam did not show cover splitting, whereas the cover splitting shown in Figure 3.51(c) was observed on the back side of the beam. Nonetheless, cover splitting was sudden and abrupt, resulting in a sharp drop in the beam's capacity.
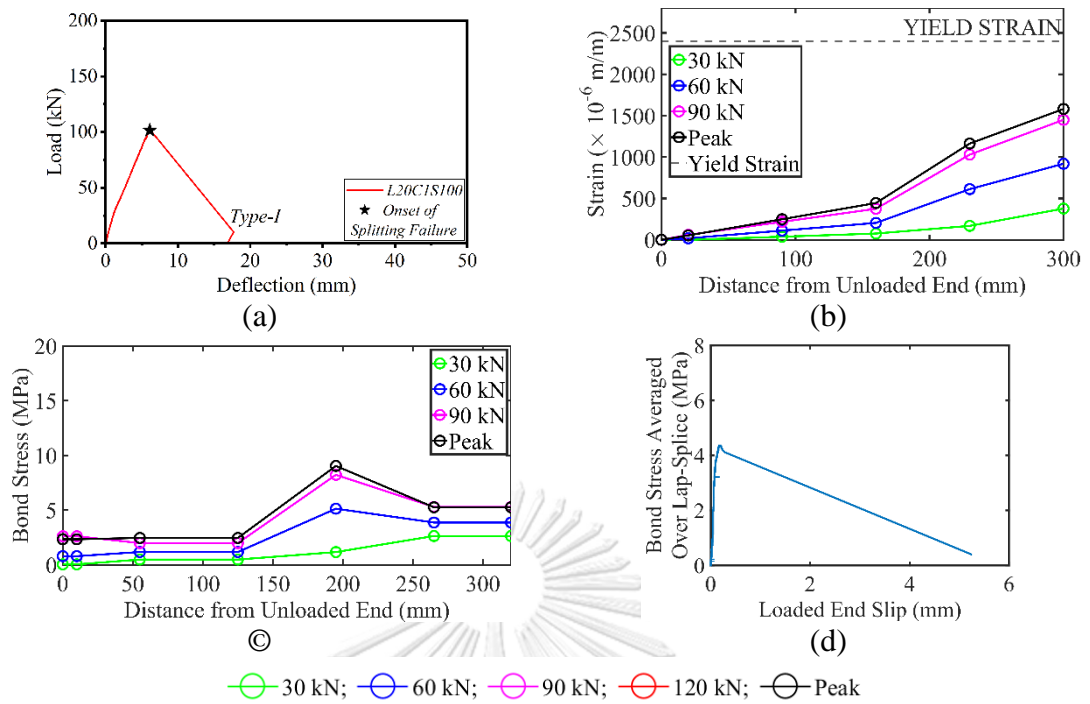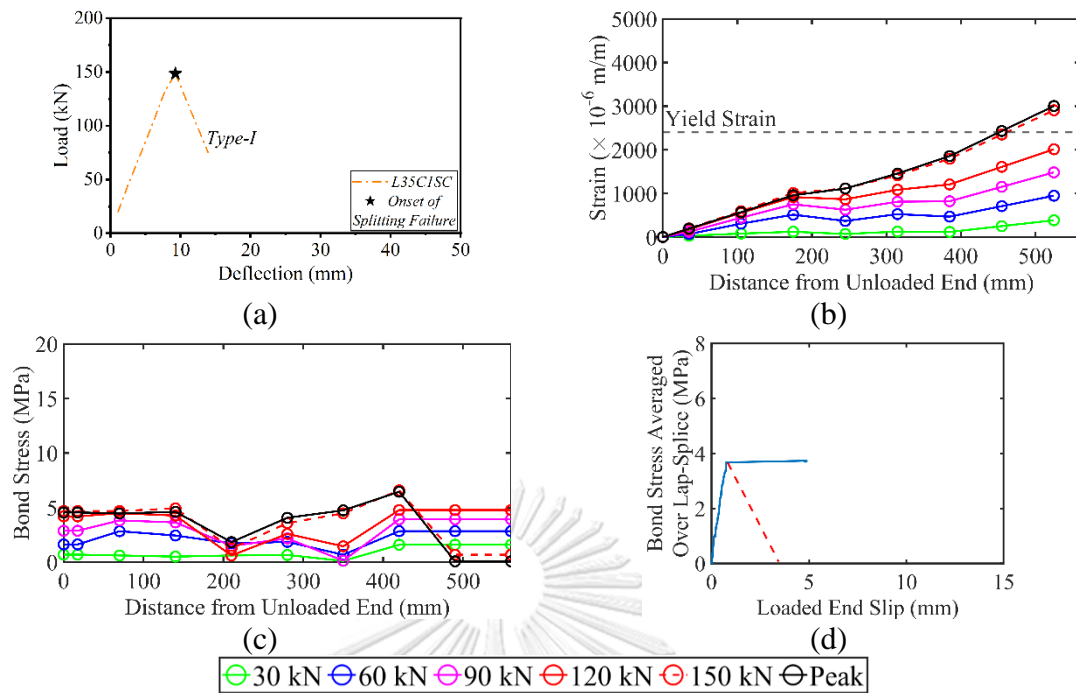
Figure 3.50 Experimental results for L35C1SC (a) load-deflection response, (b) strain distribution along splice, (c) bond stress distribution along splice, and (d) bond stress-slip relation.
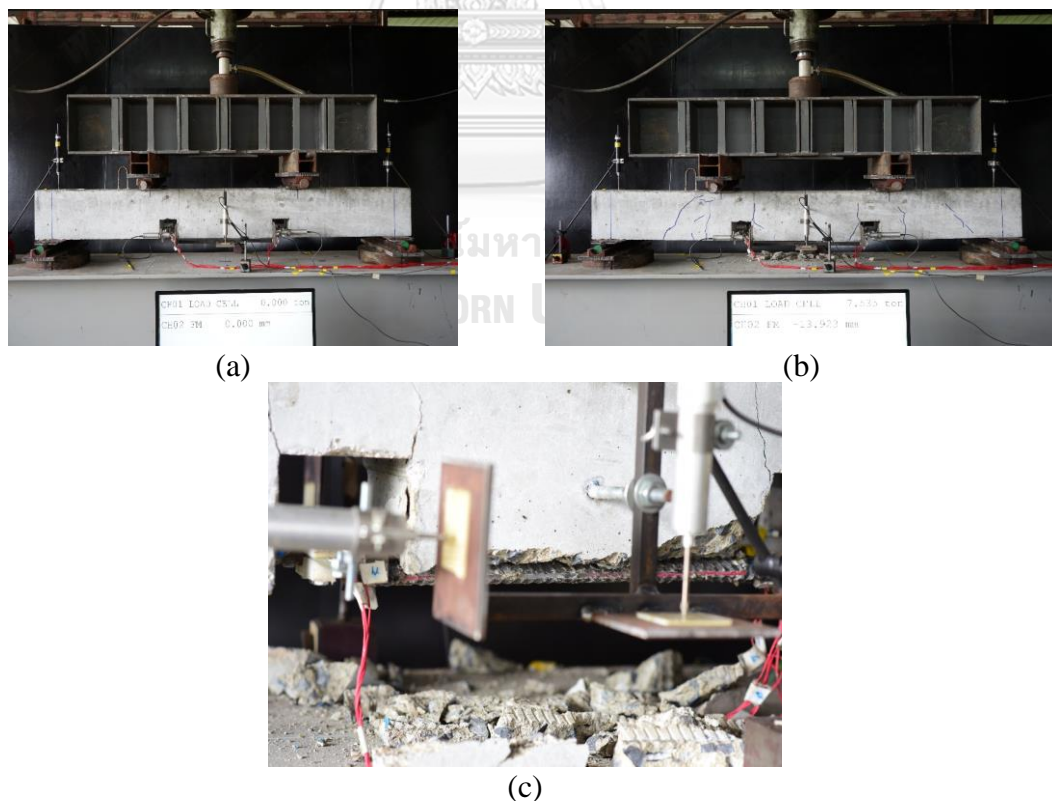
Figure 3.51 L35C1SC during test (a) start of test, (b) at failure, and (c) splitting failure with cover delamination.

ii.   Beam L35C1S200

Beam L35C1S200 was strengthened with HSS collars at 200 mm spacing. As shown in Figure 3.52(a), a sudden drop in the load was not observed, indicating splitting failure was suppressed. Rather, a fully ductile response of Type-III was observed till the stroke capacity of displacement transducers. The maximum sustained load was 155 kN. The strain distributions along the lap splice are shown in Figure 3.52(b). Towards the loaded end, bond stresses first dropped at 150 kN load ascribed to the circumferential contraction due to yielding. However, as the loading progressed, inelastic strains increased at the loaded end resulting in the recovery of bond stresses within the inelastic zone. This is reflected in Figure 3.52(c), where inelastic bond stresses at peak load are higher than those at 150 kN load. Since the beam did not undergo abrupt failure, the peak bond stress was maintained till large slip values, as shown in Figure 3.52(d). Figure 3.53(b) shows that the beam was able to undergo large inelastic deformations without compromising sustained load. Neither splitting failure was observed. Figure 3.53(c) shows bottom and face splitting cracks at the end of the lap splice. However, these cracks were restrained at their origin.
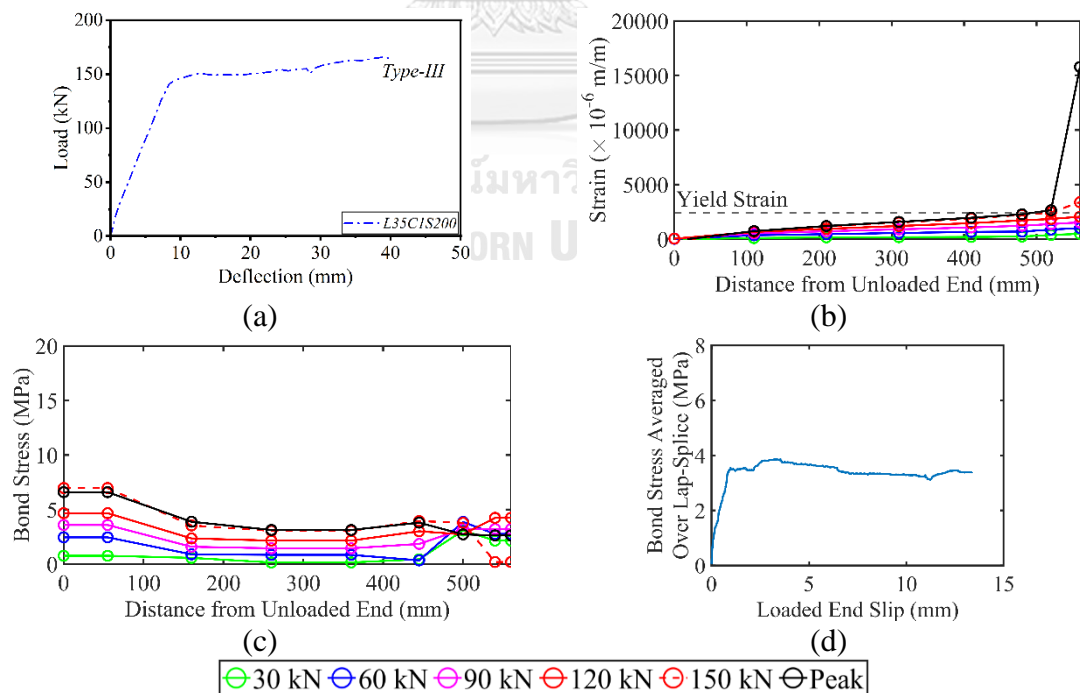
Figure 3.52 Experimental results for L35C1S200 (a) load-deflection response, (b) strain distribution along splice, (c) bond stress distribution along splice, and (d) bond stress-slip relation.

(a)　　　　　　　　　　　　(b)

(c)
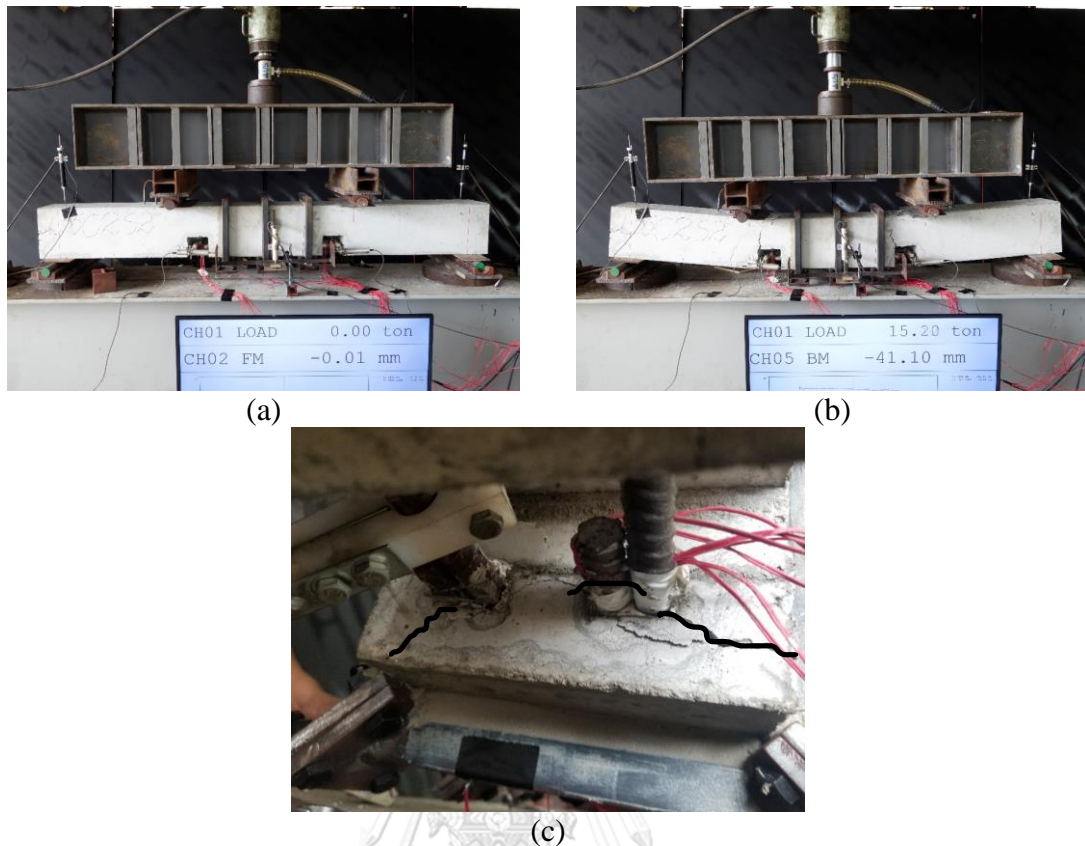
Figure 3.53 L35C1S200 during test (a) start of test, (b) at failure, and (c) splitting failure with cover delamination.

iii.　Beam L35C1S75

Beam L35C1S75 was strengthened with collars at 75 mm spacing. It contained a total of 8 collars along its splice length. Figure 3.54(a) shows that this beam demonstrated a ductile load-deflection response of Type-III. The maximum sustained load was 172 kN. The test was stopped at this point as one of the steel plates over the bottom roller supports slipped. Figure 3.54(b) shows that around 29% of the loaded end exhibited yielding. Figure 3.54(c) shows bond-stress distribution along the splice length. Bond stresses were roughly uniform towards the loaded end. Figure 3.54(d) shows that the maximum bond stress was 3.6 MPa. Figures 3.50a and 3.60b show visuals before and after the test, respectively. As shown in Figure 3.55(b), large deflections were sustained without significant damage within the splice zone. Figure 3.55(c) shows the onset of bottom and face splitting, but sufficient confining pressure would mean that these cracks could not propagate within the splice zone.
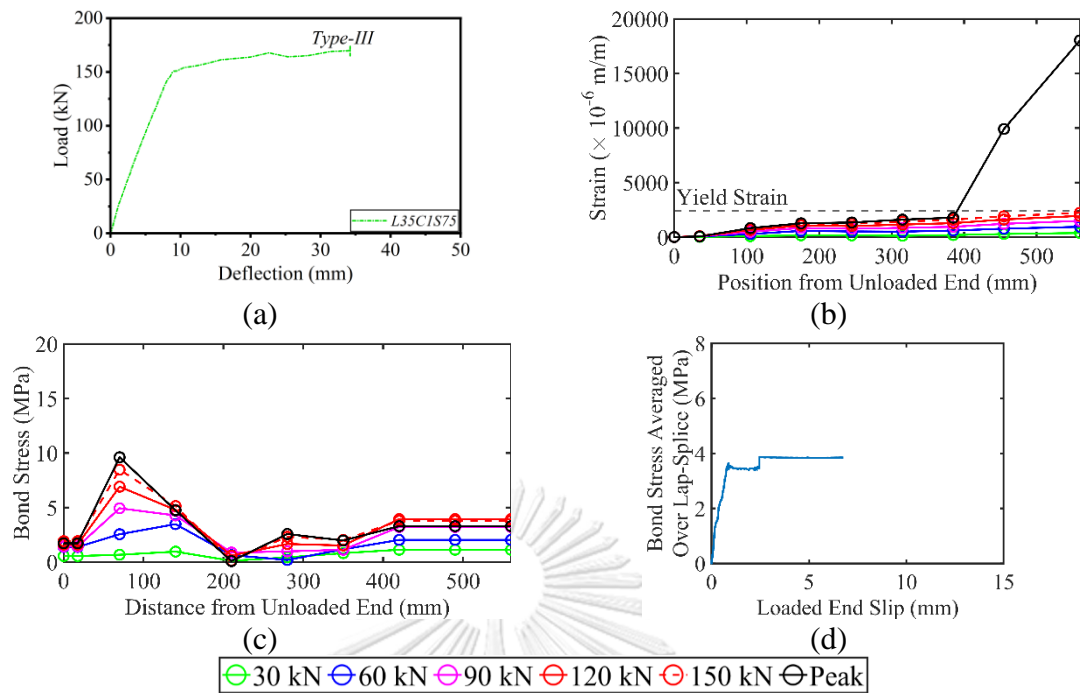
Figure 3.54 Experimental results for L35C1S75 (a) load-deflection response, (b) strain distribution along splice, (c) bond stress distribution along splice, and (d) bond stress-slip relation.
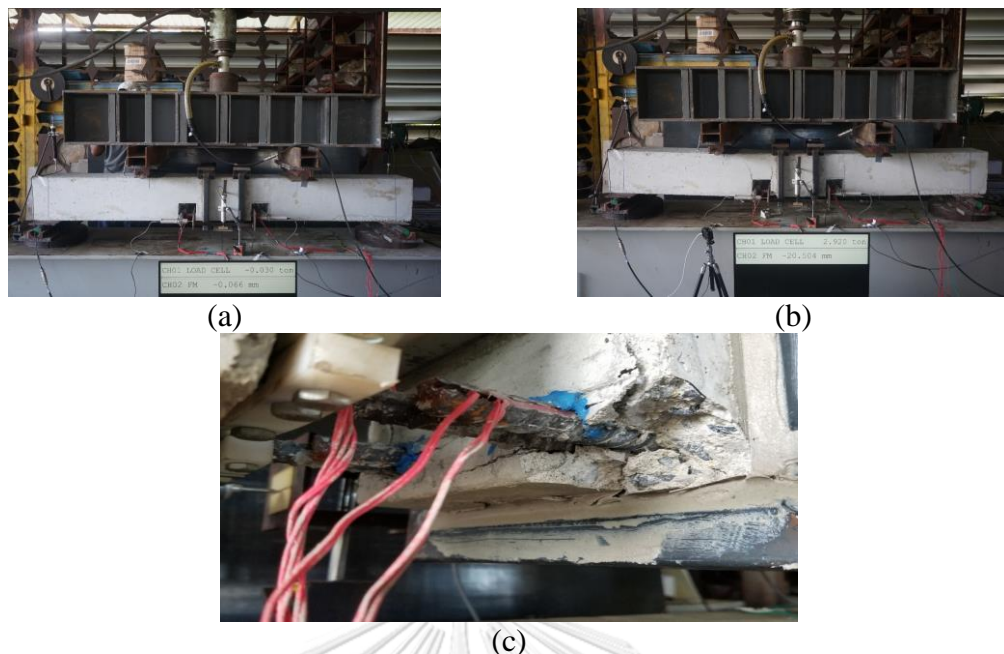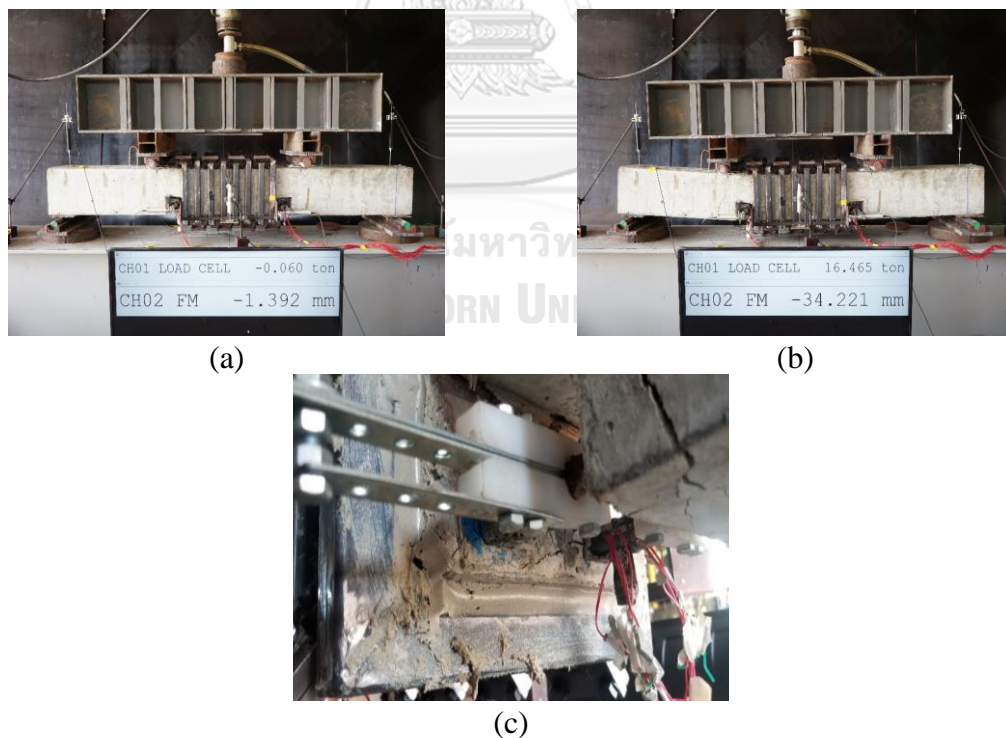

Figure 3.55 L35C1S75 during test (a) start of test, (b) at failure, and (c) splitting cracks at splice ends without cover delamination.

iv. Beam L35C2SC

Beam L35C2S0 was the control beam in subgroup L35C2. With a long lap splice length in addition to a large concrete cover, this beam was able to undergo some ductility. At this point, an abrupt drop in the sustained load occurred. Figure 3.56(b) shows that the maximum inelastic strain was 11000 microns and approximately 20% of the loaded end showed yielding. Figure 3.56(c) demonstrates that roughly uniform bond stress distribution was observed within the inelastic zone. Bond stress decreased substantially as the loaded end yielded at the peak load. The bond stress-slip relation is shown in Figure 3.56(d), comprising a stiff ascending branch followed by a slight drop that may be ascribed to the yielding. This relation is presented till a slip value of approximately 1.29 mm. Beyond this point, splitting failure occurred, and strain gage readings were not reliable. A dotted line is shown to complete this relation that agrees with the bond stress-slip response of other control beams. Figure 3.57 presents the visuals of this beam before and after the test. Figure 3.57(b) shows that the lap splice region of this beam collapsed at failure. Figure 3.57(c) shows the splitting along the splice.
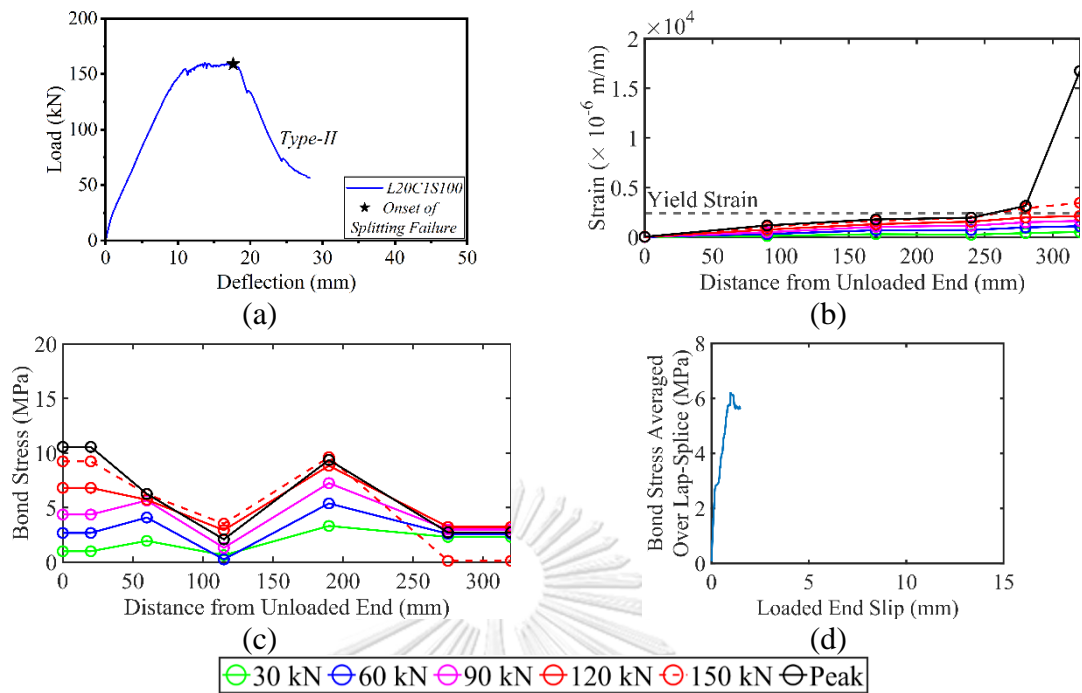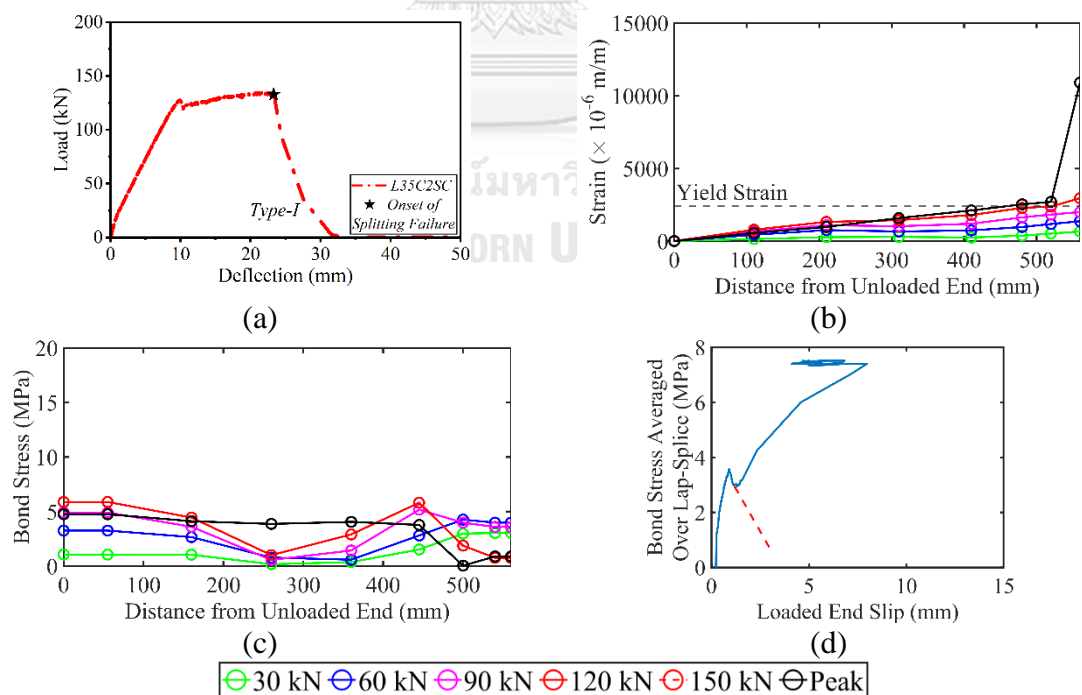

Figure 3.56 Experimental results for L35C2SC (a) load-deflection response, (b) strain distribution along splice, (c) bond stress distribution along splice, and (d) bond stress-slip relation.

(a)   (b)

(c)
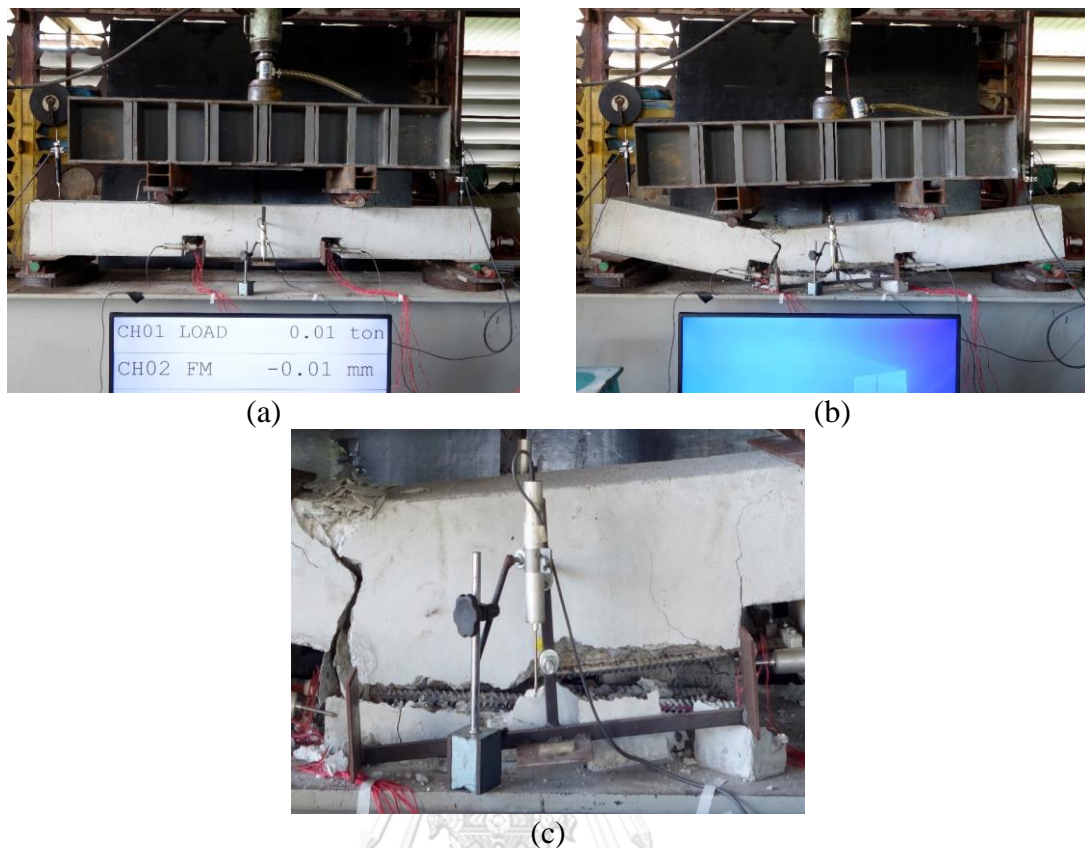
Figure 3.57 L35C2SC during test (a) start of test, (b) at failure, and (c) splitting failure with cover delamination.

v.   Beam L35C2S200

Beam L35C2S200 also demonstrated a typical response of that of a ductile beam (Type-III). The peak sustained load was 149 kN at the stroke limit of displacement transducers. High inelastic strains concentrated near the loaded end with roughly 27% of the splice length showed yielding. Bond stresses remained uniform within the elastic zone and degraded towards the loaded end due to yielding, as shown in Figure 3.58(c). Shown in Figure 3.58(d) is the bond stress-slip relation. Peak bond stress was 3.4 MPa which dropped due to yielding beyond this point. From there, bond stress remained constant as the loaded-end slip increased. Figure 3.59(b) shows that this beam sustained large deflections without being failed in splitting. This suggests that steel collars at 200 mm were sufficient for this beam to inhibit splitting failure. Bottom and face splitting cracks initiated at the splice end (see Figure 3.59(c)) but did not propagate along the splice length.
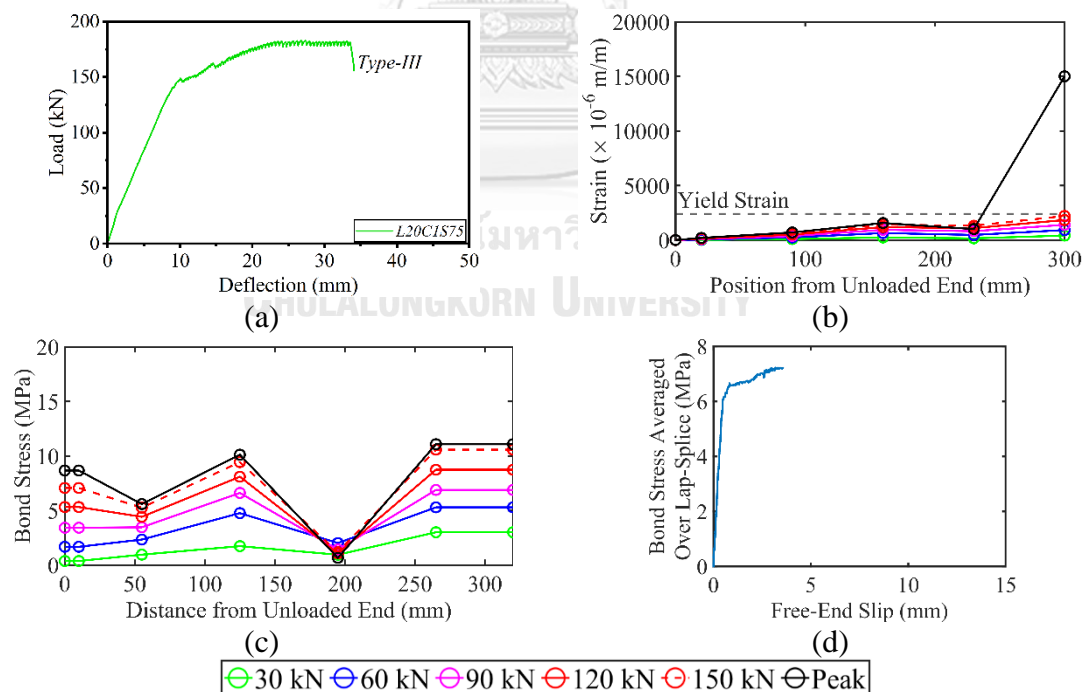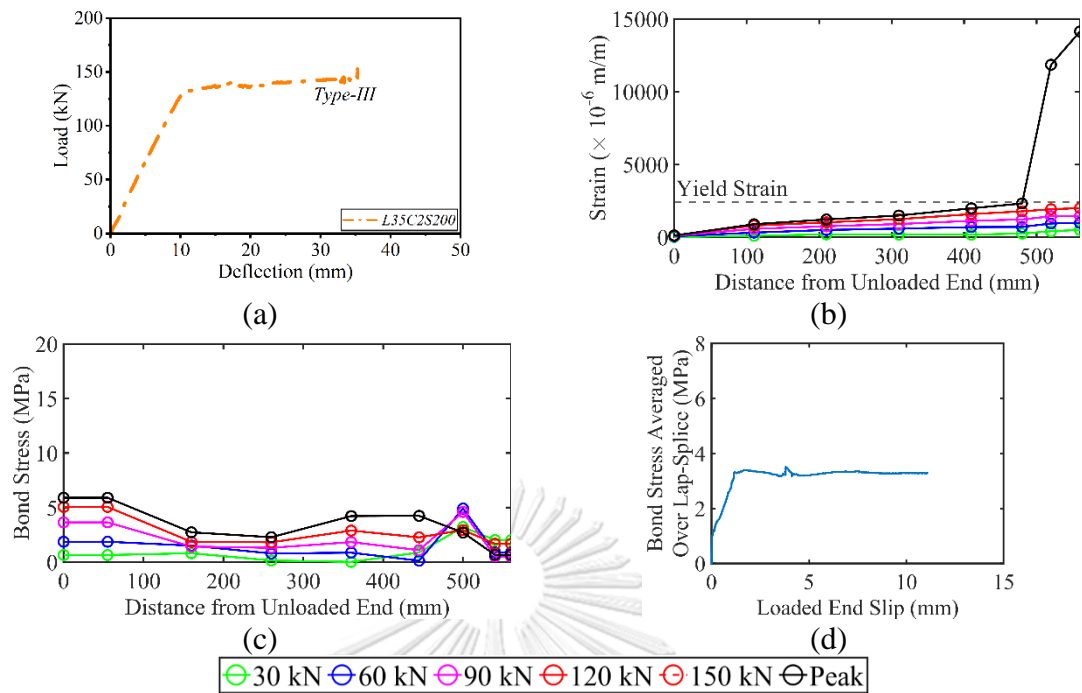
Figure 3.58 Experimental results for L35C2S200 (a) load-deflection response, (b) strain distribution along splice, (c) bond stress distribution along splice, and (d) bond stress-slip relation.
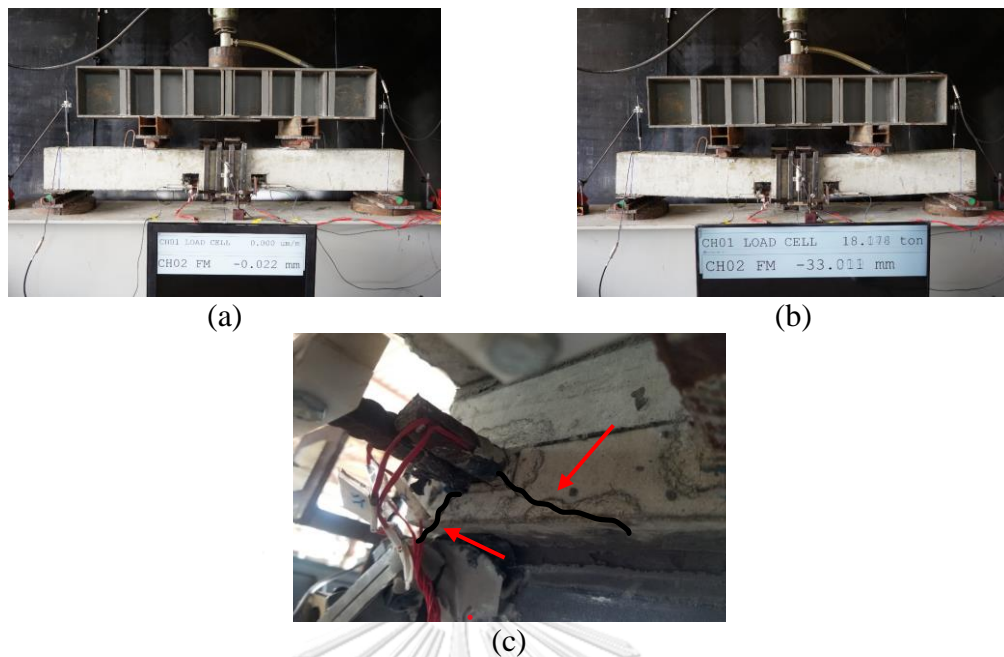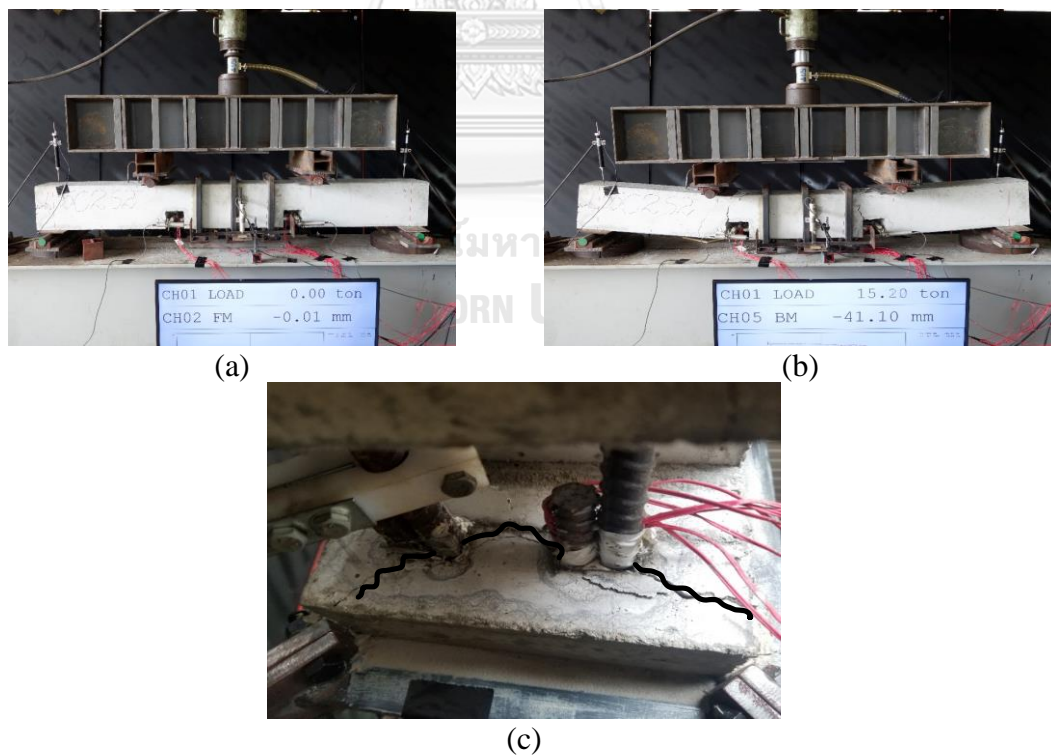

Figure 3.59 L35C2S200 during test (a) start of test, (b) at failure, and (c) splitting cracks at splice ends without cover delamination.

vi.   Beam L35C2S100

Beam L35C2S100 was strengthened by HSS collars at 100 mm spacing. This beam demonstrated a ductile response of Type-III, as shown in Figure 3.60(a). From the steel strain distributions along the splice in Figure 3.60(b), large inelastic strains were observed near the loaded end. It can be seen that roughly 28% of the splice length at the loaded end exhibited yielding. Bond stresses were uniform within the elastic zone, as shown in Figure 3.60(c). It is shown in Figure 3.60(b) that the slope of the inelastic branch of steel strains was small at a load of 150 kN. At the peak load, this slope increased substantially, causing bond stresses at that location to increase again. It must be mentioned that none of the strain gages at loaded ends of all ductile beams measured strains beyond 18000 microns. Due to this limit, inelastic bond stresses could not be measured accurately. Their magnitudes and distribution would have been different had the strains beyond this limit been recorded. The bond stress-slip response is shown in Figure 3.60(d). Like other beams, a stiff ascending branch followed a slight drop in peak bond stress (i.e., 3.5 MPa). Beyond this point, bond stress remained constant as the free-end slip increased.
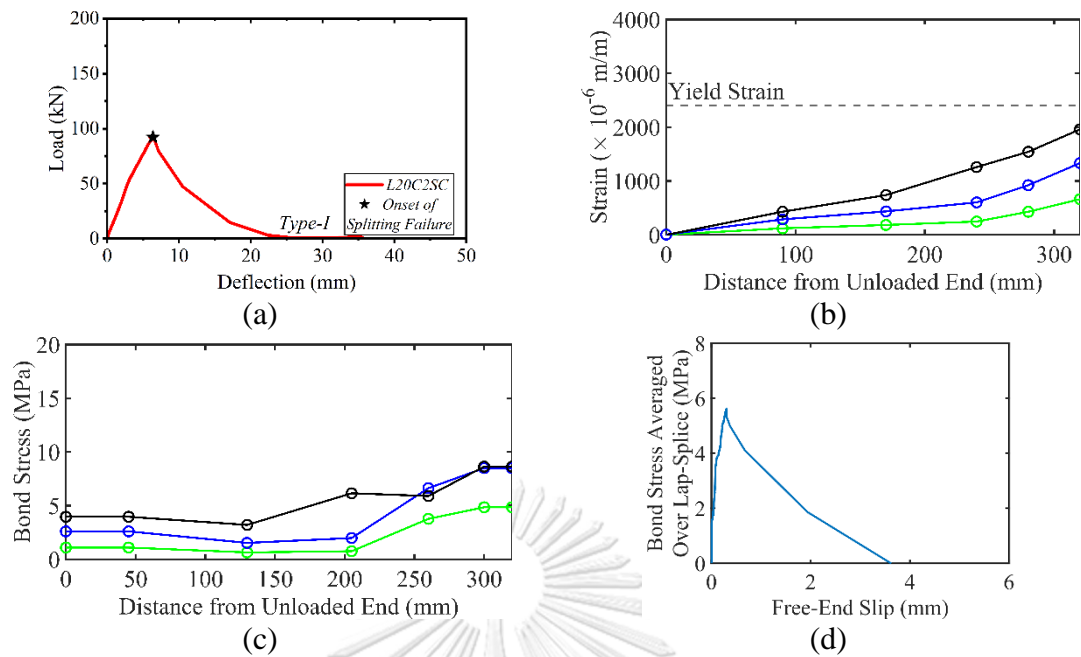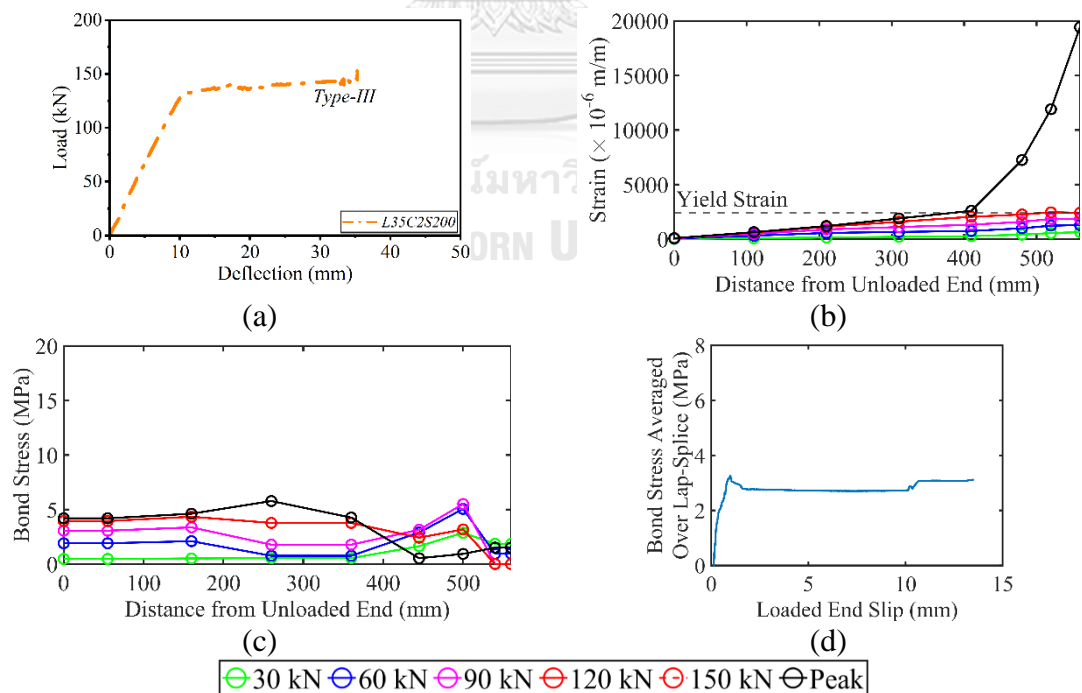
Figure 3.60 Experimental results for L35C2S100 (a) load-deflection response, (b) strain distribution along splice, (c) bond stress distribution along splice, and (d) bond stress-slip relation.

(a)

(b)

(c)

(d)
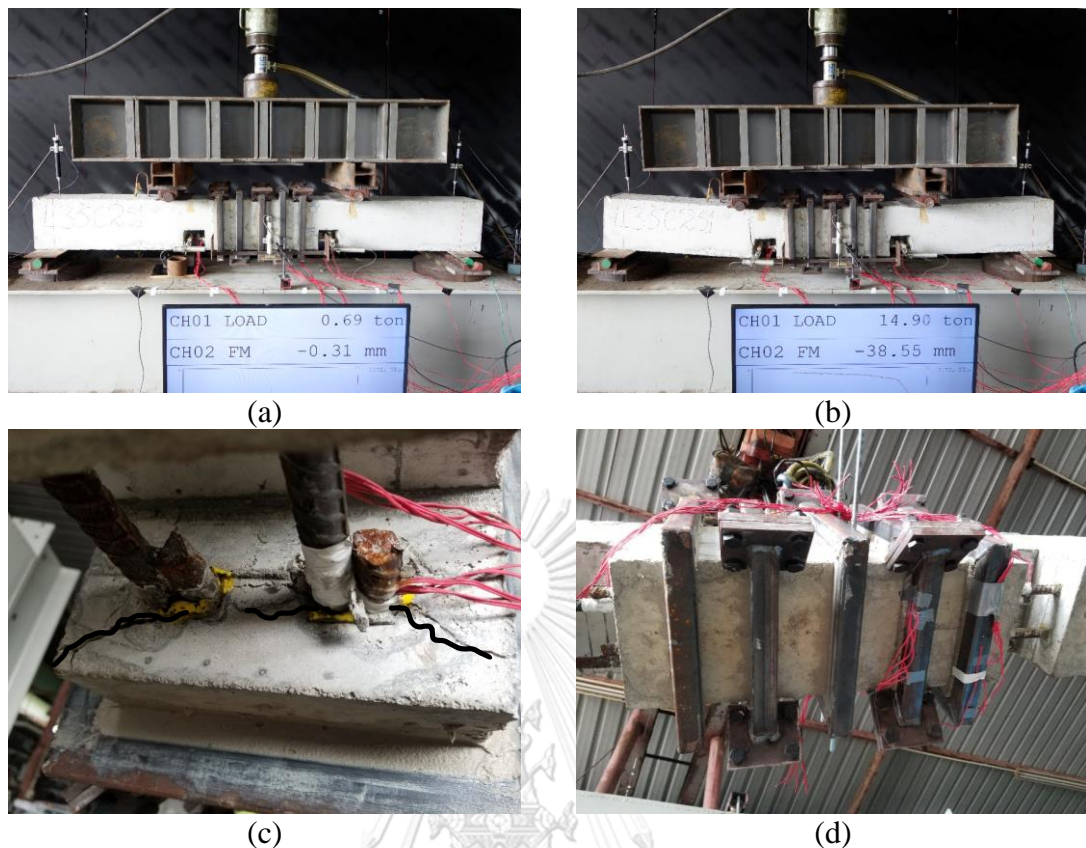
Figure 3.61 L35C2S100 during test (a) start of test, (b) at failure, (c) splitting cracks at splice ends, and (d) no propagation of splitting cracks along lap splice.

vii.   Comparison of Group 3 Results

Figure 3.62 presents the comparison between the load-deflection response of the beams tested in series L35. Both the control beams L35C1SC and L35C2SC experienced splitting. However, a larger concrete cover in the beam L35C2SC than that of the beam L35C1SC helped it achieve not only the higher peak load but also the corresponding deflection. All the strengthened beams exhibited ductile response (Type-III). This means that the application of HSS collars at 200 mm was sufficient to suppress splitting failure (Type-I) observed in the corresponding control beams. Further, HSS collars at 100 mm spacing were more than required to prevent splitting.

Failure modes of the beams in subgroup L35C1 are presented in Figure 3.63. It can be seen that the control beam L35C1SC failed in splitting, whereas the application of HSS collars both at 100 mm and 200 mm spacing suppressed splitting failure. Further, as shown in Figure 3.63(c & d), splitting cracks that appeared at lap

splice ends were successfully restrained from traveling along the splice length, thus keeping the cover intact and imparting high ductility.

(a)   (b)
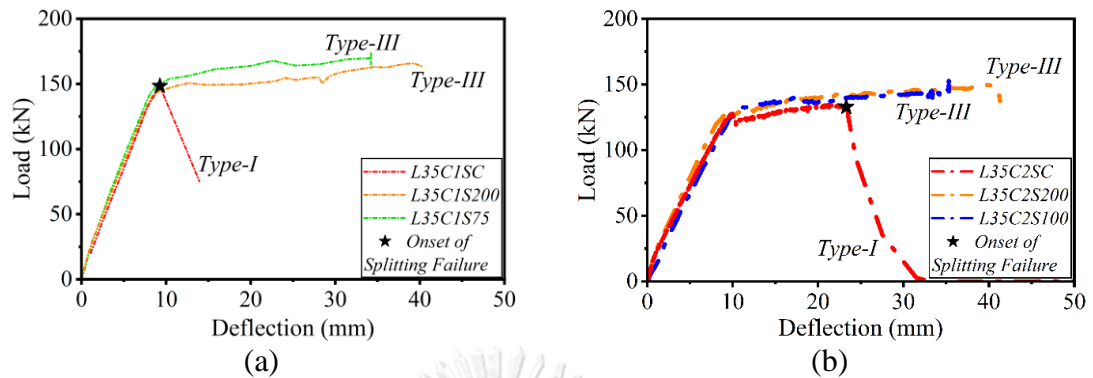
Figure 3.62 Comparison of load-deflection response of Group 3 beams (a) Subgroup C1 and (b) Subgroup C2.

(a)   (b)

(c)   (d)
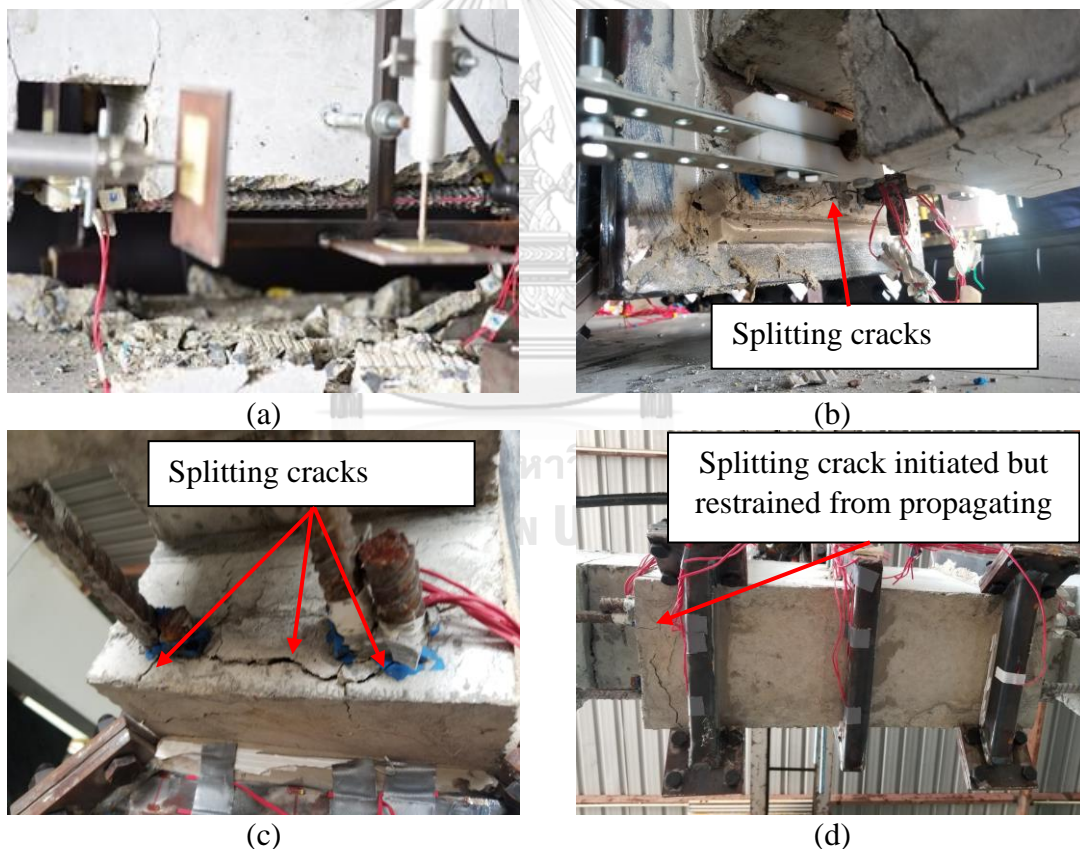
Figure 3.63 Comparison of failure modes of series L35C1 (a) L35C1SC (b) L35C1S75 (c & d) L35C1S200.

Failure modes of beams in Subgroup L35C2 are shown in Figure 3.64. Failure modes observed in this category were similar to those of the beams in Subgroup L35C1. Control beam L35C2SC failed in brittle splitting (Type-I) (Figure 3.64(a)).

Both the strengthened beams allowed the initiation of splitting cracks at splice ends, but those cracks were restrained from traveling along the splice length.
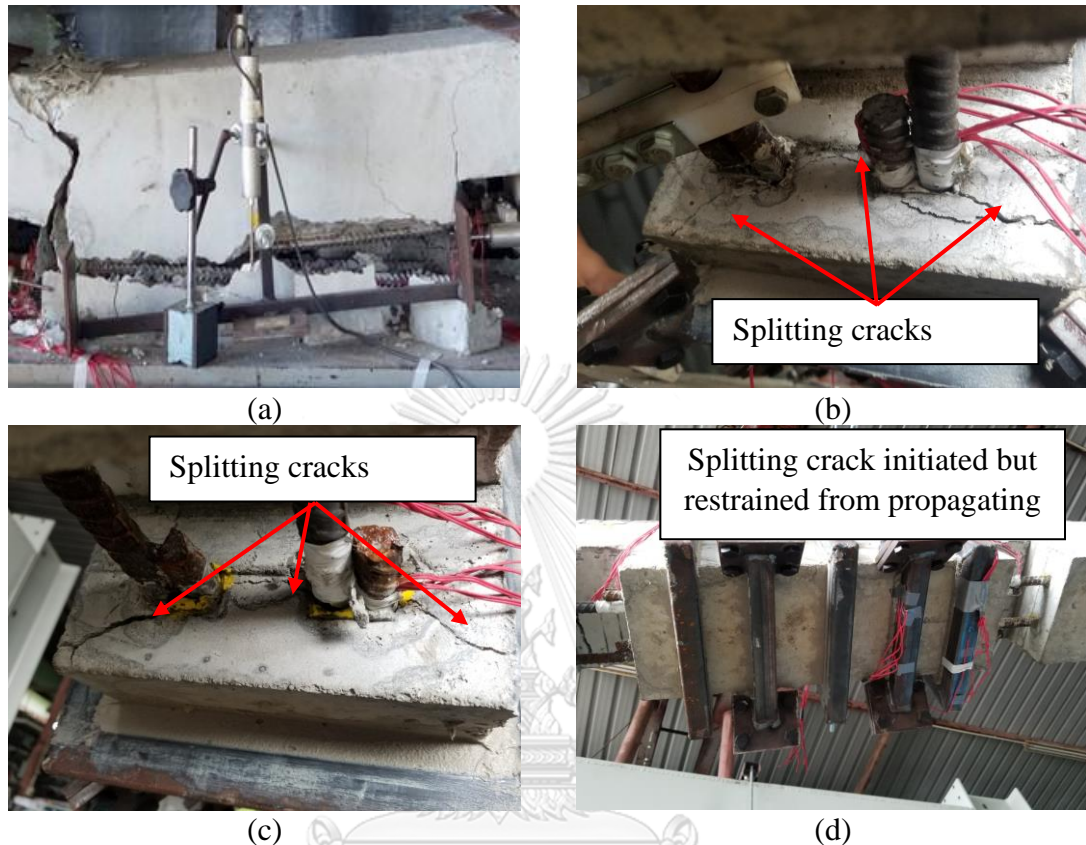
Figure 3.64 Comparison of failure modes of series L35C2 (a) L35C2SC (b) L35C2S200 (c & d) L35C2S100.

A summary of experimental results of series L35 beams is provided in Table 3.7, including average bond stress along the lap splice and increase in bond stress as a result of HSS collar confinement. It is evident that though the behavior of the beams was changed from Type-I to Type-III due to the confinement by HSS collars, no increase in the bond strength was observed.

Table 3.7 Summary of peak loads and bond strengths of Group 3 beams.

Beam ID	Peak Load (kN)	Increase in Peak Load (%)	Mode of Failure	τ (MPa)	$\Delta\tau$ (MPa)
L35C1SC	155.1	-	Type-I	3.7	-
L35C1S200	167.0	7.7	Type-III	3.5	-0.2
L35C1S100	172.1	11.0	Type-III	3.6	-0.1
L35C2SC	134.4	-	Type-I	3.6	-
L35C2S200	149.5	11.2	Type-III	3.4	-0.2
L35C2S100	150.6	12.1	Type-III	3.5	-0.1

3.6.4. Comparison of Experimental Results of All Beams

i.   Comparison of Control Beams

Figure 3.65 presents a comparison of load-deflection curves of control beams tested in this study. It is mentioned that these curves are generated by normalizing load at each deflection, corresponding to the concrete strength of 27.4 MPa. As expected, the lowest peak load was sustained by beams with the shortest lap splice, i.e., L20C1SC and L20C2SC. Following that, the weakest beam was expected to be the Beam L28C1SC. As can be seen in Figure 3.65, Beam L28C1SC demonstrated a higher peak load than those in series L20 but the lowest among the remaining beams. Beam L28C2SC reached the yield point where softening was expected to occur (as for beam L35C2SC). Both the beams L28C2SC and L35C1SC failed at this point. The only control beam exhibiting small ductility was L35C2SC, i.e., furnishing the longest splice length in conjunction with the larger cover between 16 mm and 26 mm. All the control beams exhibited Type-I failure irrespective of the concrete cover and lap splice length.
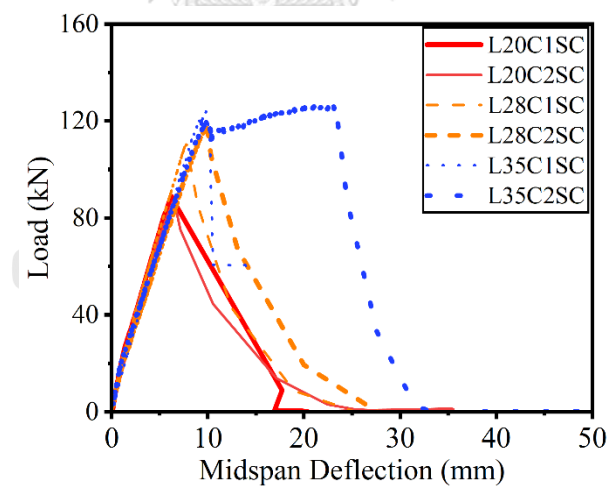
Figure 3.65 Comparison of load-deflection curves of control beams.

Figure 3.66 presents strain distribution along the lap splice of control beams. Vertical lines are plotted to differentiate the regions of all groups. Further, the dotted lines are plotted for 26 mm cover beams, whereas solid lines represent beams with 16 mm cover. There is a consistent trend observed. All solid lines exhibited lower values

than their corresponding dotted lines highlighting the importance of larger concrete covers. It can be seen that the maximum lap splice strain in the control beams of subgroups L20C1, L20C2, and L28C1 was lower than the yield strain. The lap splice strain at the loaded end of control beams in subgroups L28C2 and L35C1 was slightly higher than the yield strain. The control beam in Subgroup L35C2 exhibited large inelastic strains at the loaded ends of the lap splice. This observation is important as it directly affects the improvement in the bond strength due to external confinement, as will be discussed later. Nonetheless, the improvement in the maximum lap splice strain with increasing cover and lap splice length is evident. In general, higher lap splice strains are observed for larger concrete covers with the same lap splice length. Similarly, higher lap splice strains are observed for longer lap splices with the same concrete covers.
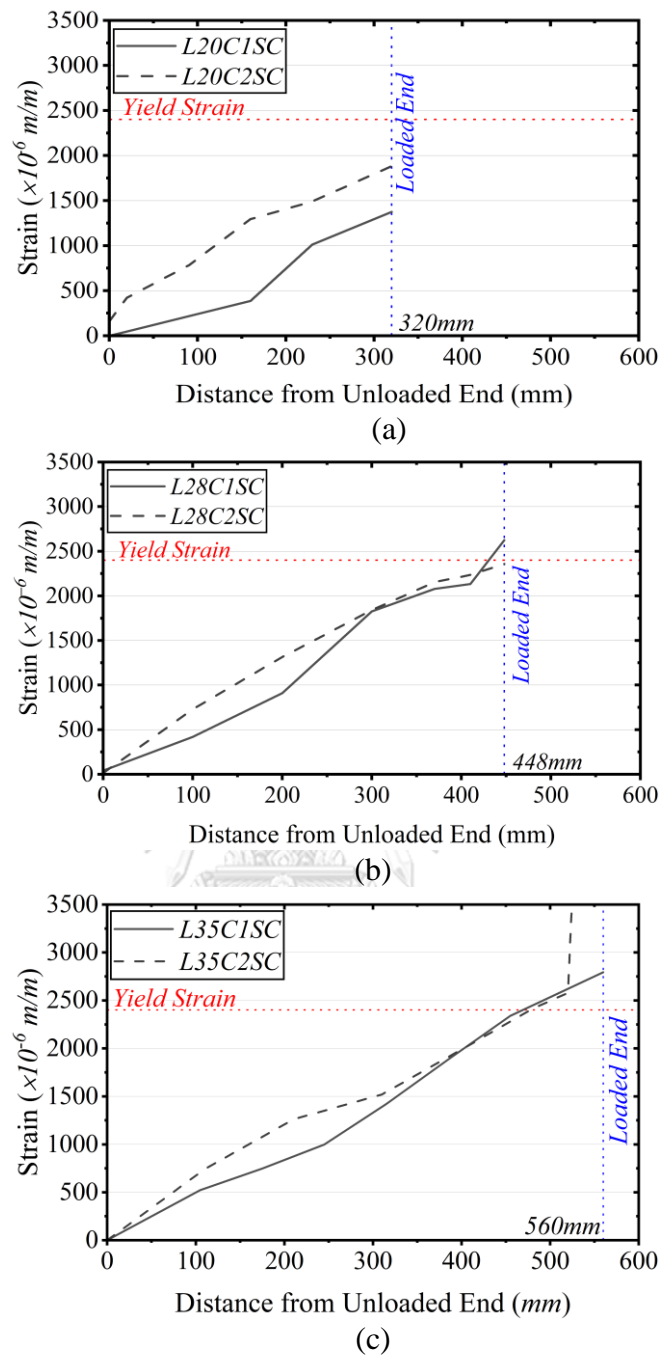
Figure 3.66 Comparison of strain distribution along lap splices in the control beams of (a) Group 1, (b) Group 2, and (c) Group 3.

ii.   Comparison of Beams Strengthened with HSS Collars at 100 mm

A comparison of load-deflection curves of beams strengthened with HSS collars at 75 mm and 100 mm spacing is presented in Figure 3.67. All beams demonstrated the ductile load-deflection response of Type-III except Beam

L20C1S100. For the L20C1 series, the ductile response was provided by the beam L20C1S75. This explains that for Subgroup L20C1, the demand for external confining pressure was highest. This was expected as it furnished the shortest lap splice length, i.e., $20d_b$ and smallest concrete cover, i.e., 16 mm. It must be mentioned that load-deflection curves in Figure 3.72 are normalized, corresponding to common concrete strength of 27.4 MPa. Variation in peak strengths may be ascribed to the method of normalizing concrete strength.
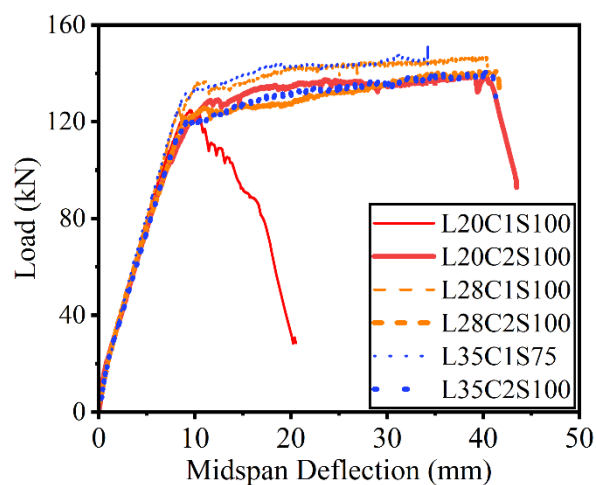
Figure 3.67 Comparison of load-deflection curves of beams strengthened with HSS collars spaced at 100 mm.

iii. Comparison of Beams Strengthened with HSS Collars at 200 mm

A comparison of load-deflection curves of beams strengthened with HSS collars at 200mm spacing is presented in Figure 3.68. Beams L20C1S200, L20C2S200, and L28C1S200 were not able to prevent splitting failures suggesting the requirement of a closer spacing of HSS collars than provided was required. Beams L28C2S200, L35C1S200, and L35C2S200 demonstrated ductile response and suppressed splitting failure. This suggests that there are two parameters affecting the demand for external confining pressure. One of them is the concrete cover: this is because beams L28C1S200 and L28C2S200 furnished 16 mm and 26 mm controlling concrete covers, respectively. Apart from that, all other structural details were similar. Still, Beam L28C1S200 could not achieve a full ductile response due to its lower concrete cover. Another parameter is lap splice length: beams L28C1S200 and

L35C1S200 were fabricated with similar details except for the length of the lap splice. Consequently, Beam L35C1S200 demonstrated a ductile response suggesting that external confinement of HSS collars spaced at 200 mm was sufficient to suppress splitting failure, whereas similar confinement was found insufficient for Beam L28C1S200.
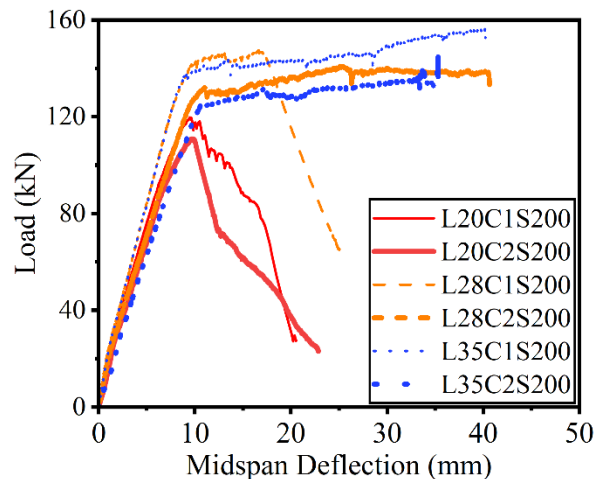
Figure 3.68 Comparison of load-deflection curves of beams strengthened with HSS collars spaced at 200 mm.

3.7. Increase in Bond Strength by HSS Collars Confinement

It has been well known that the application of external confinement on substandard lap splices improves the bond between lap spliced bars and surrounding concrete. Several researchers have carried out experimental works to strengthen lap splices by confining them with FRP wraps. For example, Harajli et al. [51] performed experiments on lap splice beam specimens. A lap splice of $5d_b$ was provided in the constant moment region. The lap splice region was strengthened using steel fibers or CFRP sheets. In general, the bond strength was improvement by increasing the fiber content or the number of CFRP sheets irrespective of the size of concrete cover. Bournas and Triantafillou [66] tested cantilever RC columns with lap splice of $20d_b$ and $40d_b$. The lap spliced regions were strengthened using either CFRP sheets or textile reinforced mortar (TRM) jackets. It was observed that the application of CFRP or TRM jackets on columns with $20d_b$ lap splice increased the bond strength considerably. On the contrary, no improvement in the bond strength in columns with

$40d_b$ lap splice was observed as shown in Figure 3.69. Garcia et al. [52] tested lap spliced RC beams with lap splice of $25d_b$. The effect of varying CFRP sheets on the bond strength of lap spliced bars was investigated. The bond strength of lap spliced bars was found to increase as the number of CFRP sheets increased, irrespective of the size of the controlling concrete cover.
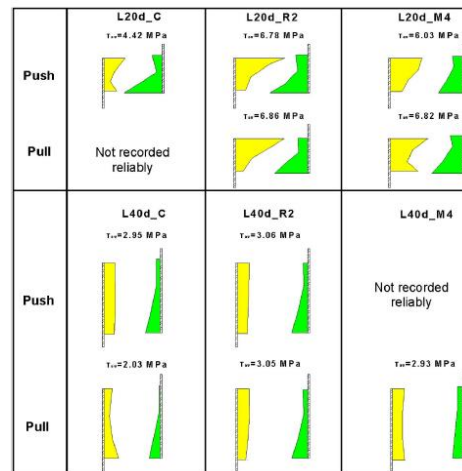
Figure 3.69 Measured bond strength along the lap splice of RC columns tested by Bournas and Triantafillou [66].

These observations on the improvement of bond strength indicate that it is dependent on the length of the lap splice mainly. The present study used three lap splice lengths of $20d_b$, $28d_b$, and $35d_b$. Figure 3.70 shows the increase in bond strength of normalized bond strengths with respect to concrete strength of 27.4 MPa $\Delta\tau^*$ as a function of the confinement ratio of HSS collars ρ which is defined as

$$\rho = \frac{2A_{sc}}{sb} \qquad 3.6$$

where A_{sc} is the cross-sectional area of HSS collars, s is the center-to-center spacing of HSS collars, and b is the width of the section experiencing bending. It can be seen that a substantial improvement in the bond strength was observed for Subgroup L20C1. The improvement in the bond strength in subgroups L20C2, L28C1, and L28C2 was lower than the improvement in Subgroup L20C1. Finally, no improvement in the bond strength was observed for Group 3 specimens.
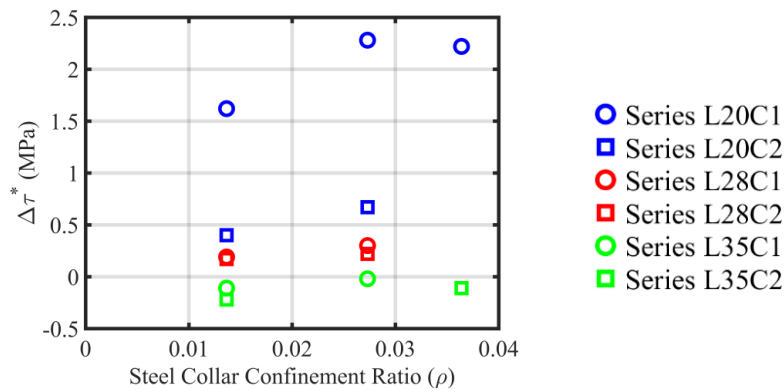
Figure 3.70 Effect of confinement ratio of HSS collars on the increase in the normalized bond strength.

3.8. Summary

This chapter summarizes the efficiency of HSS collars in preventing brittle splitting failures associated with substandard lap splices. A total of nineteen beams were tested: seven beams in Group 1 with a lap splice length of $20d_b$, six beams in Group 2 with a lap splice length of $28d_b$, and six beams in Group 3 with a lap splice length of $35d_b$. Further, three beams in each group were constructed with a controlling cover of 26 mm, whereas the controlling cover in the remaining beams was 16 mm. For beams in each group with a common concrete cover, HSS collars of size 32 mm $\times$ 32 mm $\times$ 2.3 mm were provided at a center-to-center spacing of 100 mm and 200 mm. An additional beam in Group 1 with a controlling cover of 16 mm was strengthened by HSS collars at a spacing of 75 mm. It was found that for beams in Group 1 and a controlling cover of 16 mm, HSS collars at 75 mm were needed to prevent splitting failure and achieve a ductile response. In the same group with a 26 mm controlling cover, HSS collars at 100 mm spacing were sufficient to prevent splitting failure. In Group 2, HSS collars at 100 mm and 200 mm spacing were required to prevent splitting failure in beams with 16 mm and 26 mm controlling cover, respectively. Finally, HSS collars with 200 mm spacing were required to prevent splitting failure in Group 3 beams. It was observed that a closer spacing of HSS collars was required as the concrete cover and lap splice decreased. The bond stress distribution along the lap splice indicated a substantial drop near the loaded ends of lap splices due to yielding. For beams sufficiently confined with HSS collars, the bond stress-slip response included a stiff ascending branch till the peak bond

stress (bond strength), followed by a stable bond stress-slip branch. Finally, it was observed that the increase in the bond strength was predominant in beams with a $20d_b$ lap splice. As the concrete cover and lap splice length increased, the increase in the bond strength reduced. No increase in the bond strength was observed for beams with a $35d_b$ lap splice.

Chapter 4 Development of Design Equation for HSS Collar Confinement on Substandard Lap splices

One of the main objectives of the present study was to propose an equation for the design of HSS collars to strengthen substandard lap splices. The adopted experimental framework in Chapter 3 was designed in a way to achieve this objective. Detailed strain measurements along the lap splices were carried out with the aim of estimating the bond strengths of the lap splices in unstrengthened and strengthened conditions. Some previous studies have demonstrated that the bond strength can be used as an indicator for the improvement in the behavior of substandard lap splices after strengthening. Based on this, design equations for external confinement were proposed. The following section highlights some of the previous works on this issue.

4.1. Existing Studies on the Design of External Confinement Based on Bond Strength

Harajli [63] utilized the equation by Harajli et al. [51] for the increase in the bond strength due to CFRP confinement as

$$\frac{U_{CFRP}}{\sqrt{f_c'}} = \frac{2E_f n_f t_f}{8000 n_s d_b} \leq 0.40 \qquad 4.1$$

where E_f is the elastic modulus of CFRP, n_f is the number of CFRP sheets, t_f is the thickness of a single CFRP sheet, n_s is the number of lap spliced pairs in tension, and d_b is the diameter of the lap spliced bar. Harajli [63] combined Eq. 4.1 linearly with the equation of Orangun et al. [116] for the bond strength in unstrengthened concrete, which is given as

$$\frac{U_P}{\sqrt{f_c'}} = 0.1 + 0.25 \left(\frac{c}{d_b} \right) + 4.15 \left(\frac{d_b}{l_s} \right) \qquad 4.2$$

where c is the controlling concrete cover and l_s is the length of the lap splice. Harajli [63] proposed the following equation for the design of a CFRP sheet to strengthen a given substandard lap splice of length l_s.

$$n_f t_f = \frac{1000 n_s d_b}{E_f \left(\frac{l_s}{d_b}\right)} \left[\left(\frac{f_s}{\sqrt{f_c'}} - 16.6\right) - \frac{l_s}{d_b}\left(\frac{c}{d_b} + 0.4\right) \right] \qquad 4.3$$

Harajli [63] proposed to use a value of $1.25 f_y$ as the minimum development stress f_s in Eq. 4.3. A detailed experimental program was carried out to strengthen lap splices in circular and rectangular columns. It was found that the predictions of the proposed Eq. 4.3 were in good agreement with the number of CFRP sheets used in experiments.

Later, Elsouri and Harajli [119] extended this concept. However, instead of using the equation by Orangun et al. [116] to estimate the bond strength in unstrengthened concrete, several other equations available in the literature were compared. The authors recommended using $f_s = 1.25 f_y$ when the actual yield strength of lap spliced bars is known and $f_s = 1.85 f_y$ in the absence of such information. Among the various models of bond strength in unstrengthened concrete, the authors recommended using the model by Darwin et al. [120] with the resulting equation for CFRP design given as

$$\left(f_c'^{\frac{1}{4}} \frac{12 t_d A_{tr}}{s_t n_s d_b} + \frac{E_f n_f t_f}{1000 n_s d_b} \right) = \frac{f_s}{\sqrt{f_c'}} \frac{d_b}{l_s} - \frac{1.84\, c_m/d_b + 56.4\, d_b/l_s + 0.92}{f_c'^{\frac{1}{4}}} \qquad 4.4$$

Garcia et al. [52] proposed the following equation to predict the increase in the bond strength of substandard lap splices due to the confinement by CFRP sheets.

$$\Delta \tau^* = 1.15 \sqrt{f_o} \leq 0.40 \qquad 4.5$$

$$f_o = \frac{n_f t_f \epsilon_{f,o} E_f}{n_b (c_{min} + d_b)} \qquad 4.6$$

where $\epsilon_{f,o}$ is the splitting tensile strain of concrete. Garcia et al. [52] proposed the following steps to estimate the quantity of CFRP confinement for substandard lap splices.

a. Estimate the bond stress corresponding to the onset of yielding at the loaded end.

b. Estimate the bond strength in unstrengthened concrete by using any models in the literature.

c. Take the difference between the first two steps to estimate the increase in the bond strength that is required to develop yielding.

    d.   Equate the value obtained in step "c" to Eq. 4.5 to estimate the required CFRP confinement.

4.2. Limitations of Bond Strength

The previous section explains the design approach of external confinement for substandard lap splices. The bond strength-based approach utilizes an existing equation that predicts the bond strength enhancement due to external confinement. However, it was observed in Chapter 3 that some beams exhibited yielding in unstrengthened conditions. For instance, see the results of Beams L28C2SC, L35C1SC, and L35C2SC. Despite achieving yield at the loaded ends of lap splices, these beams suffered Type-I brittle splitting failure. Further, the bond strength-based design cannot be applied to these beams. This is because the bond strength corresponding to the lap splice yielding is already achieved in unstrengthened conditions. Therefore, no further increase in the bond strength can be expected after strengthening. This was proved by the experimental bond strength results of Beams L28C2SC, L35C1SC, and L35C2SC, as no improvement in the bond strength was observed after confinement by HSS collars. However, this does not mean that HSS collars did not influence the behavior of these beams. It was observed that the Type-I failure was changed to Type-III ductile failure without increasing the bond strength values. As previously noted, the bond stress averaged over the lap splice tends to stabilize after yielding occurs at the loaded end. This observation is important because it imposes an upper limit on the bond strength [63, 117]. The bond strength that can be mobilized at the onset of yielding, τ_y, is defined as

$$\tau_y = \frac{f_y d_b}{4l_s} \qquad\qquad 4.7$$

where f_y is the yield strength of the bar, d_b is the diameter of the bar, and l_s is the lap splice length. Table 4.1 presents experimental bond strengths of lap spliced specimens in the literature that experienced yielding of lap spliced bars. The experimental bond strengths were compared to analytical bond strengths calculated using Eq. 4.7. Figure 4.1 shows the experimental and analytical bond strengths mobilized in lap splices. A good correlation indicates that the upper limit of the bond strength within a lap splice corresponds to the onset of yielding. This implies that for lap splices that mobilize

yielding near their loaded ends, the upper limit on the bond strength corresponds to Eq. 4.7. Therefore, no further increase in the bond strength is expected due to external confinement for lap splices that can develop yielding. For instance, the lap splices in the control beams of Subgroups L35C1 and L35C2 exhibited yielding. As a result, the upper limit on the bond strength corresponding to the onset of yielding τ_y was achieved. Therefore, the strengthened beams in Subgroups L35C1 and L35C2 did not exhibit the increase in the bond strength.

Table 4.1 Strengthened specimens with lap splices exhibiting yielding.

Reference	Specimen Name	f_y (MPa)	d_b (mm)	l_s/d_b	Bond Strength from Experiments, τ (MPa)	τ_y (MPa)
Turk et al. [121]	B.SCC.16	503	16	19.34	6.4	6.5
Bournas and	L20d_R2				6.8	6.5
Triantafillou [66]	L20D_M4	523	14	20	6.4	6.5
	L40d_R2			40	3.2	3.3
	L40d_M4				2.9	3.3
Helal [122]	LC20-D12-PTMS2	530	12	25	5.3	5.3
	LC10F1				5.2	5.5
Garcia et al. [52]	LC10F2				5.5	5.5
	LC20F1	551	12	25	4.9	5.5
	LC20F2				5.2	5.5
	LC27F1		16		4.8	5.5
	LC27F2				5.2	5.5

Note: f_y =yield strength of lap spliced bars; d_b =steel bar diameter; l_s = lap splice length; τ = bond strength from experiments; and τ_y = bond strength corresponding to the onset of yielding calculated using Eq. (4.7).
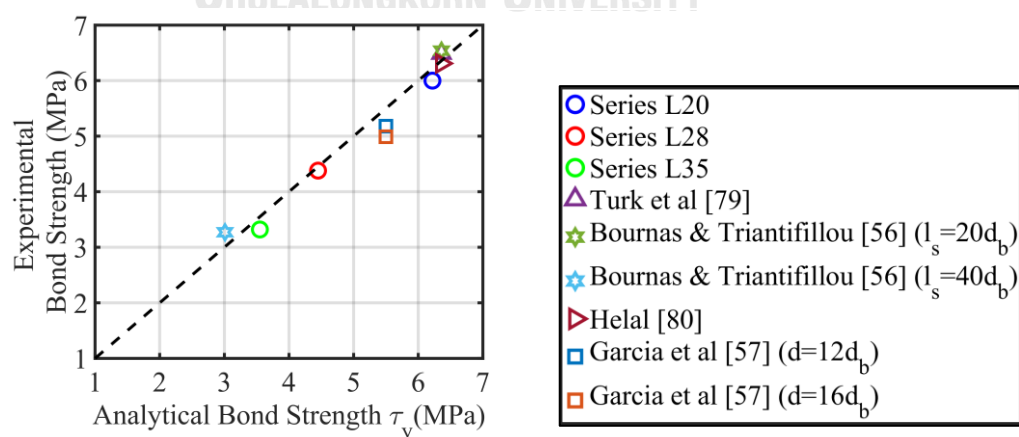
Figure 4.1 Comparison of experimental bond strength and analytical bond strength τ_y for specimens with yielding in lapped bars.

The bond strength has been used to determine the required amount of confinement for short lap splices. The bond strength for short lap splices can be significantly increased by providing additional confinement to reach the maximum bond strength. As observed from this study with various lap splice lengths, enhancement of the bond strength is bounded by the bond strength corresponding to the onset of yielding. The study indicates that as the lap splice length increased to $35d_b$, the margin for the improvement in the bond strength vanished. This observation is substantiated by the experimental bond strength of the specimen with a lap splice length of $40d_b$ tested by Bournas and Triantafillou [66]. Based on these findings, the bond strength alone cannot characterize the improvement of lap splices by external confinement, particularly if the ductile behavior needs to be achieved. Therefore, another parameter should be used to relate the enhancement of lap splices to external confinement.

4.3. Interfacial Fracture Energy

As discussed in Chapter 3, failure ranges from brittle (Type I) to ductile (Type III) modes depending on the amount of the confinement ratio of HSS collars. It was discussed in Section 4.3 that the bond strength can reflect the improvement in structural behavior up to the onset of lap splice yielding, whereas it cannot sufficiently indicate the improvement beyond the onset of lap splice yielding. Hence, not only the bond strength but also the post-yield behavior of lap splices should be considered in determining the confinement ratio of HSS collars to achieve ductile failure. Malek et al. [123] investigated the bond stress distributions in the post-yield range of well-confined bars in cantilever beams. Pseudo-static pushover tests were performed on four cantilever beams without lap splice. Strain profiles along tensile bars were measured, and the corresponding bond stresses were estimated. At the peak load, the distribution of steel bar strains along the embedment length was nonlinear, with negligible strains at free ends and peak strains at fixed ends of the cantilever beams. Since the steel strain and the corresponding bond stress are directly related, the bond stress profile along the embedment length was also nonlinear. Using regression on the estimated bond stress profile, Malek et al. [123] proposed the following equation to define the bond stress distribution along a well-confined bar in concrete:

$$\tau_b = \begin{cases} \tau_{max}\left(\dfrac{\epsilon}{\epsilon_y}\right)^{0.3} ; & \epsilon \leq \epsilon_y \\[3mm] \tau_{max}\left[1 - 0.8\left(1 - e^{0.7\left(1-\frac{\epsilon}{\epsilon_y}\right)}\right)\right] ; & \epsilon > \epsilon_y \end{cases} \qquad 4.8$$

where τ_b is the bond stress of a well-confined bar at a strain ϵ, ϵ_y is the yield strain, and τ_{max} is the maximum bond stress at the end of the pre-yield zone. The definition of a well-confined bar refers to an embedded bar that is long enough to prevent pullout and splitting failures and undergoes yielding. Therefore, Eq. 4.8 provides the bond stress distribution for both the pre-yield and post-yield zones. By following the study of Haskett et al. [124], Malek et al. [123] proposed equations for calculating the interfacial fracture energy in the pre-yield zone G_1, and that in the post-yield zone G_2 by integrating the areas under the bond stress-steel strain relationships of Eq. 4.8 as

$$G_1 = \int_0^{\epsilon_y} \tau_{max}\left(\frac{\epsilon}{\epsilon_y}\right)^{0.3} d\epsilon \qquad 4.9$$

$$G_2 = \int_{\epsilon_y}^{\epsilon_u} \tau_{max}\left(1 - 0.8\left(1 - e^{0.7\left(1-\frac{\epsilon}{\epsilon_y}\right)}\right)\right) d\epsilon \qquad 4.10$$

where ϵ_u is the fracture strain of the embedded bar. The interfacial fracture energy within the pre-yield and post-yield zones is shown in Figure 4.2.
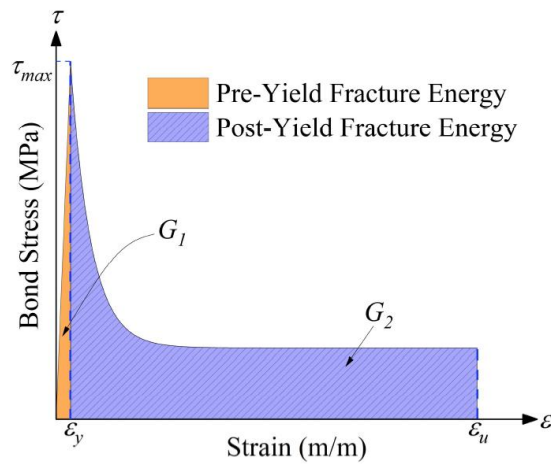
Figure 4.2 Visualization of interfacial fracture energy within pre-yield G_1 and post-yield zone G_2 by Malek et al. [123].

The strain distribution along the embedded length of reinforcement measured by Malek et al. [123] was nonlinear in pre-yield and post-yield zones. On the other hand, the strain distribution measured along the lap splice of beams in the present study was linear in the pre-yield zones. This is because the present study focuses on substandard lap splices, whereas the length of the embedded bar used by Malek et al. [123] was long enough to allow yielding and prevent splitting failure. It has also been reported that the strain distribution along a substandard lap splice is linear [52]. Therefore, to extend the concept of the interfacial fracture energy to the beams tested in the present study, it is proposed to use the observed linear strain distribution within the pre-yield zones, which results in uniform bond stress in the pre-yield zone. The cases of sufficiently confined beams in each of the subgroups are presented in Figure 4.3. A portion of the lap splice yielded near the loaded end in sufficiently confined beams. The length of the pre-yield zone was computed using the measured strain profile along the lap splice at peak loads, as shown in Figure 4.3. The calculated lengths of pre-yield and post-yield zones in sufficiently confined beams, i.e., specimens with Type-III failure, are shown in Table 4.2. The average length of the lap spliced bars exhibiting yielding was about 25% of the lap splice length which agrees with the recommendations of Fawzy et al. [125].
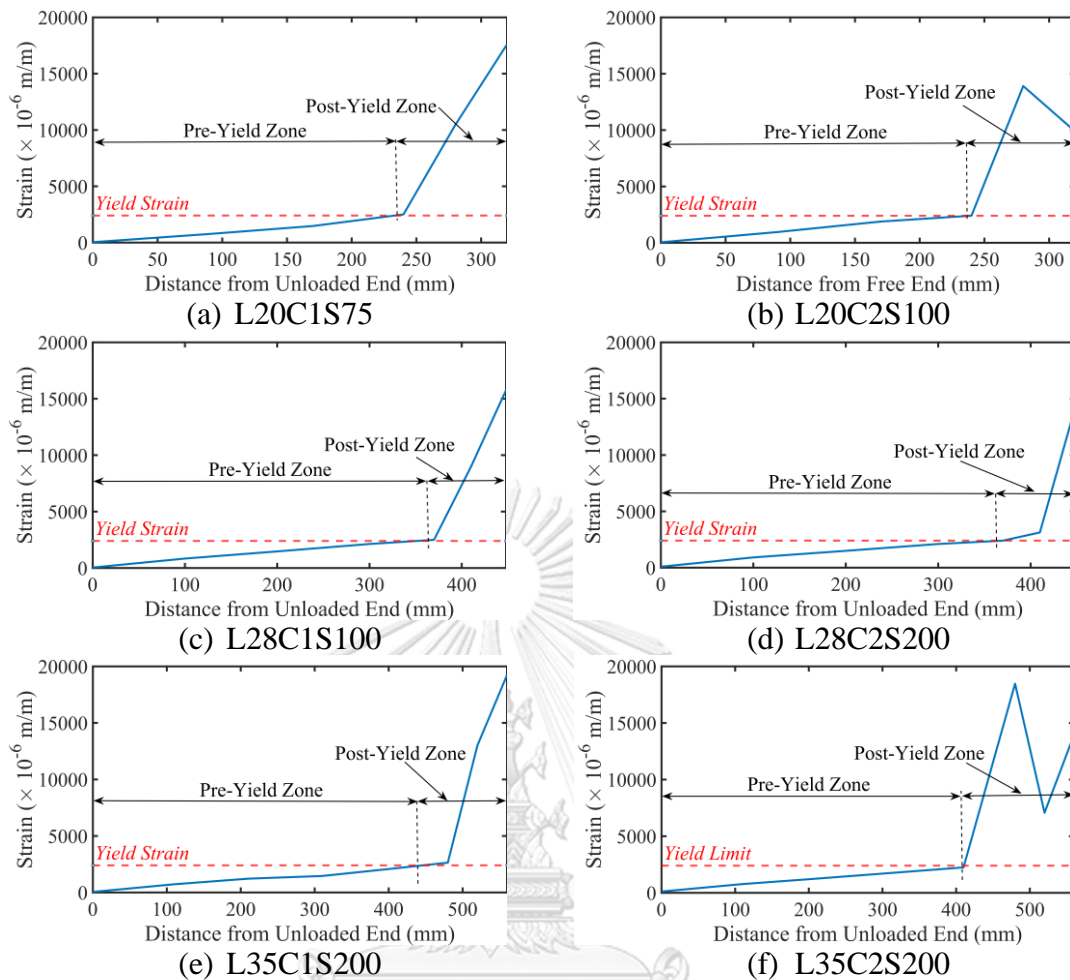
Figure 4.3 Pre-yield and post-yield zones along lap splices of sufficiently confined beams.

Table 4.2 Lengths of pre-yield and post-yield zones in sufficiently confined beams.

Beam ID	Length of pre-yield zone l (mm)	Length of post-yield zone $l_s - l$ (mm)	$\frac{(l_s - l)}{l_s} \times 100$ (%)
L20C1S75	235	85	26.5
L20C2S100	240	80	25.0
L28C1S100	350	98	22.0
L28C2S100	330	118	26.3
L28C2S200	337	111	24.8
L35C1S100	395	165	29.5
L35C1S200	420	140	25.0
L35C2S100	405	155	27.7
L35C2S200	405	155	27.7

Note: l = length of the pre-yield zone; l_s = length of the lap splice.

The mean bond strength in the pre-yield zone $\bar{\tau}_1$ can be determined from the measured strain distributions. Since bond stress was uniform within pre-yield zones, $\bar{\tau}_1$ is proposed to be τ_{max} for sufficiently confined beams and can be determined from

$$\bar{\tau}_1 = \tau_{max} = \frac{f_y d_b}{4l} \qquad 4.11$$

where l is the length of the pre-yield zone for sufficiently confined beams and can be taken as 75% of the length of the lap splice l_s. According to Malek et al. [123], the interfacial fracture energy obtained from the mean bond strength $\bar{\tau}_2$ within the post-yield zone G_2 can be expressed as

$$G_2 = \bar{\tau}_2\left(\epsilon_u - \epsilon_y\right) \qquad 4.12$$

where $\bar{\tau}_2$ is the mean bond strength within the post-yield zone. $\bar{\tau}_2$ can be estimated from experimental bond stress profiles along lap splices of control and insufficiently confined beams. It is important to note that the fracture strain of the lap spliced bars was 0.073, whereas the maximum recorded strain at loaded ends of sufficiently confined beams did not exceed 0.018 due to the failure of strain gages. Therefore, the observed strain distribution within post-yield zones of lap splices in sufficiently confined beams could not be completely captured. Since splitting failure was inhibited in sufficiently confined beams of the present study, it is reasonable to assume the strain profile within post-yield zones of lap splices to be similar to that proposed by Malek et al. [123]. This is because the distribution of steel strains and the corresponding bond stresses within the post-yield zones proposed by Malek et al. [123] correspond to those of well-confined bars. Similarly, sufficiently confined lap splices in the present study demonstrated yielding and high inelastic strains near their loaded ends while preventing splitting failures. Hence, the mean bond strength within post-yield zones $\bar{\tau}_2$ in sufficiently confined beams was obtained as

$$\bar{\tau}_2 = \frac{G_2}{\left(\epsilon_u - \epsilon_y\right)} \qquad 4.13$$

where G_2 is determined from Eq. 4.10. The interfacial fracture energy within the pre-yield zone G_1 and that within the post-yield zone G_2 are presented in Table 4.3. Further, lengths of pre-yield and post-yield zones of lap splices are also presented. The interfacial fracture energy in the pre-yield zone G_1 was calculated as the product of the calculated bond strength in the pre-yield zone $\bar{\tau}_1$ and the yield strain ϵ_y. The

mean bond strength calculated from strain measurements within the post-yield zone $\overline{\tau_2}$ was used for the calculation of the interfacial fracture energy within post-yield zones G_2 of control and insufficiently confined beams, whereas $\overline{\tau_2}$ was calculated from Eq. 4.13 for sufficiently confined beams. The total interfacial fracture energy G of the beams was calculated as

$$G = G_1 + G_2 \qquad\qquad 4.14$$

The last column of Table 4.3 presents the percentage of the increase in the interfacial fracture energy of strengthened beams ΔG over the interfacial fracture energy of control beams G_o. It is important to note that a substantial increase in the interfacial fracture energy ΔG for all subgroups was observed irrespective of the lap splice length and concrete cover. For instance, an increase of 387.9% in the interfacial fracture energy was observed for the strengthened beam L35C2S200, whereas the same beam did not exhibit an increase in its bond strength (see Table 4.3). Similar behavior can also be observed for the cases of Beams L35C1S200 and L28C2S200. Another important observation is that ΔG varied inversely with the lap splice length and concrete cover. For Subgroup L20C1, the maximum increase in the interfacial fracture energy was 2162.9%, whereas Subgroup L20C2 exhibited this increase up to 1200.9%. This suggests that to achieve the same increase in the interfacial fracture energy, a larger cover and a longer lap splice length would require a lower amount of HSS collar confinement.

Table 4.3 Summary of interfacial fracture energy of pre-yield and post-yield zones of beams.

ID	l (mm)	$l_s - l$ (mm)	$\overline{\tau_1}$ (MPa)	$\overline{\tau_2}$ (MPa)	G_1 (MPa)	G_2 (MPa)	G (MPa)	G_o (MPa)	ΔG (MPa)	$\frac{\Delta G}{G_o} \times 100$ (%)
L20C1SC	320	0	3.8	0.0	0.0062	0.00	-	0.0062	-	-
L20C1S200	320	0	5.4	0.0	0.0118	0.00	0.0118	-	0.0056	90.3
L20C1S100	255	65	7.8	1.4	0.0187	0.02	0.0387	-	0.0325	524.4
L20C1S75	235	85	8.5	2.1*	0.0203	0.12	0.1403	-	0.1341	2162.9
L20C2SC	320	0	5.3	0.0	0.0106	0.00	-	0.0106	-	-
L20C2S200	320	0	5.7	0.0	0.0136	0.00	0.0136	-	0.0030	28.3
L20C2S100	240	80	8.3	2.1*	0.0199	0.12	0.1379	-	0.1273	1200.9
L28C1SC	420	28	4.7	0.0	0.0114	0.00	-	0.0114	-	-
L28C1S200	365	83	5.4	0.1	0.0131	0.00	0.0131	-	0.0017	14.9
L28C1S100	350	98	5.7	1.4*	0.0136	0.08	0.0946	-	0.0832	729.8
L28C2SC	415	33	4.8	0.0	0.0115	0.00	-	0.0115	-	-
L28C2S200	355	93	5.6	1.4*	0.0132	0.08	0.0930	-	0.0815	708.7
L28C2S100	350	98	5.7	1.4*	0.0137	0.08	0.0937	-	0.0822	714.8
L35C1SC	500	60	4.0	0.1	0.0096	0.00	-	0.0096	-	-
L35C1S200	440	120	4.5	1.1*	0.0110	0.07	0.0760	-	0.0664	691.7
L35C1S100	435	125	4.6	1.1*	0.0110	0.07	0.0760	-	0.0664	691.7
L35C2SC	450	110	4.4	0.6	0.0106	0.01	-	0.0166	-	-
L35C2S200	410	150	4.8	1.2*	0.0120	0.07	0.0810	-	0.0644	387.9
L35C2S100	402	158	4.9	1.2*	0.0120	0.07	0.0810	-	0.0644	387.9

Note: l = *length of pre-yield zone;* l_s = *length of lap splice;* $\overline{\tau_1}$ = *mean bond strength in pre-yield zone;* $\overline{\tau_2}$ = *mean bond strength in post-yield zone;* G_1 = *fracture energy in pre-yield zone;* G_2 = *fracture energy in post-yield zone;* $G = G_1 + G_2$ = *total fracture energy;* ΔG = *increase in fracture energy of strengthened beams over control beams;* * *represents mean bond stress in post-yield zone calculated using Eq. (10).*

4.4. Equation to predict the increase in interfacial fracture energy

The increase in the interfacial fracture energy of strengthened beams ΔG against the confinement ratio of HSS collars ρ is shown in Figure 4.4. Experimental results of Beams L28C2S100, L35C1S75, and L35C2S100 were excluded because an HSS collar spacing of 200 mm was found sufficient to achieve Type-III failure. As a result, reducing the collar spacing to 75 mm or 100 mm in Subgroups L28C2, L35C1, and L35C2 did not result in an increase in the interfacial fracture energy. It is evident that ΔG shows some relation with ρ. The form of Eq. 4.15 was found to correlate well with the increase in the interfacial fracture energy of strengthened beams as

$$\Delta G = a \times (1 + \rho)^b (R_{ls})^c \qquad 4.15$$

$$R_{ls} = \frac{l_s}{l_{s,ACI}} \qquad \qquad 4.16$$

where l_s is the provided lap splice length, and $l_{s,ACI}$ is the lap splice length required by ACI 318-19 [62] as determined from

$$l_{s,ACI} = \frac{9}{10} \frac{f_y}{\sqrt{f_c'}} \frac{d_b}{\left(c/d_b\right)} \qquad \qquad 4.17$$

where f_y is the yield strength of bars in MPa, f_c' is the compressive strength of concrete in MPa, d_b is the bar diameter in mm, and c is the controlling cover in mm. The parameter $l_{s,ACI}$ was chosen as it involves all variables that affect the bond strength, i.e., concrete cover, yield strength of bars, and the concrete compressive strength. In this study, the values of normalized R_{ls} ranged from 0.23 to 0.65. Nonlinear regression was performed using the classical Gauss-Newton method. From the regression analysis, the following equation was obtained:

$$\Delta G = 0.040 \times (1 + \rho)^{118.81} \times (R_{ls})^{2.09} \qquad \qquad 4.18$$

The accuracy of Eq. 4.18 in predicting the increase in the interfacial fracture energy of strengthened beams due to HSS collar confinement is shown in Figure 4.5. Pearson's correlation coefficient r of 0.92 suggests that a good agreement between experimental and predicted values of ΔG is obtained.
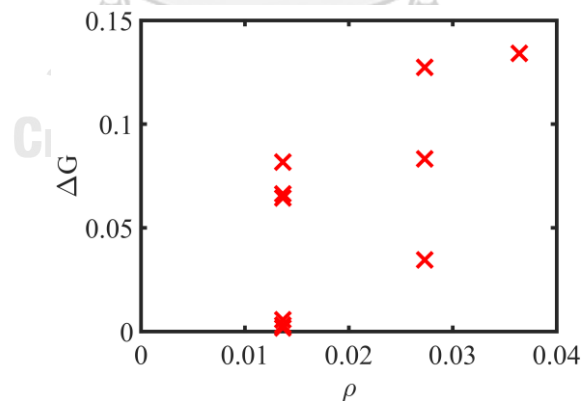
Figure 4.4 Dependence of ΔG on the confinement ratio of HSS collars ρ.
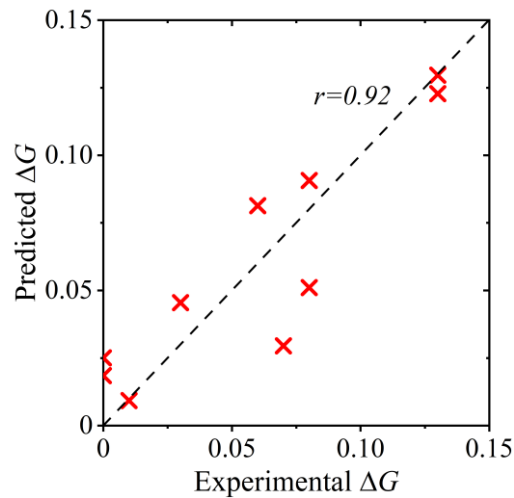
Figure 4.5 Comparison of the increase in the interfacial fracture energy of strengthened beams from prediction and experiment.

4.4.1. Determination of Required Confinement Ratio of HSS Collars and Application

For a substandard lap splice, the required confinement ratio of HSS collars ρ needs to be determined to change the failure mode from the brittle mode to the ductile mode. The approach to estimate the confinement ratio of HSS collars ρ is provided in Section 4.5.1. The derivation provided in this section involves an estimation of the bond strength in unstrengthened beams. Therefore, the accuracy of several existing bond strength models is assessed in Section 4.5.2. Finally, an application example is provided in Section 4.5.3.

i. Interfacial Fracture Energy of Lap splice in Unstrengthened Beams, $\boldsymbol{G_o}$

For a uniform bond stress distribution along the lap splice, the interfacial fracture energy of the lap splice in an unstrengthened beam G_o can be obtained as the product of the bond strength in an unstrengthened beam τ_o and the maximum strain ϵ_s that the lap splice can sustain. The available interfacial fracture energy G_o of an unstrengthened beam is calculated as

$$G_o = \tau_o \epsilon_s \qquad\qquad 4.19$$

The bond strength in an unstrengthened beam τ_o can be calculated from a suitable bond strength model discussed in Section 4.5.2. Knowing τ_o, the maximum

strain ϵ_s that the lap splice can sustain in an unstrengthened beam in Eq. 4.19 can be calculated from the equilibrium between the steel stress and the bond strength using

$$\epsilon_s = \frac{4\tau_o l_s}{d_b E_s} \qquad\qquad 4.20$$

where E_s is the Young's modulus of steel bars. From Eq. 4.19 and Eq. 4.20, the interfacial fracture energy in an unstrengthened beam is given as

$$G_o = \frac{4\tau_o^2 l_s}{d_b E_s} \qquad\qquad 4.21$$

ii. Total Interfacial Fracture Energy Corresponding to Type-III Failure, G

The total interfacial fracture energy comprises the energy contributed from the pre-yield zone G_1 and that from the post-yield zone G_2 of a lap splice. The interfacial fracture energy within the pre-yield zone G_1 can be estimated by the product of the mean bond strength in the pre-yield zone τ_{max} and the yield strain ϵ_y. For the post-yield zone of the lap splice, the interfacial fracture energy G_2 can be estimated using the formulation of Malek et al. [123]. To estimate the total interfacial fracture energy, the lengths of the pre-yield and the post-yield zones of a lap splice are required. It was discussed in Section 4.3 that for a sufficiently confined lap splice, the length of the post-yield zone could be taken as 25% of the lap splice length. The interfacial fracture energy in the pre-yield zone G_1 is determined from

$$G_1 = \tau_{max}\epsilon_y = \frac{f_y d_b}{4 \times 0.75 l_s}\epsilon_y = \frac{f_y d_b}{3 l_s}\epsilon_y \qquad\qquad 4.22$$

The mean bond strength within the post-yield zone $\overline{\tau_2}$ is calculated using Eq. 4.13. The calculation of $\overline{\tau_2}$ using Eq. 4.13 requires the value of the interfacial fracture energy in the post-yield zone G_2 that can be estimated using Eq. 4.10. Note that τ_{max} in Eq. 4.10 is the mean bond strength mobilized within the pre-yield zone of the lap splice and is calculated from Eq. 4.11. The total interfacial fracture energy G is then calculated using Eq. 4.14.

iii. Additional interfacial fracture energy to achieve Type-III failure, ΔG

Knowing the interfacial fracture energy within an unstrengthened beam and the total interfacial fracture energy required to achieve Type-III failure, it is possible

to estimate the amount of the additional interfacial fracture energy that is required from HSS collars to prevent brittle failure. It is the difference between the interfacial fracture energy in an unstrengthened beam G_o and the total interfacial fracture energy G corresponding to Type-III failure. The additional interfacial fracture energy required to exhibit Type-III failure is given by

$$\Delta G = G - G_o = \frac{f_y d_b}{3l_s}\epsilon_y + \int_{\epsilon_y}^{\epsilon_u} \tau_{max}\left(1 - 0.8\left(1 - e^{0.7\left(1-\frac{\epsilon}{\epsilon_y}\right)}\right)\right) d\epsilon - \frac{4\tau_o^2 l_s}{d_b E_s} \qquad 4.23$$

iv. Required Confinement Ratio of HSS Collars, ρ

Substituting Eq. 4.18 into Eq. 4.23 yields the following equation to estimate the required confinement ratio of HSS collars to achieve ductile failure for a substandard lap splice.

$$\rho = \left[\frac{1}{0.040 R_{ls}^{2.09}}\left\{\frac{f_y d_b}{3l_s}\epsilon_y + (\tau_{max}\Psi) - \frac{4\tau_o^2 l_s}{d_b E_s}\right\}\right]^{\frac{1}{118.81}} - 1.00 \qquad 4.24$$

where

$$\Psi = \int_{\epsilon_y}^{\epsilon_u}\left(1 - 0.8\left(1 - e^{0.7\left(1-\frac{\epsilon}{\epsilon_y}\right)}\right)\right) d\epsilon \qquad 4.25$$

The variation of Ψ for various values of ϵ_y and ϵ_u is presented in Figure 4.6.
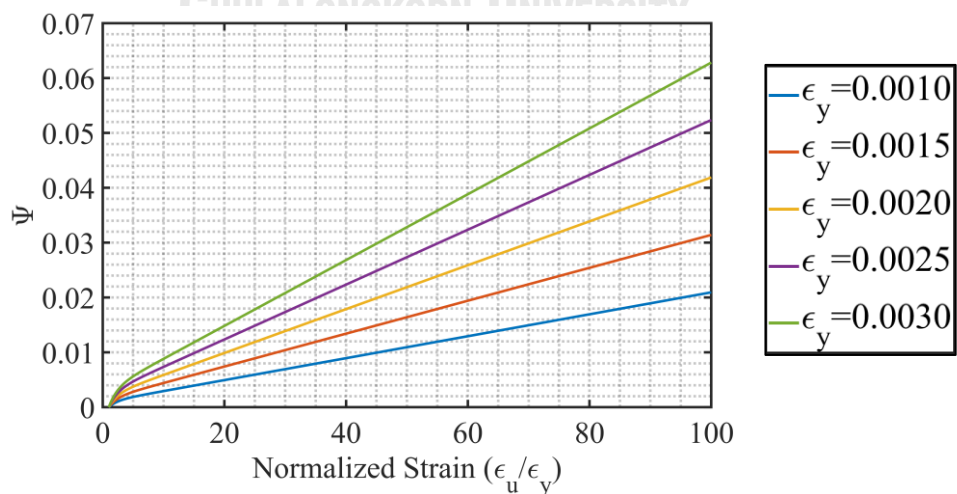
Figure 4.6 Variation of Ψ for different ϵ_y and ϵ_u.

The confinement ratio of HSS collars for each subgroup that resulted in Type-III failure is given in Table 4.4. It is evident that Eq. 4.24 resulted in a close approximation of the experimental confinement ratio of HSS collars. The last column of Table 4.4 provides the difference between experimental and predicted ρ. The values of R_{ls} for six subgroups are also reported in Table 4.4. Overall, the predicted ρ values by the proposed Eq. 4.24 agree well with experimental results. For Beams L28C2S200 and L35C1S200, the predicted confinement ratios of HSS collars are overestimated. In Subgroups L28C2, L35C1, and L35C2, the widest collar spacing was 200 mm, which is slightly smaller than the spacing required. This is because the transition from Group L28 to Group L35 resulted in an increase in the lap splice length. This resulted in an overestimation of the confinement ratio of HSS collars for Beams L28C2S200 and L35C1S200. However, the predicted ρ values are conservative for the design purpose. The proposed equation for ρ should be limited to R_{ls} values ranging from 0.23 to 0.65. In addition, the shear strength of the section must be checked and compared with the flexural capacity of the section corresponding to the lap splice failure. The proposed equation for ρ cannot be applied to strengthen shear-critical sections. In this regard, a calculation procedure for shear strength and flexural strength corresponding to lap splice failure is presented in Appendix A2.

Table 4.4 Confinement ratio of HSS collars for beams that exhibited Type-III failure.

Subgroup	Beam	R_{ls}	Experimental ρ	Predicted ρ	Difference (%)
L20C1	L20C1S75	0.23	0.0364	0.0379	+4.1
L20C2	L20C2S100	0.37	0.0273	0.0290	+6.2
L28C1	L28C1S100	0.32	0.0273	0.0288	+5.4
L28C2	L28C2S200	0.52	0.0137	0.0183	+33.5
L35C1	L35C1S200	0.40	0.0137	0.0200	+46.0
L35C2	L35C2S200	0.65	0.0137	0.0142	+3.6

Note: ρ = required confinement ratio of HSS collars and R_{ls} is computed for each subgroup corresponding to a normalized concrete strength of 27 MPa.

4.4.2. Bond Strength Models for Unstrengthened Beams

Accurate prediction of the bond strength of unstrengthened beams τ_o is essential to estimate the required confinement ratio of HSS collars. Several previous

bond strength models are summarized in Table 8. Their accuracy is assessed by comparing their predictions with the experimental results of the control beams of the present study. In addition, two control specimens of Bournas & Triantafillou [66] and three control specimens of Garcia et al. [52] were also included to extend the range of specimens. Average values of the ratio of test to prediction bond strengths are provided in Table 4.5. It is observed that all models underestimated the bond strength in unstrengthened beams except the model of Harajli [59]. This is because the model by Harajli [59] does not incorporate the effect of lap splice length on the bond strength. It was observed that the bond strength of control beams decreased as the splice length increased. As a result, the model by Harajli [59] overestimated the bond strengths of the L28 and L35 groups. The test-to-prediction ratios of all models against lap splice lengths are shown in Figure 4.7. The models of Zuo and Darwin [14] [88] and Lettow and Eligehausen [126] consistently produced test-to-prediction ratios close to 1. Therefore, it is recommended to use the model by Zuo and Darwin [14] or the model by Lettow and Eligehausen [126] to estimate the bond strength of bars in unstrengthened beams.

Table 4.5 Existing bond strength models for unstrengthened beams.

Model	Expression	Test/Prediction (averaged)
Orangun et al. [116]	$\tau_o = \sqrt{f_c'}\left(0.1 + 0.25\left(\frac{c_{min}}{d_b}\right) + 4.15\left(\frac{d_b}{l_s}\right)\right)$	1.21
Esfahani and Rangan [55]	$\tau_o = \tau \times \left(\frac{1 + \frac{1}{M}}{1.85 + 0.024\sqrt{M}}\right)\left(0.88 + 0.12\frac{c_{med}}{c_{min}}\right)$ where, $$M = \cosh\left(0.0022l_s\sqrt{\frac{rf_c'}{d_b}}\right)$$ $$\tau = 4.9\frac{\frac{c_{min}}{d_b} + 0.5}{\frac{c_{min}}{d_b} + 3.6}f_{ct}$$ $$f_{ct} = 0.55\sqrt{f_c'}$$	1.14
Zuo and Darwin [14]	$\tau_o = f_c^{0.25}\left[(1.43l_s(c_{min} + 0.5d_b) + 56.2A_b) \times \left(\frac{0.1c_{max}}{c_{min}} + 0.9\right)\right]$	1.02
CEB-FIP model code [118]	$\tau_o = \dfrac{1.64\left(\frac{f_c' - 2.75}{10}\right)^{2/3}}{1.15 - 0.1\frac{c_{min}}{d_b}}$	1.20
Lettow and Eligehausen [126]	$\tau_o = \left(\frac{d_b}{4l_s}\right)24.2\left(\frac{l_s}{d_b}\right)^{0.55}(f_c')^{0.25}\left(\frac{c_{min}}{d_b}\right)^{\frac{1}{3}}\left(\frac{c_{max}}{c_{min}}\right)^{0.1}\left(\frac{20}{d_b}\right)^{0.2}$	0.99
Harajli [59]	$\tau_o = 0.75\sqrt{f_c'}\left(\frac{c_{min}}{d_b}\right)^{2/3}$	0.82

Note: f_{ct} = tensile strength of concrete; τ_o = bond strength in an unstrengthened beam; $c_{min}, c_{med},$ and c_{max} = minimum, median, and maximum values of bottom concrete cover, side concrete cover, and one-half of the clear spacing between consecutive pairs of lapped bars; A_b = cross-sectional area of a single lapped bar.
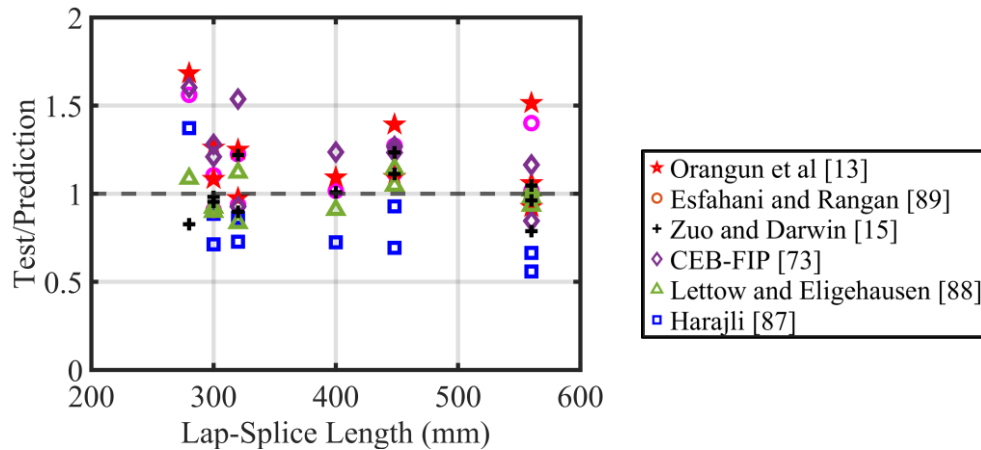
Figure 4.7 Test/Prediction ratios for different unstrengthened bond strength models.

4.4.3. Application Example

As an example, the procedure for determining the required confinement ratio of HSS collars ρ is demonstrated for the beams in Subgroup L20C1. The maximum bond strength within the pre-yield zone of the lap splice is estimated using Eq. 4.11 as

$$\tau_{max} = \frac{f_y d_b}{4 \times 0.75 l_s} = \frac{497 \times 16}{4 \times 0.75 \times 320} = 8.28 \text{ MPa} \qquad 4.26$$

The ratio of the provided lap splice length to that required by ACI 318-19 [62] R_{ls} is $320/1100 = 0.29$. The bond strength in an unstrengthened beam τ_o is estimated using the model by Lettow and Eligehausen [126] as 4.53 MPa. The interfacial fracture energy in an unstrengthened beam is estimated using Eq. 4.21 as

$$G_o = \frac{4\tau_o^2 l_s}{d_b E_s} = \frac{4 \times 4.53^2 \times 320}{16 \times 207000} = 0.00175 \text{ MPa} \qquad 4.27$$

To estimate the interfacial fracture energy in the post-yield zone G_2, Eq. (4.10) is used, and the value of G_2 is estimated as 0.135 MPa. The value of the interfacial fracture energy within the pre-yield zone is estimated using Eq. 4.22 as

$$G_1 = \frac{f_y d_b}{3 l_s} \epsilon_y = \frac{497 \times 16}{3 \times 320} \times 0.0024 = 0.01988 \text{ MPa} \qquad 4.28$$

The total interfacial fracture energy G is the summation of G_1 and G_2 and is equal to 0.155 MPa. The additional interfacial fracture energy ΔG required to achieve Type-III failure is estimated as 0.153 MPa from the difference between the total interfacial

fracture energy, i.e., 0.155 MPa, and the interfacial fracture energy in an unstrengthened beam, i.e., 0.00175 MPa. Equating ΔG to Eq. 4.18 yields

$$\Delta G = 0.153 = 0.040 \times (1 + \rho)^{118.81} \times (R_{ls})^{2.09} \qquad (4.29)$$

From this, ρ is estimated to be 0.0379, as shown in Table 4.5. Then, the size and spacing of HSS collars can be determined from Eq. 3.6.

4.4.4. Limitation of the Proposed Equation

The proposed Eq. 4.24 was formulated based on the experimental results of lap splice with R_{ls} values ranging from 0.23 to 0.65. Therefore, the application of the proposed equation should be limited to R_{ls} values within this range. In addition, the size and strength of the bolts used in the present study must be adopted as the minimum criteria. The yield strength of HSS collars must at least be 400 MPa.

Chapter 5 Nonlinear Fiber Modelling of RC Beams with HSS Collars

In this chapter, nonlinear fiber modeling of RC beams using *OpenSees* is discussed. The fiber modeling of control and HSS collar strengthened beams are discussed separately. The main objectives of performing nonlinear fiber modeling of beams are: (1) to assess the efficiency of existing models to estimate the splice strength of substandard lap spliced bars and (2) to assess the efficiency of the model by Chapman and Driver [99] to estimate the compressive stress-strain relation of HSS collar confined concrete by including the effect of flexural stiffness and adopting an incremental collar pressure scheme, as presented in Chapter 2. Section 5.1 discusses the issues in substandard lap spliced members, Section 5.2 discusses the strategies to include the effect of a substandard lap splice into a nonlinear fiber model, and modeling of steel fibers strengthened with HSS collars, the strategies to model concrete fibers strengthened with internal steel confinement and strengthened with external HSS collars are discussed in Section 5.3, the *OpenSees* modeling and its results for the control beams tested in this study are presented in Section 5.4, and Section 5.5 presents the nonlinear fiber modeling of HSS collar strengthened beams by incorporating the strategies discussed in Section 5.2 and 5.3.

5.1. Issues Related to Substandard Lap Splices

Several experimental programs on RC members with substandard lap splices are presented in the literature. However, only a few of them measured the behavior of substandard lap splices in the form of strain measurements. Due to the premature splitting failure attributed to the substandard lap splice length, the lap splices are unable to achieve their full capacity. As a result, the strains measured along the lap splice in substandard lap splices are below the yield strain. There may also exist some cases when the lap splice achieves yielding but still fails without achieving the fracture strength as observed for Beams L28C2SC, L35C1SC, and L35C2SC. Figure 5.1(a) presents the strain measurements along a $20d_b$ lap splice at the base of an RC column tested by Malek et al. [7]. It can be seen that the maximum strains were below

the yield strain for both the starter and column bars. Bournas and Triantafillou [66] also measured strains along a $20d_b$ and $40d_b$ lap splice as shown in Figure 5.1(b). It was observed that the maximum lap splice strain in the $20d_b$ lap splice was significantly lower than the yield strain, whereas the maximum strain in $40d_b$ lap splice was equal to the yield strain. Despite achieving the yield strain in $40d_b$ lap splice, the column failed in brittle manner due to the lap splice failure. Figure 5.1(c) presents strain along the $28d_b$ lap splice measured by Kruavit [76]. The yield strain of lap spliced bars was 0.0021. It can be seen in Figure 5.1(c) that the yield strain was achieved only in the push direction. Nonetheless, the column failed prematurely due to the lap splice failure. Figure 5.1(d) presents strain distribution along a $25d_b$ lap splice in a simply supported RC beam. Again, the lap splice could not achieve its yield capacity at its failure.

Considering observations presented in the preceding paragraph, it can be concluded that the splice strength associated with a substandard lap splice is limited and varies with the lap splice length. Therefore, this issue can be incorporated into the nonlinear modeling of RC members with substandard lap splices.

(a)
(b)

(c)
(d)
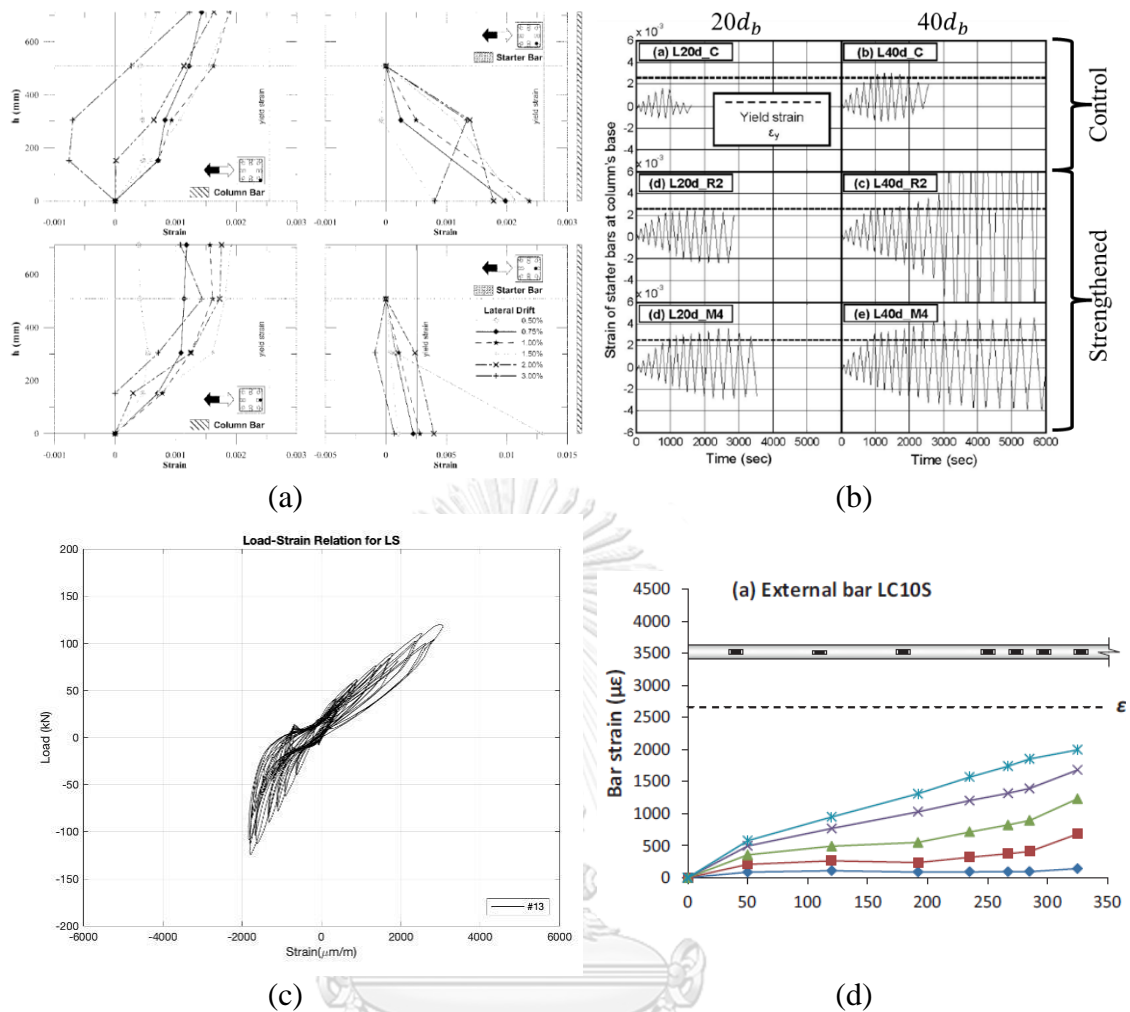
Figure 5.1 Strain measured along substandard lap splice by (a) Malek et al. [7]. (b) Bournas and Triantafillou [66], (c) Kruavit [76], and (d) Garcia et al. [52].

5.2. Method to Model RC Members with Substandard Unstrengthened and Strengthened Lap splices

5.2.1. Modelling Unstrengthened Lap splices

It was discussed in Section 5.1 that the strength of a substandard lap splice at its failure is well below its full capacity. Therefore, this effect can be included in the nonlinear model to involve the premature failure attributed to the short length of the lap splice. For example, Tariverdilo et al. included the effect of substandard lap splice in RC columns by modifying the stress-strain relation of steel fibers in the lap splice element of the model. Some approaches are present in the literature to estimate the peak capacity of substandard lap splices. It has been reported that the maximum stress

that a substandard lap splice can transfer is lower than the tensile capacity of the lapped bars [29, 127]. In old constructions, the length of the lap splice was short enough to limit the maximum stress below the yield limit. To estimate the maximum stress that a lap splice can transfer, a few of the methods are summarized below.

In earlier sections, it was found that the model of Lettow & Eligehausen [126] best predicts plain concrete bond strengths with minimum difference. Their equation is presented in Eq. 5.1.

$$\tau_c = \left(\frac{d_b}{4l_s}\right) 24.2 \left(\frac{l_s}{d_b}\right)^{0.55} (f_c')^{0.25} \left(\frac{c_{min}}{d_b}\right)^{\frac{1}{3}} \left(\frac{c_{max}}{c_{min}}\right)^{0.1} \left(\frac{20}{d_b}\right)^{0.2} \qquad 5.1$$

From equilibrium between bar force and bond stress, Eq. 5.1 can be used to predict steel stress at splitting. Recognizing that maximum uniform bond stress is limited to the yield stress, an upper limit on Eq. 5.2 is proposed, i.e., maximum bar force is limited to the yield strength of lapped bars.

$$f_s = \frac{4l_s}{d_b}\left(\frac{d_b}{4l_s}\right) 24.2 \left(\frac{l_s}{d_b}\right)^{0.55} (f_c')^{0.25} \left(\frac{c_{min}}{d_b}\right)^{\frac{1}{3}} \left(\frac{c_{max}}{c_{min}}\right)^{0.1} \left(\frac{20}{d_b}\right)^{0.2} \leq f_y \qquad 5.2$$

Recognizing that spliced bars and hooks that do not meet modern seismic requirements are unable to achieve their full capacity, FEMA 356 [128] proposed the following equation to estimate the splice strength.

$$f_s = \frac{l_s}{l_d} \times f_y \qquad 5.3$$

where l_s and l_d are provided and required lap splice lengths, respectively, as per ACI 318-19 [62] requirements. Elwood et al. [129] suggested that Eq. 5.3 does not consider the intent of ACI code expressions to develop strength greater than the yield strength of spliced bars. Further, instead of implying a strength reduction factor, the ACI equation for splice length implicitly contains an overstrength factor of 1.25 applied to the nominal yield strength of lapped bars. In this regard, it was expected that Eq. 5.3 would underestimate splitting splice strengths. Keeping in view this, Elwood et al. [129] proposed Eq. 5.4 to estimate the strength of substandard lap splices.

$$f_s = 1.25 \left(\frac{l_s}{l_d}\right)^{\frac{2}{3}} \leq f_y \qquad 5.4$$

Tariverdilo et al. [78] analyzed bond-critical RC columns using fiber-based modeling in *OpenSees*. For this, a monotonic stress-strain model for lap spliced bars was developed first, which was later used with degradation and pinching effects for hysteretic loading. It was supposed that the slip resistance was provided by truss-mechanism of 45°between spliced bars or between spliced bars and surrounding concrete, as shown in Figure 5.2. From equilibrium, tensile force is equal to the bond force.

$$T_b = A_b f_s = F_t p l_s \qquad 5.5$$

where T_b is the force developed in the spliced bar, A_b is the bar cross-section, F_t is the tensile strength of concrete taken as $0.33\sqrt{f_c'}$, p is the perimeter of the characteristic block given in Eq. 5.5, and l_s is the length of lap splice.

$$p = \frac{s}{2} + 2(d_b + c_{min}) \le 2\sqrt{2}(c_{min} + d_b) \qquad 5.6$$
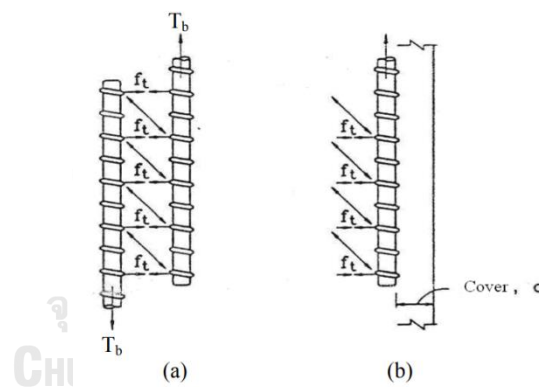
Figure 5.2 Assumed 45°slip-resistance mechanism (a) between bars (b) between bars and core concrete (Priestley et al. [79]).

Bejelo [127] proposed the following procedure:

1. Setup bond stress-slip relationship for lap splice. Maximum bond stress and corresponding slip were measured from experiments. Post-peak bond stress-slip relation was assumed to follow a linear descending branch up to a slip of 3 mm. This is the value recommended by Harajli et al. [51]. For example, Figure 5.3 presents one such relationship for beam L20C1SC.
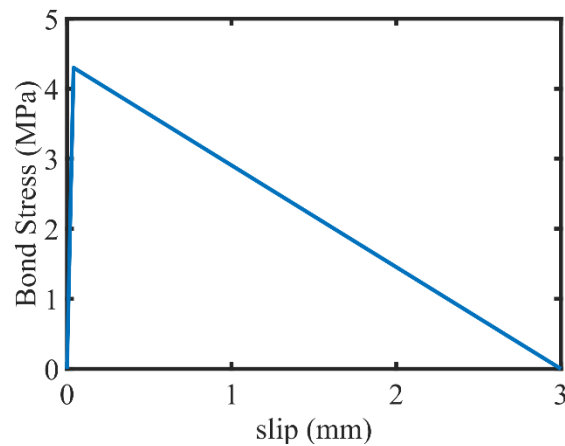
Figure 5.3 Bond stress-slip relation for beam L20C1SC.

2. This bond stress-slip relation is converted to a bond force-slip relation. To do so, bond stress corresponding to each slip value is multiplied by the critical perimeter around each lapped bar and lap splice length. The critical perimeter was estimated as per the recommendations of Belejo [127], as shown in Figure 5.4. It was estimated to be 92 mm and 122 mm for subgroups C1 and C2, respectively. Belejo [127] recommended adopting a parabolic bond stress distribution along the lap splice. Therefore, the final bond force-slip relation was estimated as:

$$f_{bond} = p \times l_s \times \frac{2}{3} u_{bond} \qquad 5.7$$

where; p, l_s, and u_{bond} are critical perimeter, lap splice length, and bond stress, respectively. Figure 5.5 presents the estimated bond force-slip relation for beam L20C1SC.
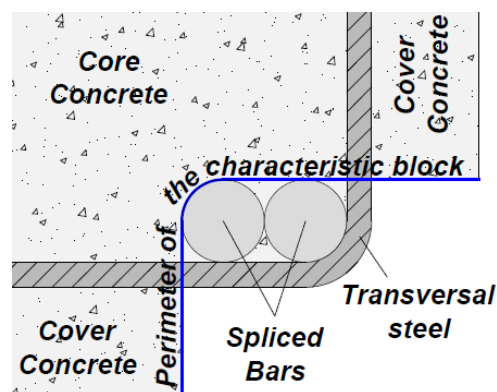
Figure 5.4 Estimation of critical perimeter (Ref: Belejo [127]).
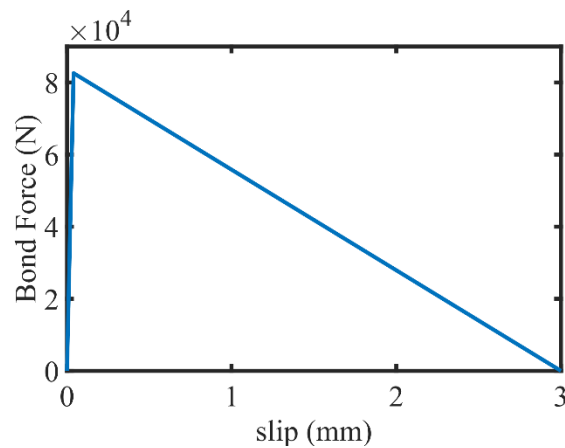
Figure 5.5 Bond force-slip relation for beam L20C1SC.

3. A series model is prepared to connect a truss element of length equal to splice length to a zero-length element. The bond force-slip relation is assigned to the zero-length element, whereas the steel constitutive relation is assigned to the truss element. Further, the area of the longitudinal steel bar is assigned to the truss element. Figure 5.6 schematically shows this process. Further, rotation and vertical translation at the free end of the spring were synchronized to those of the fixed end using *EqualDOF* command.
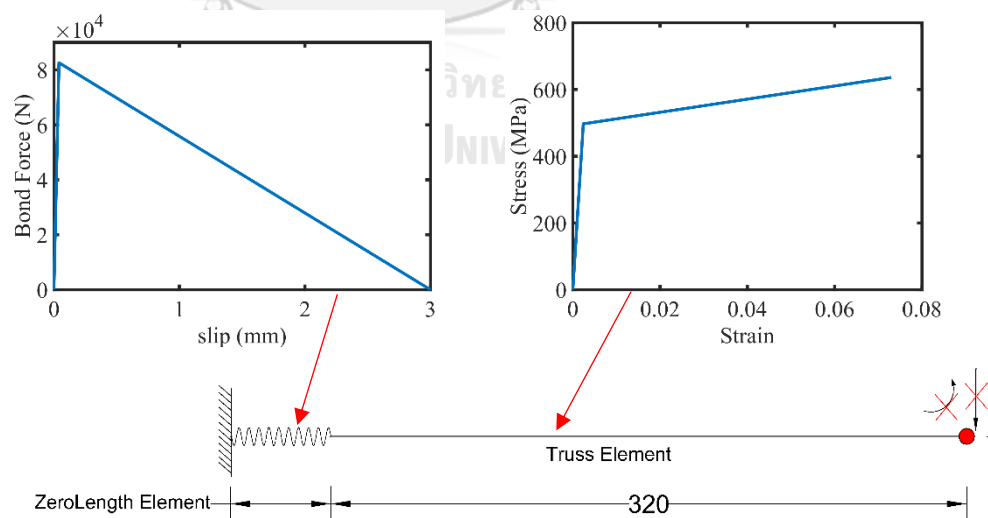
Figure 5.6 Schematics of the series element to capture modified stress-strain law.

4. Finally, a displacement-controlled analysis is performed by applying a unit load at the free end of the truss element. Displacement is recorded at the

same end, whereas reaction is recorded at the fixed end. Modified stress and strain for the steel bar are obtained by dividing the obtained displacement and reaction by lap splice length and truss area, respectively. Figure 5.7 shows the modified lap splice steel stress-strain relation for beam L28C2SC.

As shown in Figure 5.7, this method predicts that lap splice will be able to mobilize fracture strength. However, experiments revealed that this beam failed prematurely due to the splitting failure. It was further investigated that the critical perimeter around lapped bars was different from that proposed by Belejo [127].
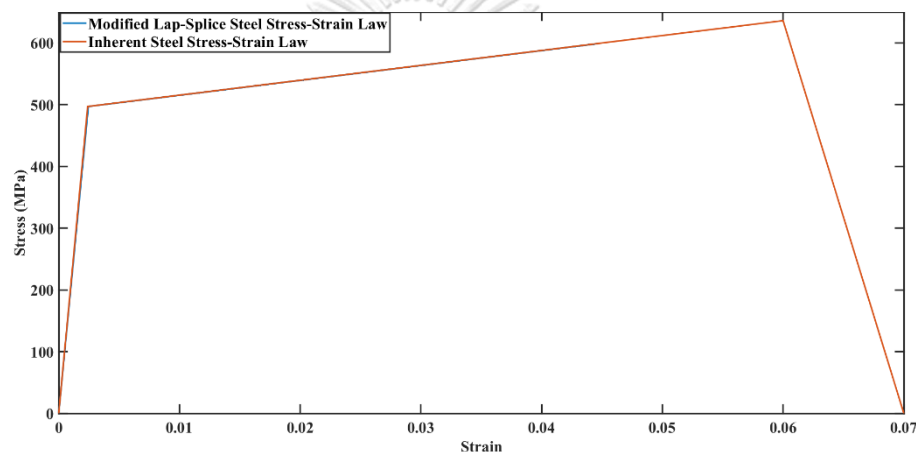
Figure 5.7 Actual vs. predicted lap splice rebar constitutive law by the procedure of Belejo [127].

As shown in Figure 5.8, the perimeter of splitting cracks is found to be smaller than that predicted by Belejo [127]. The first splitting crack appeared along the controlling cover. For instance, for beam L20C2SC, splitting is initiated between lapped bars first (see Figure 5.8). In the very next frame, a bottom-splitting crack initiated. This sequence was also observed for the remaining control beams. Therefore, the following equation is proposed to calculate the critical perimeter.

$$p = c_{min} + \frac{\pi d_b}{2} + c_{med} \qquad\qquad 5.8$$

where c_{min} minimum of the clear bottom cover, side cover, or one-half the clear spacing between consecutive pairs of lapped bars, whereas c_{med} is the median value of them.

(1) Splitting between lapped bars   (2) Bottom splitting

L20C2SC

Bottom crack first (L28C1SC)

Bottom splitting cracks and between lapped bars (L28C2SC)

Figure 5.8 Formation of splitting cracks just before splitting failure in control beams.

Following Eq. (5.2), splitting cracks follow the sequence as demonstrated in Figure 5.9.
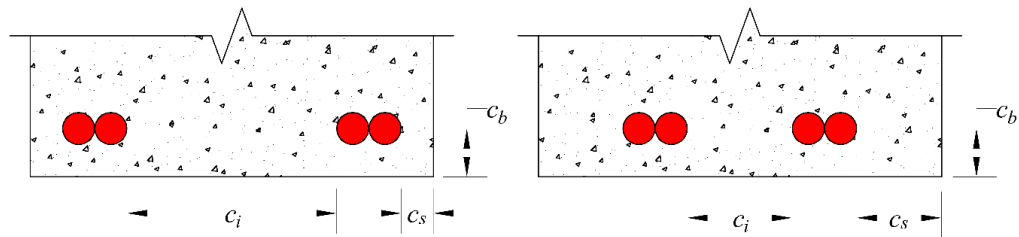
Figure 5.9 Formation of splitting cracks (left) $c_b < c_s < \frac{c_i}{2}$ (right) $c_b < \frac{c_i}{2} < c_s$.

Incorporating Eq. (5.2) and using Belejo [127] procedure, Figure 5.10 presents modified constitutive laws for lap splice tensile steel rebar.
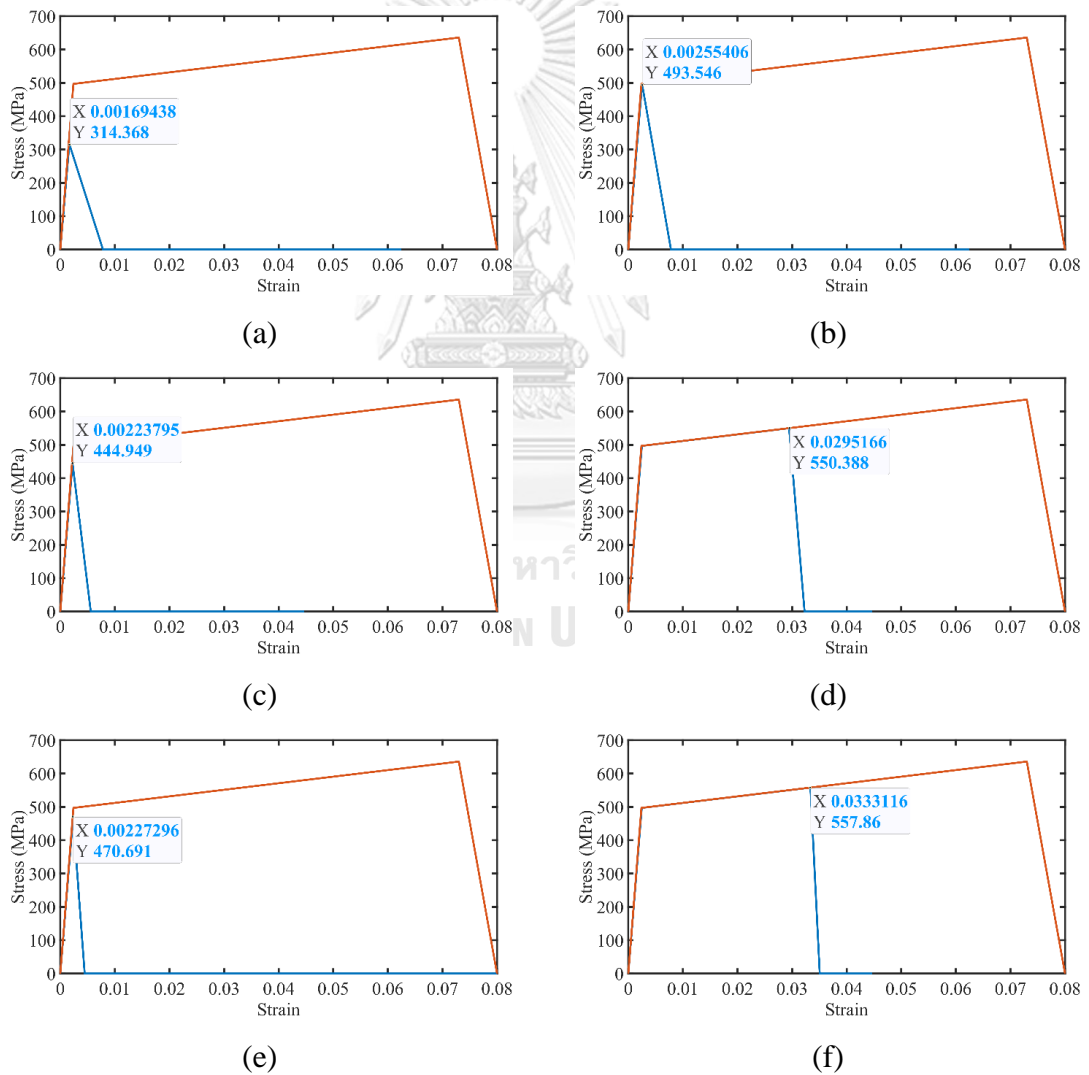
Figure 5.10 Modified lap splice rebar stress-strain law by Belejo [127] procedure (a) L20C1SC (b) L20C2SC (c) L28C1SC (d) L28C2SC (e) L35C1SC and (f) L35C2SC.

5.2.2. Modelling HSS Collar Strengthened Lap splices

Apart from the improvement in the behavior of concrete strengthened by HSS collars, it was observed that the failure mode was changed from Type-I mode to Type-III mode. As a result, the premature failure of the lap splice was prevented in sufficient confined beams. For other beams, a partial improvement in the lap splice capacity was observed. In view of this, the stress-strain response of bottom steel bars in sufficiently confined beams was modeled as the true stress-strain response obtained from the tensile test, whereas it was required to estimate the lap splice capacity in the case of insufficiently confined beams. To estimate the maximum strain that lap spliced bars sustained in insufficiently confined beams, back-calculation was performed by following the procedure shown in Figure 5.11.

Calculate increase in fracture energy due to HSS confinement
$\Delta G\ (MPa) = 0.04(1 + \rho)^{118.81} R_{ls}^{2.09}$

Calculate τ_o (Lettow & Eligehausen 2006)
$\tau_o = \left(\dfrac{d_b}{4l_s}\right) 24.2 \left(\dfrac{l_s}{d_b}\right)^{0.55} (f_c')^{0.25} \left(\dfrac{c_{min}}{d_b}\right)^{\frac{1}{3}} \left(\dfrac{c_{max}}{c_{min}}\right)^{0.1} \left(\dfrac{20}{d_b}\right)^{0.2}$

Calculate fracture energy offered by plain concrete G_o
$G_o = \dfrac{4\tau_o^2 l_s}{d_b E_s}$

Total fracture energy G
$G = G_o + \Delta G$

Calculate G corresponding to elastic zone i.e., $0.75l_s$
$G_1 = \dfrac{f_y d_b}{3l_s} \epsilon_y$

If $G \le G_1$		If $G > G_1$
$\epsilon_s = \epsilon_y$		Calculate inelastic fracture energy $G_2 = G - G_e$

Estimate maximum inelastic steel strain ϵ_s
$G_2 = \displaystyle\int_{\epsilon_y}^{\epsilon_s} \tau_{max} \left(1 - 0.8 \left(1 - e^{0.7\left(1 - \frac{\epsilon}{\epsilon_y}\right)}\right)\right) d\epsilon$

Figure 5.11 Flowchart to estimate the maximum strain that can be transferred by the lap splice in HSS collar strengthened beams, where G_t is total interfacial fracture energy.

The process demonstrated in Figure 5.11 is shown in Figure 5.12 for the case of Type-I, Type-II, and Type-III failure. The main idea is that the since the maximum strain in unstrengthened lap splices is lower than the yield strain, the total interfacial fracture energy G only comprises the pre-yield interfacial fracture energy G_1. In the case of Type-II failure, a partial improvement was observed. The total interfacial fracture energy G was greater than the pre-yield interfacial fracture energy G_1 but the post-yield interfacial fracture energy G_2 was limited to a strain ϵ_s lower than the

fracture strain ϵ_u. Therefore, the post-yield interfacial fracture energy G_2 was needed to be adjusted accordingly. This was done by following the flow of steps in Figure 5.11. Finally, the total interfacial fracture energy G in the case of Type-III failure comprises the full available interfacial fracture energy in the pre-yield and post-yield zones. For sufficiently confined beams, the maximum strain was considered to be the fracture strain. For insufficiently confined beams, the maximum strain was calculated by following the proposed procedure.
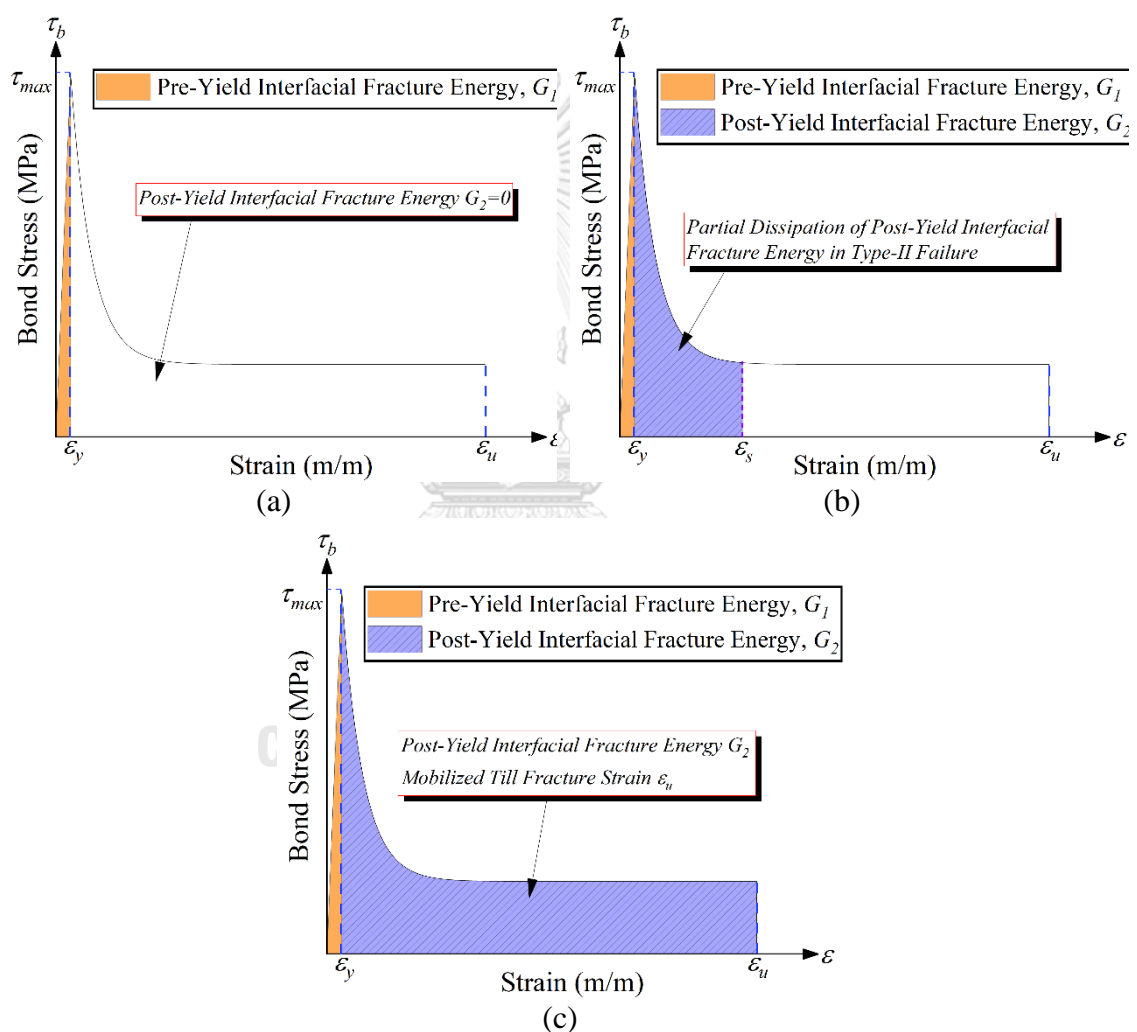
Figure 5.12 Definitions of interfacial fracture energy in lap splices with (a) Type-I failure, (b) Type-II failure, and (c) Type-III failure.

5.3. Estimation of Properties of Concrete Fibers

5.3.1. Estimation of Internal Steel Confined Concrete Strength and Strain

For concrete confined with internal stirrups in the shear-span zone, the model of Mander et al. [80] was used to estimate confined concrete properties. For convenience, the model is repeated here.

Step 1: Calculate c/c dimensions of stirrups in orthogonal directions.

$$b_c = b - 2\left(c_s + \left(\frac{d'_b}{2}\right)\right) \qquad 5.9$$

$$d_c = d - 2\left(c_b + \left(\frac{d'_b}{2}\right)\right) \qquad 5.10$$

where b and d are the beam's width and height, respectively, c_s and c_b are concrete side and bottom cover, respectively, and d'_b is the diameter of stirrups.

Step 2: Area of concrete core enclosed by centerlines of stirrups

$$A_c = b_c \times d_c \qquad 5.11$$

Step 3: Calculation of longitudinal reinforcement ratio and A_{cc}

$$\rho_{cc} = \frac{A_s}{A_c} \qquad 5.12$$

$$A_{cc} = A_c(1 - \rho_{cc}) \qquad 5.13$$

where A_{cc} is core area excluding total longitudinal steel area A_s.

Step 4: Total plan area of ineffectually confined core concrete at the level of the hoops when there are n longitudinal bars

$$w_{ib} = b - \left(2(c_s + d_b)\right) \qquad 5.14$$

$$w_{id} = d - \left(2(c_b + d_b)\right) \qquad 5.15$$

where w_{ib} and w_{id} are the clear distance between longitudinal bars in the width and height directions of the beam section, respectively.

$$A_i = \left[2\left(\frac{w_{ib}^2}{6A_c}\right) + 2\left(\frac{w_{id}^2}{6A_c}\right)\right] \qquad 5.16$$

Step 5: Confinement effectiveness coefficient k_e

$$k_e = \frac{\left[(1 - A_i)\left(1 - \frac{s}{2b_c}\right)\left(1 - \frac{s}{2d_c}\right)\right]}{1 - \rho_{cc}} \qquad 5.17$$

where s is the clear spacing between hoops.

Step 6: Confinement pressures in orthogonal directions

$$f_{ley} = \frac{2A'_s}{sb_c} \times k_e \times f_y \qquad\qquad 5.18$$

$$f_{lex} = \frac{2A'_s}{sd_c} \times k_e \times f_y \qquad\qquad 5.19$$

where A'_s and f_y are the area and yield strength of stirrups, respectively.

Step 7: Average uniform confinement pressure

$$f_{le} = \frac{f_{lex} + f_{ley}}{2} \qquad\qquad 5.20$$

Step 8: Confined peak compressive strength and corresponding strain

$$f'_{cc} = f'_c \left[-1.254 + 2.254\sqrt{1 + \frac{7.94 f_{le}}{f'_c}} - 2\frac{f_{le}}{f'_c} \right] \qquad\qquad 5.21$$

$$\epsilon'_{cc} = 0.002 \left(1 + 5\left(\frac{f'_{cc}}{f'_c} - 1 \right) \right) \qquad\qquad 5.22$$

where f'_c is unconfined cylindrical compressive strength. f'_{cc} is confined concrete compressive strength and ϵ'_{cc} is corresponding axial strain.

Step 9: Complete axial stress-strain response

$$E_{sec} = \frac{f'_{cc}}{\epsilon'_{cc}} \qquad\qquad 5.23$$

$$r = \frac{E_c}{E_c - E_{sec}} \qquad\qquad 5.24$$

$$f_{cc} = \frac{\left(r f'_{cc} \times \frac{\epsilon_{cc}}{\epsilon'_{cc}} \right)}{r - 1 + \left(\frac{\epsilon_{cc}}{\epsilon'_{cc}} \right)^r} \qquad\qquad 5.25$$

where E_{sec} is secant modulus at peak compressive strength. f_{cc} is axial stress corresponding to any axial strain ϵ_{cc}.

5.3.2. Estimation of HSS Collars Confined Concrete Strength and Strain

The concrete within the constant moment region was modeled by following the procedure of Chapman and Driver [99]. The details of the procedure are already given in Chapter 2. Here, the procedure is summarized in a flowchart, as shown in Figure 5.13. The procedure is not repeated here for conciseness. An iterative strategy

is required to trace the full stress-strain response of steel collar confined concrete. The axial strain value is assumed initially. Twelve unknowns are encountered during a particular iteration, including the equilibrium confining pressure $(\sigma_h)_i$, the secant modulus of concrete $(E_c)_i$, the Poisson's ratio $(\nu_c)_i$, the constant $(C)_i$, the strain at peak compressive strength in confined state $(\epsilon'_{cc})_i$, the secant slope of steel collar confining pressure-lateral strain relation $(E_{collar})_i$, the lateral strain $(\epsilon_l)_i$, the peak confined concrete stress $(f'_{cc})_i$, the stress corresponding to the assumed axial strain $(f_{cc})_i$, the parameters $(x)_i$ and $(r)_i$ for the Popovics [101] equation, and $(E_{sec})_i$. For each value of axial strain, the values of these twelve unknowns are assumed arbitrarily at the start of iterations. For each iteration, the values obtained in the previous iteration are used. Appendix A3 presents detail calculations along with the related MATLAB scripts to estimate compressive stress vs. strain response of HSS collar confined concrete.

จุฬาลงกรณ์มหาวิทยาลัย

CHULALONGKORN UNIVERSITY

Estimate Collar Confining Pressure vs. Lateral Strain Relation

Input General Strain Value $(\epsilon_{cc})_i$

Assume: $(\sigma_{passive})_i$, $(E_c)_i$, $(v_c)_i$, $(C)_i$, $(\epsilon'_{cc})_i$, $(E_{collar})_i$, $(\epsilon_l)_i$, $(f'_{cc})_i$, $(f_{cc})_i$, $(x)_i$, $(r)_i$, $(E_{sec})_i$

Estimate Constant C: $(\boldsymbol{C_1})_i^* = 1.914\left(\frac{(\sigma_{passive})_i}{f'_{co}}\right) + 0.719$

Estimate Secant Poisson's Ratio v_c:
$$(\boldsymbol{v_c})_i^* = v_{co}\left[(C)_i^*\left(\frac{(\epsilon_{cc})_i}{(\epsilon'_{cc})_i}\right) + 1\right] \le 0.50$$

Estimate Collar Lateral Strain ϵ_l: $(\boldsymbol{\epsilon_l})_i^* = (v_c)_i^* \times (\epsilon_{cc})_i$

Estimate Confining Pressure $(\boldsymbol{\sigma_{collar}})_i^*$ from Confining Pressure vs. Lateral Strain Relation.

Estimate Secant Slope of Confining Pressure vs. Lateral Strain Relation $(E_{collar})_i^*$:
$$(\boldsymbol{E_{collar}})_i^* = \frac{(\sigma_{collar})_i^*}{(\epsilon_l)_i^*}$$

Estimate the Equilibrium Confining Pressure $(\sigma_h)_i^*$:
$$(\boldsymbol{\sigma_{collar}})_i^* = \frac{(v_c)_i^*(\epsilon_{cc})_i}{\frac{1}{(E_{collar})_i^*} + \frac{1 - (v_c)_i^*}{(E_c)_i}}$$

Incorporate collar spacing and effectiveness:
$$(\boldsymbol{\sigma_{collar}})_i^* = (\sigma_{collar})_i^* \times \frac{t}{s'} \times \frac{(h - 0.5s')^2}{h^2}$$

Estimate Peak Confined Compressive Strength $(f'_{cc})_i^*$:
$$(\boldsymbol{f'_{cc}})_i^* = f'_{co}\left[2.254\sqrt{1 + \frac{7.94(\sigma_{collar})_i^*}{f'_{co}}} - 2\frac{(\sigma_{collar})_i^*}{f'_{co}} - 1.254\right]$$

Estimate Strain at Peak Confined Compressive Strength $(\epsilon'_{cc})_i^*$:
$$(\boldsymbol{\epsilon'_{cc}})_i^* = \epsilon'_{co}\left[1 + 5\left(\frac{(f'_{cc})_i^*}{f'_{co}} - 1\right)\right]$$

Estimate Stress Corresponding to (ϵ_{cc}): $(\boldsymbol{f_{cc}})_i^* = \frac{(f'_{cc})_i^*(x)_i(r)_i}{(r)_i - 1 + (x)_i^{r_i}}$

Estimate $(x)_i^*$: $(\boldsymbol{x})_i^* = \frac{(\epsilon_{cc})_i}{(\epsilon'_{cc})_i^*}$

Estimate $(r)_i^*$: $(\boldsymbol{r})_i^* = \frac{E_{co}}{E_{co} - ((f'_{cc})_i^*/(\epsilon'_{cc})_i^*)}$

Estimate Secant Modulus of Concrete $(E_c)_i^*$: $(\boldsymbol{E_c})_i^* = \frac{(f_{cc})_i^*}{(\epsilon_{cc})_i}$

Estimate Secant Modulus of Concrete $(E_c)_i^*$: $(\boldsymbol{E_c})_i^* = \frac{(f_{cc})_i^*}{(\epsilon_{cc})_i}$

No?   Check the Tolerance of Assumed and Estimated Values:
$$\forall\ |(value)_i - (value)_i^*| < \boldsymbol{tolerance}$$ *Yes?*

Update all $(value)_i$ with $(value)_i^*$

Input New $(\epsilon_{cc})_i$

Figure 5.13 Flowchart to trace the compressive stress-strain response of HSS collar confined concrete by Chapman and Driver [99].

To follow the procedure given in Figure 5.13, it is required to have the confining pressure vs. lateral strain relation of HSS collars. For this purpose, an approach similar to the approach of Chapman and Driver [99] is adopted. The ends of steel collars were assumed fixed. Therefore, two analysis stages were defined, as shown in Figure 5.14. In the first analysis stage, the confining pressure was increased till the formation of plastic hinges at the collar ends. After the formation of plastic hinges at collar ends, the second analysis stage started, and the collar pressure was further increased till the formation of another plastic hinge in the middle of the HSS collar element, as shown in Figure 5.14. The complete procedure and the corresponding equations are already presented in Chapter 2.
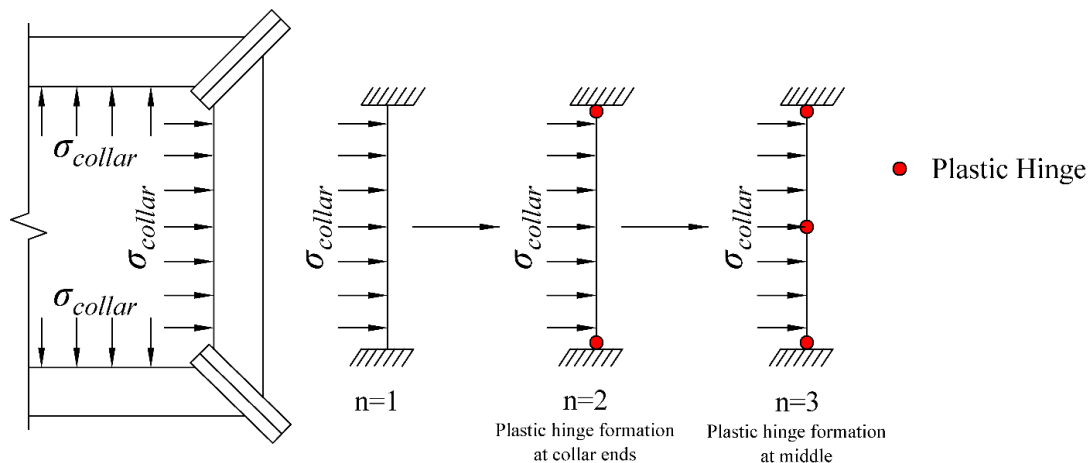
Figure 5.14 The plastic collapse mechanism of HSS steel collars under progressive lateral expansion.

5.4. Non-Linear Fiber Modelling of Unstrengthened Beams

Though experimental testing is the most dependable way to evaluate the behavior of structural members, it is difficult to consider every variable in the testing program. This makes an analytical approach an important tool for predicting structural performance and advanced structural design. The following sections summarize the analytical modeling of tested beams. Appendix A4.1 presents a sample OpenSees script for nonlinear modeling of an unstrengthened beam.

5.4.1. Element Discretization

A nonlinear finite element model of the beam was developed in *OpenSees* [130]. Since all control beams experienced sudden splitting, whereas HSS collars inhibited such brittle failures, different constitutive material models within lap splice zones were desired. Each element was modeled using the displacement-based beam-column element of *OpenSees*. For each element, five integration points were used, and Gauss-Lobatto quadrature rules were applied. One-half of each beam about the centerline was modeled owing to the symmetry. Each beam was discretized into four elements. Element 1 spanned the shear span of each beam, i.e., from the loading point to the left support. The length of element 2 ranged from the loading point to the left starting point of the notch, element 3 modeled the notch, and element 4 modeled the lap spliced part of the beam. The complete discretization of beams is shown in Figure 5.15.
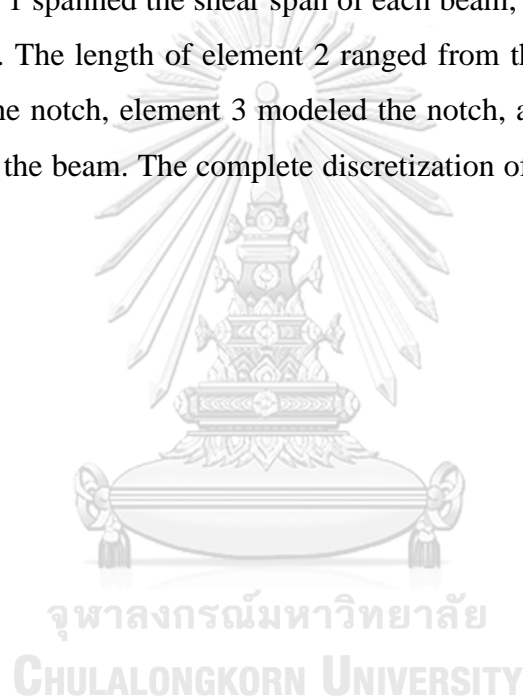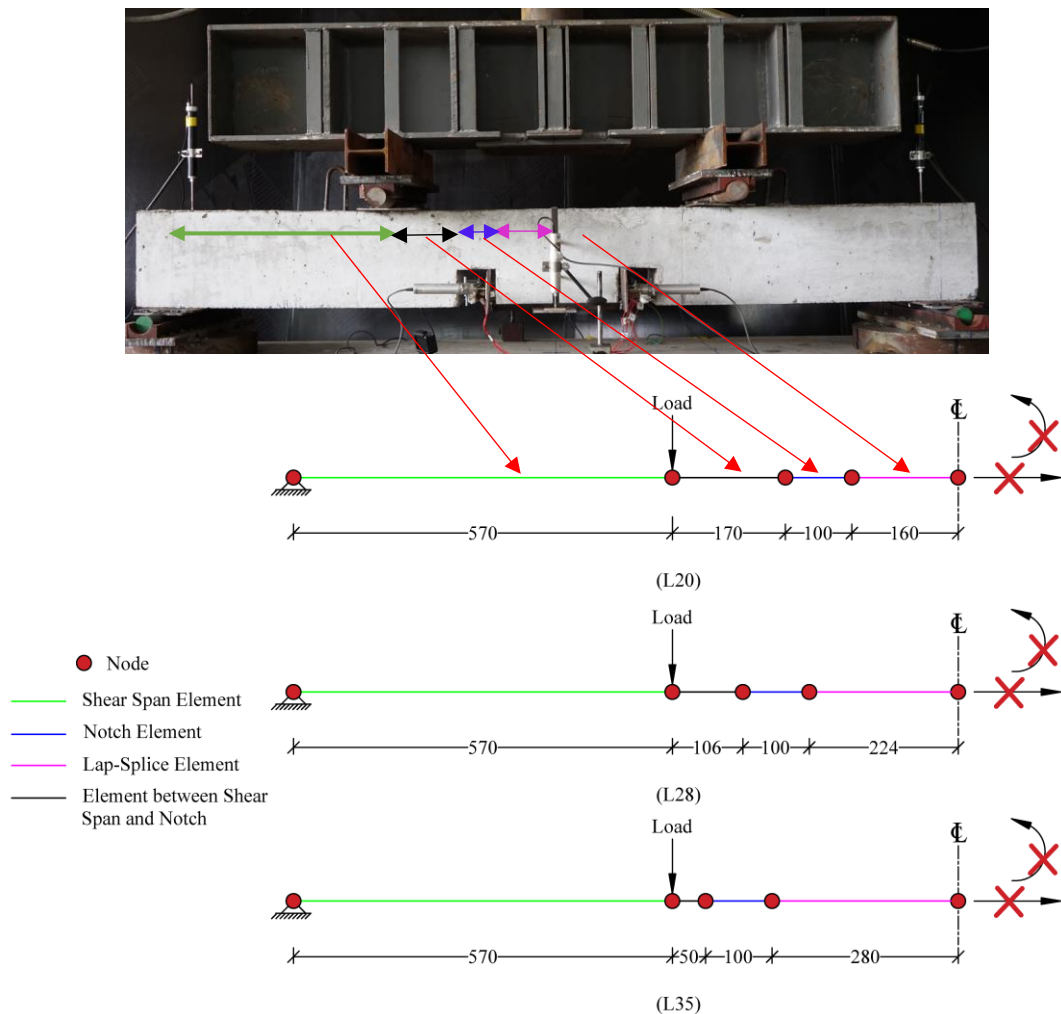
Figure 5.15 Beam length discretization for (a) Group L20, (b) Group L28, and (c) Group L35.

5.4.2. Cross-Section Modelling

Within the shear span, core concrete was modeled using confined concrete, whereas cover concrete was modeled using unconfined concrete, as shown in Figure 5.16(a). Since no internal confinement was provided in the form of stirrups, all the section within the lap spliced zone was considered unconfined, and subsequently, unconfined material properties were assigned to them. As shown in Figure 5.16, fiber discretization for the lap splice zone was the same as the section within the shear-span zone. For the notch (element 3), concrete fibers were omitted for the lower 100 mm of the section to replicate the actual section within the notch, as shown in Figure 5.16(c).
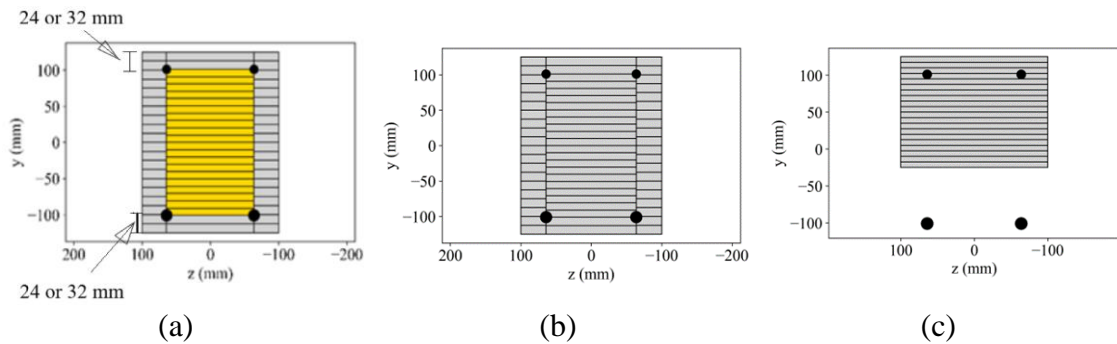
Figure 5.16 Section definition within (a) element 1 (b) element 2 and 4, and (c) element 3.

5.4.3. Modeling of Concrete Fibers

For unconfined concrete, concrete strength obtained from axial compression results was used as the peak strength. The corresponding strain was assumed to be -0.002. Figure 5.17 presents complete axial stress-strain curves for all control beams, including confined and unconfined curves. Table 5.1 presents peak compressive strengths and corresponding strains for both stirrup-confined and unconfined concrete. Concrete was modeled using *Concrete04* uniaxial material, which is based on the recommendations of Popovics [101]. The ultimate strain ϵ_{cu} was taken corresponding to the 80% and 20% drop in the peak compressive strength f'_{cc} for unconfined and confined concrete, respectively.
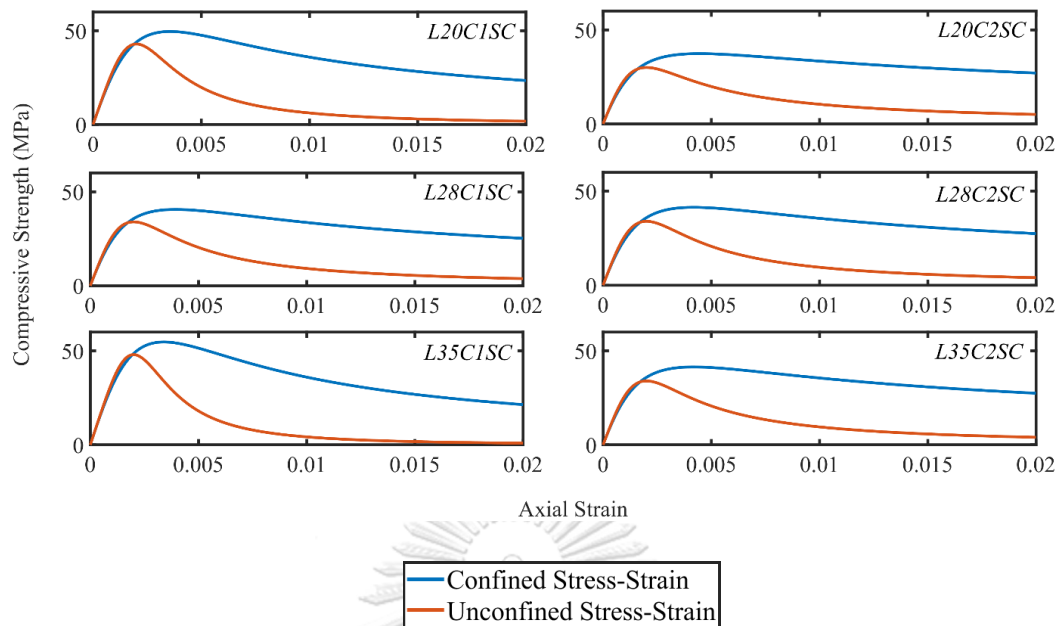
Figure 5.17 Compressive stress-strain response of the cover and core concrete in control beams.

Table 5.1 Summary of peak compressive strength f'_{cc}, strain corresponding to peak compressive strength ϵ'_{cc}, and the crushing strain ϵ_{cu} for concrete in control beams.

Beam ID	f'_{cc} (MPa)		ϵ'_{cc}		ϵ_{cu}	
	Unconfined	Confined	Unconfined	Confined	Unconfined	Confined
L20C1SC	−43.00	−47.71	−0.0020	−0.0034	−0.0030	−0.0083
L20C2SC	−30.00	−40.58	−0.0020	−0.0040	−0.0030	−0.0155
L28C1SC	−34.70	−40.58	−0.0020	−0.0039	−0.0030	−0.0120
L28C2SC	−34.70	−41.42	−0.0020	−0.0042	−0.0030	−0.0120
L35C1SC	−43.00	−47.71	−0.0020	−0.0034	−0.0030	−0.0075
L35C2SC	−34.70	−41.42	−0.0020	−0.0042	−0.0030	−0.0012

5.4.4. Modeling of Steel Fibers

Steel rebars were modeled using *Hysteretic* material available in the *OpenSees* library. A bilinear approximation was used for constitutive steel law for steel rebars within the shear span. As described in earlier chapters, a bilinear approximation was carried out of the actual tensile stress-strain relationship. As shown in Figure 5.18, the blue dotted line represents this approximation that was used to describe longitudinal steel rebars within the shear span region. It was observed in tests that steel rebars did not yield in the case of control beams. Therefore, their stress-strain relationship needed to be modified. The splice strengths calculated by the four methods described

earlier are presented in Table 5.2. The modified stress-strain relations obtained by using four models are shown in Figure 5.19.
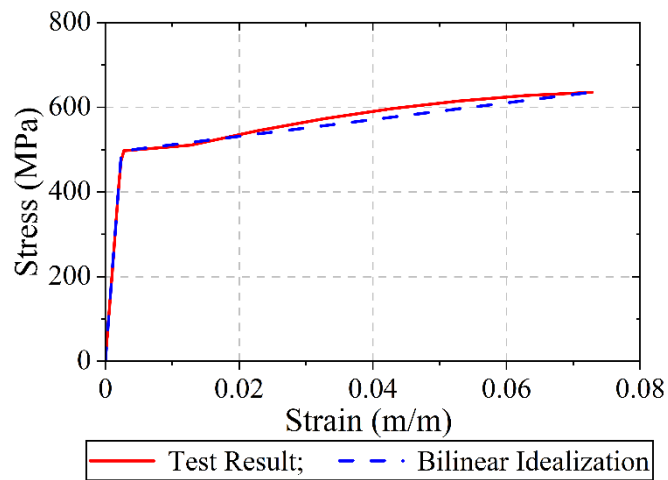
Figure 5.18 Longitudinal steel stress-strain relation for *Hysteretic* material.

Table 5.2 Predicted splice strengths by analytical models.

Beam ID	Predicted $f_{s,max}$ (MPa)			
	Belejo [127]	Tariverdilo et al. [78]	Elwood et al. [129]	Lettow & Eligehausen [126]
L20C1SC	312	322	324	360
L20C2SC	493	331	404	377
L28C1SC	443	381	364	402
L28C2SC	555	464	476	451
L35C1SC	470	497*	497*	493
L35C2SC	557	497*	497*	497*

Upper limit on yield strength reached.
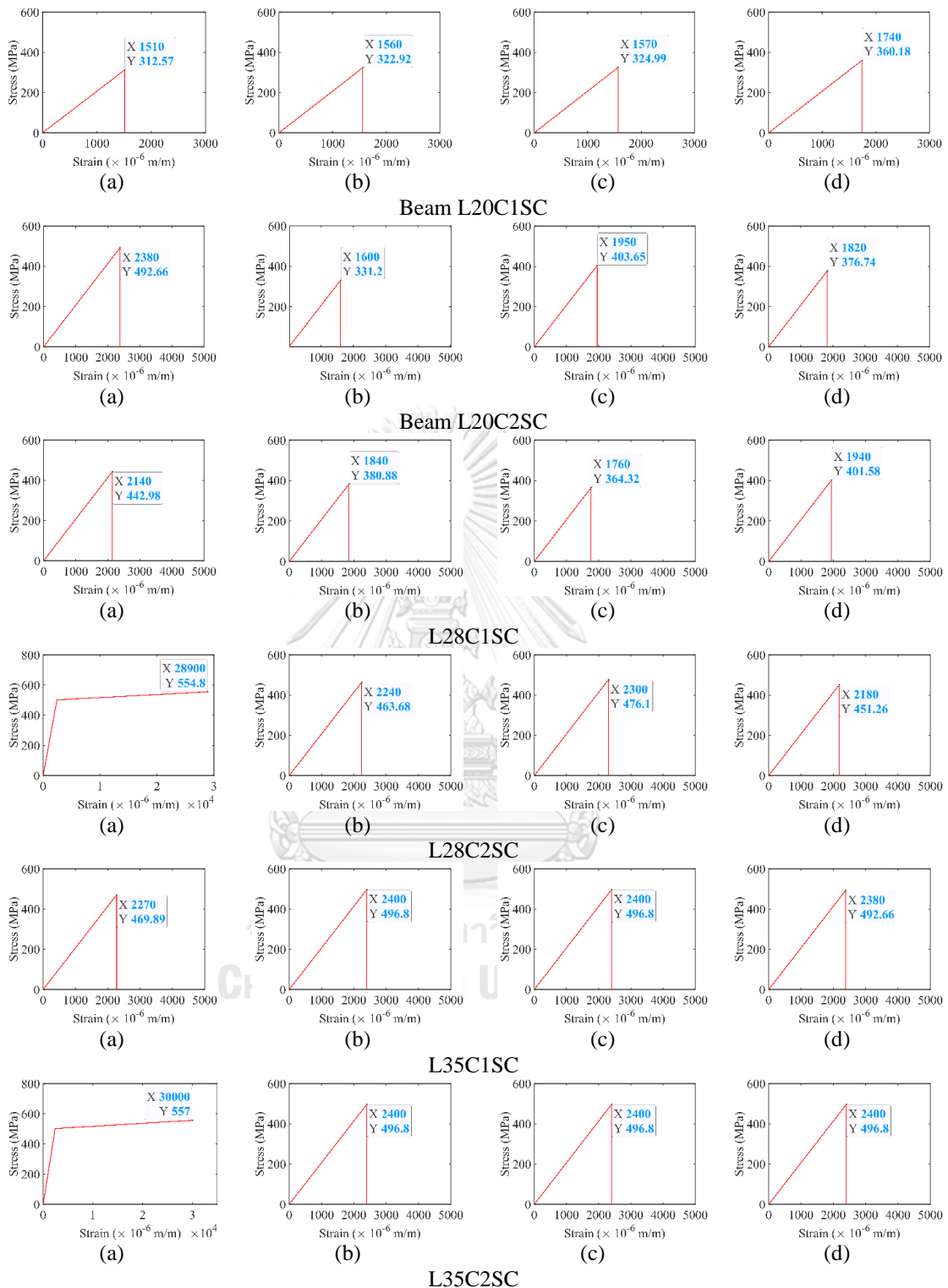
Figure 5.19 Modified stress-strain relations of lap spliced bars estimated by the models of (a) Belejo, (b) Tariverdilo et al., (c) Elwood et al., and (d) Lettow and Eligehausen.

5.4.5. Comparison of Predicted and Experimental Load-Deflection Curves

The comparison of the analytically predicted load-deflection response of control beams with experimental results is presented in Figure 5.20. It can be seen that *OpenSees* predictions provided a close match with experimental results in terms of the initial stiffness of all the control beams. A comparison of the peak loads with experimental values is presented in Table 5.3. The best performance was observed for the model of modified Belejo [127], which is characterized by an average percentage error of 6.8%. This is followed by the model of Lettow and Eligehausen [126], which produced an average percentage error of 7.1%. It is to be noted that the ductile region of the Beam L35C2SC could not be captured by the adopted modeling scheme. This is because a brittle stress-strain response for the concrete in the constant moment region was adopted due to no confinement by transverse reinforcement. Though the model by Modified Belejo [127] resulted in a yield plateau of lap spliced steel bars till stress of 557 MPa, the brittle drop in the capacity of unconfined concrete resulted in a drop in the predicted load-deflection curve.

Table 5.3 Comparison of predicted and experimental peak loads of control beams.

Beam ID	Experimental Peak Load (kN)	Predicted Peak Load (kN)							
		Modified Belejo [127]		Tariverdilo et al. [78]		Elwood et al. [129]		Lettow & Eligehausen [126]	
		Value	Error (%)	Value	Error (%)	Value	Error (%)	Value	Error (%)
L20C1SC	102.2	92.0	-9.9	94.2	-7.8	94.9	-7.1	94.9	-7.1
L20C2SC	92.4	101.0	+9.3	83.5	-9.6	94.9	+2.7	90.5	-2.1
L28C1SC	115.1	111.7	-2.9	99.4	-13.6	95.9	-16.7	103.9	-9.7
L28C2SC	124.4	125.4	+0.8	114.6	-7.9	117.1	-5.9	112.8	-9.1
L35C1SC	155.4	139.1	-10.5	144.2	-7.2	141.8	-8.7	141.0	-9.3
L35C2SC	127.4	137.0	+7.5	120.5	-5.4	120.5	-5.4	120.5	-5.4
Average Difference			*6.8*		*8.6*		*7.8*		*7.1*

Upper limit on yield strength reached.
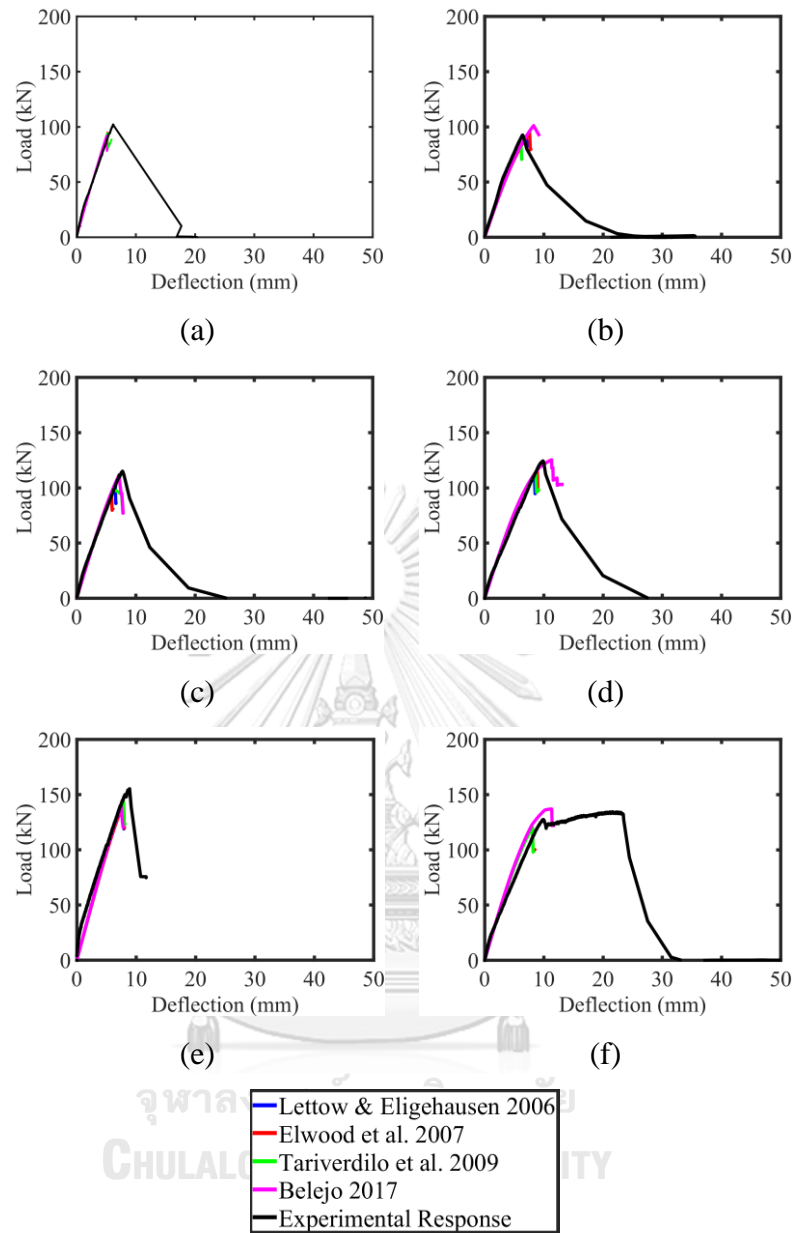
Figure 5.20 Comparison of analytical load-deflection response of control beams with their experimental results (a) Beam L20C1SC, (b) Beam L20C2SC, (c) Beam L28C1SC, (d) Beam L28C2SC, (e) Beam L35C1SC, and (f) Beam L35C2SC.

5.5. Non-Linear Fiber Modelling of Strengthened Beams

5.5.1. Element Discretization

The element discretization in the case of HSS collar strengthened beams was the same as that for the control beams. One element was used for the shear span, one element was used for the notch, one element was used for the lap splice zone, and one

element was used for the region between the loading point and the start of the notch, as shown in Figure 5.21. Appendix A4.2 presents a sample *OpenSees* script for nonlinear modeling of an HSS collar strengthened beam.
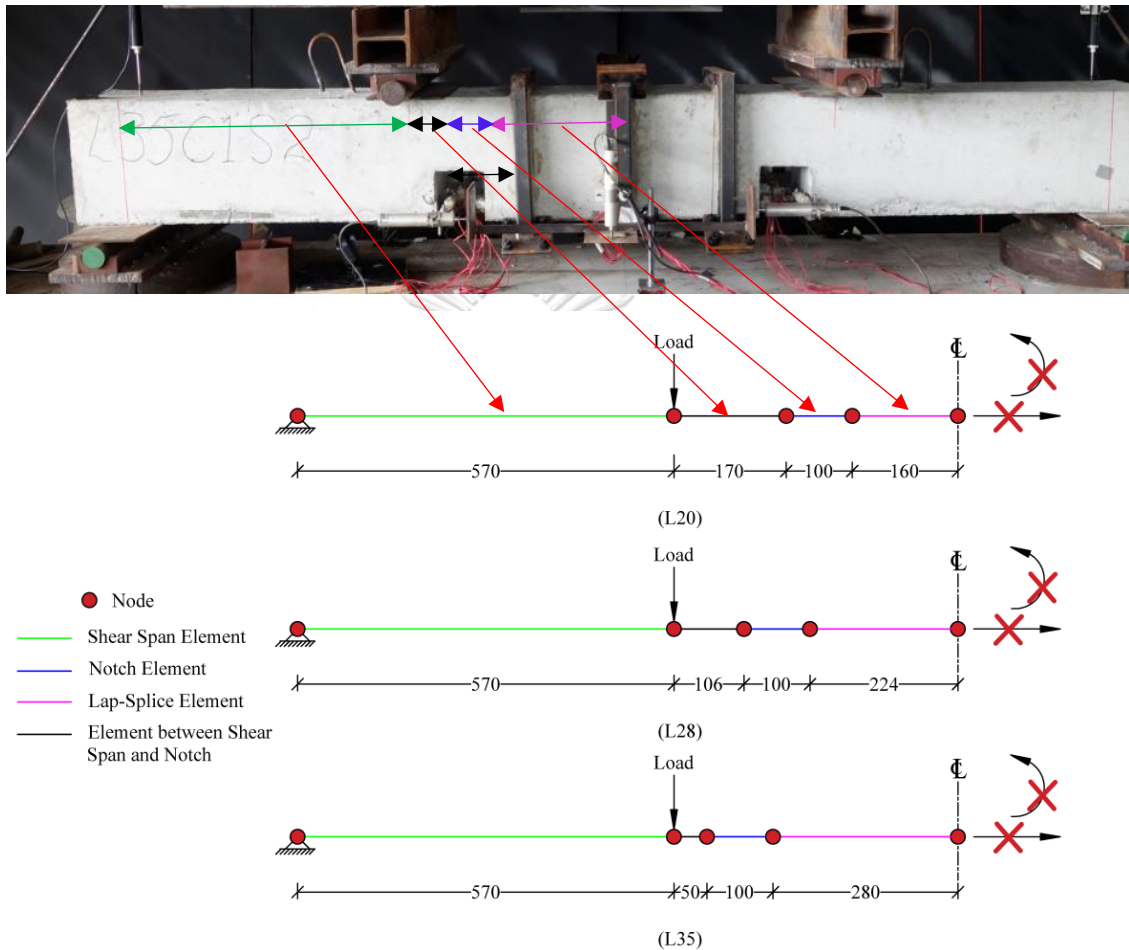
Figure 5.21 Element discretization for HSS collar strengthened beams in (a) Group L20, (b) Group L28, and (c) Group L35.

5.5.2. Cross-Section Modelling

The discretization of sections was the same as that for unstrengthened beams, with the only difference in the type of concrete fibers within the constant moment region. For HSS collar strengthened beams, the cross-section within the constant moment region was considered to be fully confined, whereas the cross-section within the shear zone was the same as that of unstrengthened beams, as shown in Figure 5.22. The discretization was performed only along the local y-axis because no load

was applied in the local z-direction of the section. The core and the vertical covers were divided into twenty fibers, whereas the bottom and top covers were divided into two fibers along the local y-axis.

(a)   (b)   (c)
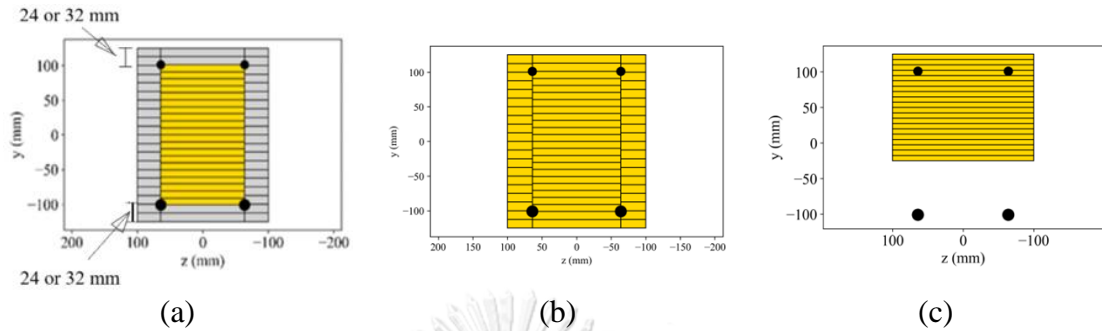
Figure 5.22 Cross-section discretization within (a) shear span, (b) element 2 and 4, and (c) element 3.

5.5.3. Modeling of Concrete Fibers

Concrete fibers within the shear span were modeled using a similar procedure as those in unstrengthened beams. Concrete fibers within the constant moment regions in strengthened beams were considered confined under the influence of HSS collars.

By following the procedure of Chapman and Driver [99] and assuming only two analysis stages, the resulting collar pressure vs. lateral strain relation is plotted in Figure 5.23. The collar pressure corresponding to plastic hinge formation at collar ends was estimated as 10.2 MPa, whereas an additional collar pressure of 3.3 MPa was required to achieve the plastic hinge at the middle of the collar element. Similarly, the lateral collar strain corresponding to the first and second analysis stages was estimated as 681×10^{-6} m/m and 1000×10^{-6} m/m, respectively. Beyond the lateral strain of 1000×10^{-6} m/m, a constant collar pressure of 13.5 MPa was assumed. The resulting concrete stress-strain relation was modeled using *Concrete04* material in *OpenSees*. Like the modeling of unstrengthened beams, three points, including the peak compressive stress f'_{cc}, strain at peak compressive stress ϵ'_{cc}, and the ultimate strain were required ϵ_{cu}. The ultimate strain ϵ_{cu} was defined as the value corresponding to the 20% drop in the peak compressive stress.
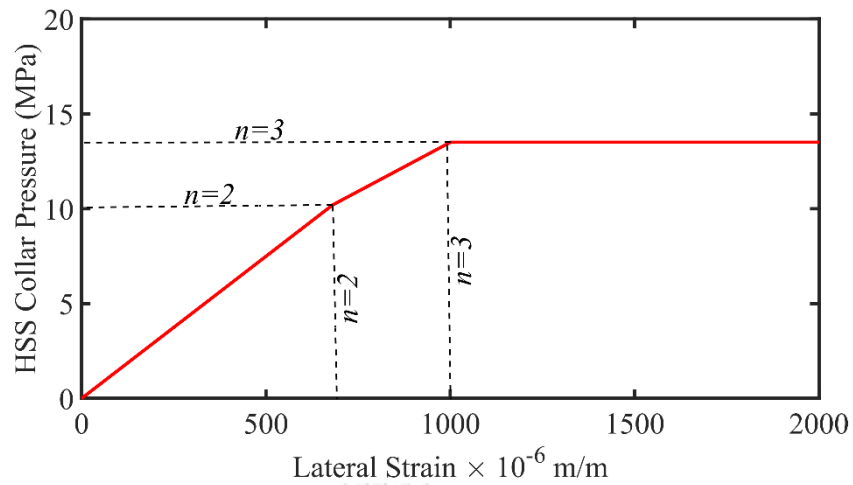
Figure 5.23 HSS collar pressure vs. lateral strain relation for beam collars.

The calculated values of peak compressive stress, strain at peak compressive stress, and ultimate strain are presented in Table 5.4, whereas the complete stress-strain response of HSS collar strengthened beams is shown in Figure 5.24. For comparison, stress-strain relations of the corresponding unconfined concrete are also plotted by using the model of Popovics.

Table 5.4 Summary of peak compressive strength, strain corresponding to peak compressive strength, and the crushing strain for concrete in HSS collar strengthened beams.

Beam ID	f'_{cc} (MPa)		ϵ'_{cc}		ϵ_{cu}	
	Unconfined	Confined	Unconfined	Confined	Unconfined	Confined
L20C1S200	-27.4	-29.8	-0.0020	-0.0035	-0.0030	-0.0091
L20C1S100	-29.5	-44.6	-0.0020	-0.0110	-0.0030	-0.0440
L20C1S75	-48.0	-72.4	-0.0020	-0.0120	-0.0030	-0.0470
L20C2S200	-34.7	-37.1	-0.0020	-0.0030	-0.0030	-0.0071
L20C2S100	-34.7	-50.0	-0.0020	-0.0080	-0.0030	-0.0350
L28C1S200	-34.9	-37.4	-0.0020	-0.0029	-0.0030	-0.0066
L28C1S100	-34.9	-50.6	-0.0020	-0.0080	-0.0030	-0.0340
L28C2S200	-34.9	-37.4	-0.0020	-0.0030	-0.0030	-0.0070
L35C1S200	-34.9	-37.4	-0.0020	-0.0030	-0.0030	-0.0070
L35C1S100	-34.9	-37.4	-0.0020	-0.0030	-0.0030	-0.0070
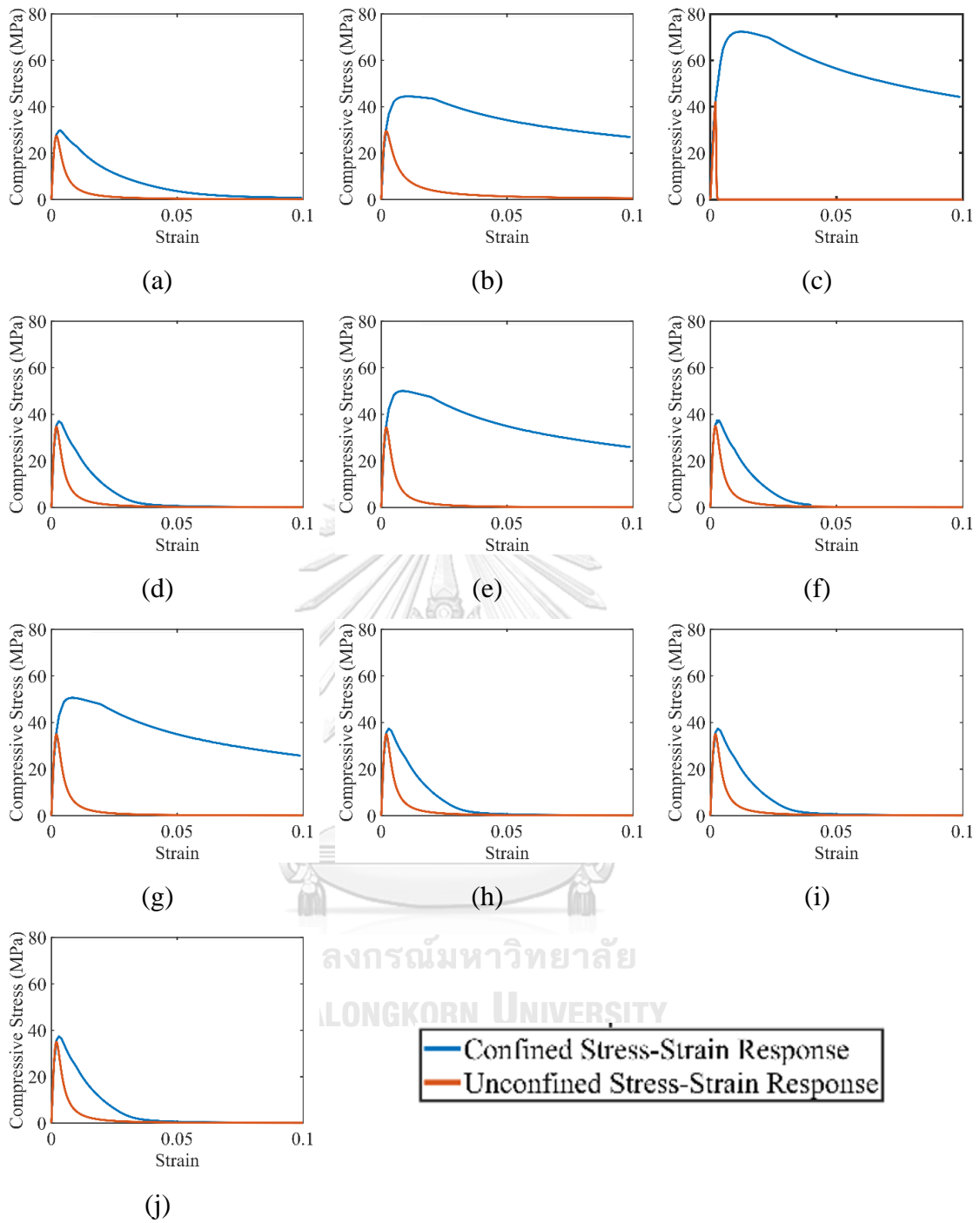
Figure 5.24 Stress-strain response of HSS collar strengthened concrete calculated by using the procedure of Chapman and Driver for beam (a) L20C1S200, (b) L20C1S100, (c) L20C1S75, (d) L20C2S200, (e) L20C2S100, (f) L28C1S200, (g) L28C1S100, (h) L28C2S200, (i) L35C1S200, and (j) L35C2S200.

5.5.4. Modeling of Steel Fibers

A summary of maximum lap splice strain calculated by using the approach shown in Figure 5.11 is presented in Table 5.5. It can be seen that for sufficiently confined beams L20C1S75, L20C2S100, L28C1S100, and L35C2S200, the maximum lap splice strain was greater than 0.073 (which is the fracture strain of lap spliced bars used in this study). For sufficiently confined beams L28C2S200 and L35C1S200, the maximum strain was smaller than the fracture strain. This is again attributed to the regression error in the equation for the increase in the interfacial fracture energy due to HSS collar confinement, as described in Chapter 4. The maximum lap splice strain calculated for all beams was input as the maximum value in the stress-strain response of bars within the constant moment region.

Table 5.5 Summary of maximum lap splice strain calculated by using the approach of Figure 5.11.

Beam ID	ΔG	τ_o	ϵ_o	G_o	G	G_1	G_2	ϵ_s
L20C1S200	0.01	4.13	0.0016	0.0066	0.0160	0.0199	-0.0040	0.0024*
L20C1S100	0.05	4.19	0.0016	0.0068	0.0567	0.0199	0.0368	0.0210
L20C1S75	0.13	4.74	0.0018	0.0087	0.1384	0.0199	0.1185	0.1137
L20C2S200	0.03	4.92	0.0019	0.0093	0.0344	0.0199	0.0145	0.0040
L20C2S100	0.13	4.92	0.0019	0.0093	0.1322	0.0199	0.1123	0.1000
L28C1S200	0.02	3.76	0.0020	0.0077	0.0262	0.0142	0.0120	0.0046
L28C1S100	0.10	3.76	0.0020	0.0077	0.0983	0.0142	0.0841	0.1006
L28C2S200	0.05	4.23	0.0023	0.0097	0.0608	0.0142	0.0466	0.0437
L35C1S200	0.03	3.40	0.0023	0.0078	0.0373	0.0114	0.0259	0.0280
L35C2S200	0.08	3.55	0.0024	0.0085	0.0899	0.0114	0.0783	0.0990

Maximum strain is assumed to be ϵ_y

The stress-strain relations of beams with Type-II failure are shown in Figure 5.25. Table 5.6 presents the comparison of predicted and experimental peak lap splice strains. It can be seen that the predicted strains are close to the experimental strains. For Beam L20C1S100, the predicted strain is higher than the experimental strain.

Table 5.6 Comparison of predicted and experimental peak lap splice strains.

Beam ID	Experimental ϵ_s	Predicted ϵ_s
L20C1S200	0.00225	0.00240
L20C1S100	0.01600	0.02100
L20C2S200	0.00295	0.00400
L28C1S200	0.00310	0.00460
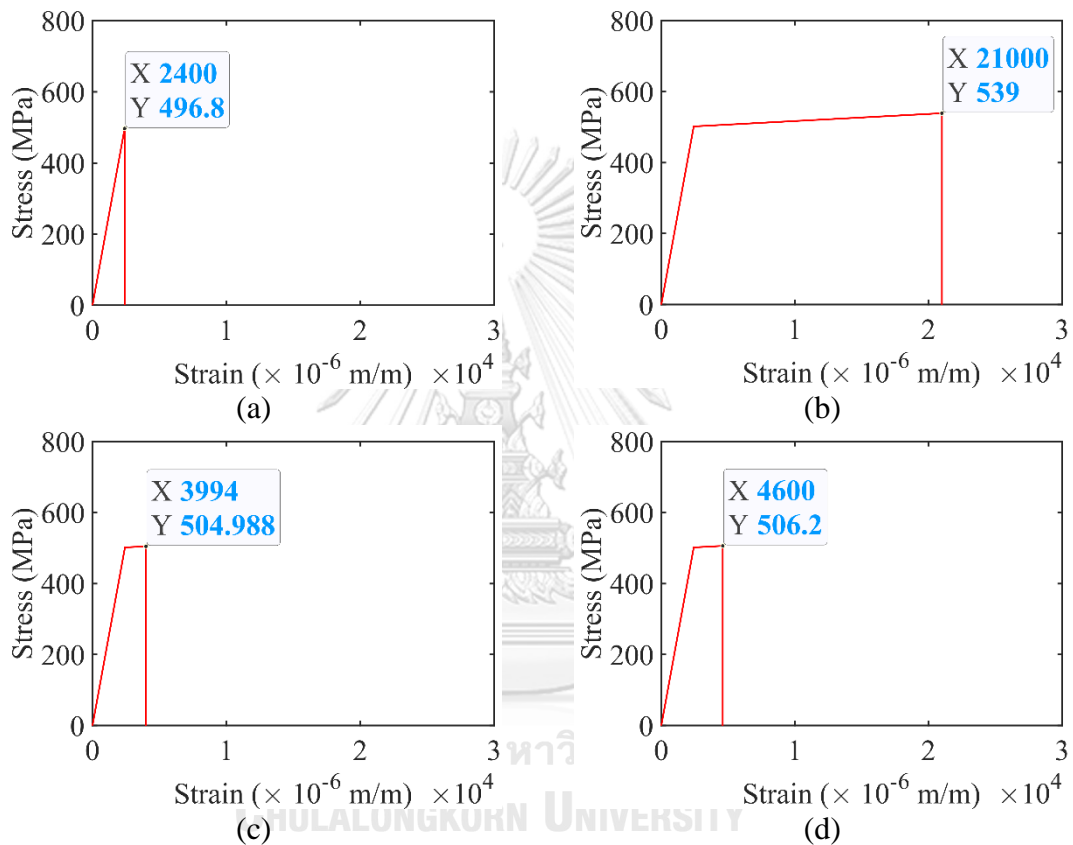
Figure 5.25 Stress-strain relations of lap spliced bars in beams with Type-II failure (a) L20C1S200, (b) L20C1S100, (c) L20C2S200, and (d) L28C1S200.

5.5.5. Comparison of Experimental and Predicted Load-Deflection Curves of HSS Collar Strengthened Beams

A comparison of the experimental and predicted load-deflection curves for HSS collar sufficiently confined beams is shown in Figure 5.26. It is evident that the experimental load-deflection curves of beams L20C1S75, L20C2S100, and L28C1S100 are accurately traced by *OpenSees* predictions. The experimental load-deflection curves of beams L28C2S200, L35C1S200, and L35C2S200 were traced by

OpenSees predictions till the onset of the second branch. Beyond that, a softening behavior was observed for *OpenSees* predictions in contrast to the stable experimental load-deflection behavior. This can be attributed to the low axial ductility of concrete predicted by the procedure of Chapman and Driver [99] for these beams (see Figure 5.24(h), Figure 5.24 (i), and Figure 5.24 (j)). This discrepancy may arise from the fact that the confinement ratios of steel collars used by Chapman and Driver [99] ranged from 0.030 to 0.054. At the same time, the confinement ratios used in this study ranged from 0.01365 to 0.0364. The confinement ratio of HSS collars in beams L28C2S200, L35C1S200, and L35C2S200 was 0.01365, which is significantly outside the range of the ratios used by Chapman and Driver [99]. Therefore, further studies on the axial strengthening of HSS collars with low confinement ratios are suggested to correctly predict their stress-strain response.
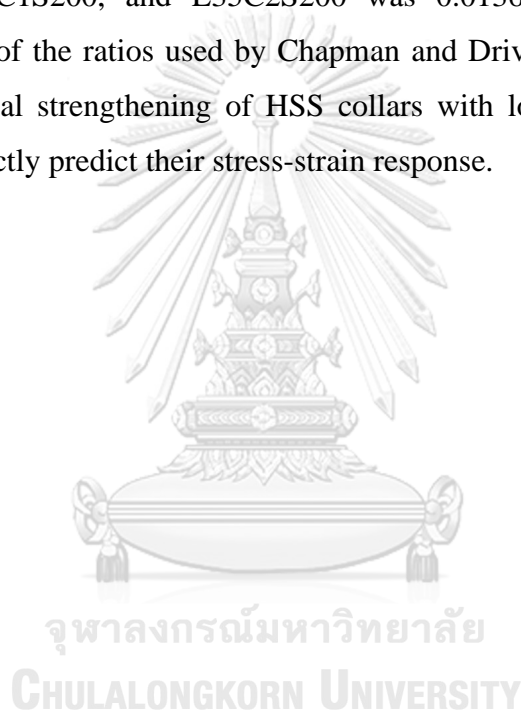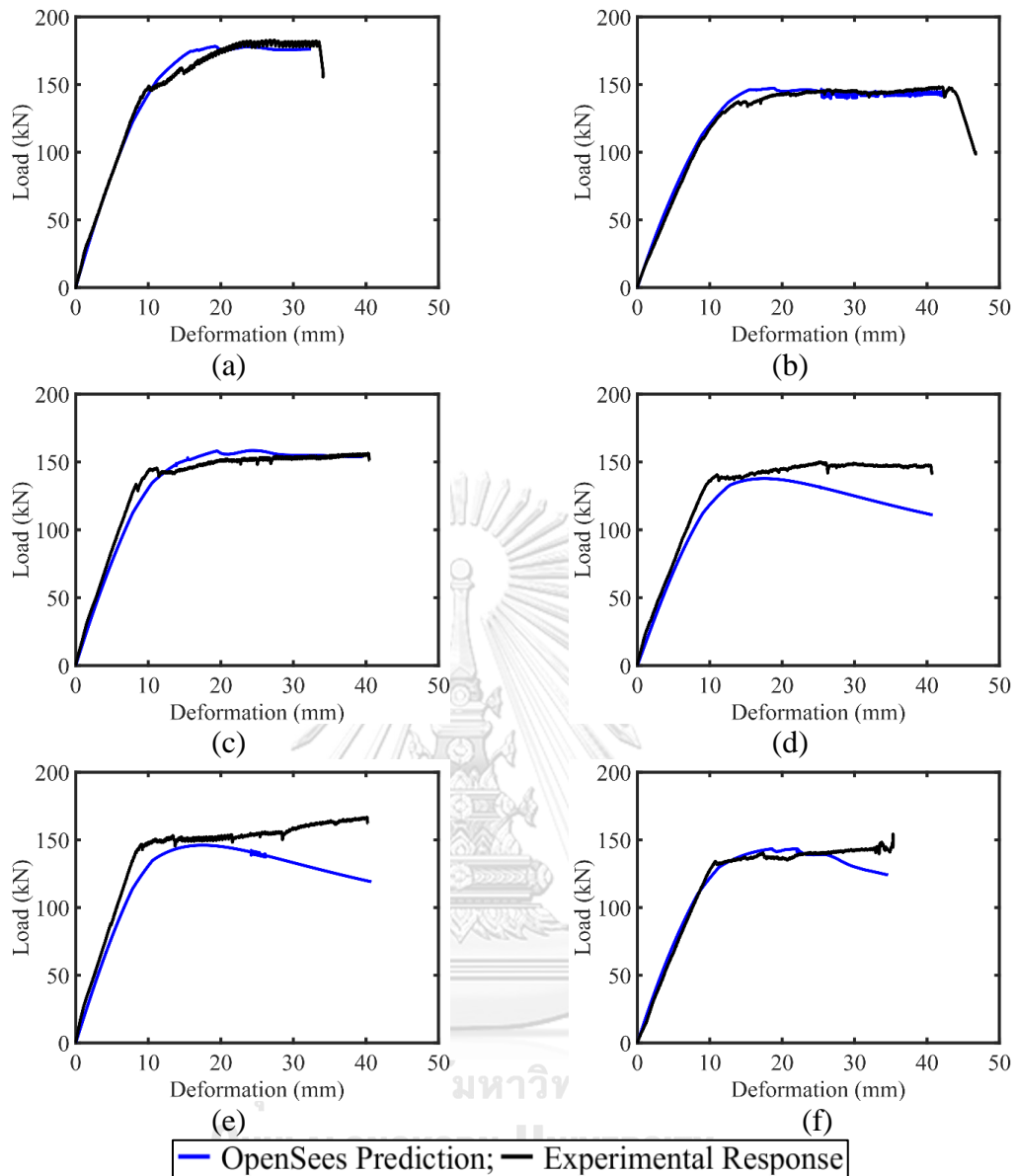
Figure 5.26 Comparison of predicted vs. experimental load-deflection curves for sufficiently confined beam (a) L20C1S75, (b) L20C2S100, (c) L28C1S100, (d) L28C2S200, € L35C1S200, and (f) L35C2S200.

The comparison of the experimental and predicted load-deflection response of insufficiently confined beams is shown in Figure 5.27. The experimental load-deflection curves are predicted with reasonable accuracy, especially the brittle drop in the capacity due to the lap splice failure.
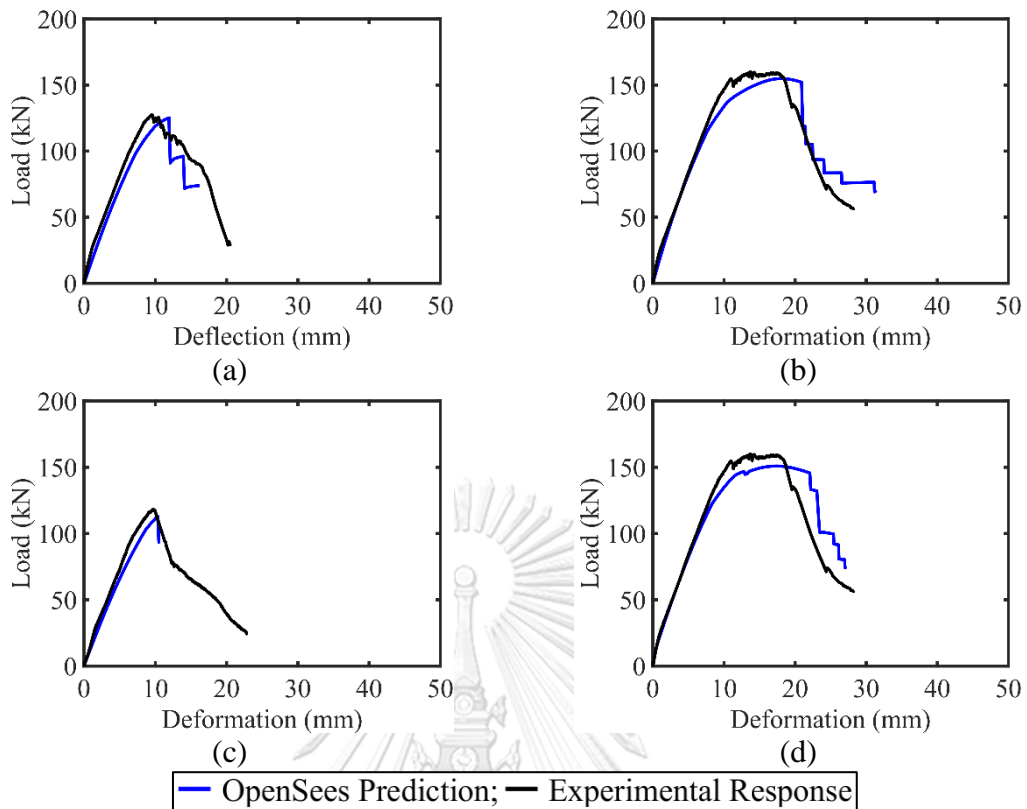
Figure 5.27 Comparison of predicted vs. experimental load-deflection curves for insufficiently confined beam (a) L20C1S200, (b) L20C1S100, (c) L20C2S200, and (d) L28C1S200.

5.6. Summary

In this chapter, *OpenSees* was used to predict the load-deflection response of beams tested in this study. Displacement-based beam-column elements were used to model half of the beam due to symmetry. In general, the proposed methodology in this chapter resulted in close agreement with experimental results for both the control and HSS collar strengthened beams. To predict the lap splice failure of Type-II beams, an analytical procedure was proposed based on the interfacial fracture energy. The predicted load-deflection response of beams with Type-II failure was in good agreement with experimental results. Concrete fibers were modeled by using the procedure of Chapman and Driver by incorporating the effect of flexural stiffness in estimating the collar confining pressure. The results show that the procedure of Chapman and Driver provided good agreements of experimental load-deflection curves in terms of initial stiffness and peak load. The experimental load-deflection curves of beams L28C2S200, L35C1S200, and L35C2S200 were traced by *OpenSees*

predictions till the onset of the second branch. Beyond that, a softening behavior was observed for *OpenSees* predictions in contrast to the stable experimental load-deflection behavior. This can be attributed to the low axial ductility of concrete predicted by the procedure of Chapman and Driver [99] for these beams (see Figure 5.24(h), Figure 5.24(i), and Figure 5.24(j)). This discrepancy may arise from the fact that the confinement ratios of steel collars used by Chapman and Driver [99] ranged from 0.030 to 0.054. In comparison, the confinement ratios used in this study ranged from 0.01365 to 0.0364. The confinement ratio of HSS collars in beams L28C2S200, L35C1S200, and L35C2S200 was 0.01365, which is significantly outside the range of the ratios used by Chapman and Driver [99]. Therefore, further studies on the axial strengthening of HSS collars with low confinement ratios are suggested to correctly predict their stress-strain response.
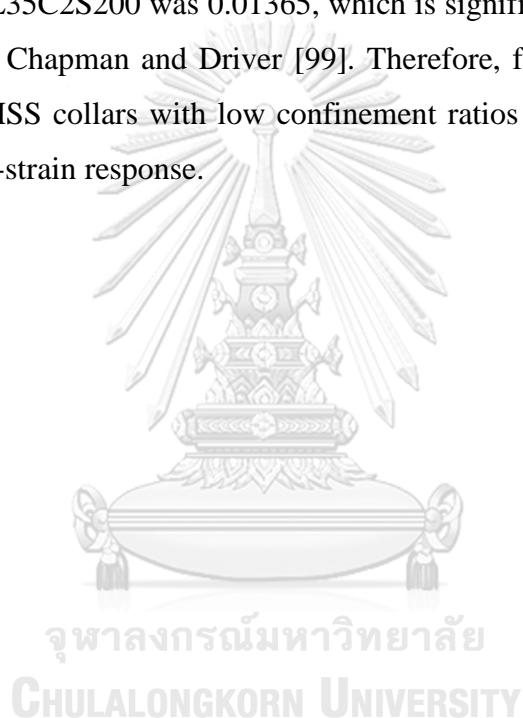
Chapter 6 Non-Linear Fiber Modelling of Columns with HSS Collars

It was shown in Chapter 5 that a nonlinear fiber model of RC members with HSS collar confined concrete fibers having stress-strain relation estimated by the model of Chapman and Driver resulted in close agreement with experimental results. In this chapter, the nonlinear fiber analysis is further extended to control, and HSS collar strengthened RC columns subjected to the hysteretic response. The experimental backbone load-deflection response of beams was predicted with good accuracy in Chapter 5. However, the strength and stiffness degradation in the case of hysteretic loading need to be addressed in a different manner in nonlinear fiber analysis. Further, the more realistic lateral loading on RC columns is not monotonic but reverse cyclic. Therefore, a member subjected to reverse cyclic loading is expected to experience rapid strength and stiffness degradation due to the accumulation of damage. Therefore, this chapter investigates the parameters in OpenSees to accurately predict the hysteretic response of control and HSS collar strengthened columns by incorporating the pinching and hysteretic strength and stiffness degradation.

At present, the only study on the strengthening of RC columns with substandard lap splices using HSS collars was performed by Kruavit [76]. Four RC columns were tested with a substandard lap splice of $28d_b$ with one column in as-built condition, whereas three columns were strengthened by HSS collars at spacings of 100 mm, 200 mm, and 333 mm. The remaining details can be found in Chapter 2. The following sections describe the non-linear fiber modeling of the four columns separately.

6.1. Method to Model Unstrengthened RC Columns with Substandard Lap splices

In Chapter 2, three modeling schemes were described to predict the hysteretic lateral load-deflection response of RC columns with substandard lap splices,

including the approaches of Tariverdilo et al. [78], Alvi et al. [89], and Opabola et al. [93]. The following sections describe the modeling strategy for the control column of Kruavit [76] by following each of the three approaches. The modeling strategies of Tariverdilo et al. [78] and Alvi et al. [89] are distributed plasticity-based, whereas the strategy of Opabola et al. [93] assumes concentrated plasticity at the base of the column. Appendix A4.3 presents the *OpenSees* script for nonlinear modeling of the unstrengthened column.

6.2. Modeling of Strengthened Flexure Control RC Columns

The non-linear fiber elements in *OpenSees* can capture the axial and flexural deformations only [131]. In the case of flexure-control columns, the shear effect can be ignored [132]. The lateral deformation in the case of flexural-controlled columns comprises the flexure deformation and an additional deformation that arises due to the yield penetration of anchored bars into the footing, as shown in Figure 6.1. In the case of a lap splice at the column base, there exists an additional slip due to the relative slip of lap spliced bars [133]. In the present study, the lap splice was incorporated by following the model of Tariverdilo et al. [89], which has been addressed in Chapter 2 in detail.
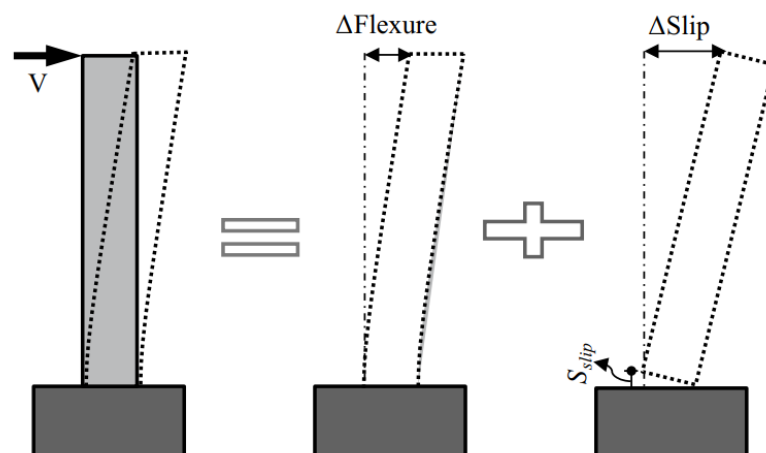
Figure 6.1 Lateral deformation components of a cantilever column (Wang et al. [134]).

The slip of reinforcing bars in anchorage cause rigid-body deformations causing greater drifts being additive to flexural deformation [135]. This can contribute

up to 40% to the total lateral deformation [136]. The yielding of the bar inside the footing causes extension resulting in a slip at the column-footing interface, which is also called "strain penetration" [86]. In the literature, two approaches are found to model the slip due to the strain penetration effect: (1) the micro-model approach and (2) the macro-model approach. A summary of the two approaches is shown in. From a computational perspective, macro-models are effective and practical, and the basis used directly reflects the strain penetration mechanism [137]. Hence, macro-models are preferred due to their simplicity and easy integration in fiber elements [138, 139].
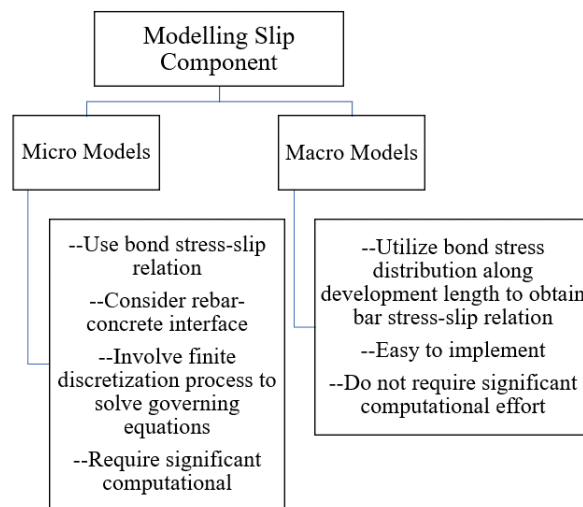
Figure 6.2 Approaches to model strain penetration.

In the present study, the model by Pan et al. [138] was used to incorporate the effect of strain penetration. This model is based on the most common approach to incorporate slip contribution to lateral deformation by adopting a stepped bond stress distribution proposed by Sezen and Setzler [135]. To include the effect of yield penetration of starter bars inside the footing, a macroscopic methodology by Pan et al. [138], who utilized the idea of Sezen and Setzler [135], was used, as shown in Figure 6.3. According to Pan et al. [138], the slip along the embedded bar can be obtained by integrating strain along the embedment length l_d as

$$slip = \int_0^{l_d} \epsilon(x)dx \qquad 6.1$$

Along the development length l_d, a stepped bond stress distribution was assumed with bond stress equal to $1.0\sqrt{f_c'}$ within the elastic length of the

development length and bond stress equal to $0.5\sqrt{f_c'}$ within the inelastic length. The development length l_d can be obtained by taking an equilibrium between the bond stress and steel stress as

$$l_d = \begin{cases} \dfrac{f_s d_b}{4u_b} & (f_s < f_y) \\[2ex] l_{dy} + l_d' = \dfrac{f_y d_b}{4u_b} + \dfrac{(f_s - f_y)d_b}{4u_b'} & (f_s > f_y) \end{cases} \qquad 6.2$$

The integration of Eq. 6.1 yields the following equation for the slip in elastic and strain hardening range as

$$slip = \begin{cases} \dfrac{\epsilon_s l_d}{2} & (f_s < f_y) \\[2ex] slip_y + slip' = \dfrac{\epsilon_y l_{dy}}{2} + \displaystyle\int_{l_{dy}}^{l_{dy}+l_d'} \epsilon(x)dx & (f_s > f_y) \end{cases} \qquad 6.3$$

$$slip_y = \frac{\epsilon_y l_{dy}}{2} = \frac{\epsilon_y f_y d_b}{8u_b} \qquad 6.4$$

$$slip_u = slip_y + slip_{sh} = \epsilon_y\left(\frac{f_y d_b}{8u_b} + \frac{f_y d_b}{4u_b'}(k_3 - 1)\left(\frac{2}{3}k_1 + \frac{1}{3}k_2\right)\right) \qquad 6.5$$

where $slip_y$ is the total slip in the elastic range, $slip_{sh}$ is the total slip in strain hardening range, and $slip_u$ is the total slip along the anchorage. The factors k_1, k_2, and k_3 are the factors used to describe the shape of stress-strain relation and are suggested to be 4.23, 46.9, and 1.36, respectively. In this way, the stress-strain relation of steel bars is modified as

$$\sigma = \begin{cases} \dfrac{E_s \epsilon}{k_o'} & (0 < \epsilon \le k_o'\epsilon_y) \\[2ex] f_y & (k_o'\epsilon_y < \epsilon \le k_1'\epsilon_y) \\[2ex] k_3 f_y + \dfrac{E_s(1 - k_3)}{\epsilon_y(k_2' - k_1')^2}(\epsilon - k_2'\epsilon_y)^2 & (k_1'\epsilon_y < \epsilon \le k_2'\epsilon_y) \\[2ex] k_3 f_y + \dfrac{E_s(1 - k_3)}{\epsilon_y(k_2 - k_1)^2}(\epsilon - k_2'\epsilon_y)^2 & (k_2'\epsilon_y < \epsilon) \end{cases} \qquad 6.6$$

where

$$k_o' = 1 + \alpha_y \qquad 6.7$$
$$k_o' = 1 + \alpha_y \qquad 6.8$$
$$k_1' = k_1 + \alpha_y \qquad 6.9$$
$$k_2' = k_2 + \alpha_y + \alpha_{sh} \qquad 6.10$$

$$\alpha_y = \frac{f_y d_b}{8 u_b L_e} \qquad \qquad 6.11$$

$$\alpha_{sh} = \frac{f_y d_b}{4 u_b' L_e} (k_3 - 1) \left(\frac{2}{3} k_1 + \frac{1}{3} k_2 \right) \qquad 6.12$$
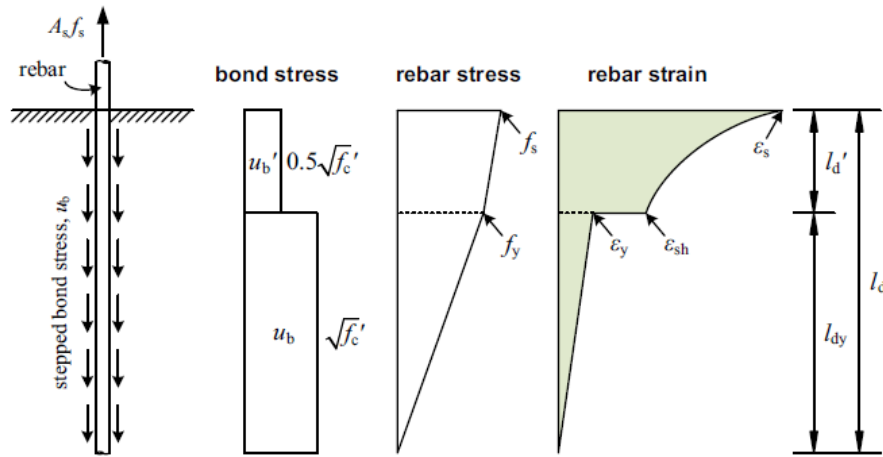
Figure 6.3 Anchorage slip model by Sezen and Setzler [135].

6.3. Application of Nonlinear Fiber Modelling on Control RC Column

6.3.1. Element Discretization

The length of the column was discretized, as shown in Figure 6.4. One element with a length equal to the lap splice length was used at the column base, whereas the remaining length of the column was modeled by using three elements of equal length for the approach of Tariverdilo et al. [78]. A *dispBeamColumn* element was used for all the elements. The model for the approach of Alvi et al. [89] was similar, with an additional zero-length spring at the column base to account for the additional deformation due to the slip of lap spliced bars. An elastic element with a length equal to the length of the column with a zero-length spring at the base was used to follow the approach of Opabola et al. [93]. An example of element discretization is shown in Figure 6.5.
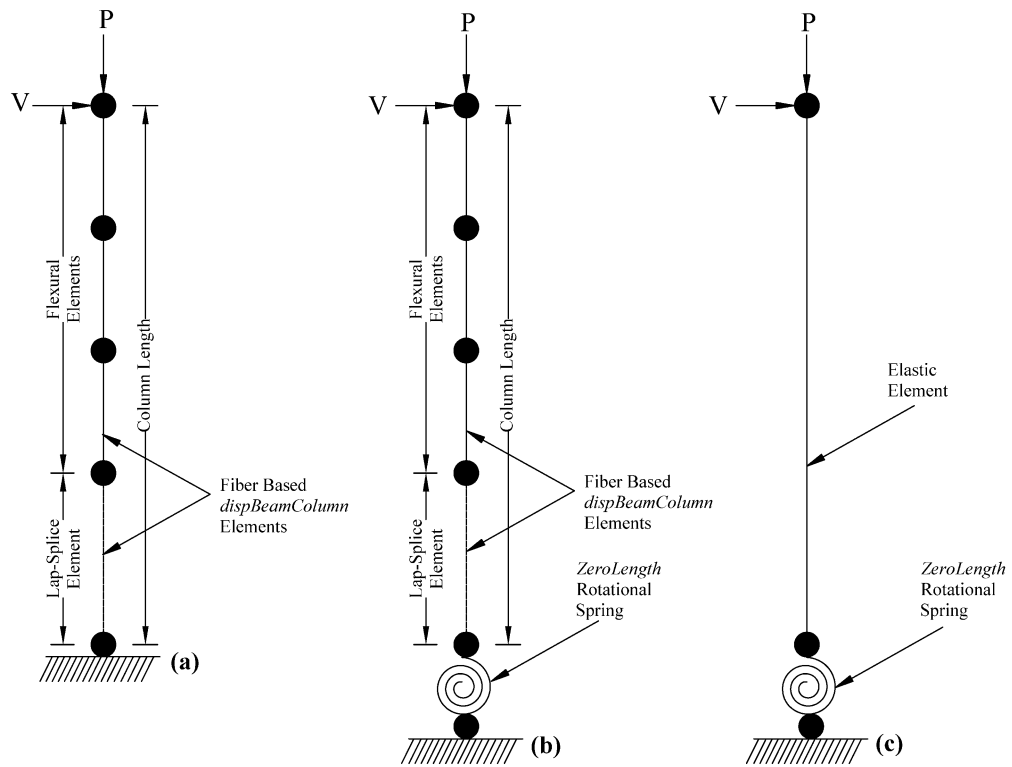
Figure 6.4 Element discretization of the control column tested by Kruavit for the approach of (a) Tariverdilo et al. [78], (b) Alvi et al. [89], and (c) Opabola et al. [93].
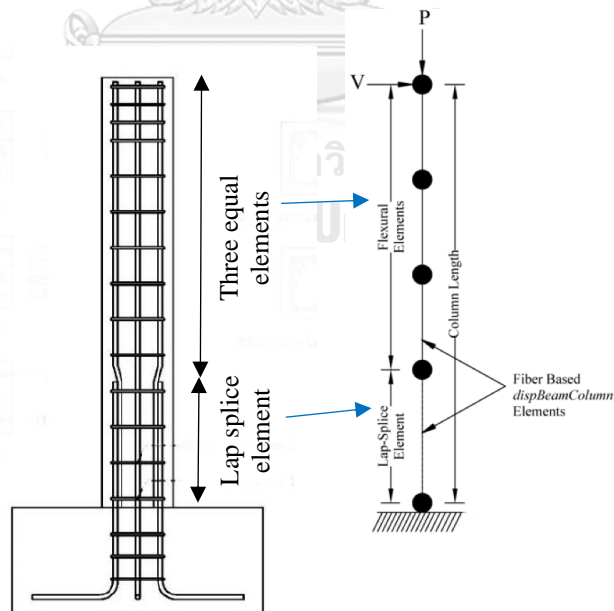
Figure 6.5 Element discretization of control column tested by Kruavit [76] (lap splice element is 700 mm long and each flexural element outside lap splice is 500 mm long).

6.3.2. Section Discretization

The core concrete was discretized into 20 fibers in both the local y- and z-direction, as shown in Figure 6.6. The side cover concrete was discretized into 20 fibers in the local y-direction and two fibers in the local z-direction, whereas the top and bottom cover was modeled by 20 fibers in the local z-direction and two fibers in the local y-direction. Several existing studies were explored to assess an accurate mesh size in the modeling of RC columns. A summary of mesh sizes for core and cover concrete obtained in the literature is presented in Table 6.1. Based on this, a mesh size of 20 fibers each in local y- and z-directions was selected.

Table 6.1 Summary of core and cover mesh sizes (Note: All units are in "mm").

Study	Member Type	Member Length	Section Size	Core Fibers	Cover Fibers	Curvature
Mehary et al. [140]	Column	2540	610x610	24x24	20x2	Single
Wang et al. [141]	Column	4400	600x600	10x10	10x2	Double
Yao and Wu [142]	Column	1425	400x370	23x23	23x2	Single
Wang et al. [143]	Column	560	280x280	22x22	22x2	Single
Su et al. [144]	Column	3000	600x600	20x20	20x2	Single
Wang et al. [145]	Column	1000	350x350	20x20	20x2	Single
Rasulo et al. [146]	Column	1350	450x450	28x28	28x4	Single
Abbas et al. [147]	Column	1250	270x270	13x13	13x2	Single
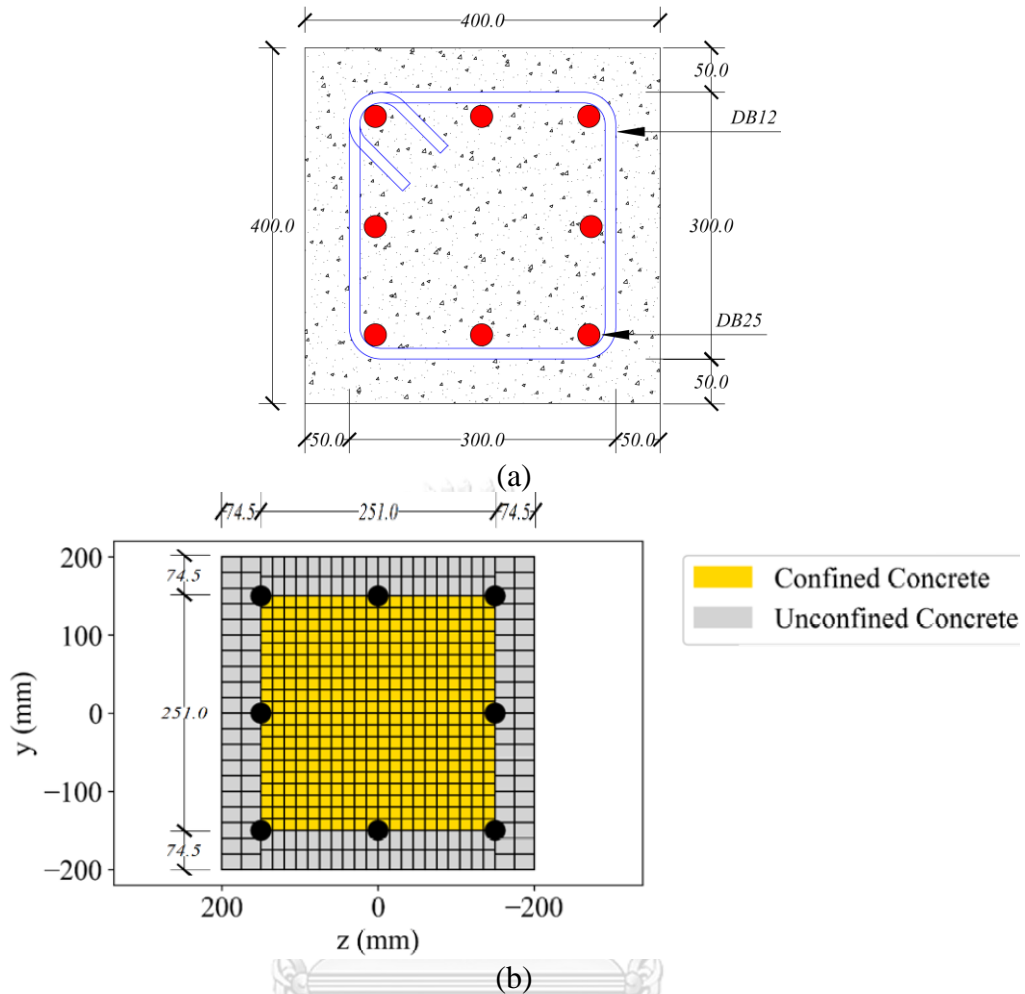
Figure 6.6 Fiber section discretization for the control lap spliced column tested by Kruavit [76] (a) actual section and (b) fiber discretization.

6.3.3. Concrete Fibers

The modeling of the concrete fibers was performed by using *Concrete02* material in *OpenSees*. The formulations of Mander et al. [80] were used to obtain the confined concrete stress-strain properties. The unconfined concrete strength was -23.6 MPa, whereas the confined peak compressive stress and the corresponding strain obtained from Mander et al. [80] model were -30.0 MPa and -0.003, respectively. The strain corresponding to the peak unconfined strength was input as -0.002. The crushing strain for the cover concrete was input as -0.003, whereas the crushing strain for core concrete was input as the value that corresponded to the 20% reduction in the peak compressive strength. The complete stress-strain relation obtained from Mander et al. [80] model is shown in Figure 6.7.
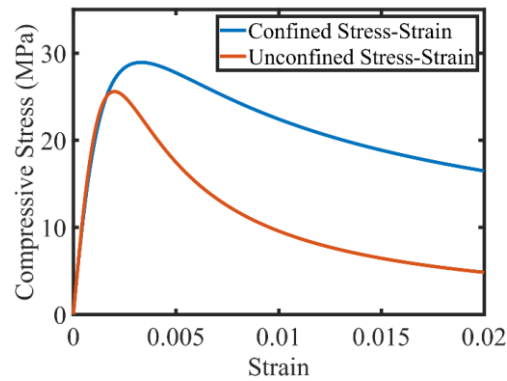
Figure 6.7 Stress-strain relation for concrete fibers of RC column tested by Kruavit [76].

6.3.4. Steel Fibers

The steel fibers within the lap splice zone were assigned a modified stress-strain relation, as shown in Figure 6.8, and were modeled by using *Hysteretic* material. The maximum steel stress at the onset of lap splice failure f_s was computed by following the recommendations of Tariverdilo et al. [78] and Alvi et al. [89]. The splice stress f_s computed by the model of Tariverdilo et al. [78] was equal to the yield stress i.e., 449 MPa at a strain ϵ_s of 0.0047, whereas the residual stress f_r was 130 MPa at a strain ϵ_r of 0.02. The splice stress f_s computed by the model of Alvi et al. was 420 MPa. The residual stress f_r was used as 130 MPa at a strain ϵ_r of 0.0215. The value of α for the rotational spring stiffness was obtained as 2.907, and the values of parameters *pinchX* and *pinchY* for the *Hysteretic* material were 0.33 and 0.18, respectively, whereas the values of *pinchX* and *pinchY* recommended by Tariverdilo et al. [78] were 0.8 and 0.3, respectively. The stress-strain curves of lap spliced bars are shown in Figure 6.9. The model of Tariverdilo et al. inclusively models the slip of lap splice by modifying the stress-strain response in the form of a reduced slope. However, the model by Alvi et al. does not consider the effect of lap splice slip at the material level. Instead, an additional zero-length rotational spring element is used at the column's base to model lap splice slip.
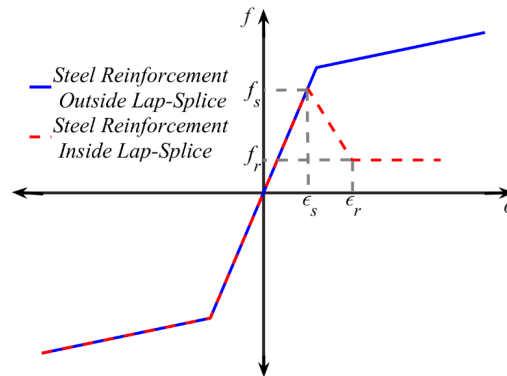
Figure 6.8 Stress-strain relation for steel fibers.
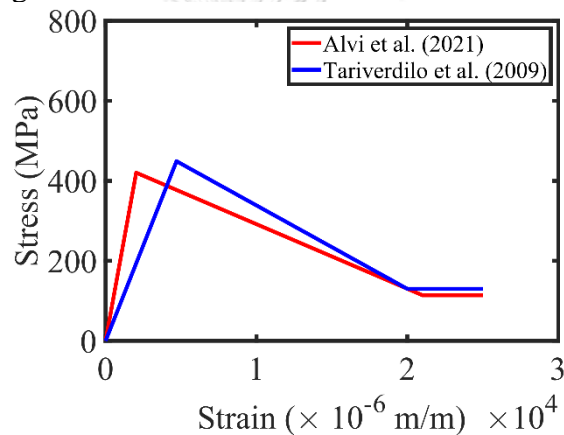
Figure 6.9 Stress-strain curves of lap spliced bars in control column.

The model of Opabola et al. [93] requires several parameters for the rotational spring, as shown in Figure 6.10. The parameters on the moment rotation curve in Figure 6.10 were estimated by following the procedure of Opabola et al. [93]. The maximum splice stress was estimated to be 420 MPa. From sectional analysis on *Response2000*, the moment capacity corresponding to the splice stress of 420 MPa was estimated to be 260.4 kN-m. The corresponding lateral force capacity was estimated at 118.64 kN. The undamaged shear strength of the section V_o was estimated as

$$V_o = \frac{A_v f_{yt} d}{s} + \left(\frac{0.5\sqrt{f'_{co}}}{a/d} \sqrt{1 + \frac{N}{0.5\sqrt{f'_{co}} A_g}} \right) 0.8 A_g \qquad 6.13$$

where A_v is the cross-sectional area of transverse reinforcement passing shear plane, f_{yt} is the yield strength of transverse reinforcement, d is the effective depth of

section, s is the center-to-center spacing of transverse reinforcement, f'_{co} is the unconfined concrete strength, a is the shear span, N is the axial load, and A_g is the gross area of the cross-section. The undamaged shear strength of the section V_o was estimated to be 266.78 kN which is greater than 118.64 kN. Hence, the column was bond critical. The effective flexural rigidity EI_{eff} is given as

$$EI_{eff} = \alpha \left[0.27 \left(\frac{a}{d} \right) - 0.07 \right] \tag{6.14}$$

where α is a parameter estimated from Table 5 of ASCE/SEI 41-17 [148] as 0.3. The elastic rotation capacity was estimated as

$$\theta_e = \frac{V_{max} a^2}{3 EI_{eff}} \tag{6.15}$$

The elastic rotation capacity was estimated as θ_e 0.82%. The value of pre-capping rotation capacity θ_p was estimated as

$$\theta_p = 0.75\% \leq 3.9 - 0.9 \frac{A'_s f_s}{A_v f_{yt} \left(\frac{l_{s,prov}}{s} \right)} \leq 3\% \tag{6.16}$$

The value of θ_p was estimated as 2.55%. The value of b_{nl} was estimated as

$$b_{nl} = 0.15 K \frac{h}{a} \left[1 - \frac{N}{0.7 f'_c A_g} \right] = 7.17\% \tag{6.17}$$

Finally, the post-capping rotation capacity was estimated as $b_{nl} - \theta_p = 4.62\%$. The residual moment capacity at axial failure M_{res} was estimated as

$$\frac{M_{res}}{M_b} = 0.2 - 0.4 \frac{N}{A_g f'_c} = 0.167 \tag{6.18}$$

where M_b is the moment capacity of the section corresponding to the maximum transferrable lap splice stress f_s. Finally, the stiffness deterioration parameter Λ was suggested to be 0.40, whereas the pinching behavior parameter was estimated as

$$\kappa = 0.6 - \frac{0.0002}{\rho_t} = 0.55 \tag{6.19}$$

where ρ_t is transverse reinforcement ratio. The calculated moment-rotation relation is shown in Figure 6.11.
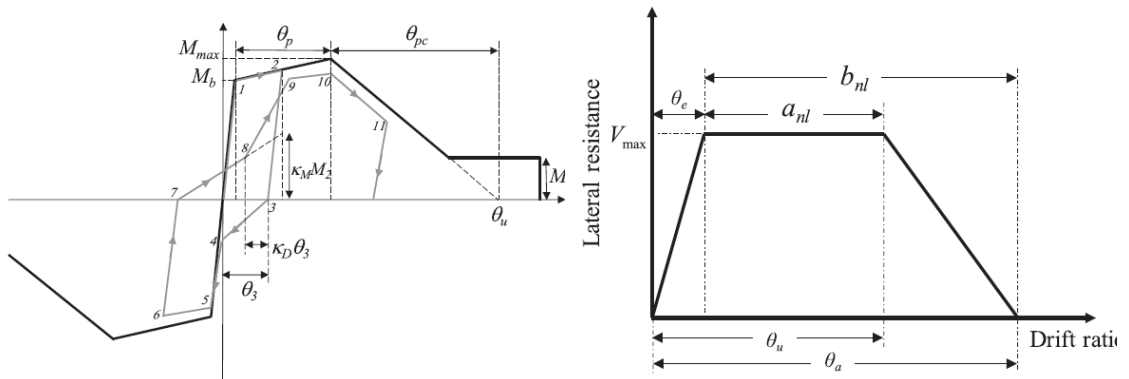
Figure 6.10 Parameters required for the model of Opabola et al. [93].
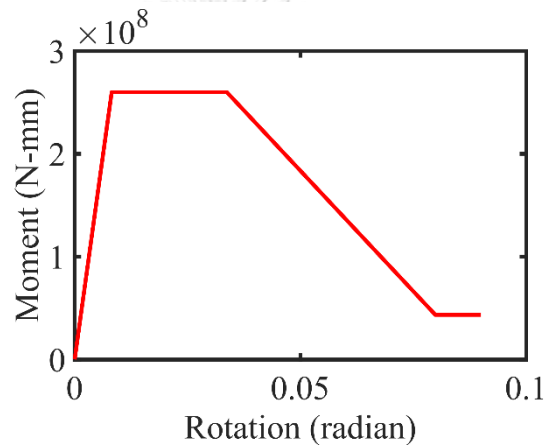
Figure 6.11 Moment-rotation relation of control column to be assigned to the rotational spring in the model by Opabola et al. [93].

6.3.5. Assessment of Numerical Models for Lap splice Control Column

Three numerical models are presented in the previous section to model deficient lap spliced RC columns. Figure 6.12 presents the comparison of experimental versus analytical hysteretic responses of the lap spliced column. From visual inspection, it is evident that all four models were able to capture peak strength, initial stiffness, and post-peak drop in lateral strength with reasonable accuracy. The residual strength was overestimated by the model of Alvi et al. [89]. It is evident from visual inspection that unloading stiffness, reloading stiffness, and strength degradation are well matched with experimental results for *Pinching4* material calibration. The models of Alvi et al. [89] and Opabola et al. [93] seem to underestimate the pinching behavior.
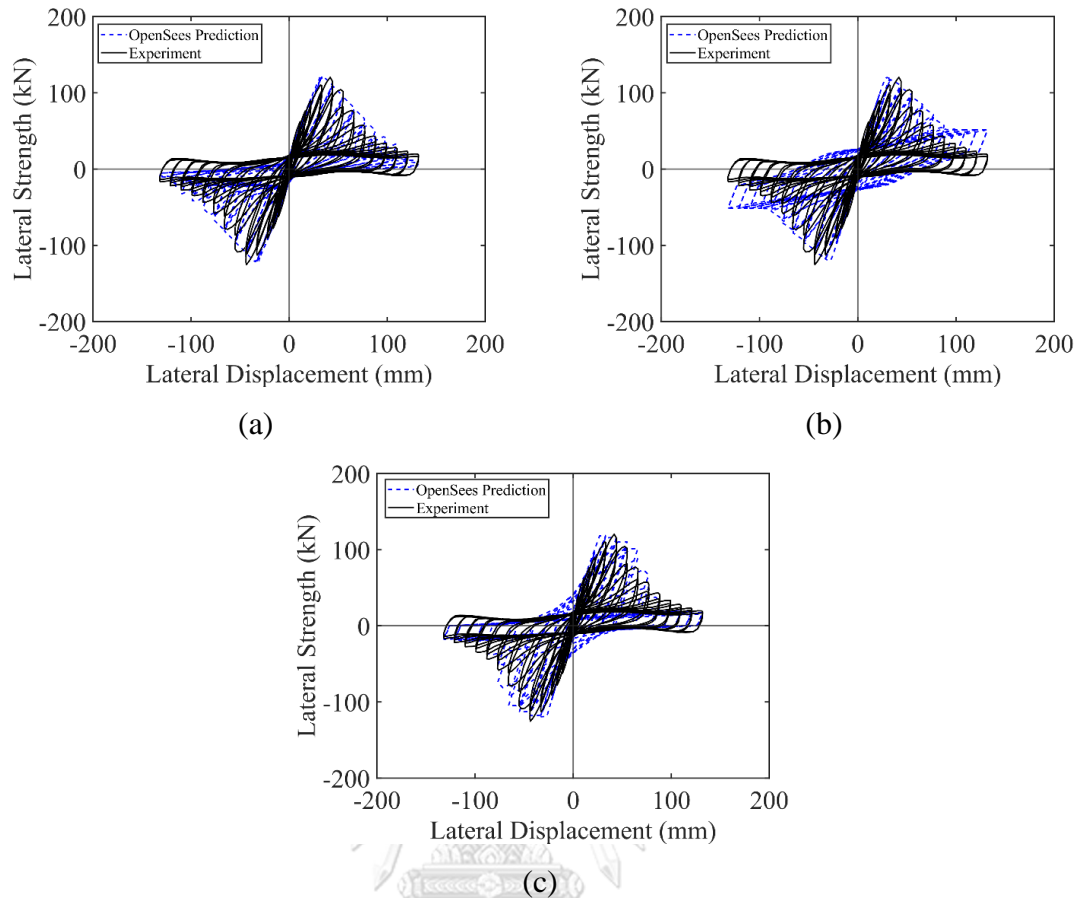
Figure 6.12 Comparison of experimental versus analytical response of lap spliced column (control) (a) Tariverdilo et al. [78], (b) Alvi et al. [89], and (c) Opabola et al. [93].

Table 6.2 provides key backbone parameters for all three models and their difference from experimental results. It can be observed that percentage differences between experimental and analytical peak strengths from all models were below 4%.

Table 6.2 Comparison of key backbone parameters for control lap splice column

Models/Key Parameters	Experiment	Tariverdilo et al. [78]		Alvi et al. [89]		Opabola et al. [93]	
		Value	Error (%)	Value	Error (%)	Value	Error (%)
Peak Strength P_u (kN)	120.3	121.7	1.2	119.1	-1.0	116.7	-2.9
Displacement at $0.8P_u$ (mm)	55.8	53.5	-4.0	55.1	-1.2	67.0	20.1
Dissipated energy (kN-m)	177.0	171.2	-3.2	234.4	32.4	166.5	-5.9

In addition to the backbone of hysteretic response, strength and stiffness degradation under cyclic loading as well as pinching behavior should be well

approximated in order to provide a correct approximate of dissipated energy. The energy dissipated by all four models was compared to that computed from the experimental curve, as shown in Figure 6.13. Total energy dissipation approximated by the model of Alvi et al. [89] was higher than that of experimental results. The model of Tariverdilo et al. [78] and Opabola et al. [93] slightly underestimated the total dissipated energy. Given that no calibration was implemented for the models of Tariverdilo et al. [78] and Opabola et al. [93], their good agreement with experimental results suggests that they can be used to model deficient lap spliced behavior of RC columns.
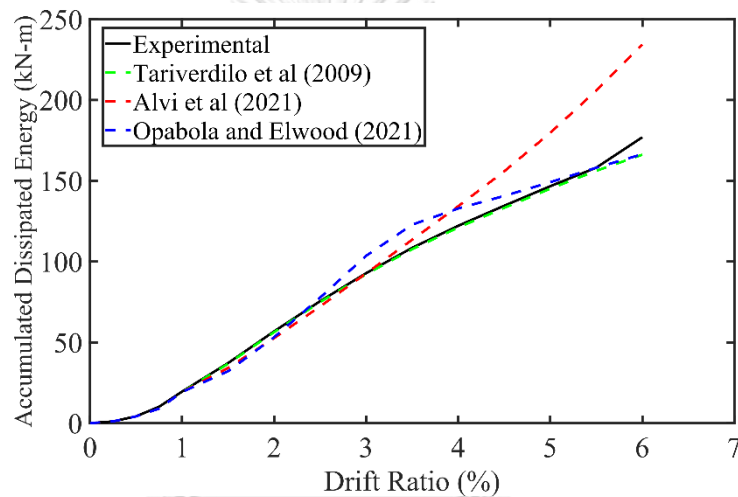
Figure 6.13 Comparison of dissipated energy from existing models and experimental results (Lap spliced control column).

6.4. Non-Linear Fiber Modelling of HSS Collar Strengthened Columns

Kruavit [76] tested three columns strengthened with HSS collars spaced at 100 mm, 200 mm, and 333 mm, respectively. The strengthening height of the columns above its base was 1100 mm. Before proceeding to the nonlinear modeling of HSS strengthened columns, the required amount of the HSS confinement ratio is first calculated using the proposed equation.

$$\rho = \left[\frac{1}{0.04R_{ls}^{2.09}} \left\{ \frac{f_y d_b}{3l_s} \epsilon_y + \left(\int_{\epsilon_y}^{\epsilon_u} \tau_{max} \left(1 - 0.8 \left(1 - e^{0.7\left(1 - \frac{\epsilon_s}{\epsilon_y}\right)} \right) \right) d\epsilon \right) - \frac{4\tau_o^2 l_s}{d_b E_s} \right\} - 1.00 \right]^{\frac{1}{118.81}} \qquad 6.20$$

where f_y, d_b, and l_s are 449 MPa, 25 mm, and 700 mm, respectively. τ_p is the bond stress that is offered by the plain concrete, which is calculated using the formulation of Lettow & Eligehausen [126] given as

$$\tau_o = \left(\frac{d_b}{4l_s}\right) 24.2 \left(\frac{l_s}{d_b}\right)^{0.55} (f_c')^{0.25} \left(\frac{c_{min}}{d_b}\right)^{\frac{1}{3}} \left(\frac{c_{max}}{c_{min}}\right)^{0.1} \left(\frac{20}{d_b}\right)^{0.2} = 3.40\ MPa \qquad 6.21$$

The required development length required as per ACI 318-19 is $54d_b = 1350$ mm. From this, $R_{ls} = \frac{700}{1350} = 0.52$. Using these values, the required HSS confinement ratio ρ is 0.0186. The required spacing s for HSS collars 50 mm × 50 mm × 2.3 mm can be calculated.

$$\rho = \frac{2A_{sc}}{sb} \qquad 6.22$$

where A_{sc} and b are the area of HSS collars (439 mm^2) and width of the section (400 mm). From Eq. 6.22, the required spacing of the collars is 118 mm. From beam tests, it was noticed that fully confined beams were able to develop the full capacity of lap spliced bars. Thus, it can be established that HSS collars applied at 100 mm were able to develop the full capacity of lap spliced bars. For HSS collars at 333 mm and 200 mm, the constitutive stress-strain relationship of lap spliced bars must be modified. Appendix A4.4 presents the *OpenSees* script for nonlinear modeling of the HSS collar strengthened column.

6.4.1. Element Discretization

Since HSS collars were provided to a lower 1100 mm region of RC columns, element discretization was performed to add three *dispBeamColumn* elements for the bottom 1300 mm, whereas the remaining length of columns was divided into two equal *dispBeamColumn* elements, as shown in Figure 6.14 and Figure 6.15. The length of each element was taken equal to the plastic hinge length calculated by the recommendations of Priestley et al. [79] as

$$L_p = 0.08L + 0.022f_y d_b \qquad 6.23$$

where L is the column length.
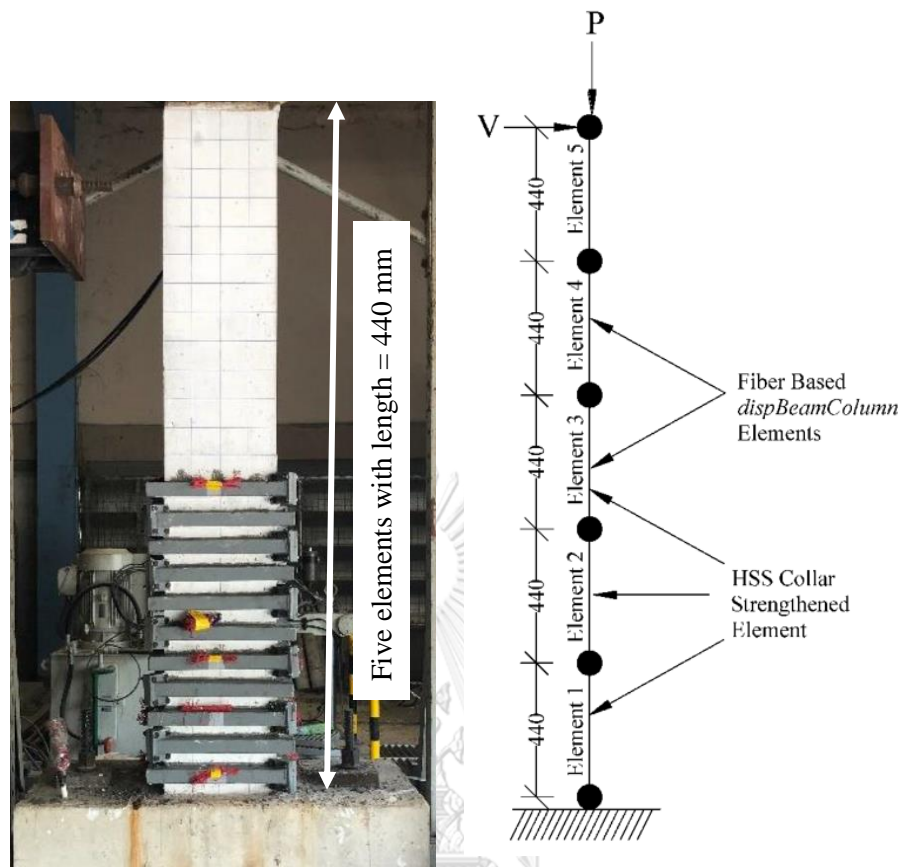
Figure 6.14 Element discretization of strengthened columns tested by Kruavit [76].

6.4.2. Fiber Section

The fiber sections were discretized in a similar way as those in the control column. However, the element strengthened by HSS collars was considered fully confined under the influence of HSS collars. For the remaining portion, core concrete and cover concrete were modeled differently, as shown in Figure 6.15. Twenty fibers were used for the core concrete in each local y- and z-directions.

Elements 4 and 5

Elements 2 and 3

Element 1

Confined Concrete
Unconfined Concrete
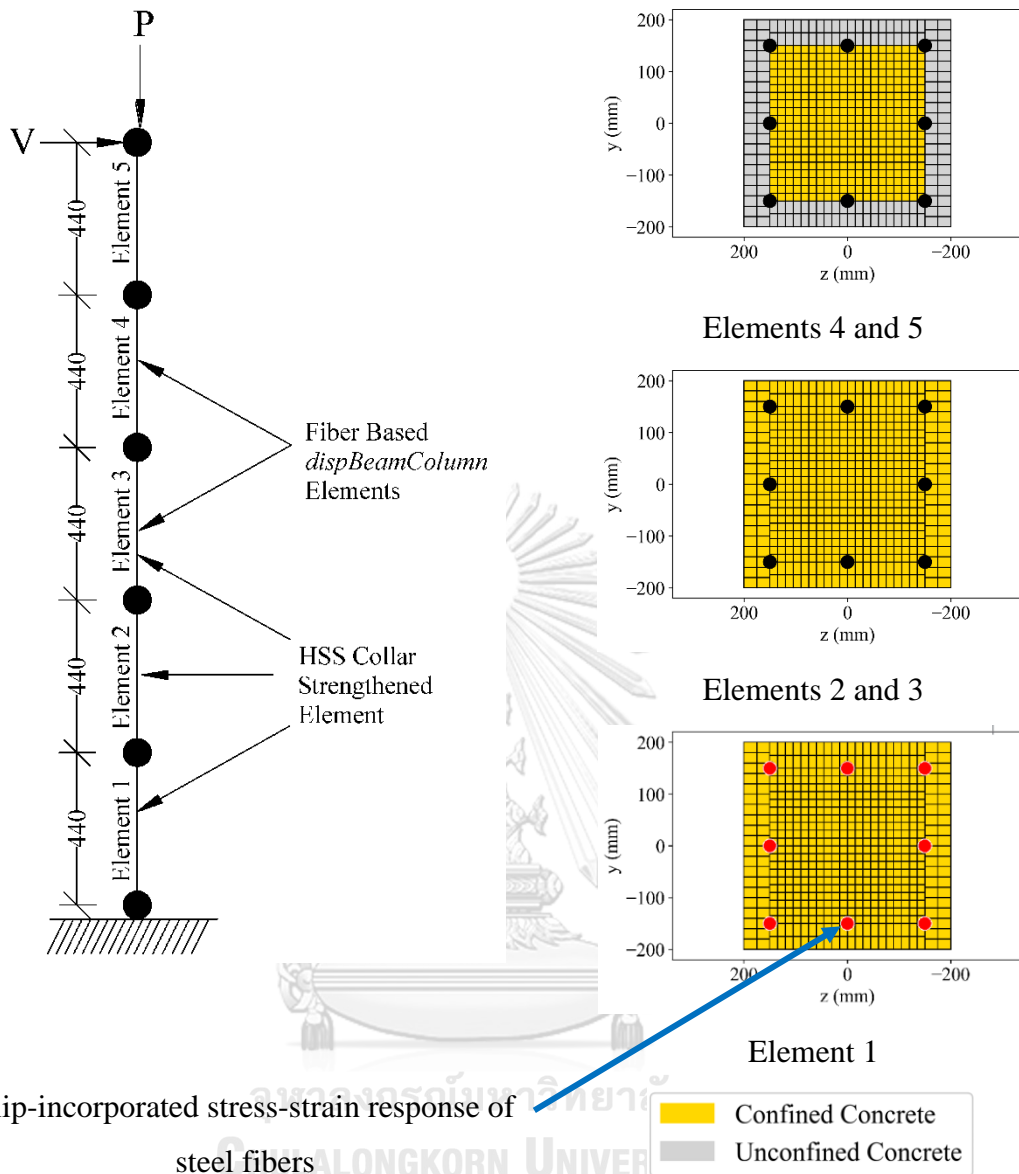
Slip-incorporated stress-strain response of steel fibers

Figure 6.15 Element and fiber section discretization of HSS collar strengthened columns tested by Kruavit [79].

6.4.3. Concrete Fibers

Concrete fibers outside the strengthened zone were modeled by using the same stress-strain relation as those in the control column. For concrete fibers in the HSS collar strengthened element, the formulation of Chapman and Driver [99] was used to predict the compressive stress-strain relation. The confining pressure vs. lateral strain relation of HSS collars used by Kruavit [76] is shown in Figure 6.16. The resulting stress-strain relations are shown in Figure 6.17.
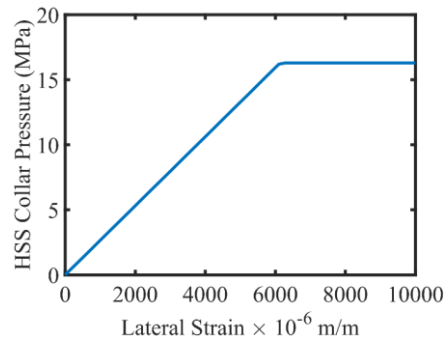
Figure 6.16 Collar pressure vs. lateral strain relation for the collars used by Kruavit [76].
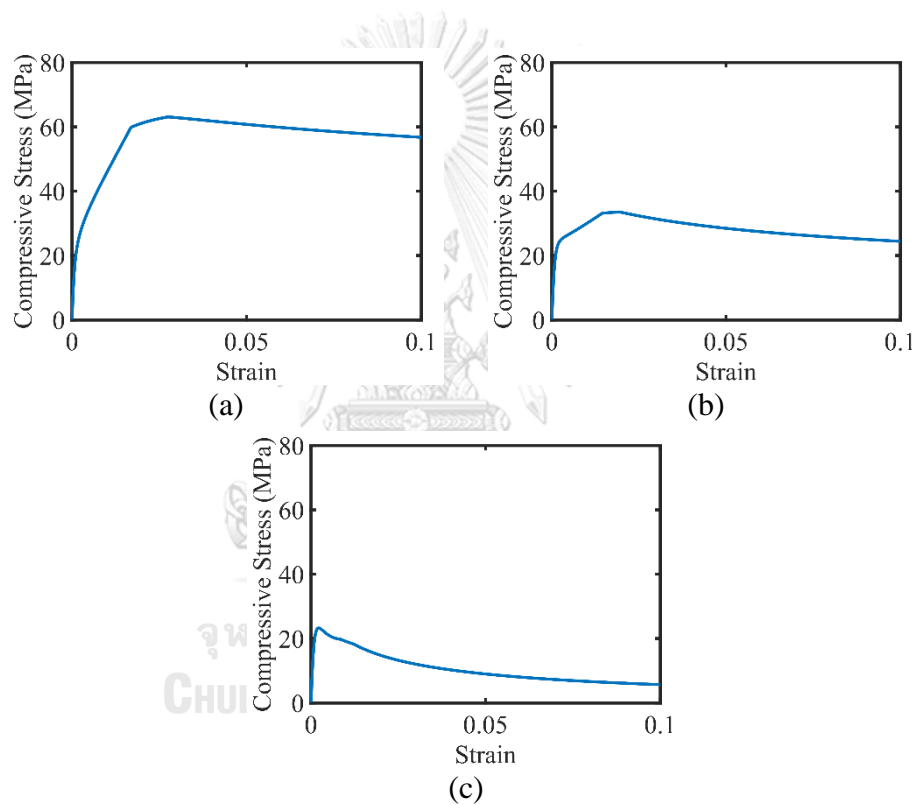
Figure 6.17 Stress-strain response of HSS collar strengthened concrete in columns tested by Kruavit [76] for HSS collars spaced at (a) 100 mm, (b) 200 mm, and (c) 333 mm.

6.4.4. Steel Fibers

The stress-strain response of steel fibers outside the strengthened zone was used the same as that obtained from the uniaxial tensile test on steel bars. As discussed earlier, the minimum spacing of steel collars with an area of 439 mm² required to achieve ductile failure was 118 mm. Therefore, no modification in the

stress-strain response of steel fibers was performed for the column strengthened with HSS collars spaced at 100 mm.

To estimate the maximum stress that can be developed by the lap splice strengthened by HSS collars spaced at 200 mm and 333 mm, the same procedure as that used for the beams was used. For the column strengthened with HSS collars spaced at 333 mm, the increase in fracture energy ΔG was estimated as 0.022 MPa. The fracture energy offered by the plain concrete G_o was estimated as 0.0062 MPa. Thus, the total fracture energy G computed was 0.0282 MPa. Fracture energy corresponding to elastic zone G_1 was 0.0117. Since G_e was lower than G, the maximum lap splice strain was greater than the yield strain. Its value was computed to be 0.0073. In a similar way, the maximum tensile strain that can be developed by the lap spliced bars strengthened with HSS collars spaced at 200 mm was estimated as 0.01962. To model lap splice behavior, *Hysteretic* material in *OpenSees* was used. The residual strength of the lap splice f_r after attaining the peak strength was computed following the recommendation of Tariverdilo et al. [78]. It was given in Eq. 6.24 as

$$n_l n_t \mu A_h f_h = n A_b f_r \qquad\qquad 6.24$$

where n_l, n_t, A_h, f_h, n, and A_b are the number of legs of transverse reinforcement, the total number of transverse reinforcements within splice length, area of transverse reinforcement, yield strength of transverse reinforcement, number of longitudinal spliced bars, and area of a single longitudinal bar, respectively. The residual stress f_r calculated for HSS collars spaced at 333 mm and 200 mm was 260 MPa and 350 MPa, respectively. The yield strength of the lap spliced bars was 449 MPa at the corresponding strain of 0.00218. The fracture strain of lap spliced bars was 628 MPa at the corresponding strain of 0.070. By following the procedure of Pan et al., Figure 6.18 compares the modified stress-strain response of lap spliced bars in comparison with the actual stress-strain response.
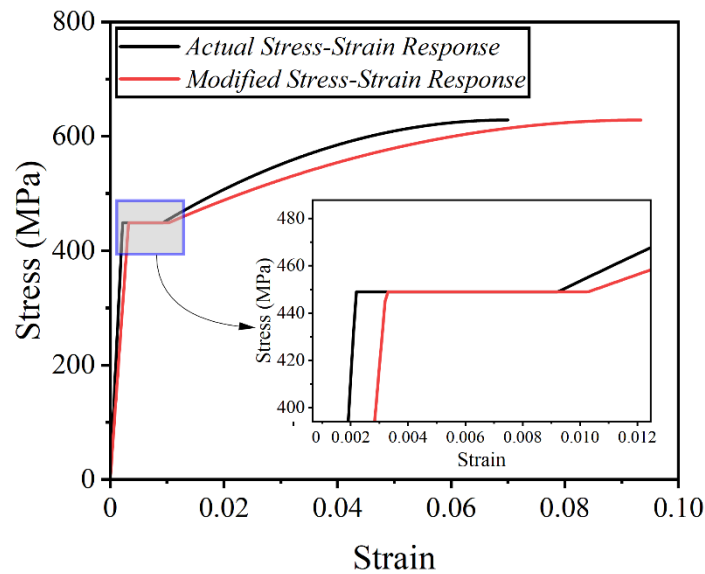
Figure 6.18 Actual stress-strain response vs. slip-incorporated stress-strain response of lap spliced bars.

The *Hysteretic* material offers two damage parameters, namely *damage1* and *damage2,* to include the strength degradation due to ductility and energy, respectively. Both damage parameters work by increasing the target strain during reloading cycles. As a result, the stiffness of the reloading branch is reduced, resulting in a reduced strength at the target ductility in a reloading cycle, as shown in Figure 6.19. The value of damage parameters ranges from 0.0 to 1.0, with 1.0 being the maximum damage. Two more parameters in *Hysteretic* material can be used, namely *pinchX* and *pinchY,* to account for the pinching effects. The value of pinching parameters also ranges from 0.0 to 1.0. The parameter *pinchX* (p_x) defines the displacement during the reloading cycle where the slope changes to the target displacement (i.e., point P), whereas the parameter *pinchY* defines the ratio of the magnitude of stress/load at point P to the maximum stress/load in the previous cycle as shown in Figure 6.20. Thus, a combination of both these parameters is required to calibrate the target hysteretic response. The *Hysteretic* material in *OpenSees* was used to model the stress-strain behavior of longitudinal reinforcement. For element 1 in Figure 6.15, the modified stress-strain relation was assigned to the longitudinal bars, whereas the actual stress-strain relation was assigned to longitudinal bars in the remaining elements.
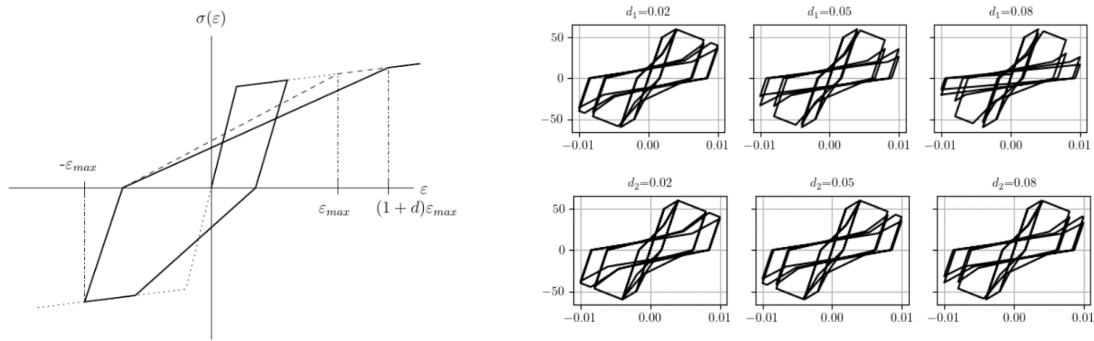
Figure 6.19 Effect of damage parameters (*d1* and *d2*).
(https://portwooddigital.com/2022/04/17/hysteretic-damage-parameters/)
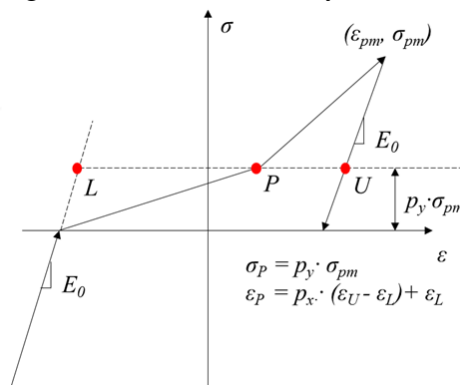
Figure 6.20 Definition of pinching parameters of *Hysteretic* material in *OpenSees*.

6.4.5. RC Column with HSS Collars at 100 mm

The comparison of the predicted hysteretic response with the experimental response is shown in Figure 6.24. Three cases are presented: (1) predicted response without including anchorage slip effect and strength degradation parameters of *Hysteretic* material, (2) predicted response with the inclusion of slip effect and without including the damage parameters, and (2) predicted response with the inclusion of slip effect and damage parameters.

A calibration process was carried out by following the procedure of Kashani et al. [149], who used different combinations of *pinchX* and *pinchY* parameters. For each combination, the error between the energy predicted dissipated energy and experimental dissipated energy was carried. The combination corresponding to the least error was selected, as shown in Figure 6.21.

Combination	1	2	3	4	5	6	7	8	9
Pinch *x*	0.2	0.2	0.2	0.4	0.4	0.4	0.7	0.7	0.7
Pinch *y*	0.8	0.6	0.4	0.8	0.6	0.4	0.8	0.6	0.4
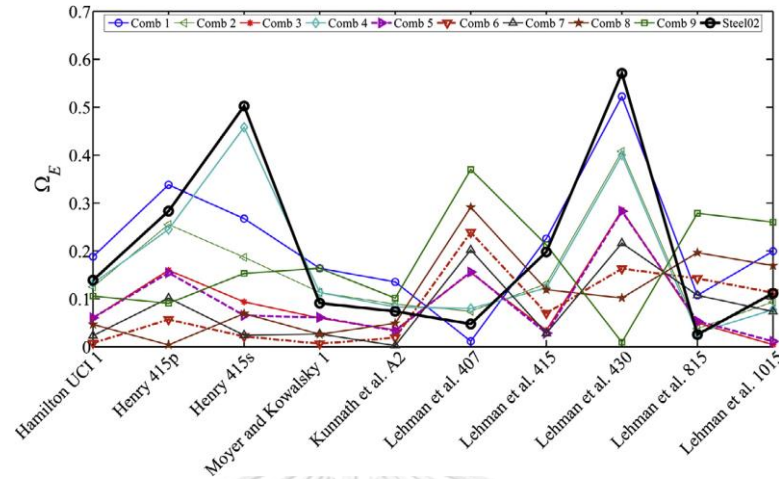
Figure 6.21 Calibration of pinching parameters based on dissipated energy [149].

The calibration process was performed by following the procedure of Kashani et al. [149]. It was noticed that no hysteretic damage was observed in the specimens of Kashani et al. [149]. Hence, the damage parameters of *Hysteretic* material were taken as 0.0. In the case of RC columns in this study, hysteretic damage was observed. Hence, damage parameters varied from 0.005 to 0.025, as shown in Table 6.3. It can be seen in Figure 6.22 that the combination of *pinchX* and *pinchY* with a value of 0.5 for each resulted in the lowest error in energy dissipation Ω_E.

Table 6.3 Combinations of pinching and damage parameters to calibrate the column strengthened with HSS collars at 100 mm spacing.

Combination	Ω_E (%)						
	Pinching Parameters		damage1 and damage2				
	pinchX	pinchY	0.005	0.01	0.015	0.02	0.025
Combo-1	0.8	0.2	51.6	55.0	59.2	64.5	69.2
Combo-2	0.7	0.3	30.0	34.7	41.7	49.1	55.9
Combo-3	0.6	0.4	06.6	10.4	18.1	28.1	35.4
Combo-4	0.5	0.5	17.2	14.3	07.7	04.2	15.1
Combo-5	0.4	0.6	41.7	39.2	32.5	18.4	06.2
Combo-6	0.3	0.7	66.6	64.4	57.4	42.9	29.7
Combo-7	0.2	0.8	95.6	94.7	88.2	79.6	68.8
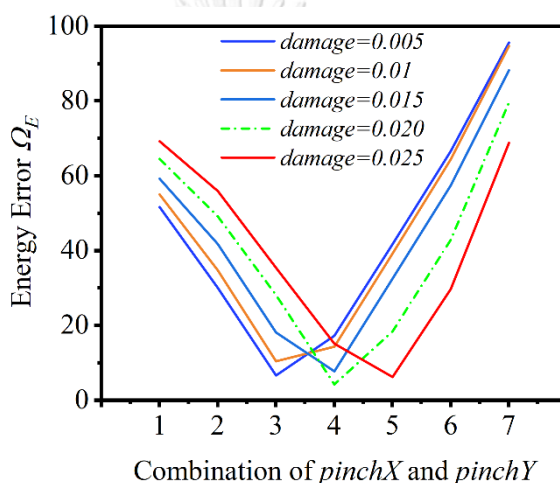
Figure 6.22 Variation of error in dissipated energy for different combinations of pinching and damage parameters.

However, the selection of a particular damage value is again subjected to how closely the experimental hysteretic response is predicted. As shown in Figure 6.23, the damage value of 0.02 closely approximated the experimental hysteretic response. Therefore, a value of 0.5 is recommended for *pinchX* and *pinchY* parameters, whereas a value of 0.020 is recommended for *damage1* and *damage2* parameters of *Hysteretic* material while performing the cyclic analysis of HSS collar sufficiently confined RC columns.

damage1=damage2=0.005   damage1=damage2=0.01   damage1=damage2=0.015

damage1=damage2=0.02   damage1=damage2=0.025
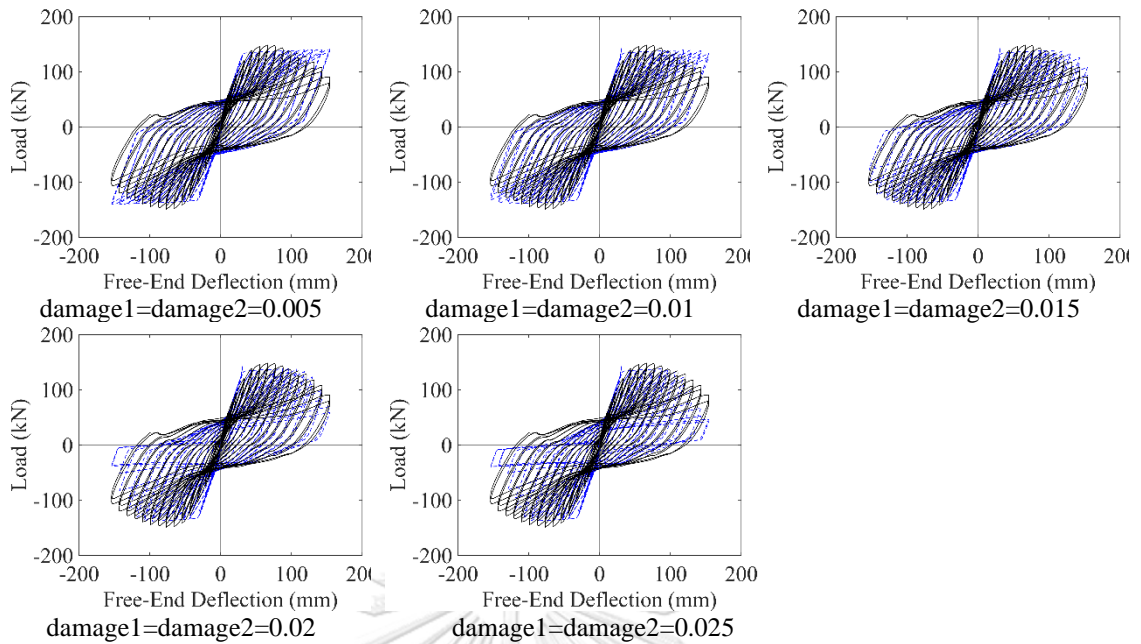
Figure 6.23 Variation of hysteretic response with damage parameter values for a fixed value of 0.5 of *pinchX* and *pinchY* parameters.

pinchX=0, *pinchY*=1, *damage1=damage2*=0, no slip

pinchX=0.4, *pinchY*=0.5, *damage1*=0, *damage2*=0, no slip

pinchX=0.4, *pinchY*=0.5, *damage1*=0, *damage2*=0, slip included

pinchX=0.5, *pinchY*=0.5, *damage1*=0.020, *damage2*=0.02, slip included
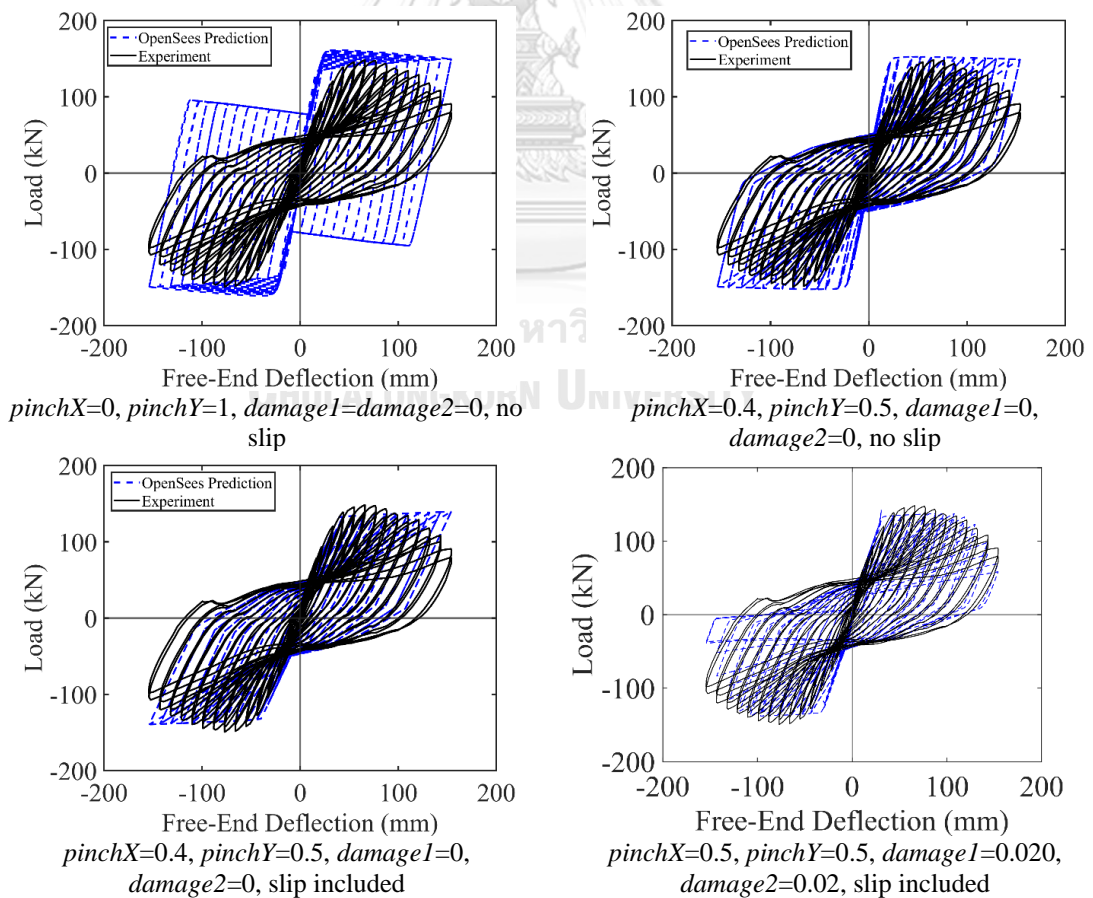
Figure 6.24 Calibration process of the hysteretic response of RC column strengthened with HSS collars at 100 mm.

As shown in Figure 6.24, a good agreement between the hysteretic experimental and predicted response is obtained. Experimental and analytical ductility were computed using the ductility index shown in Figure 6.25. The ductility index was calculated using Eq. 6.25.

$$\mu = \frac{\Delta_u}{\Delta_y} \qquad\qquad 6.25$$

where Δ_u and Δ_y correspond to the ultimate displacement demand and displacement at the onset of yielding, respectively.
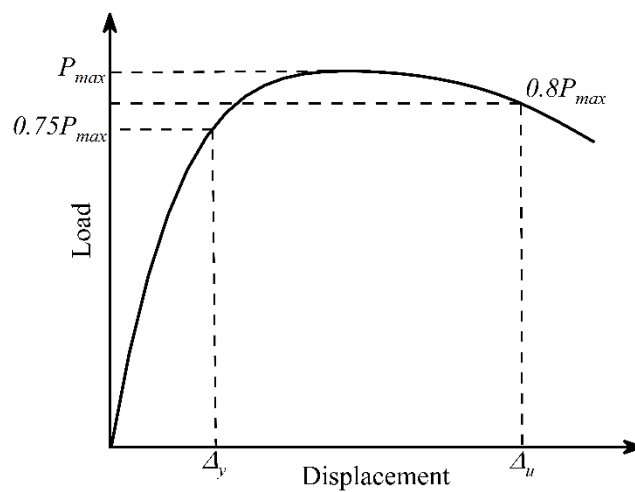
Figure 6.25 Displacement ductility index calculation [150].

The comparison of experimental and predicted displacement ductility μ for the column strengthened with HSS collars at 100 mm is shown in Figure 6.26. The experimental μ was computed as 4.45, whereas the predicted μ was 4.51. Thus, a good agreement between the experimental and predicted ductility was obtained with a difference of 1.35%.
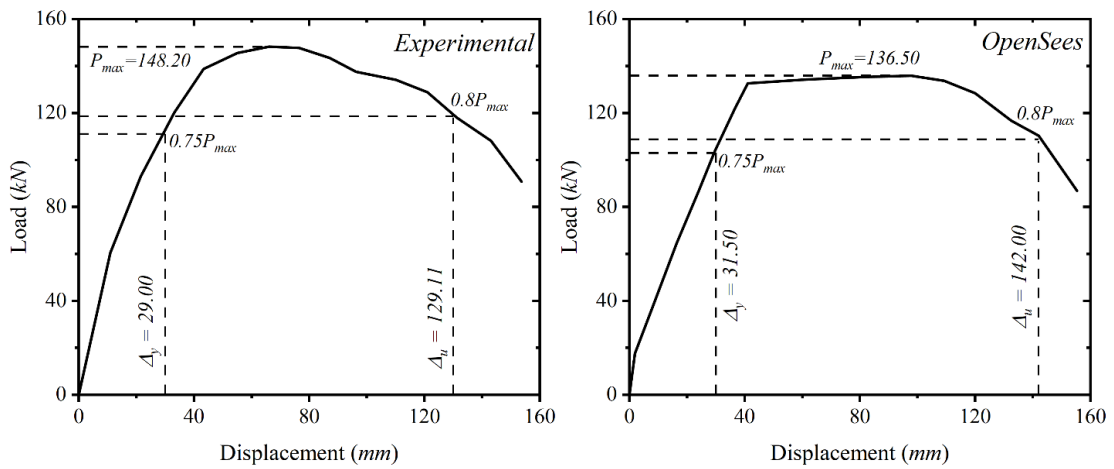
Figure 6.26 Comparison of predicted and experimental displacement ductility for the column strengthened with HSS collars at 100 mm.

The comparison of predicted and experimental energy dissipation for the column strengthened with HSS collars at 100 mm is shown in Figure 6.27. Overall, the experimental accumulated dissipated energy versus drift ratio is well captured by the *OpenSees* model. The maximum energy dissipated by the *OpenSees* model was 510.37 kN-m, whereas the corresponding experimental value was 517.48 kN-m. This suggests a good agreement between the experimental and predicted total dissipated energy with a difference of -1.37%. The experimental lateral load capacity was 148.20 kN, whereas the corresponding predicted value was 136.50 kN. The difference between the peak experimental and predicted lateral load capacities was -7.77%.
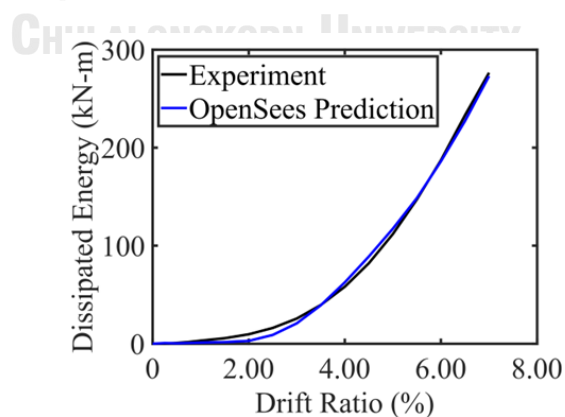
Figure 6.27 Comparison of predicted and experimental energy dissipation for the column strengthened with HSS collars at 100 mm.

6.4.6. RC Column with HSS Collars at 200 mm

RC column strengthened with HSS collars at 200 mm was modeled in *OpenSees*, similar to the column strengthened with HSS collars at 100 mm. However, it was found that the minimum required spacing of HSS collars with the area of 439 mm² was 118 mm. Therefore, the maximum lap splice strain was estimated at 0.01962. An upper limit on the maximum stress was applied, corresponding to the strain of 0.01962 in the definition of *Hysteretic* material for Elements 1 and 2. The modified steel stress-strain relation was used for steel fibers of Element 1, whereas the actual steel stress-strain relation was assigned to steel fibers in the remaining elements. The strain on modified steel stress-strain relation corresponding to the actual value of 0.01962 was found to be 0.0256 at a stress of 485 MPa. The residual stress f_r was found to be 350 MPa at a strain of 0.050. The calibration process of the *Hysteretic* material resulted in *pinchX* and *pinchY* values of 0.8 and 0.5, respectively. It is interesting to observe that the *pinchX* and *pinchY* values for the column strengthened with HSS collars at 100 mm were 0.4 and 0.5, respectively. Thus, an increased pinching was observed when the spacing of HSS collars was reduced to 200 mm. The comparison of the predicted and experimental hysteretic response is shown in Figure 6.28.
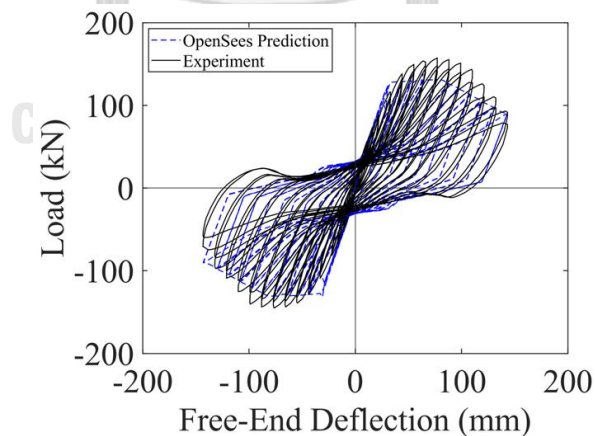
Figure 6.28 Comparison of the experimental and predicted hysteretic load-deflection response of the column strengthened with HSS collars at 200 mm.

The comparison of predicted and experimental displacement ductility for the column strengthened with HSS collars at 200 mm is shown in Figure 6.29. The

predicted lateral capacity was found to be 8.93% lower than the experimental lateral load capacity. The experimental displacement ductility index μ was 3.55, whereas the predicted displacement ductility index μ was 3.61. Thus, a good agreement between the experimental and predicted displacement ductility index μ was obtained with a difference of 1.69%. The comparison of predicted and experimental energy dissipation for the column strengthened with HSS collars at 200 mm is shown in Figure 6.30. Overall, the experimental accumulated dissipated energy versus drift ratio is well captured by the *OpenSees* model. The maximum energy dissipated by the *OpenSees* model was 397.40 kN-m, whereas the corresponding experimental value was 391.48 kN-m. This suggests a good agreement between the experimental and predicted total dissipated energy with a difference of 1.51%.
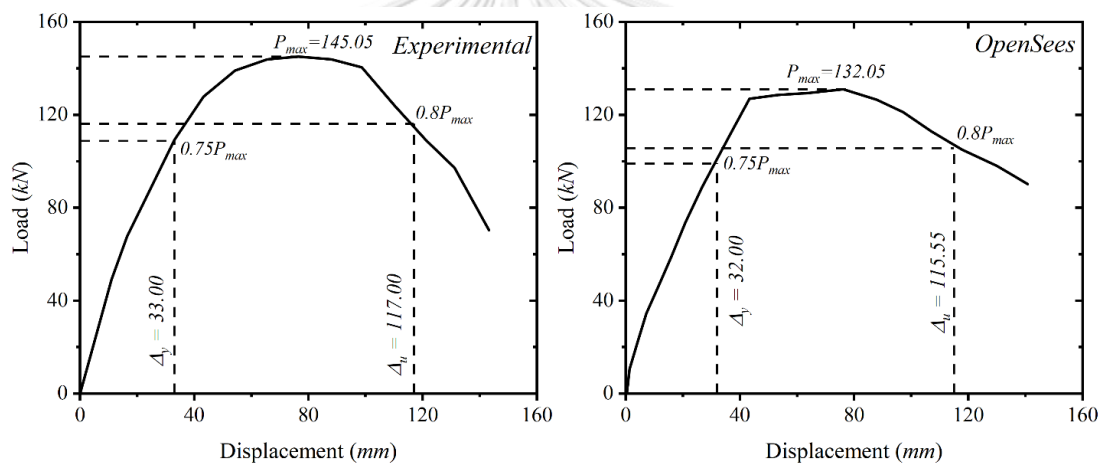
Figure 6.29 Comparison of predicted and experimental displacement ductility for the column strengthened with HSS collars at 200 mm.
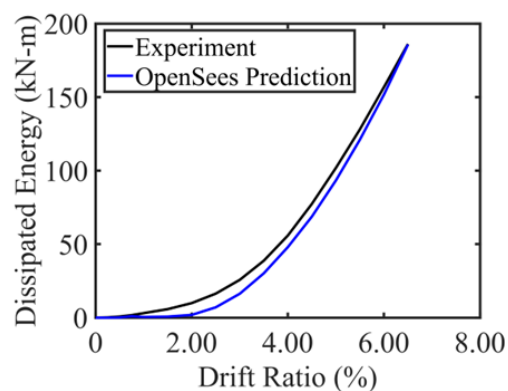
Figure 6.30 Comparison of predicted and experimental energy dissipation for the column strengthened with HSS collars at 200 mm.

6.4.7. RC Column with HSS Collars at 333 mm

RC column strengthened with HSS collars at 333 mm was modeled in *OpenSees,* similar to the columns strengthened with HSS collars at 100 mm and 200 mm. However, it was found that the minimum required spacing of HSS collars with the area of 439 mm^2 was 118 mm. Therefore, the maximum lap splice strain was estimated at 0.0073. An upper limit on the maximum stress was applied, corresponding to the strain of 0.0073 in the definition of *Hysteretic* material for Elements 1 and 2. The modified steel stress-strain relation was used for steel fibers of Element 1, whereas the actual steel stress-strain relation was assigned to steel fibers in the remaining elements. The strain on modified steel stress-strain relation corresponding to the actual value of 0.0073 was found to be 0.0082 at a stress of 463 MPa. The residual stress f_r was found to be 260 MPa at a strain of 0.030. The calibration process of the *Hysteretic* material resulted in *pinchX* and *pinchY* values of 0.8 and 0.25, respectively. It is interesting to observe that the *pinchX* and *pinchY* values for the column strengthened with HSS collars at 100 mm were 0.4 and 0.5, respectively. Thus, an increased pinching was observed when the spacing of HSS collars was reduced to 333 mm. The pinching in the column strengthened with HSS collars at 333 mm was more severe than the pinching in the column strengthened with HSS collars at 200 mm. The comparison of the predicted and experimental hysteretic response is shown in Figure 6.31.
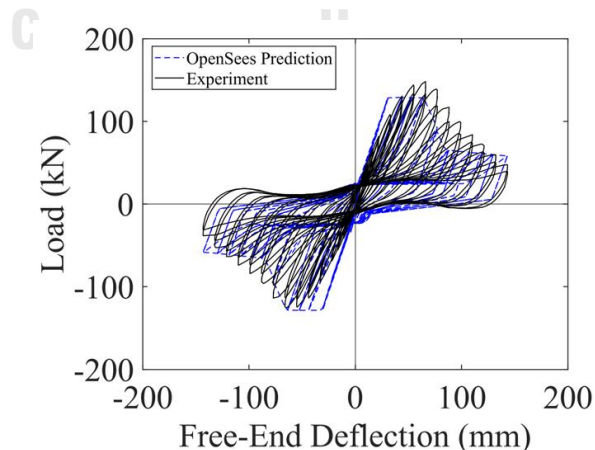
Figure 6.31 Comparison of the experimental and predicted hysteretic load-deflection response of the column strengthened with HSS collars at 333 mm.

The comparison of predicted and experimental displacement ductility for the column strengthened with HSS collars at 333 mm is shown in Figure 6.32. The predicted lateral capacity was found to be 8.93% lower than the experimental lateral load capacity. The experimental displacement ductility index μ was 2.75, whereas the predicted displacement ductility index μ was 2.97. Thus, a good agreement between the experimental and predicted displacement ductility index μ was obtained with a difference of 8.0%. The comparison of predicted and experimental energy dissipation for the column strengthened with HSS collars at 333 mm is shown in Figure 6.33. Overall, the experimental accumulated dissipated energy versus drift ratio is well captured by the *OpenSees* model. The maximum energy dissipated by the *OpenSees* model was 241.50 kN-m, whereas the corresponding experimental value was 259.48 kN-m. This suggests a good agreement between the experimental and predicted total dissipated energy with a difference of -6.93%.
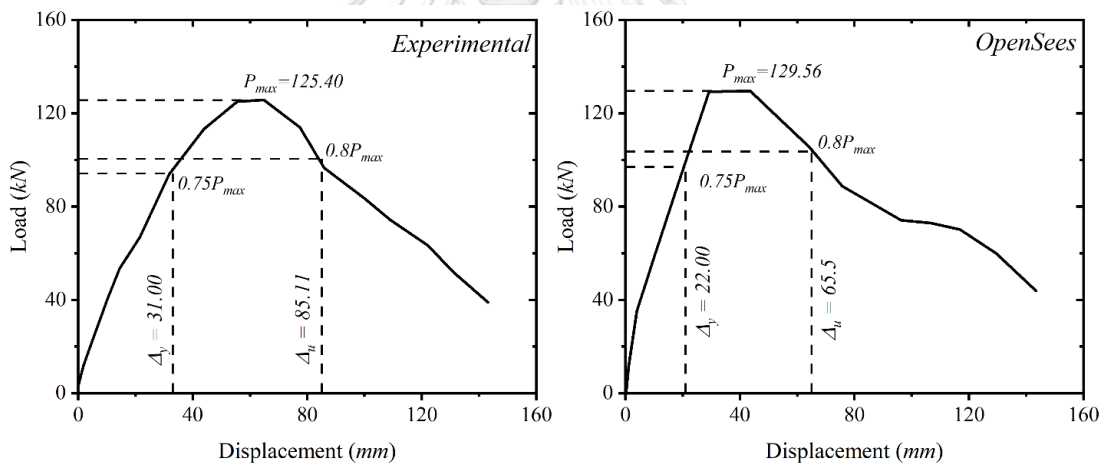
Figure 6.32 Comparison of predicted and experimental displacement ductility for the column strengthened with HSS collars at 333 mm.
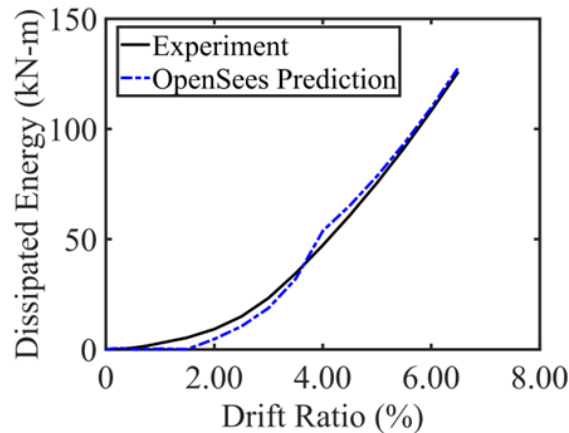
Figure 6.33 Comparison of predicted and experimental energy dissipation for the column strengthened with HSS collars at 333 mm.

6.5. Summary

In this chapter, the non-linear fiber modeling of the beams tested in this study and RC columns tested by Kruavit [76] by using *OpenSees* is discussed. To model RC beams in this study, a half model was prepared using *OpenSees* due to the symmetry across the midspan. Beams were modeled by using two displacement-based elements: one within the shear span and one within the constant moment region. For the control beams, all the fibers within the constant moment region were considered unconfined, whereas the core concrete fibers in shear span were modeled by the model of Mander et al. [80]. The stress-strain relation of bottom steel bars in the constant moment region was modified by placing an upper limit on the maximum stress. To estimate the maximum stress corresponding to the splitting failure in substandard lap splices, four existing models were assessed, including the models by Lettow and Eligehausen [126], Elwood et al. [129], Tariverdilo et al. [78], and Belejo [127]. It was observed that the model by Belejo [127] overestimated the splice strength. A modification was applied to the Belejo [127] model. It was found that the modified Belejo [127] resulted in the closest agreement with the failure load of the control beams, followed by the Lettow and Eligehausen [126] model. The next step was to assess the performance of *OpenSees* in predicting the monotonic load-deflection behavior of HSS collar confined beams. For this purpose, the fibers within the shear span were modeled in a similar way as those in control beams. Recognizing the observation

made by Chapman and Driver [99], steel collars behave differently from the internal steel confinement such that the collar confining pressure increases as the axial strain is increased, a procedure proposed by Chapman and Driver [99] was adopted to model concrete confined by HSS collars. It was observed that a softening of the load-deflection curves was predicted by *OpenSees* model for HSS collars spaced at 200 mm, whereas the load-deflection curves predicted by *OpenSees* model for HSS collars spaced at 100 mm closely matched the experimental results. This may be attributed to the large spacing of 200 mm whose corresponding confinement ratio lies outside the range tested by Chapman and Driver [99]. Therefore, the post-peak branch of the concrete stress-strain behavior exhibited steep softening that underestimated the effect of HSS collars spaced at 200 mm.

The control column tested by Kruavit [76] was modeled by both distributed plasticity methods (Tariverdilo et al. [78] and Alvi et al. [89]) and the concentrated plasticity method (Opabola et al. [93]). It was found that the initial stiffness and strength degradation were correctly modeled by both methods. However, the pinching behavior was underestimated by the model of Opabola et al. [93] and Alvi et al. [89]. Further, the residual lateral strength at failure was overestimated by the model of Alvi et al. [89]. The experimental dissipated energy, peak lateral strength, lateral strength at failure, and initial stiffness were correctly modeled by Tariverdilo et al. [78] model. Finally, HSS collars strengthened columns tested by Kruavit [76] were modeled using *OpenSees*. The HSS collars confined concrete fibers were modeled using the recommendations of Chapman and Driver [99]. It was found that the lateral deflection of RC columns predicted by *OpenSees* was underestimated. Therefore, the deflection contribution by strain penetration was included in the model by using the method of Pan et al. [138] by modifying the stress-strain relation of steel fibers within the plastic hinge zone. It was observed that the strain penetration contribution to lateral deflection predicted by the method of Pan et al. [138] resulted in a close agreement of lateral deflection with experimental results. The hysteretic strength degradation and pinching were calibrated by using the parameters damage and pinching parameters of the *Hysteretic* material in *OpenSees*. The predicted dissipated energy, lateral strength, and ductility were in good agreement with the experimental results. However, the

lateral deflection of the column strengthened by HSS collars spaced at 333 mm was underestimated.

Chapter 7 Conclusions and Recommendations

7.1. Conclusions

The present study investigated the effectiveness of hollow steel section (HSS) collars in preventing brittle splitting failures associated with substandard lap splices. An experimental framework was designed, including nineteen simply supported beams, each incorporating substandard lap splices at its midspan. Analytical modeling of beams with and without HSS collars was performed by using *OpenSees*. The analytical modeling was further extended to HSS collar strengthened RC columns tested by Kruavit [76]. The following important conclusions can be drawn.

1. Splitting cracks were initiated in all beams, irrespective of the presence of HSS collars. These cracks resulted in sudden delamination of concrete cover along the lap splice of control beams (Type-I failure). For beams with insufficient confinement by HSS collars, these cracks propagated along the lap splice, indicating that ample dilation of concrete cover had occurred, resulting in splitting failure (Type-II failure). In sufficiently confined beams, splitting cracks were completely restrained at their origin, i.e., ends of lap splices (Type-III failure). Post-test inspection revealed no splitting cracks along lap splices of sufficiently confined beams. The maximum increase in the peak sustained load after confinement by HSS collars was observed for Subgroup L20C1, which was 82.6%. For Subgroup L20C2, the maximum increase in the peak sustained load was 59.6%.

2. For beams that exhibited ductile response (Type-III failure), strain along lapped bars revealed yielding near loaded ends for an average distance of 25% of the lap splice length and high inelastic strains in post-yield zones of lap splices.

3. It was found that the bond strength is limited to the onset of yielding in lapped bars. For instance, the bond strength of Beam L35C1SC was 3.67 MPa, and it exhibited Type-I failure. After confinement by HSS collars, the failure of Beam L35C1S200 was changed to Type-III failure, whereas its bond strength remained at 3.65 MPa. Therefore, the bond strength alone is insufficient to

characterize confinement for lap splices that exhibit yielding at their loaded ends in unstrengthened beams.

4. The interfacial fracture energy was used to relate the improvement in the behavior of strengthened beams to the confinement ratio of HSS collars. An equation to estimate the bond strength in the pre-yield zone was proposed based on the observed linear strain distribution. Bond strengths in pre-yield and post-yield zones were used to calculate the total interfacial fracture energy. The interfacial fracture energy was found to relate well with the confinement ratio of HSS collars.

5. Nonlinear regression analysis was performed to propose an equation to estimate the increase in the interfacial fracture energy relating to the confinement by HSS collars. An analytical procedure was proposed considering the interfacial fracture energy within the pre-yield and post-yield zones of lapped bars to estimate the required confinement ratio of HSS collars for substandard lap splices. The required confinement ratios of HSS collars were found to agree with the experiment, while the required confinement ratios of HSS collars was overestimated in some cases.

6. Nonlinear fiber modeling using *OpenSees* was performed to predict the load-deflection curves of all beams tested in this present study. The models by Tariverdilo et al. [78], Elwood et al. [129], Lettow and Eligehausen [126], and Belejo [127] were compared to predict the lap splice strength at splitting failure in control beams. The failure load of control beams was well predicted by the models of Lettow and Eligehausen [126] and Belejo [127. To model HSS collar strengthened beams, an approach by Chapman and Driver {Chapman, 2006 #263] was adopted to estimate the compressive stress-strain relation of concrete confined by HSS collars. A good correlation between the experimental and *OpenSees* predicted load-deflection curves was obtained. It was observed that a softening of the load-deflection curves of beams was predicted by the *OpenSees* model for HSS collars spaced at 200 mm, whereas the load-deflection curves predicted by the *OpenSees* model for HSS collars spaced at 100 mm closely matched the experimental results. This may be

attributed to the large spacing of 200 mm, whose corresponding confinement ratio lies outside the range tested by Chapman and Driver [99].

7. The control column tested by Kruavit [76] was modeled by both distributed plasticity methods (Tariverdilo et al. [78] and Alvi et al. [89]) and the concentrated plasticity method (Opabola et al. [93]). It was found that the initial stiffness and strength degradation were correctly modeled by both methods. However, the pinching behavior was underestimated by the model of Opabola et al. [93] and Alvi et al. [89]. Further, the residual lateral strength at failure was overestimated by the model of Alvi et al. [89]. The experimental dissipated energy, peak lateral strength, lateral strength at failure, and initial stiffness were correctly modeled by Tariverdilo et al. [78] model. The model by Tariverdilo et al. [78] is recommended to predict the cyclic behavior of RC columns with substandard lap splices. Finally, HSS collars strengthened columns tested by Kruavit [76] were modeled using *OpenSees*. The method of Pan et al. [138] was used to include the effect of strain penetration by modifying the stress-strain relation of steel fibers within the plastic hinge zone. It was observed that the strain penetration contribution to lateral deflection predicted by the method of Pan et al. [138] resulted in a close agreement of lateral deflection with experimental results. The hysteretic strength degradation and pinching were calibrated by using the damage and pinching parameters of the *Hysteretic* material in *OpenSees*. The predicted dissipated energy, lateral strength, and ductility were in good agreement with the experimental results. Further, the *pinchX* and *pinchY* values of the *Hysteretic* material in *OpenSees* should be taken as 0.50, whereas the *damage1* and *damage2* parameters should be taken as 0.020 to accurately model the hysteretic behavior of columns sufficiently confined by HSS collars.

7.2. Recommendations

The following recommendations are proposed for future research on strengthening substandard lap splices by using HSS collars.

1. The model by Chapman and Driver [99] was found to predict the compressive stress-strain response of concrete confined by HSS collars with good accuracy only for spacing of 100 mm and above. The post-peak stress-strain relation of concrete confined by HSS collars at 200 mm spacing was characterized by a quick drop that underestimated the axial ductility. This is because the corresponding load-deflection response predicted by HSS collars demonstrated a softening behavior in the post-yield region, whereas no such softening was observed in the experimental response. It is suggested to perform compressive tests on column specimens strengthened by HSS collars having confinement ratios within the range adopted in this study. This can have two advantages: (1) The actual post-peak compressive stress-strain behavior of HSS collar confined concrete can be obtained especially for the confinement ratios of HSS collars adopted in the present study, and (2) the procedure by Chapman and Driver [99] to establish stress-strain curves of HSS collar confined concrete requires an iterative procedure. Regression analysis can be performed to directly propose equations for various points along the experimental stress-strain curve of HSS collar confined concrete (For instance, see [39]).

2. In Chapter 4, a design equation to estimate the required confinement ratio of HSS collars was proposed to strengthen substandard lap splices. The predicted confinement ratios of HSS collars for Subgroups L28C2 and L35C2 were higher than the corresponding experimental values. This is because a constant spacing of 200 mm for HSS collars was provided in all subgroups. In reality, the demand for external HSS collar confinement in subgroups L28C2, L35C1, and L35C2 would have been lower than that supplied by HSS collars at 200 mm due to a larger concrete cover and longer lap splice length. It is suggested to test additional beams in subgroups L28C1, L35C1, and L35C2 with HSS collar confinement ratios smaller than those used in the present study. In this way, an improved design equation for the design of HSS collar confinement can be proposed.

3. The present study targeted substandard lap splices with R_{ls} values ranging from 0.23 to 0.65. It is recommended to explore lap splices with R_{ls} values outside this range.

REFERENCES

[1] Bayraktar A, Altunişik AC, Pehlivan M. Performance and Damages of Reinforced Concrete Buildings During the October 23 and November 9, 2011 Van, Turkey, Earthquakes. Soil Dynamics and Earthquake Engineering. 2013;53:49-72.

[2] Eberhard M, Baldridge S, Marshall J, Mooney W, Rix G. Haiti Earthquake of January 12, 2010: USGS/EERI advance reconnaissance team report. Reston, Virginia: US Geological Survey Open-File Report; 2013.

[3] Esper P, Tachibana E. Lessons from the Kobe Earthquake. Geological Society, London, Engineering Geology Special Publication. 1998;15:105-116.

[4] Cooper JD, Friedland IM, Buckle IG, Nimis RB, McMullin Bobb N. The Northridge Earthquake: Progress Made, Lessons Learned in Seismic-Resistant Bridge Design. Public Roads, Federal Highway Administration. 1994;58:26-36.

[5] Haroun MA, Elsanadedy HM. Fiber-Reinforced Plastic Jackets for Ductility Enhancement of Reinforced Concrete Bridge Columns with Poor Lap-Splice Detailing. Journal of Bridge Engineering. 2005;10:749-757.

[6] Yakut A, Gülkan P, Sadik Bakir B, Tolga Yilmaz M. Re-examination of Damage Distribution in Adapazarı: Structural Considerations. Engineering Structures. 2005;27:990-1001.

[7] Melek M, Wallace JW. Cyclic Behavior of Columns with Short Lap Splices. ACI Structural Journal. 2004;101:802-811.

[8] ACI 318-19: Building Code Requirements for Structural Concrete and Commentary. American Concrete Institute. Farmington Hills, MI, USA: American Concrete Institute; 2019.

[9] Kim CG, Park HG, Eom TS. Effects of Type of Bar Lap Splice on Reinforced Concrete Columns Subjected to Cyclic Loading. ACI Structural Journal. 2019;116:183-194.

[10] Sharma K, Deng L, Noguez CC. Field Investigation on the Performance of Building Structures During the April 25, 2015, Gorkha Earthquake in Nepal. Engineering Structures. 2016;121:61-74.

[11] Al-Quraishi H, Al-Farttoosi M, AbdulKhudhur R. Tension Lap Splice Length of Reinforcing Bars Embedded in Reactive Powder Concrete (RPC). Structures. 2019;19:362-368.

[12] Orangun CO, Jirsa JO, Breen JE. A Reevaluation of Test Data on Development Length and Splices. ACI Journal. 1977;12:114-122.

[13] Darwin D, Zuo J, Tholen ML, Idun EK. Development Length Criteria for Conventional and High Relative Rib Area Reinforcing Bars. ACI Structural Journal. 1996;93:347-359.

[14] Zuo J, Darwin D. Splice Strength of Conventional and High Relative Rib Area Bars in Normal and High-Strength Concrete. ACI Structural Journal. 2000;97:630-641.

[15] Alyousef R, Topper T, Al-Mayah A. Effect of the Thickness of Concrete Cover on the Fatigue Bond Strength of GFRP Wrapped and Non-Wrapped Reinforced Concrete Beams Containing a Lap Splice. Structures. 2016;6:1-8.

[16] James K W, James G M. Reinforced Concrete: Mechanics and Design. 6th ed: Pearson; 2012.

[17] McCormac JC, Brown RH. Design of Reinforced Concrete. 10th ed: John Wiley & Sons.; 2015.

[18] Zadeh VZ, Eshghi S. Nonlinear Finite Element Modeling of GFRP-Strengthened Slender Rectangular RC Columns with Confinement Deficiency in Plastic Hinge Zone. Jordan Journal of Civil Engineeirng. 2018;12:173-187.

[19] Chai YH, Priestley MJN, Seible F. Seismic Retrofit of Bridge Columns by Steel Jacketing. Bridge Engineering Conference, Transportation Research Record No 1290. Denver, Colorado1991.

[20] Priestley MJN, Seible F. Design of Seismic Retrofit Measures for Concrete and Masonry Structures. Construction and Building Materials. 1995;9:365-377.

[21] Aboutaha RS, Engelhardt MU, Jirsa JO, Kreger MF. Retrofit of Concrete Columns with Inadequate Lap splices by the Use of Rectangular Steel Jackets. Earthquake Spectra. 1996;12:693-714.

[22] Lehman DE, Gookin SE, Nacamull AM, Moehle JP. Repair of Earthquake-Damaged Bridge Columns. ACI Structural Journal. 2001;98:233-242.

[23] Vandoros KG, Dritsos SE. Concrete Jacket Construction Detail Effectiveness when Strengthening RC Columns. Construction and Building Materials. 2008;22:264-276.

[24] Daudey X, Filiatrault A. Seismic Evaluation and Retrofit with Steel Jackets of Reinforced Concrete Bridge Piers Detailed with Lap-Splices. Canadian Journal of Civil Engineering. 2011;27:1-16.

[25] Xu CX, Peng S, Deng J, Wan C. Study on Seismic Behavior of Encased Steel Jacket-Strengthened Earthquake-Damaged Composite Steel-Concrete Columns. Journal of Building Engineering. 2018;17:154-166.

[26] Chrysanidis T, Tegos I. Axial and Transverse Strengthening of R/C Circular Columns: Conventional and New Type of Steel and Hybrid Jackets Using High-Strength Mortar. Journal of Building Engineering. 2020;30.

[27] Cao S, Wu C, Wang W. Behavior of FRP Confined UHPFRC-filled Steel Tube Columns Under Axial Compressive Loading. Journal of Building Engineering. 2020;32.

[28] Chang SY, Chen TW, Tran NC, Liao WI. Seismic Retrofitting of RC Columns with RC Jackets and Wing Walls with Different Structural Details. Earthquake Engineering and Engineering Vibration. 2014;13:279-292.

[29] Juntanalikit P, Jirawattanasomkul T, Pimanmas A. Experimental and Numerical Study of Strengthening Non-Ductile RC Columns with and without Lap Splice by Carbon Fiber Reinforced Polymer (CFRP) Jacketing. Engineering Structures. 2016;125:400-418.

[30] Raza S, Khan MKI, Menegon SJ, Tsang HH, Wilson JL. Strengthening and Repair of Reinforced Concrete Columns by Jacketing: State-of-the-Art Review. Sustainability 2019;11.

[31] Hamad BS, Rteil AA, Salwan BR, Soudki KA. Behavior of Bond-Critical Regions Wrapped with Fiber-Reinforced Polymer Sheets in Normal and High-Strength Concrete. Journal of Composites for Construction. 2004;8:248-257.

[32] Al-Obaidi S, Saeed YM, Rad FN. Flexural Strengthening of Reinforced Concrete Beams with NSM-CFRP Bars using Mechanical Interlocking. Journal of Building Engineering. 2020;31.

[33] Harajli MH. Bond Strengthening of Lap Spliced Reinforcement using External FRP Jackets: An Effective Technique for Seismic Retrofit of Rectangular or Circular RC Columns. Construction and Building Materials. 2009;23:1265-1278.

[34] Seible F, Priestley MJN, Hegemier GA, Innamorato D. Seismic Retrofit of RC Columns with Continuous Carbon Fiber Jackets. Journal of Composites for

Construction. 1997;1:52-62.

[35] Harries K, Ricles J, Pissiki S, Sause R. Seismic Retrofit of Lap Splices in Nonductile Columns Using CFRP Jackets. ACI Structural Journal. 2006;103:226-236.

[36] Ghosh KK, Sheikh SA. Seismic Upgrade with Carbon Fiber-Reinforced Polymer of Columns Containing Lap-Spliced Reinforcing Bars. ACI Structural Journal. 2007;104:227-236.

[37] ElGawady M, Endeshaw M, McLean D, Sack R. Retrofitting of Rectangular Columns with Deficient Lap Splices. Journal of Composites for Construction. 2009;14:22-35.

[38] Kim IS, Jirsa JO, Bayrak O. Use of Carbon Fiber-Reinforced Polymer Anchors to Repair and Strengthen Lap Splices of Reinforced Concrete Columns. ACI Structural Journal. 2011;108:630-640.

[39] Hussain Q, Ruangrassamee A, Tangtermsirikul S, Joyklad P, Wijeyewickrema AC. Low-Cost Fiber Rope Reinforced Polymer (FRRP) Confinement of Square Columns with Different Corner Radii. Buildings 2021;11:355-379.

[40] Wang LM, Wu YF. Effect of Corner Radius on the Performance of CFRP-Confined Square Concrete Columns. Engineering Structures. 2008;30:493-505.

[41] Zeng JJ, Guo YC, Gao WY, Li JZ, Xie JH. Behavior of Partially and Fully FRP-Confined Circularized Square Columns under Axial Compression. Construction and Building Materials. 2017;152:319-332.

[42] Pantelides CP, Yan Z, Reaveley LD. Report No. UT-05.03: Shape Modification of Rectangular Columns Confined with FRP Composites. Salt Lake City, UT United States2004.

[43] Lin ML, Chen PC, Tsai KC, Yu YJ, Liu JG. Seismic Steel Jacketing of Rectangular RC Bridge Columns For the Mitigation of Lap-Splice Failures. Earthquake Engineering & Structural Dynamics. 2010;39:1687-1710.

[44] Hussain MA, Driver RG. Experimental Investigation of External Confinement of Reinforced Concrete Columns by Hollow Structural Section Collars. ACI Structural Journal. 2005;102:242-251.

[45] ACI Committee 408R-03: Bond and Development of Straight Reinforcing Bars in Tension. 2003.

[46] Mathey RG, Watstein D. Investigation of Bond In Beam and Pull-Out Specimens with High-Yield -Strength Deformed Bars. ACI Journal Proceedings. 1961;57:1071-1090.

[47] Abrishami HH, Mitchell D. Analysis of Bond Stress Distributions in Pullout Specimens. Journal of Structural Engineering. 1996;122:255-261.

[48] Feldman LR, Bartlett FM. Bond Stresses Along Plain Steel Reinforcing Bars in Pullout Specimens. ACI Structural Journal. 2007;104:685-697.

[49] McCabe SL, Darwin D, Choi OC, Hadje-Ghaffari H. Application of Fracture Mechanics to Steel-Concrete Bond Analysis. ACI Special Publication. 1992;134:101-114.

[50] Rizkalla SH, El-Haacha R, Elagroudy H. Bond Characteristics of High-Strength Steel Reinforcement. ACI Structural Journal. 2006;103:771-782.

[51] Harajli MH, Hamad BS, Rteil AA. Effect of Confinement on Bond Strength between Steel Bars and Concrete. ACI Structural Journal. 2004;101:595-603.

[52] Garcia R, Helal Y, Pilakoutas K, Guadagnini M. Bond Behaviour of Substandard Splices in RC beams Externally Confined with CFRP. Construction and Building

Materials. 2014;50:340-351.

[53] Garcia R, Helal Y, Pilakoutas K, Guadagnini M. Bond Strength of Short Lap Splices in RC Beams Confined with Steel Stirrups or External CFRP. Materials and Structures. 2015;48:277-293.

[54] Helal Y, Garcia R, Pilakoutas K, Guadagnini M, Hajirasouliha I. Strengthening of Short Splices in RC Beams using Post-Tensioned Metal Straps. Materials and Structures/Materiaux et Constructions. 2016;49:133-147.

[55] Esfahani MR, Rangan BV. Bond between Normal Strength and High-Strength Concrete (HSC) and Reinforcing Bars in Splices in Beams. ACI Structural Journal. 1998;95:272-280.

[56] Hamad BS. Bond Strength Improvement of Reinforcing Bars with Specially Designed Rib Geometries. ACI Structural Journal. 1995;92:3-13.

[57] Harajli MH, Hamad BS, Karam K. Bond-slip Response of Reinforcing Bars Embedded in Plain and Fiber Concrete. Journal of Materials in Civil Engineering. 2002;14.

[58] Hamad BS, Soudki KA, Harajli MH, Rteil AA. Experimental and Analytical Evaluation of Bond Strength of Reinforcement in Fiber-Reinforced Polymer-Wrapped High-Strength Concrete Beams. ACI Structural Journal. 2004;101:747-754.

[59] Harajli MH. Effect of Confinement using Steel, FRC, or FRP on the Bond Stress-Slip Response of Steel Bars under Cyclic Loading. Materials and Structures 2006;39:621-634.

[60] Lynn AC, Moehle JP, Mahin SA, Holmes WT. Seismic Evaluation of Existing Reinforced Concrete Building Columns. Earthquake Spectra. 1996;12:715-739.

[61] Ghobarah A, Aziz TS, Biddah A. Rehabilitation of Reinforced Concrete Frame Connections Using Corrugated Steel Jacketing. ACI Structural Journal. 1997;94:282-294.

[62] ACI 318-19: Building Code Requirements for Structural Concrete and Commentary. Farmington Hills, MI, USA2019.

[63] Harajli MH. Seismic Behavior of RC Columns with Bond-Critical Regions: Criteria for Bond Strengthening Using External FRP Jackets. Journal of Composites for Construction. 2008;12:69-79.

[64] Choi E, Choi DH, Chung YS, DesRoches R. Seismic Protection of Lap-Spliced RC Columns Using SMA Wire Jackets. Magazine of Concrete Research. 2015;64:239-252.

[65] Xiao Y, Ma R. Seismic Retrofit of RC Circular Columns Using Prefabricated Composite Jacketing. Journal of Structural Engineering. 1997;123:1357-1364.

[66] Bournas DA, Triantafillou TC. Bond Strength of Lap-Spliced Bars in Concrete Confined with Composite Jackets. Journal of Composites for Construction. 2011;15:156-167.

[67] Ghobarah A, Biddah A, Mahgoub M. Seismic rRhabilitation of Beam-Column Joints Using FRP Laminates. Journal of Earthquake Engineering. 2001;5:113-129.

[68] Bousias S, Spathis AL, Fardis MN. Seismic Retrofitting of Columns with Lap Spliced Smooth Bars Through FRP or Concrete Jackets. Journal of Earthquake Engineering. 2007;11:653-674.

[69] Kalogeropoulos GI, Tsonos AG. Effectiveness of R/C Jacketing of Substandard R/C Columns with Short Lap Splices. Structural Monitoring and Maintenance. 2014;1:273-292.

[70] Mugahed Amran YH, Alyousef R, Rashid RSM, Alabduljabbar H, Hung CC.

Properties and Applications of FRP in Strengthening RC Structures: A Review. Structures. 2018;16:208-238.

[71] Mostofinejad D, Ilia E. Confining of Square RC Columns with FRP Sheets Using Corner Strip–Batten Technique. Construction and Building Materials. 2014;70:269-278.

[72] Wang LM, Wu YF. Effect of Corner Radius on the Performance of CFRP-Confined Square Concrete Columns: Test. Engineering Structures. 2008;30:493-505.

[73] Liu J, Driver RG, Lubell AS. Experimental Study on Short Concrete Columns with External Steel Collars. ACI Structural Journal. 2011;108:360-369.

[74] Pudjisuryadi P, Tavio T, Suprobo P. Performance of Square Reinforced Concrete Columns Externally Confined by Steel Angle Collars Under Combined Axial and Lateral Load. Procedia Engineering. 2015;125:1043-1049.

[75] Dirikgil T. Experimental Investigation of the Contributions of CFRP and Externally Collar Strengthening to the Seismic Performance of RC Columns with Different Cross-Sections. Structures. 2020;24:266-281.

[76] Kruavit P. Seismic Enhancement of Reinforced Concrete Columns with Lap Splices using External Steel Collars [Ph.D. Thesis]. Bangkok, Thailand: Chulalongkorn University; 2019.

[77] Richart FE, Brandtzæg A, Brown RL. A Study of the Failure of Concrete Under Combined Compressive Stresses. Bulletins - Engineering Experiment Station. 1928.

[78] Tariverdilou S, Farjadi A, Barkhordari M. Fragility Curves For Reinforced Concrete Frames With Lap-Spliced Columns. International Journal of Engineering. 2009;22:213-224.

[79] Priestley MJN, Seible F, Calvi GM. Seismic Design and Retrofit of Bridges: John Wiley & Sons, Inc.; 1996.

[80] Mander JB, Priestley MJN, Park R. Observed Stress Strain Behavior of Confined Concrete. Journal of Structural Engineering. 1988;114:1827-1849.

[81] Choi E, Jeon JS, Lee JH, Park SH, Ha S. Assessment of Probabilistic Seismic Performance of RC Columns Jacketed by FRP Winding Wires Using Analytical Models. Engineering Structures. 2018;171:629-646.

[82] Lowes LN, Mitra N, Altoontash A. A Beam-Column Joint Model for Simulating the Earthquake Response of Reinforced Concrete Frames: PEER Report 2003/10. University of California, Berkeley; 2004.

[83] Park YJ, Ang AHS. Mechanistic Seismic Damage Model for Reinforced Concrete. Journal of Structural Engineering. 1985;111:722-739.

[84] McKenna F. OpenSees: A Framework for Earthquake Engineering Simulation. Computing in Science & Engineering. 2011;13:58-66.

[85] Zhang Y, DesRoches R, Tien I. Impact of Corrosion on Risk Assessment of Shear-Critical and Short Lap-Spliced Bridges. Engineering Structures. 2019;189:260-271.

[86] Zhao J, Sritharan S. Modeling of Strain Penetration Effects in Fiber-Based Analysis of Reinforced Concrete Structures. ACI Structural Journal. 2007;104:133-141.

[87] Zhang Y, Tien I. Methodology for Regularization of Force-Based Elements to Model Reinforced Concrete Columns with Short Lap Splices. Journal of Engineering Mechanics. 2020;146.

[88] Coleman J, Spacone E. Localization Issues in Force-Based Frame Elements. Journal of Structural Engineering. 2001;127:1257-1265.

[89] Alvi MH, Lee CS, Jeon J-S. Model Development and Seismic Performance Evaluation of Rectangular Reinforced Concrete Columns with Short Lap Splices in

Existing Building Frames. Engineering Structures. 2021;245.

[90] Cho J-Y, Pincheira JA. Inelastic Analysis of Reinforced Concrete Columns with Short Lap Splices Subjected to Reversed Cyclic Loads. ACI Structural Journal. 2006;103:280-290.

[91] Harajli MH. Development/Splice Strength of Reinforcing Bars Embedded in Plain and Fiber Reinforced Concrete. ACI Structural Journal. 1994;91:511-520.

[92] Razvi S, Saatcioglu M. Design of R/C Columns for Confinement Based on Lateral Drift. Ottawa Carleton Earthquake Engineering Research Center; 1996.

[93] Opabola EA, Elwood KJ, Liel AB. Evaluation of Seismic Performance of As-built and Retrofitted Reinforced Concrete Frame Structures with Lap Splice Deficiencies. Earthquake Engineering & Structural Dynamics. 2021;50:3138-3159.

[94] ASCE. Seismic Evaluation and Retrofit of Existing Buildings (41-17). 2017.

[95] Pudjisuryadi P, Tavio, Suprobo P. Analytical Confining Model of Square Reinforced Concrete Columns using External Steel Collars. International Journal of ICT-aided Architecture and Civil Engineering. 2013;1:1-18.

[96] Xiao Y, Wu H. Retrofit of Reinforced Concrete Columns Using Partially Stiffened Steel Jackets. Journal of Structural Engineering. 2003;129:725-732.

[97] Razvi S, Saatcioglu M. Confinement Model for High-Strength Concrete. Journal of Structural Engineering. 1999;125:281-289.

[98] Tabsh SW. Stress-Strain Model for High-Strength Concrete Confined by Welded Wire Fabric. Journal of Materials in Civil Engineering. 2007;19:286-294.

[99] Chapman JR, Driver RG. Structural Engineering Report 263: Behaviour of Collared Concrete Columns Under Concentric or Eccentric Loads. University of Alberta, Canada; 2006.

[100] Fam AZ, Rizkalla SH. Confinement Model for Axially Loaded Concrete Confined by Circular Fiber-Reinforced Polymer Tubes. ACI Structural Journal. 2001;98:451-461.

[101] Popovics S. A Numerical Approach to the Complete Stress-Strain Curve of Concrete. Cement and Concrete Research. 1973;3:583-599.

[102] Mains RM. Measurement of the Distribution of Tensile and Bond Stresses Along Reinforcing Bars. Journal of the American Concrete Institute. 1951;48:225-252.

[103] Perry ES, Thompson JN. Bond Stress Distribution on Reinforcing Steel in Beams and Pullout Specimens. Journal of the American Concrete Institute. 1966;63:865-876.

[104] Viwathanatepa S. Report No. UCB/EERC-79/22 Effects of Generalized Loadings on Bond of Reinforcing Bars Embedded in Confined Concrete Blocks. University of California; 1979.

[105] Kankam CK. Relationship of Bond Stress, Steel Stress, and Slip in Reinforced Concrete. Journal of Structural Engineering. 1997;123:79-85.

[106] Weathersby JH. Investigation of Bond Slip between Concrete and Steel Reinforcement under Dynamic Loading Conditions [Ph.D. Thesis]. USA: Louisiana State University and Agricultural & Mechanical College; 2003.

[107] Lee B, Mulheron M. Fluctuation of Bond Stress–Slip Behaviour of Deformed Bar under Displacement Control. Magazine of Concrete Research. 2015;64:863-875.

[108] Lagier F, Massicotte B, Charron JP. Experimental Investigation of Bond Stress Distribution and Bond Strength in Unconfined UHPFRC Lap Splices under Direct Tension. Cement and Concrete Composites. 2016;74:26-38.

[109] Lee SW, Kang SB, Tan KH, Yang EH. Experimental and Analytical Investigation on Bond-Slip Behaviour of Deformed Bars Embedded in Engineered Cementitious

Composites. Construction and Building Materials. 2016;127:494-503.

[110] Kaklauskas G, Sokolov A, Ramanauskas R, Jakubovskis R. Reinforcement Strains in Reinforced Concrete Tensile Members Recorded by Strain Gauges and FBG Sensors: Experimental and Numerical Analysis. Sensors 2019;19:200-221.

[111] Kang SB, Wang S, Long X, Wang DD, Wang CY. Investigation of Dynamic Bond-Slip Behaviour of Reinforcing Bars in Concrete. Construction and Building Materials. 2020;262:1208-1224.

[112] Long X, Wang CY, Zhao PZ, Kang SB. Bond Strength of Steel Reinforcement under Different Loading Rates. Construction and Building Materials. 2020;238.

[113] Malek M, Wallace JW, Conte JP. PEER Report 2003/04: Experimental Assessment of Columns with Short Lap Splices Subjected to Cyclic Loads. University of California, San Diego; 2003.

[114] Mahrenholtz C. Seismic Bond Model for Concrete Reinforcement and the Application to Column-to-Foundation Connections [Ph.D. Thesis]: Institut für Werkstoffe im Bauwesen der Universität Stuttgart 2012.

[115] Harajli MH. Axial stress–strain relationship for FRP confined circular and rectangular concrete columns. Cement and Concrete Composites. 2006;28:938-948.

[116] Orangun CO, Jirsa JO, Breen JE. A Reevaluation of Test Data on Development Length and Splices. ACI Journal. 1977;74:114-122.

[117] Shima H, Chou LL, Okamura H. Micro and Macro Models for Bond in Reinforced Concrete. University of Tokyo, Journal of the Faculty of Engineering. 1987;39:133-194.

[118] FIB Bulletin 10: Bond of Reinforcement in Concrete. Laussane, Switzerland: The International Federation for Structural Concrete; 2000.

[119] ElSouri AM, Harajli MH. Seismic Repair and Strengthening of Lap Splices in RC Columns: Carbon Fiber–Reinforced Polymer versus Steel Confinement. Journal of Composites for Construction. 2011;15:721-731.

[120] Darwin D, Lutz LRA, Zuo J. Recommended Provisions and Commentary on Development and Lap Splice Lengths for Deformed Reinforcing Bars in Tension. ACI Structural Journal. 2005;102:892-900.

[121] Turk K, Benli A, Calayir Y. Bond Strength of Tension Lap-Splices in Full Scale Self-Compacting Concrete Beams. Turkish J Eng Env Sci. 2008;32:386-386.

[122] Helal Y. Seismic Strengthening of Deficient Exterior RC Beam-Column Sub-assemblages using Post-tensioned Metal Strips [Ph.D. Thesis]. UK: University of Sheffield; 2012.

[123] Malek A, Scott A, Pampanin S, Hoult NA. Postyield Bond Deterioration and Damage Assessment of RC Beams Using Distributed Fiber-Optic Strain Sensing System. Journal of Structural Engineering. 2019;145.

[124] Haskett M, Oehlers DJ, Mohamed Ali MS. Local and Global Bond Characteristics of Steel Reinforcing Bars. Engineering Structures. 2008;30:376-383.

[125] Fawzy T, Khalil AH, Atta A, Afefy HM, Ellithy M. Experimental and Analytical Study on Tension Lap Splices in Nonconventional Concrete Using Different Techniques. Structural Concrete. 2021;22:911-925.

[126] Lettow S, Eligehausen R. Formulation of Application Rules for Lap Splices in the New fib Model Code. Presentation, Task group 45, Bond models, Stuttgart, Germany. Stuttgart, Germany2006.

[127] Belejo A. Evaluation of Ground MotionDuration Effects on the Damage

Prediction of Building and Bridge Structural and Soil-Structural Systems [Ph.D. Thesis]. USA: Oregon State University; 2017.

[128] FEMA. Prestandard and Commentary for the Seismic Rehabilitation. Washington, DC, USA2000.

[129] Elwood KJ, Matamoros AB, Wallace JW, Lehman DE, Heintz JA, Mitchell AD et al. Update to ASCE/SEI 41 Concrete Provisions. https://doiorg/101193/12757714. 2007;23:493-523.

[130] McKenna F. OpenSees: A Framework for Earthquake Engineering Simulation. Computing in Science & Engineering. 2010;13:58-66.

[131] Spacone E, Filippou FC, Taucer FF. Fiber Beam–Column Model for Non-Linear Analysis of R/C Frames: Part I. Formulation. Earthquake Engineering & Structural Dynamics. 1996;25:711-725.

[132] Li L, Wang W, Shi P. Modelling Catastrophic Degradation of Flexural-Dominated RC Columns at Ultimate Displacements Based on Fibre Beam-Column Model. Journal of Building Engineering. 2022;45.

[133] Girard A, Legeron F, Roy N. A Model for Seismic Performance Assessment of Bridge Piers. 15th WCEE Lisbon2012.

[134] Wang JH, Cai GC, Si Larbi A. Lateral Behavior of Rectangular Concrete Columns Reinforced by Partially Debonded High-Strength Reinforcements Based on a Proposed Equivalent Stress Block. Bulletin of Earthquake Engineering. 2021;19:1901-1930.

[135] Sezen H, Setzler EJ. Reinforcement Slip in Reinforced Concrete Columns. ACI Structural Journal. 2008;105:280-289.

[136] Sezen H, Moehle JP. Seismic Tests of Concrete Columns with Light Transverse Reinforcement. ACI Structural Journal. 2006;103:842-855.

[137] Alsiwat JM, Saatcioglu M. Reinforcement Anchorage Slip under Monotonic Loading. Journal of Structural Engineering. 1992;118.

[138] Pan WH, Tao MX, Nie JG. Fiber Beam–Column Element Model Considering Reinforcement Anchorage Slip in the Footing. Bulletin of Earthquake Engineering. 2017;15:991-1018.

[139] Syed M, Moeini M, Okumus P, Elhami-Khorasani N, Ross BE, Kleiss MCB. Analytical Study of Tessellated Structural-Architectural Reinforced Concrete Shear Walls. Engineering Structures. 2021;244.

[140] Mehary S, Dusicka P, Bazaez R. Effect of Subduction Earthquake-Based Loading History on Substandard RC Square Columns. Journal of Bridge Engineering. 2017;23.

[141] Wang Z, Wang J, Liu J, Han F, Zhang J. Large-Scale Quasi-Static Testing of Precast Bridge Column with Pocket Connections using Noncontact Lap-Spliced Bars and UHPC Grout. Bulletin of Earthquake Engineering. 2019;17:5021-5044.

[142] Yao L-Z, Wu G. Fiber-Element Modeling for Seismic Performance of Square RC Bridge Columns Retrofitted with NSM BFRP Bars and/or BFRP Sheet Confinement. Journal of Composites for Construction. 2016;20.

[143] Wang Z, Wang J, Liu T, Zhang F. Modeling Seismic Performance of High-Strength Steel–Ultra-High-Performance Concrete Piers with Modified Kent–Park Model using Fiber Elements. Advances in Mechanical Engineering. 2016;8.

[144] Su J, Dhakal RP, Junjie W. Fiber-Based Damage Analysis of Reinforced Concrete Bridge Piers. Soil Dynamics and Earthquake Engineering. 2017;96:13-34.

[145] Wang F, Yu Y, Zhao X-Y, Xu J-J, Xie T-Y, Deresa S. Performance Evaluation of

Reinforced Recycled Aggregate Concrete Columns under Cyclic Loadings. Applied Sciences. 2019;9:1460-1482.

[146] Rasulo A, Pelle A, Lavorato D, Fiorentino G, Nuti C, Briseghella B. Finite Element Analysis of Reinforced Concrete Bridge Piers Including a Flexure-Shear Interaction Model. Applied Sciences. 2020;10:2209-2224.

[147] Abbass A, Attarnejad R, Ghassemieh M. Seismic Assessment of RC Bridge Columns Retrofitted with Near-Surface Mounted Shape Memory Alloy Technique. Materials (Basel). 2020;13:1701-1725.

[148] ASCE/SEI. Seismic Evaluation and Retrofit of Existing Buildings. ASCE. 2017.

[149] Kashani MM, Lowes LN, Crewe AJ, Alexander NA. Nonlinear Fibre Element Modelling of RC Bridge Piers Considering Inelastic Buckling of Reinforcement. Engineering Structures. 2016;116:163-177.

[150] Odaa SA, Hason MM, Sharba AAK. Self-Compacting Concrete Beams Reinforced With Steel Fiber Under Flexural Loads: A Ductility Index Evaluation. Materials Today: Proceedings. 2021;42:2259-2267.

[151] AISC. LRFD Specification for Structural Steel Buildings American Institute of Steel Construction; 1999.

Appendix

A1. Estimation of Collar Size

In Figure A1.1, the design of the HSS element was carried out by forming a yield mechanism at the middle and corners of the restraining element. In the case of a beam exposed to monotonic load, only the bottom element was assumed to undergo confinement demands. Under the equilibrium of external and internal work done, Eq. (A1.1) was obtained. Simplification of Eq. (A1.1) yielded Eq. (A1.2) for the plastic moment capacity of the restraining bottom HSS element.

$$f_l \times s \times \left(\frac{1}{2} \times \theta \times \frac{b}{2} \times b\right) = 4 \times M_p \times \theta \qquad (A1.1)$$

$$M_p = \frac{f_l b^2 s}{16} \qquad (A1.2)$$

Knowing nominal axial and flexural capacities of the collar and adopting the failure criteria for steel under combined axial and flexural loading (AISC 1999) [151], the value of f_l can be estimated for a given HSS element.

$$\left.\begin{array}{ll} \dfrac{p}{\phi p_n} + \dfrac{8m}{9\phi m_n} = 1 & \qquad for\ \dfrac{p}{\phi p_n} \geq 0.2 \\[3mm] \dfrac{p}{2\phi p_n} + \dfrac{m}{\phi m_n} = 1 & \qquad for\ \dfrac{p}{\phi p_n} < 0.2 \end{array}\right\} \qquad (A1.3)$$

where ϕp_n and ϕm_n are nominal axial and flexural capacities of the HSS element.
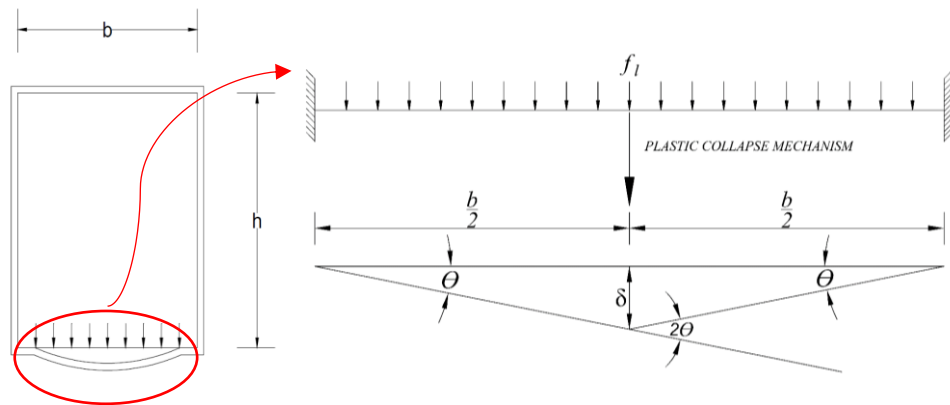
Figure A1.1 Analytical model of confining HSS element.

Eq. (A5) can be solved to estimate f_l, i.e., the pressure generated by HSS collars. Assuming a wall thickness of 2.3 mm and by varying the cross-sectional dimensions of HSS, a relation between the generated pressure and section size was obtained. Hussain and Driver [44] argued that concrete at the level of HSS collars is fully confined. However, the confinement effectiveness reduces between HSS collars. This is schematically described in Figure A1.2. Confinement effectiveness coefficient k_e was derived analogous to Mander et al. [80] with the difference that no unconfined area was assumed at the level of HSS collars. Eq. (A1.4) presents the calculation of k_e.

$$k_e = \left(1 - \frac{s'}{2b}\right)\left(1 - \frac{s'}{2d}\right) \tag{A1.4}$$

$$f_{le} = k_e f_l \tag{A1.5}$$

where f_{le} is the effective confinement pressure generated by HSS collars. Using equilibrium between Eq. (3.1) and Eq. (A1.5), collar spacing was estimated to be 75 mm against the confinement demand of the weakest beam, i.e., L20C1SC, as shown in Figure A1.3.
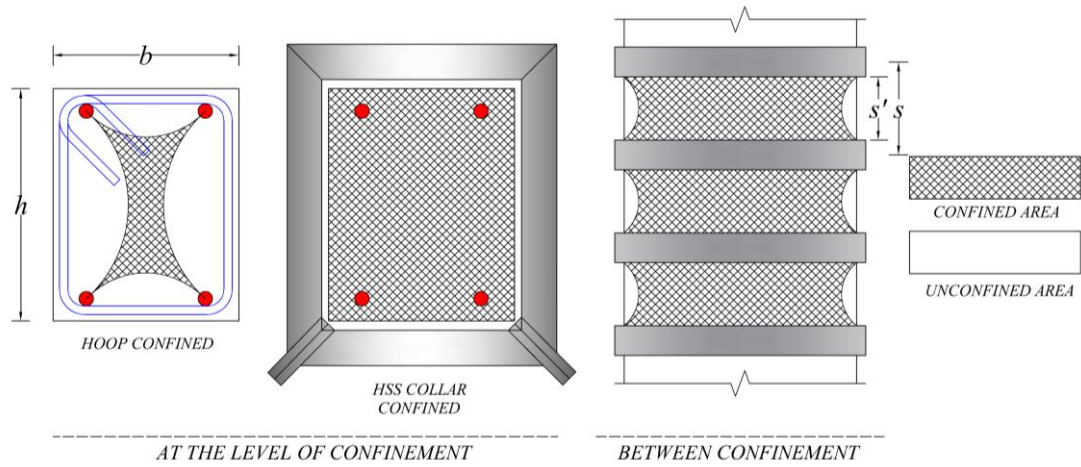
Figure A1.2. Schematic representation of confined area by HSS collar confinement.
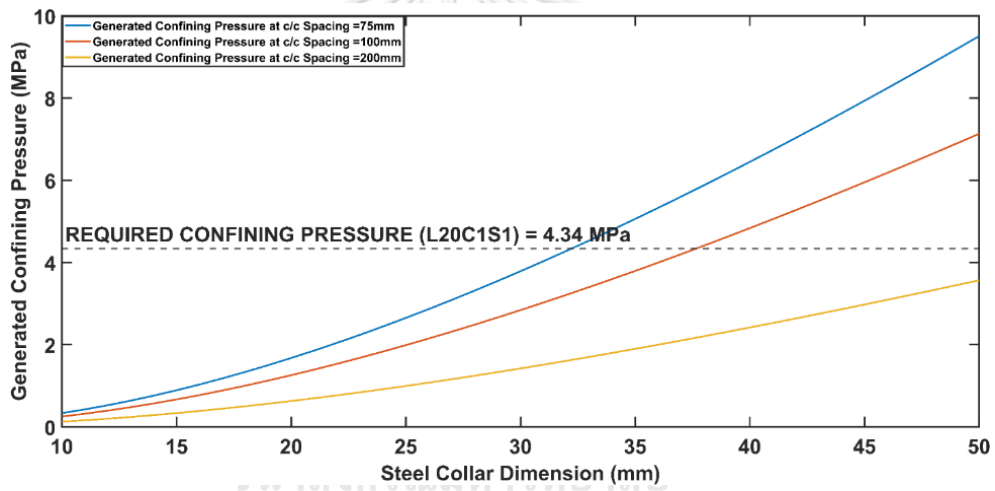
Figure A1.3 Estimated confining pressure vs. steel collar dimension.

A2. Estimation of Shear and Flexural Capacity of RC Section with Substandard Lap Splice

The following procedure was proposed by Opabola et al. [93] to estimate the shear and flexural capacity of a section with a substandard lap splice. The method by Opabola et al. [93] should only be used in Section 6.3 when the calculated flexural capacity is lower than shear capacity. This example shows the computation of shear and flexural strength of the section. To compute the flexural strength, modification is made corresponding to the maximum lap splice stress. For the columns modeled in this study, the maximum splice stress was estimated to be 420 MPa. From sectional analysis on *Response2000*, the moment capacity corresponding to the splice stress of 420 MPa was estimated to be 260.4 kN-m. The corresponding lateral force capacity was estimated at 118.64 kN. The undamaged shear strength of the section V_o was estimated as

$$V_o = \frac{A_v f_{yt} d}{s} + \left(\frac{0.5\sqrt{f'_{co}}}{\frac{a}{d}} \sqrt{1 + \frac{N}{0.5\sqrt{f'_{co}} A_g}} \right) 0.8 A_g \qquad (A2.1)$$

where A_v is the cross-sectional area of transverse reinforcement passing shear plane, f_{yt} is the yield strength of transverse reinforcement, d is the effective depth of section, s is the center-to-center spacing of transverse reinforcement, f'_{co} is the unconfined concrete strength, a is the shear span, N is the axial load, and A_g is the gross area of the cross-section. The undamaged shear strength of the section V_o was estimated to be 266.78 kN which is greater than 118.64 kN. Hence, the column was bond critical

A3. Examples to Estimate HSS Collar Confined Compressive Stress-Strain Relation of Concrete

Beam Example

Data:

$$Collar\ dimension = t = 32\ mm$$

$$Section\ dimension = h = 200\ mm$$

$$HSS\ collar\ yield\ strength = f_y = 400\ MPa$$

Solution:

$$plastic\ modulus\ of\ HSS\ collar\ section = z = \frac{t^3}{4} - \frac{(t - th)}{4} = 3.05 \times 10^3\ mm^3\ (A3.1)$$

$$plastic\ moment\ capacity\ of\ section = M_p = f_y \times z = 1.22 \times 10^6\ N - mm\ (A3.2)$$

Step:1 Estimate collar pressure-lateral strain relation.

Assume a small collar pressure; let's say:

$$\sigma_1 = 0.1\ MPa \tag{A3.3}$$

The axial force is:

$$f_1 = \frac{\sigma_1 th}{2} \tag{A3.4}$$

By assuming the fixed-fixed collar end condition, the moment generated at the collar end is given as:

$$M_1 = \frac{\sigma_1 th^2}{12} \tag{A3.5}$$

In the first step, the total axial force f_{1t} and total bending moment M_{1t} are

$$f_{1t} = f_1 \tag{A3.6}$$

$$M_{1t} = M_1 \tag{A3.7}$$

The following equation is solved for $M_{n,total}$

$$\left(\frac{F_{n,total}}{F_y}\right)^2 + \left(\frac{M_{n,total}}{M_p}\right) = 1.0 \qquad (A3.8)$$

If $M_1 < M_{n,total}$, we increment σ_1. This is repeated till $M_1 = M_{n,total}$. At this point, a plastic hinge at the collar ends is developed. For the beam case, the σ_1 corresponding to the development of the first plastic hinge was 10.0 MPa. At this point, the collar ends (which were initially fixed) are now free to rotate. Hence, the collar element is treated as simply supported. For a simply supported structure, the value of C is 8, i.e., the coefficient of the moment at midspan. The moment at midspan is calculated corresponding to the development of plastic hinge at collar ends which is given as $\sigma_n th^2/24$. The same process is repeated, but at each collar pressure, the moment value obtained from $\sigma_n th^2/24$ is added. When the moment at midspan becomes equal to $M_{n,total}$, the second plastic hinge is formed. The collar pressure corresponding to the development of plastic hinge at midspan was calculated to be 2.8 MPa.

After calculating the collar pressures corresponding to the development of plastic hinges, the corresponding lateral strain values are required. Chapman and Driver proposed equations to estimate axial and lateral strain in the collar, as shown in Table A3.1. For the fixed-fixed end condition, the bending deflection along the collar length is shown in Figure A3.1, which is calculated when the collar pressure is 10.0 MPa, i.e., the development of the first plastic hinge. The area under this curve is calculated and divided by the length of the member to estimate the average bending deflection. To this deflection, the axial deflection component is added to get the total deflection Δ_{total}. For the beams, the average bending deflection was 0.009 mm, and axial deflection was 0.06 mm at the development of the first plastic hinges at collar ends. The lateral strain is then calculated as

$$\epsilon_{lat} = \frac{2\Delta_{total}}{h} \qquad (A3.9)$$

Table A3.1. Proposed equations to estimate bending and axial deflections by Chapman and Driver.

Analysis Stage * n	Beam End Condition	Elastic Deflection Curve $\Delta(x)$ **	Bending Deflection Δ_{bend}	Axial Deflection Δ_{axial}
1	fixed / fixed	$\dfrac{\sigma_n t x^2 (h-x)^2}{24 E_s I_{collar}}$	$\dfrac{\sigma_n t h^4}{720 E_s I_{collar}}$	$\dfrac{\sigma_n t h^2}{4 A_{collar} E_s}$
2	fixed / pinned	$\dfrac{\sigma_n t x (h^3 - 3hx^2 + 2x^3)}{48 E_s I_{collar}}$	$\dfrac{\sigma_n t h^4}{320 E_s I_{collar}}$	$\dfrac{\sigma_n t h^2}{4 A_{collar} E_s}$
3	pinned / pinned	$\dfrac{\sigma_n t x (h^3 - 2hx^2 + x^3)}{24 E_s I_{collar}}$	$\dfrac{\sigma_n t h^4}{120 E_s I_{collar}}$	$\dfrac{\sigma_n t h^2}{4 A_{collar} E_s}$

* These stages correspond to a collar with a mixed bolted/continuous end condition

** The quantity x represents the distance from the beam end (pinned end for stage 2)

Figure A3.1 Bending deflection along the collar length at the formation of the plastic hinge at collar ends.

A similar procedure is repeated for the development of a plastic hinge at midspan corresponding to the confining pressure of 2.8 MPa. Figure A3.2 shows the bending deflection along the collar length at the formation of the plastic hinge at the midspan of the collar. The average lateral deflection was estimated as 0.02 mm, and axial deflection was estimated as 0.019 mm. Figure A3.3 shows the collar pressure vs. lateral strain relation for the beams.
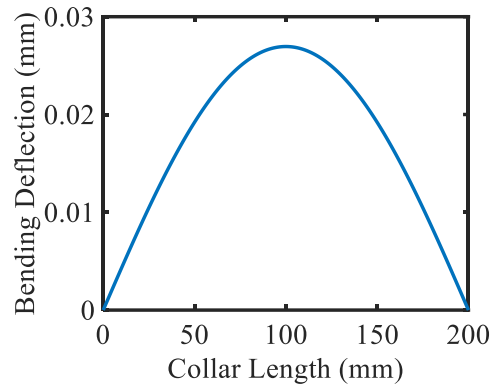
Figure A3.2 Bending deflection along the collar length at the formation of the plastic hinge at collar midspan.
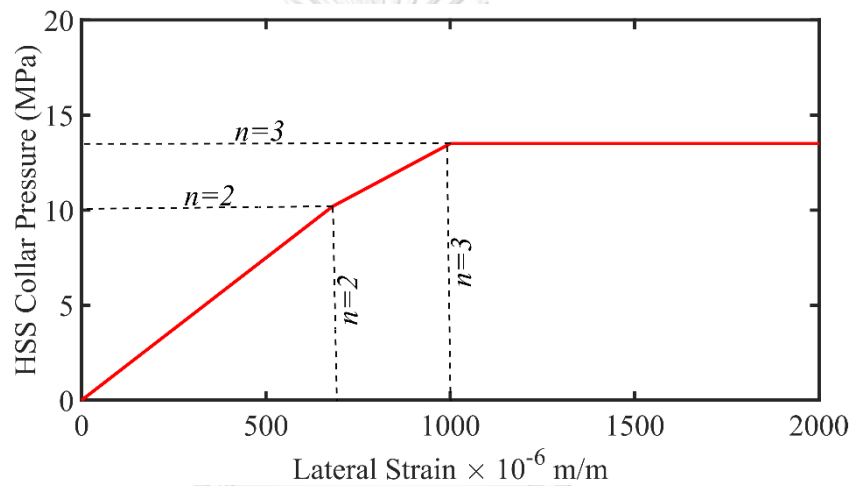
Figure A3.3 Collar pressure vs. lateral strain relation for beams.

Step 2: Estimation of compressive stress-strain relation.

As mentioned in detail in Chapter 2, the process of estimating the compressive stress-strain relation proposed by Chapman and Driver is iterative. The iterative process is highlighted in Figure A3.5. At the start of the iteration, we randomly assume values for the 12 unknowns. We assume a low value of axial strain ϵ_{cc}, let's say, -0.0001. Twelve unknowns are encountered during a particular iteration, including the equilibrium confining pressure $(\sigma_{collar})_i$, the secant modulus of concrete $(E_c)_i$, the Poisson's ratio $(\nu_c)_i$, the constant $(C)_i$, the strain at peak compressive strength in a confined state $(\epsilon'_{cc})_i$, the secant slope of steel collar confining pressure-lateral strain relation $(E_{collar})_i$, the lateral strain $(\epsilon_l)_i$, the peak confined concrete stress $(f'_{cc})_i$, the stress corresponding to the assumed axial strain

$(f_{cc})_i$, the parameters $(x)_i$ and $(r)_i$ for the Popovics equation, and $(E_{sec})_i$. For instance, the MATLAB script is shown below for Beam L20C1S100 (see Figure A3.4).

Figure A3.4 Beam L20C1S100.

```
clc; clearvars; close all;
```

Known Parameters

```
sig1=10.2;  % pressure corresponding to formation of fixed-end plastic hinge
sig2=3.3;   % pressure corresponding to formation of midspan plastic hinge
s1=0.000681;  % lateral strain corresponding to formation of fixed-end plastic hinge
s2=0.001;  % lateral strain corresponding to formation of midspan plastic hinge
s=100; %center to center spacing of collar
h=200; % width of section (mm)
t=32; % dimension of HSS section (mm)
fco=29.5; % unconfined compressive strength
eco=0.002; % strain at unconfined compressive strength
sc=s-t; % clear spaing between collars
kdis=t/sc;
if kdis>1
    kdis=1;
end
keff=((h-(0.5*sc))^2)/h^2; k=keff*kdis; %effectiveness coefficient for collar pressure
```

Assuming Initial Values

```
sigmah=0.1; % assumed initial confining pressure
Eco=4700*sqrt(fco);   % assumed secant mod of elasticity of con
vc=0.15;    % assumed poisson's ratio
C=1;    % assumed constant C
ecc=0.005; % assumed strain at peak stress
Ect=7062; % assumed secant modulus of confining pressure vs. lateral strain
el=0.001; % assumed lateral strain
fcc=30; % assumed peak stress of concrete
x=1; r=1; % assumed parameters of confined concrete curve
Esec=5000; % assumed modulus of concrete at peak stress
Ec=27000; fc=fco;
vco=0.15; % initial Poisson's ratio
```

Function to Perform Iterations

```
Ecc=[0.00001:0.001:0.1];
[FcMander] =
Mander(sig1,sig2,s1,s2,fco,eco,k,sigmah,Eco,vc,vco,Ecc,ecc,Ec,C,el,Ect,fcc,x,r,Esec,fc
);
plot(Ecc,FcMander); hold on;
xlabel('Strain')
ylabel('Compressive Stress (MPa)')
ylim([0 80])
xlim([0 0.1])
hold on;
```
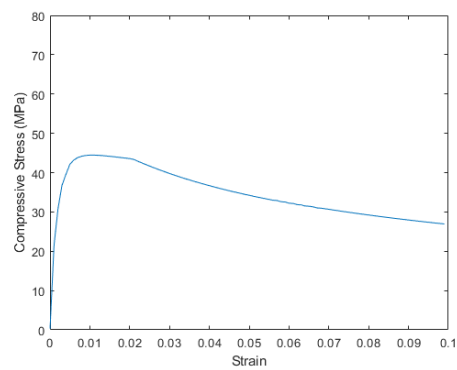

Generating Stress-Strain Response of Unconfined Concrete

```
fcc1=fco;
Esec1=fcc1/0.002;
Ec1=4700*sqrt(fcc1);
r1=Ec/(Ec-Esec1);
ec=[0:0.0001:0.1];
FCC1=(r1*fcc1.*(ec./0.002))./(r1-1+(ec./0.002).^r1);
plot(ec,FCC1);
legend('Confined Stress-Strain Response','Unconfined Stress-Strain Response')
```
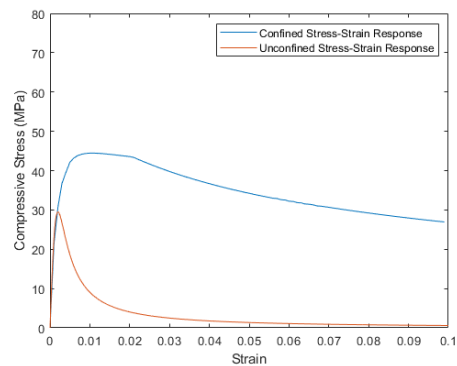


```
function [FcMander] =
Mander(sig1,sig2,s1,s2,fco,eco,k,sigmah,Eco,vc,vco,Ecc,ecc,Ec,C,el,Ect,fcc,x,r,Esec,fc
)
```

```matlab
%   This function performs iterations for the procedure of Chapman and Driver.
for i=1:length(Ecc)
ec=Ecc(i);
if i==1

    C1=1.914*(sigmah/fco)+0.719; % initial C
    vc1=((C1*(ec/ecc))+1)*vco;
    if vc1>0.5
    vc1=0.5;
    end
    el1=vc1*ec;
    if el1<=s1
      sigmact=7062*(el1);
    elseif el1>s2
    sigmact=sig1+sig2;
    else
    sigmact=sig1+1681.818*(el1-s1);
    end
    Ect1=sigmact/el1;
    sigmah1=((vc1*ec)/((1/Ect1)+((1-vc1)/Ec)));
    sigmah1=sigmah1*k;
    fcc1=(fco*((-1.254+(2.254*sqrt(1+((7.94*sigmah1)/fco))))-((2*sigmah1)/fco)));
%    fcc1=fco*(1+2.4*(sigmah1/fco)^0.7); %Cusson and Paultre 1995
    ecc1=eco*(1+5*((fcc1/fco)-1));

    x1=ec/ecc1;
    Esec1=fcc1/ecc1;
    r1=(Eco/(Eco-Esec1));
    fc1=(fcc1*x1*r1)/(r1-1+x1^r1);
    Ec1=fc1/ec;
else
    C=C1; vc=vc1; el=el1; Ect=Ect1; sigmah=sigmah1; fcc=fcc1;
    ecc=ecc1; x=x1; Esec=Esec1; r=r1; fc=fc1; Ec=Ec1;
    C1=1.914*(sigmah/fco)+0.719; % initial C
    vc1=((C1*(ec/ecc))+1)*vco;
    if vc1>0.5
    vc1=0.5;
    end
    el1=vc1*ec;
    if el1<=s1
      sigmact=7062*(el1);
    elseif el1>s2
    sigmact=sig1+sig2;
    else
    sigmact=sig1+1681.818*(el1-s1);
    end
    Ect1=sigmact/el1;
    sigmah1=((vc1*ec)/((1/Ect1)+((1-vc1)/Ec)));
    sigmah1=sigmah1*k;
    fcc1=(fco*((-1.254+(2.254*sqrt(1+((7.94*sigmah1)/fco))))-((2*sigmah1)/fco)));
%    fcc1=fco*(1+2.4*(sigmah1/fco)^0.7); %Cusson and Paultre 1995
    ecc1=eco*(1+5*((fcc1/fco)-1));

    x1=ec/ecc1;
```

```matlab
    Esec1=fcc1/ecc1;
    r1=(Eco/(Eco-Esec1));
    fc1=(fcc1*x1*r1)/(r1-1+x1^r1);
    Ec1=fc1/ec;
end

nitr=1;maxitr=1000;

rat1=(abs(C1-C)/C)*100; rat2=(abs(vc1-vc)/vc)*100; rat3=(abs(el1-el)/el)*100;
rat4=(abs(Ect1-Ect)/Ect)*100; rat5=(abs(sigmah1-sigmah)/sigmah)*100; rat6=(abs(fcc1-
fcc)/fcc)*100;
rat7=(abs(ecc1-ecc)/ecc)*100; rat8=(abs(x1-x)/x)*100; rat9=(abs(Esec1-Esec)/Esec)*100;
rat10=(abs(r1-r)/r)*100; rat11=(abs(fc1-fc)/fc)*100; rat12=(abs(Ec1-Ec)/Ec)*100;
while ((rat1>2) || (rat2>2) || (rat3>2) || (rat4>2) || ...
        (rat5>2) || (rat6>2) || (rat7>2) || (rat8>2) || ...
        (rat9>2) || (rat10>2) || (rat11>2) || (rat12>2))
    nitr=nitr+1;

    C=C1; vc=vc1; el=el1; Ect=Ect1; sigmah=sigmah1; fcc=fcc1;
    ecc=ecc1; x=x1; Esec=Esec1; r=r1; fc=fc1; Ec=Ec1;
    C1=1.914*(sigmah/fco)+0.719; % initial C
    vc1=((C1*(ec/ecc))+1)*vco;
    if vc1>0.5
        vc1=0.5;
    end
    el1=vc1*ec;
    if el1<=s1
        sigmact=7062*(el1);
    elseif el1>s2
        sigmact=sig1+sig2;
    else
        sigmact=sig1+1681.818*(el1-s1);
    end
    Ect1=sigmact/el1;
    sigmah1=((vc1*ec)/((1/Ect1)+((1-vc1)/Ec)));
    sigmah1=sigmah1*k;
    fcc1=(fco*((-1.254+(2.254*sqrt(1+((7.94*sigmah1)/fco))))-((2*sigmah1)/fco)));
%     fcc1=fco*(1+2.4*(sigmah1/fco)^0.7); %Cusson and Paultre 1995
    ecc1=eco*(1+5*((fcc1/fco)-1));
    x1=ec/ecc1;
    Esec1=fcc1/ecc1;
    r1=(Eco/(Eco-Esec1));
    fc1=(fcc1*x1*r1)/(r1-1+x1^r1);
    Ec1=fc1/ec;
    rat1=(abs(C1-C)/C)*100; rat2=(abs(vc1-vc)/vc)*100; rat3=(abs(el1-el)/el)*100;
    rat4=(abs(Ect1-Ect)/Ect)*100; rat5=(abs(sigmah1-sigmah)/sigmah)*100;
rat6=(abs(fcc1-fcc)/fcc)*100;
    rat7=(abs(ecc1-ecc)/ecc)*100; rat8=(abs(x1-x)/x)*100; rat9=(abs(Esec1-
Esec)/Esec)*100;
    rat10=(abs(r1-r)/r)*100; rat11=(abs(fc1-fc)/fc)*100; rat12=(abs(Ec1-Ec)/Ec)*100;
    if nitr>maxitr
        break
    end
end
```

```
FcMander(i)=fc1;
end
end
```

This program calculates collar confining pressures at the onset of plastic hinge formations

```
clc; clear all; close all;
```

Input Data

```
sig=0.1; %initial pressure (MPa)
t=32; % collar size (mm)
h=200; % beam width (mm)
Fy=120000; % yield force (Fy*A)
b=32; hh=32
s=100; % collar spacing (c/c)
sc=s-t; % collar spacing (clear)
bi=b-2*2.3; hhi=hh-2*2.3;
z=((b*hh^2)/4)-((bi*hhi^2)/4); %plastic section modulus
Mp=1.219717600000000e+06;
```

Start of Program

```
Mn=(sig*t*h^2)/12; % moment at collar ends
Fn=(sig*t*h)/2; % axial force in collar
alpha=(1-(Fn/(Fy))^2)*Mp;
i=1;
sigma(i)=sig;
```

```
while Mn<alpha
    i=i+1;
    sig=sig+0.1;
    Mn=(sig*t*h^2)/12;
    Fn=(sig*t*h)/2;
    alpha=(1-(Fn/(0.9*Fy))^2)*Mp*0.9;
    sigma(i)=sig;
end
```

```
M1=(sigma(end)*t*h^2)/24; %moment at midspan till plastic hinge formation at fixed
supports (fixed fixed support)
sig2=0.1;
Fn2=(sig2*t*h)/2;
Fnt=Fn+Fn2; %total axial force till this step
alpha2=(1-(Fnt/(Fy))^2)*Mp;
k=1;
sigma2(k)=sig2;
M2=(sig2*t*h^2)/8;
MT=M1+M2;
```

```
while MT<alpha2
    k=k+1;
    sig2=sig2+0.1;
    Fn2=(sig2*t*h)/2;
    Fnt=Fn+Fn2; %total axial force till this step
    alpha2=(1-(Fnt/(0.9*Fy))^2)*Mp*0.9;
    M2=(sig2*t*h^2)/8;
    MT=M1+M2;
    sigma2(k)=sig2;
end
S1=sigma(end); %pressure corresponding to formation of 1st plastic hinge
S2=sigma2(end); %pressure corresponding to formation of 2nd plastic hinge
```

Estimate Collar Confining Pressure vs. Lateral Strain Relation

↓

Input General Strain Value $(\epsilon_{cc})_i$

↓

Assume: $(\sigma_{passive})_i$, $(E_c)_i$, $(\nu_c)_i$, $(C)_i$, $(\epsilon'_{cc})_i$, $(E_{collar})_i$, $(\epsilon_l)_i$, $(f'_{cc})_i$, $(f_{cc})_i$, $(x)_i$, $(r)_i$, $(E_{sec})_i$

↓

Estimate Constant C: $(C_1)_i^* = 1.914 \left(\frac{(\sigma_{passive})_i}{f'_{co}} \right) + 0.719$

↓

Estimate Secant Poisson's Ratio ν_c:

$$(\nu_c)_i^* = \nu_{co} \left[(C)_i^* \left(\frac{(\epsilon_{cc})_i}{(\epsilon'_{cc})_i} \right) + 1 \right] \le 0.50$$

↓

Estimate Collar Lateral Strain ϵ_l: $(\epsilon_l)_i^* = (\nu_c)_i^* \times (\epsilon_{cc})_i$

↓

Estimate Confining Pressure $(\sigma_{collar})_i^*$ from Confining Pressure vs. Lateral Strain Relation.

↓

Estimate Secant Slope of Confining Pressure vs. Lateral Strain Relation $(E_{collar})_i^*$:

$$(E_{collar})_i^* = \frac{(\sigma_{collar})_i^*}{(\epsilon_l)_i^*}$$

↓

Estimate the Equilibrium Confining Pressure $(\sigma_h)_i^*$:

$$(\sigma_{collar})_i^* = \frac{(\nu_c)_i^*(\epsilon_{cc})_i}{\dfrac{1}{(E_{collar})_i^*} + \dfrac{1 - (\nu_c)_i^*}{(E_c)_i}}$$

↓

Incorporate collar spacing and effectiveness:

$$(\sigma_{collar})_i^* = (\sigma_{collar})_i^* \times \frac{t}{s} \times \frac{\left(h - 0.5s'\right)^2}{h^2}$$

↓

Estimate Peak Confined Compressive Strength $(f'_{cc})_i^*$:

$$(f'_{cc})_i^* = f'_{co} \left[2.254 \sqrt{1 + \frac{7.94(\sigma_{collar})_i^*}{f'_{co}}} - 2 \frac{(\sigma_{collar})_i^*}{f'_{co}} - 1.254 \right]$$

↓

Estimate Strain at Peak Confined Compressive Strength $(\epsilon'_{cc})_i^*$:

$$(\epsilon'_{cc})_i^* = \epsilon'_{co} \left[1 + 5 \left(\frac{(f'_{cc})_i^*}{f'_{co}} - 1 \right) \right]$$

↓

Estimate Stress Corresponding to (ϵ_{cc}): $(f_{cc})_i^* = \frac{(f'_{cc})_i^*(x)_i(r)_i}{(r)_i - 1 + (x)_i^{r_i}}$

↓

Estimate $(x)_i^*$: $(x)_i^* = \frac{(\epsilon_{cc})_i}{(\epsilon'_{cc})_i^*}$

↓

Estimate $(r)_i^*$: $(r)_i^* = \frac{E_{co}}{E_{co} - ((f'_{cc})_i^*/(\epsilon'_{cc})_i^*)}$

↓

Estimate Secant Modulus of Concrete $(E_c)_i^*$: $(E_c)_i^* = \frac{(f_{cc})_i^*}{(\epsilon_{cc})_i}$

↓

Estimate Secant Modulus of Concrete $(E_c)_i^*$: $(E_c)_i^* = \frac{(f_{cc})_i^*}{(\epsilon_{cc})_i}$

↓

No? ← Check the Tolerance of Assumed and Estimated Values: $\forall \; |(value)_i - (value)_i^*| < tolerance$ → *Yes?*

(Left loop label) Update all $(value)_i$ with $(value)_i^*$

(Right loop label) Input New $(\epsilon_{cc})_i$

Figure A3.5. Flowchart to estimate the stress-strain relation of HSS collar confined concrete by Chapman and Driver.

A4. OpenSees Scripts

A4.1. Control Beam L20C1SC

wipe;

model basic -ndm 2 - ndf 3

file mkdir BeamNS

source SIunits.tcl;

Material Tag

set coreTag   1 ;   # core concrete

set coverTag 2 ;   # cover concrete

set steeloutsplice 3   ;   # Reinforcing steel

set steelinsplice 4   ;   # Reinforcing steel

Nominal concrete compressive strength

set   fc -43.0;

set   Ec   [expr 4700*sqrt(-1*$fc)];

Confined concrete

set fc1C -49.0;   # CONFINED concrete (mander model), maximum stress

set eps1C -0.0034;   # strain at maximum stress

set fc2C -40.0;   # ultimate stress

set eps2C -0.008;   # strain at ultimate stress

Unconfined concrete

set fc1U -43.0;   # Unconfined concrete (todeschini parabolic model), maximum stress

set eps1U -0.002;   # strain at maximum strength of unconfined concrete

set fc2U -0;   # ultimate stress

set eps2U -0.0025;   # strain at ultimate stress

set lambda 0.1;   # ratio between unloading slope at $eps2 and initial slope $Ec

Concrete tensile-strength properties

set ftC [expr 0.035*sqrt(-1*$fc1C)];# tension strength +tension

set ftU [expr 0.035*sqrt(-1*$fc1U)];# tension strength +tension

set Ets [expr $ftU/0.005];   # tension softening stiffness

Steel tensile-strength properties

set db 16;

set Fy 497;   # STEEL yield stress

set Es 207000.0;   # modulus of steel

set Fu 636.0;

#uniaxialMaterial Hysteretic $matTag $s1p $e1p $s2p $e2p <$s3p $e3p> $s1n $e1n $s2n $e2n <$s3n $e3n> $pinchX $pinchY $damage1 $damage2 <$beta>

uniaxialMaterial Hysteretic $steeloutsplice $Fy 0.0024 $Fu 0.06 -$Fy -0.0024 -$Fu -0.06 0.1 0.1 0.0 0.0 ;

uniaxialMaterial Hysteretic $steelinsplice 316 0.00153 0 0.0016 -316 -0.00153 -00 -0.0017 0.1 0.1 0.0 0.0 ;

#uniaxialMaterial Concrete04 $matTag $fc $ec $ecu $Ec <$fct $et> <$beta>

uniaxialMaterial Concrete04 $coverTag $fc1U $eps1U $eps2U 32242

uniaxialMaterial Concrete04 $coreTag $fc1C $eps1C $eps2C 32000

puts "Material Model OK"

FIBER SECTION properties

Section Geometry

set HSec [expr 250];   # beam Depth 25cm

set BSec [expr 200];   # beam Width 20cm

nodal coordinates

        node   1   0.0   0.0

        node   2   570.0   0.0

        node   3   740.0   0.0

        node   4   840.0   0.0

        node   5   1000.0 0.0

```
        #node  7      0.0    2200
```

source BuildRCrectSection.tcl

BuildRCrectSection 1 $HSec $BSec 24 36 $coreTag $coverTag $steeloutsplice 2 114.0 2 201.0 0.0 0.0 20 1 6 1

BuildRCrectSection 3 $HSec $BSec 24 36 $coverTag $coverTag $steelinsplice 2 114.0 2 201.0 0.0 0.0 20 1 6 1

puts "Fiber Section OK"

Single point constraints -- Boundary Conditions

fix 1 1 1 0;   # node DX DY RZ

fix 5 1 0 1;

set IDColTransf 1;

set ColTransfType Linear ;

geomTransf Linear 1;

Element connectivity:

set numIntgrPts 5;   # number of integration points for force-based element

set intType Lobotto;

#element elasticBeamColumn 1 1 2 50000 30000 [expr $EffIz*$IzCol] $IDColTransf; # Elastic beam

element dispBeamColumn 1 1 2 $numIntgrPts 1 $IDColTransf;

element dispBeamColumn 2 2 3 $numIntgrPts 3 $IDColTransf;

element dispBeamColumn 3 3 4 $numIntgrPts 22 $IDColTransf;

element dispBeamColumn 4 4 5 $numIntgrPts 3 $IDColTransf;

puts "Beam model Ok"

Define RECORDERS

recorder Node -file BeamNS/Disp.out   -node 5   -dof 2 disp

recorder Node -file BeamNS/Reaction.out   -node 1   -dof 2 reaction

```
 # STATIC PUSHOVER ANALYSIS ----------------------------------------------------------------------------------------------

set F 1.0;

set cdof 2;

set cnode 2;

set dU 0.001;

pattern Plain 2 "Linear" {

        load $cnode 0.0 -$F 0.0

}

constraints Transformation

numberer AMD

system BandGeneral

test NormDispIncr 10e-3 1000

algorithm NewtonLineSearch type InitialInterpolated

integrator DisplacementControl $cnode $cdof $dU 1 $dU $dU

analysis Static

set maxU 15;

set Nstep [expr int($maxU/$dU)];

analyze $Nstep

puts "Pushover analysis completed successfully"
```

A4.2. Strengthened Beam L20C1S75

wipe;

model basic -ndm 2 - ndf 3

file mkdir BeamNS

source SIunits.tcl;

Material Tag

set coreTag   1 ;   # core concrete

set coverTag 2 ;   # cover concrete

set steeloutsplice 3   ;   # Reinforcing steel

set steelinsplice 4   ;   # Reinforcing steel

Nominal concrete compressive strength

set   fc -26.0;

set   Ec   [expr 4700*sqrt(-1*$fc)];

Confined concrete

set fc1C -66.0;   # CONFINED concrete (mander model), maximum stress

set eps1C -0.012;   # strain at maximum stress

set fc2C -57.0;   # ultimate stress

set eps2C -0.047;   # strain at ultimate stress

Confined concrete for shear span

set fc1CS -48.0;   # CONFINED concrete (mander model), maximum stress

set eps1CS -0.0034;   # strain at maximum stress

set fc2CS -41.0;   # ultimate stress

set eps2CS -0.02;   # strain at ultimate stress

Unconfined concrete

set fc1U -43.0;   # Unconfined concrete (todeschini parabolic model), maximum stress

set eps1U -0.002;   # strain at maximum strength of unconfined concrete

set fc2U -8.0;   # ultimate stress

set eps2U -0.003;   # strain at ultimate stress

set lambda 0.1;   # ratio between unloading slope at $eps2 and initial slope $Ec

Concrete tensile-strength properties

set ftC [expr 0.35*sqrt(-1*$fc1C)];# tension strength +tension

set ftU [expr 0.35*sqrt(-1*$fc1U)];# tension strength +tension

set Ets [expr $ftC/0.002];   # tension softening stiffness

Steel tensile-strength properties

set db 16;

set Fy 497.0;   # STEEL yield stress

set Es 207000.0;   # modulus of steel

set Fu 636.0;

#uniaxialMaterial Hysteretic $matTag $s1p $e1p $s2p $e2p <$s3p $e3p> $s1n $e1n $s2n $e2n <$s3n $e3n> $pinchX $pinchY $damage1 $damage2 <$beta>

uniaxialMaterial Hysteretic $steeloutsplice $Fy 0.0024 $Fu 0.07 -$Fy -0.0024 -$Fu -0.073 0.1 0.1 0.0 0.0 ;

uniaxialMaterial Hysteretic $steelinsplice $Fy 0.0024 $Fu 0.07 -$Fy -0.0024 -$Fu -0.073 0.1 0.1 0.0 0.0 ;

uniaxialMaterial Concrete02 $coverTag $fc1U $eps1U $fc2U $eps2U $lambda $ftU $Ets

uniaxialMaterial Concrete02 12 $fc1CS $eps1CS $fc2CS $eps2CS $lambda $ftU $Ets

uniaxialMaterial Concrete04 $coreTag $fc1C $eps1C $eps2C 29211.0

puts "Material Model OK"

FIBER SECTION properties

Section Geometry

set HSec [expr 250];   # beam Depth 25cm

set BSec [expr 200];   # beam Width 20cm

nodal coordinates

        node   1   0.0   0.0

```
        node    2       570.0  0.0
        node    3       740.0  0.0
        node    4       840.0  0.0
        node    5       1000.0 0.0
        #node   7       0.0     2200
```

source BuildRCrectSection.tcl

BuildRCrectSection $id $HSec $BSec $coverH $coverB $coreID $coverID $steelID $numBarsTop $barAreaTop $numBarsBot $barAreaBot $numBarsIntTot $barAreaInt $nfCoreY $nfCoreZ $nfCoverY $nfCoverZ

BuildRCrectSection 1 $HSec $BSec 24 36 12 $coverTag $steeloutsplice 2 113 2 201.0 0.0 0.0 20 20 20 2

BuildRCrectSection 3 $HSec $BSec 24 36 $coreTag $coreTag $steeloutsplice 2 113 2 201.0 0.0 0.0 20 20 20 2

puts "Fiber Section OK"

Single point constraints -- Boundary Conditions

fix 1 1 1 0;   # node DX DY RZ

fix 5 1 0 1;

set IDColTransf 1;

set ColTransfType Linear ;

geomTransf Linear 1;

Element connectivity:

set numIntgrPts 5;   # number of integration points for force-based element

#element elasticBeamColumn 1 1 2 50000 30000 [expr $EffIz*$IzCol] $IDColTransf;# Elastic beam

element dispBeamColumn 1 1 2 $numIntgrPts 1 $IDColTransf;

element dispBeamColumn 2 2 3 $numIntgrPts 3 $IDColTransf;

element dispBeamColumn 3 3 4 $numIntgrPts 22 $IDColTransf;

element dispBeamColumn 4 4 5 $numIntgrPts 3 $IDColTransf;

puts "Beam model Ok"

Define RECORDERS

```
recorder Node  -file BeamNS/Disp.out                    -node  5        -dof 2  disp
recorder Node  -file BeamNS/Reaction.out    -node  1        -dof 2  reaction
# STATIC PUSHOVER ANALYSIS ------------------------------------------------------------
----------------------------------------
set F 1.0;
set cdof 2;
set cnode 2;
set dU 0.001;
pattern Plain 2 "Linear" {
        load $cnode 0.0 -$F 0.0
}

constraints Transformation
numberer AMD
system BandGeneral
#test EnergyIncr 10e-2 500
test NormDispIncr 10e-2 1000
algorithm NewtonLineSearch type InitialInterpolated
integrator DisplacementControl $cnode $cdof $dU 1 $dU $dU
analysis Static
set maxU 28;
set Nstep [expr int($maxU/$dU)];
analyze $Nstep
puts "Pushover analysis completed successfully"
```

A4.3. Control Column LS

```
wipe;

model basic -ndm 2 - ndf 3

file mkdir NS

source SIunits.tcl;

# Material Tag

set coreTag   1 ;          # core concrete

set coverTag  2 ;          # cover concrete

set steelTag  3 ;          # Reinforcing steel

set spliceTag 4 ;

# Nominal concrete compressive strength

set     fc -23.6;

set     Ec     [expr 4700*sqrt(-1*$fc)];

# Confined concrete

set fc1C -26.08;        # CONFINED concrete (mander model), maximum stress

set eps1C -0.0035;                             # strain at maximum stress

set fc2C -5.22;                                # ultimate stress

set eps2C -0.0178;                             # strain at ultimate stress

# Unconfined concrete

set fc1U $fc;           # Unconfined concrete (todeschini parabolic model), maximum
stress

set eps1U -0.002;       # strain at maximum strength of unconfined concrete

set fc2U 0;                                        # ultimate stress

set eps2U -0.004;                              # strain at ultimate stress

set lambda 0.1;         # ratio between unloading slope at $eps2 and initial slope $Ec

# Concrete tensile-strength properties

set ftC [expr 0.035*sqrt(-1*$fc1C)];# tension strength +tension

set ftU [expr 0.035*sqrt(-1*$fc1U)];# tension strength +tension

set Ets [expr $ftU/0.002];                   # tension softening stiffness
```

Steel tensile-strength properties

set db 25;

set Fy 449;   # STEEL yield stress

set Fu 642;   # STEEL ultimate stress

set Es 206000;   # modulus of steel

set Esh [expr 0.01*$Es];   # Tangent at initial strain hardening

set esh [expr ($Fy/$Es)+0.01];   # Strain corresponding to initial strain hardening

set eult 0.072; #Strain at peak stress

setting parameters for spliced bars

set fs 449;

set esp 0.0047;

set fr 130;

set esr 0.02;

Setting materials

#uniaxialMaterial Concrete02 $matTag $fpc $epsc0 $fpcu $epsU $lambda $ft $Ets

uniaxialMaterial Concrete02 $coreTag $fc1C $eps1C $fc2C $eps2C $lambda $ftC $Ets

uniaxialMaterial Concrete02 $coverTag $fc1U $eps1U $fc2U $eps2U $lambda $ftU $Ets

uniaxialMaterial Hysteretic $spliceTag $fs $esp $fr $esr -$Fy -0.00212 -$Fu -0.07 0.8 0.3 0.02 0.02

uniaxialMaterial Steel01 $steelTag $Fy $Es 0.2

puts "Material Model OK"

FIBER SECTION properties

Section Geometry

set HSec [expr 400];   # Column Depth 40cm

set BSec [expr 400];   # Column Width 40cm

set coverH [expr 50];   # Column cover to reinforcing steel NA, parallel to H is 5cm

set coverB [expr 50];   # Column cover to reinforcing steel NA, parallel to B is 5cm

```
set db 25;

set as [expr 3.14*pow($db,2)/4];

source BuildRCrectSection.tcl

# BuildRCrectSection $id $HSec $BSec $coverH $coverB $coreID $coverID
$steelID $numBarsTop $barAreaTop $numBarsBot $barAreaBot $numBarsIntTot
$barAreaInt $nfCoreY $nfCoreZ $nfCoverY $nfCoverZ

BuildRCrectSection 1 $HSec $BSec $coverH $coverB  $coreTag $coverTag
$spliceTag 3 $as 3 $as 2 $as 20 20 10 10

BuildRCrectSection 2 $HSec $BSec $coverH $coverB  $coreTag $coverTag
$steelTag 3 $as 3 $as 2 $as 20 20 10 10

puts "Fiber Section OK"

# Define Geometry

set Weight              32;      # superstructure weight in Ton

set Ls   [expr $db*28];# Section Zone2 length in mm fron base

set LCol                2200;   # column length in mm

set EffIz 0.28;                  # Effective stifness for Elastic column

# nodal coordinates:

node 1 0 0;

node 2 0 $Ls;

node 3 0 1200;

node 4 0 1700;

node 5 0 2200;

set NodeTop 5;

# Define ELEMENTS & SECTIONS -------------------------------------------------
---

set PCol [expr $Weight*1000*9.81];               # Superstructure weight in N

set ACol [expr $BSec*$HSec];                     # Cross-sectional area

set IzCol [expr $BSec*pow($HSec,3)/12]; # Column moment of inertia

# Single point constraints -- Boundary Conditions

fix 1 1 1 1;                                      # node DX DY RZ

set IDColTransf 1;
```

```
#set ColTransfType PDelta ;

geomTransf PDelta 1;

# Element connectivity:

set numIntgrPts 5;      # number of integration points for force-based element

element dispBeamColumn 1 1 2 $numIntgrPts 1 1;

element dispBeamColumn 2 2 3 $numIntgrPts 2 1;

element dispBeamColumn 3 3 4 $numIntgrPts 2 1;

element dispBeamColumn 4 4 5 $numIntgrPts 2 1;

puts "Column model Ok"

# Define RECORDERS

recorder Node  -file NS/Disp.out                  -node  5        -dof 1  disp

recorder Node  -file NS/Reaction.out  -node  1                    -dof 1  reaction

# Define Gravity Load

pattern Plain 1 Linear {

load $NodeTop  0 -$PCol 0;

        }

set Tol 1.0e-2;          # convergence tolerance for test

constraints Transformation;    # how it handles boundary conditions

numberer RCM;

system BandGeneral;  # how to store and solve the system of equations in the analysis

test NormDispIncr $Tol 500; # determine if convergence has been achieved at the end
of an iteration step

algorithm Newton;      # use Newton's solution algorithm: updates tangent stiffness at
every iteration

set NstepGravity 10;                              # apply gravity in 100 steps

set DGravity [expr 1./$NstepGravity];        # first load increment;

integrator LoadControl $DGravity;            # determine the next time step for an
analysis

analysis Static;                              # define type of analysis static or
transient
```

```
analyze $NstepGravity;                                    # apply gravity

loadConst -time 0.0;              # maintain constant gravity loads and reset time to zero


puts "Static Analysis OK"

# Define Cyclic Loading

set IDctrlNode $NodeTop;     # node where displacement is read for displacement
control

set IDctrlDOF 1;              # degree of freedom of displacement read for
displacement contro

set iDmax "0.0025 0.005 0.0075 0.01 0.015 0.02 0.025 0.03 0.035 0.04 0.045 0.05
0.055 0.06";

set Dincr [expr 0.0001*$LCol];        # displacement increment for pushover. you
want this to be very small, but not too small to slow down the analysis

set Fact $LCol;         # scale drift ratio by storey height for displacement cycles

set CycleType Full;     # you can do Full / Push / Half cycles with the proc

set Ncycles 2;          # specify the number of cycles at each peak

set Hload [expr $PCol];        # define the lateral load as a proportion of the weight so
that the pseudo time equals the lateral-load coefficient when using linear load pattern

set iPushNode "$NodeTop";           # define nodes where lateral load is applied in
static lateral analysis

pattern Plain 2 Linear {;             # define load pattern -- generalized

foreach PushNode $iPushNode {

        load $PushNode $Hload 0 0

             }

        }

source LibAnalysisStaticParameters.tcl;        #
constraintsHandler,DOFnumberer,system-of-
equations,convergenceTest,solutionAlgorithm,integrator

source LibGeneratePeaks.tcl

set fmt1 "%s Cyclic analysis: CtrlNode %.3i, dof %.1i, Disp=%.4f %s";    # format
for screen/file output of DONE/PROBLEM analysis

foreach Dmax $iDmax {
```

```
set iDstep [GeneratePeaks $Dmax $Dincr $CycleType $Fact];
            for {set i 1} {$i <= $Ncycles} {incr i 1} {
                    set zeroD 0
                    set D0 0.0
                    foreach Dstep $iDstep {
                            set D1 $Dstep
                            set Dincr [expr $D1 - $D0]
                            integrator DisplacementControl  $IDctrlNode
$IDctrlDOF $Dincr

                            analysis Static
        #--------------------------------------------first analyze command--------------------
----

                            set ok [analyze 1]
        #----------------------------------------if convergence failure--------------------
----

                            if {$ok != 0} {
                                    # if analysis fails, we try some other stuff
                                    # performance is slower inside this loop
        global maxNumIterStatic;        # max no. of iterations performed before
"failure to converge" is ret'd
                                    if {$ok != 0} {
                                            puts "Trying Newton with Initial
Tangent .."
                                            test NormDispIncr   $Tol 700 0
                                            algorithm Newton -initial
                                            set ok [analyze 1]
                                            test $testTypeStatic $TolStatic
$maxNumIterStatic    0
                                            algorithm $algorithmTypeStatic
                                    }
                                    if {$ok != 0} {
```

```
                              set putout [format $fmt1 "PROBLEM"
$IDctrlNode $IDctrlDOF [nodeDisp $IDctrlNode $IDctrlDOF] $LunitTXT]

                              puts $putout

                              return -1

                    };                              # end if

                    };                              # end if

     #--------------------------------------------------------------------------------------------
--------

                    set D0 $D1;                 # move to next step

               };                               # end Dstep

          };                                    # end i

     };                                         # end of
iDmaxCycl

     #--------------------------------------------------------------------------------------------
--------

     if {$ok != 0 } {

          puts [format $fmt1 "PROBLEM" $IDctrlNode $IDctrlDOF [nodeDisp
$IDctrlNode $IDctrlDOF] $LunitTXT]

     } else {

          puts [format $fmt1 "DONE"  $IDctrlNode $IDctrlDOF [nodeDisp
$IDctrlNode $IDctrlDOF] $LunitTXT]

     }
```

A4.4 Strengthened Column SC100

wipe;

model basic -ndm 2 - ndf 3

file mkdir NS

source SIunits.tcl;

Material Tag

set coreTag   1 ;   # core concrete

set coverTag 2 ;   # cover concrete

set steelTag 3 ;   # Reinforcing steel

set spliceTag 4 ;

set concCollTag 5;

Nominal concrete compressive strength

set   fc -23.0;

set   Ec   [expr 4700*sqrt(-1*$fc)];

Confined concrete by hoops

set fc1C -38.50;   # CONFINED concrete (mander model), maximum stress

set eps1C -0.007;   # strain at maximum stress

set fc2C -5.22;   # ultimate stress

set eps2C -0.0178;   # strain at ultimate stress

Unconfined concrete

set fc1U $fc;   # Unconfined concrete (todeschini parabolic model), maximum stressset eps1U -0.002;   # strain at maximum strength of unconfined concre

set fc2U 0;   # ultimate stress

set eps2U -0.004;   # strain at ultimate stress

set lambda 0.1;   # ratio between unloading slope at $eps2 and initial slope $Ec

Confined concrete by collars

set fc1CS -65.50;   # CONFINED concrete (mander model), maximum stress

set eps1CS -0.02;   # strain at maximum stress

set fc2CS -52;   # ultimate stress

set eps2CS -0.06;   # strain at ultimate stress

Concrete tensile-strength properties

set ftC [expr 0.035*sqrt(-1*$fc1C)]; # tension strength +tension

set ftU [expr 0.035*sqrt(-1*$fc1U)]; # tension strength +tension

set Ets [expr $ftU/0.002];   # tension softening stiffness

Steel tensile-strength properties

set db 25;

set Fy 449;   # STEEL yield stress

set Fu 642;   # STEEL ultimate stress

set Es 206000;   # modulus of steel

set Esh [expr 0.01*$Es];   # Tangent at initial strain hardening

set esh [expr ($Fy/$Es)+0.01];   # Strain corresponding to initial strain hardening

set eult 0.072;   #Strain at peak stress

setting parameters for spliced bars

set fs 449.0;

set esp 0.0098;set fr 260.0;

set esr 0.02;

Setting materials

uniaxialMaterial Concrete02 $coreTag $fc1C $eps1C $fc2C $eps2C $lambda $ftC $Ets

uniaxialMaterial Concrete02 $coverTag $fc1U $eps1U $fc2U $eps2U $lambda $ftU $Ets

uniaxialMaterial Hysteretic $spliceTag $Fy 0.007 $Fu 0.093 -$Fy -0.0021 -$Fu -0.075 0.4 0.5 0.025 0.025

#uniaxialMaterial Hysteretic $spliceTag $Fy 0.0021 $Fu 0.07 -$Fy -0.0021 -$Fu -0.075 0 1 0.0 0.0

uniaxialMaterial Hysteretic $steelTag $Fy 0.0021 $Fu 0.07 -$Fy -0.0021 -$Fu -0.075 0 1 0 0

uniaxialMaterial Concrete04 $concCollTag $fc1CS $eps1CS $eps2CS 22000

puts "Material Model OK"

Section Geometry

set HSec [expr 400];   # Column Depth 40cm

set BSec [expr 400];   # Column Width 40cm

set coverH [expr 50];   # Column cover to reinforcing steel NA, parallel to H is 5cm

set coverB [expr 50];   # Column cover to reinforcing steel NA, parallel to B is 5cm

set db 25;

set as [expr 3.14*pow($db,2)/4];

source BuildRCrectSection.tcl

BuildRCrectSection $id $HSec $BSec $coverH $coverB $coreID $coverID $steelID $numBarsTop $barAreaTop $numBarsBot $barAreaBot $numBarsIntTot $barAreaInt $nfCoreY $nfCoreZ $nfCoverY $nfCoverZ

BuildRCrectSection 1 $HSec $BSec $coverH $coverB $concCollTag $concCollTag $spliceTag 3 $as 3 $as 2 $as 12 12 5 5

BuildRCrectSection 2 $HSec $BSec $coverH $coverB $concCollTag $concCollTag $steelTag 3 $as 3 $as 2 $as 12 12 5 5

BuildRCrectSection 3 $HSec $BSec $coverH $coverB $coreTag $coverTag $steelTag 3 $as 3 $as 2 $as 12 12 5 5

Define Geometry

set Weight   36;   # superstructure weight in Ton

set Ls   [expr $db*28];# Section Zone2 length in mm fron base

set LCol   2200;   # column length in mm

set EffIz 0.28;   # Effective stifness for Elastic column

nodal coordinates:

        node 1 0 0;

        node 2 0 440;

        node 3 0 880;

        node 4 0 1320;

        node 5 0 1760;

        node 6 0 2200;

        set NodeTop 6;

Define ELEMENTS & SECTIONS ---
---

set PCol [expr $Weight*1000*9.81];   # Superstructure weight in N

set ACol [expr $BSec*$HSec];   # Cross-sectional area

set IzCol [expr $BSec*pow($HSec,3)/12];   # Column moment of inertia

Single point constraints -- Boundary Conditions

fix 1 1 1 1;   # node DX DY RZ

set IDColTransf 1;

#set ColTransfType PDelta ;

geomTransf PDelta 1;

Element connectivity:

set numIntgrPts 5;   # number of integration points for force-based
element

element dispBeamColumn 1 1 2 $numIntgrPts 1 1;

element dispBeamColumn 2 2 3 $numIntgrPts 2 1;

element dispBeamColumn 3 3 4 $numIntgrPts 2 1;

element dispBeamColumn 4 4 5 $numIntgrPts 3 1;

```
element dispBeamColumn 5 5 6 $numIntgrPts 3 1;

puts "Column model Ok"
```

```
# Define RECORDERS

recorder Node  -file NS/Disp.out                -node  6       -dof 1  disp

recorder Node  -file NS/Reaction.out  -node  1                 -dof 1  reaction
```

```
# Define Gravity Load

        pattern Plain 1 Linear {

        load $NodeTop  0 -$PCol 0;

        }
```

```
set Tol 1.0e-2;                                    # convergence tolerance for test

constraints Transformation;                        # how it handles boundary conditions

numberer RCM;                                      # renumber dof's to minimize band-width
(optimization), if you want to

system BandGeneral;                                # how to store and solve the system of
equations in the analysis

test NormDispIncr $Tol 1000;                       # determine if convergence has been
achieved at the end of an iteration step

algorithm Newton;                                  # use Newton's solution algorithm:
updates tangent stiffness at every iteration

set NstepGravity 10;                               # apply gravity in 100 steps

set DGravity [expr 1./$NstepGravity];              # first load increment;

integrator LoadControl $DGravity;                  # determine the next time step for an
analysis

analysis Static;                                   # define type of analysis static or
transient

analyze $NstepGravity;                             # apply gravity

loadConst -time 0.0;                               # maintain constant gravity loads and
reset time to zero

puts "Static Analysis OK"
```

Define Cyclic Loading

set IDctrlNode $NodeTop;   # node where displacement is read for displacement control

set IDctrlDOF 1;   # degree of freedom of displacement read for displacement control

set iDmax "0.0025 0.005 0.0075 0.01 0.015 0.02 0.025 0.03 0.035 0.04 0.045 0.05 0.055 0.06 0.065 0.07";   # vector of displacement-cycle peaks, in terms of storey drift ratio

set Dincr [expr 0.001*$LCol];   # displacement increment for pushover. you want this to be very small, but not too small to slow down the analysis

set Fact $LCol;   # scale drift ratio by storey height for displacement cycles

set CycleType Full;   # you can do Full / Push / Half cycles with the proc

set Ncycles 2;   # specify the number of cycles at each peak

set Hload [expr $PCol];   # define the lateral load as a proportion of the weight so that the pseudo time equals the lateral-load coefficient when using linear load pattern

set iPushNode "$NodeTop";   # define nodes where lateral load is applied in static lateral analysis

pattern Plain 2 Linear {;   # define load pattern -- generalized

        foreach PushNode $iPushNode {

                load $PushNode -$Hload 0 0

                }

        }

source LibAnalysisStaticParameters.tcl;   # constraintsHandler,DOFnumberer,system-of-equations,convergenceTest,solutionAlgorithm,integrator

source LibGeneratePeaks.tcl

set fmt1 "%s Cyclic analysis: CtrlNode %.3i, dof %.1i, Disp=%.4f %s";   # format for screen/file output of DONE/PROBLEM analysis

        foreach Dmax $iDmax {

                set iDstep [GeneratePeaks $Dmax $Dincr $CycleType $Fact];   # this proc is defined above

                        for {set i 1} {$i <= $Ncycles} {incr i 1} {

```
set zeroD 0

set D0 0.0

foreach Dstep $iDstep {

        set D1 $Dstep

        set Dincr [expr $D1 - $D0]

        integrator DisplacementControl  $IDctrlNode
$IDctrlDOF $Dincr

        analysis Static

#--------------------------------------------first analyze command-------------------
----

        set ok [analyze 1]

#---------------------------------------------if convergence failure--------------------
----

        if {$ok != 0} {

                # if analysis fails, we try some other stuff

                # performance is slower inside this loop
        global maxNumIterStatic;        # max no. of iterations performed before
"failure to converge" is ret'd

                if {$ok != 0} {

                        puts "Trying Newton with Initial
Tangent .."

                        test NormDispIncr   $Tol 700 0

                        algorithm Newton -initial

                        set ok [analyze 1]

                        test $testTypeStatic $TolStatic
$maxNumIterStatic   0

                        algorithm $algorithmTypeStatic

                }

                if {$ok != 0} {

                        set putout [format $fmt1 "PROBLEM"
$IDctrlNode $IDctrlDOF [nodeDisp $IDctrlNode $IDctrlDOF] $LunitTXT]

                        puts $putout
```

```
                        return -1

                };                              # end if

             };                              # end if

    #----------------------------------------------------------------------------------------
--------

                set D0 $D1;                     # move to next step

          };                                     # end Dstep

       };                                      # end i

    };                                         # end of
iDmaxCycl

    #----------------------------------------------------------------------------------------
--------

    if {$ok != 0 } {

         puts [format $fmt1 "PROBLEM" $IDctrlNode $IDctrlDOF [nodeDisp
$IDctrlNode $IDctrlDOF] $LunitTXT]

    } else {

         puts [format $fmt1 "DONE"  $IDctrlNode $IDctrlDOF [nodeDisp
$IDctrlNode $IDctrlDOF] $LunitTXT]

    }
```

A4.5 Necessary Files for OpenSees

Procedure *BuildRCrectSection*

proc BuildRCrectSection {id HSec Bsec coverH coverB coreID coverID steelID numBarsTop barAreaTop numBarsBot barAreaBot numBarsIntTot barAreaInt nfCoreY nfCoreZ nfCoverY nfCoverZ} {

BuildRCrectSection $id $Hsec $Bsec $coverH $coverB $coreID $coverID $steelID $numBarsTop $barAreaTop $numBarsBot $barAreaBot $numBarsIntTot $barAreaInt $nfCoreY $nfCoreZ $nfCoverY $nfCoverZ

Build fiber rectangular RC section, 1 steel layer top, 1 bottom, 1 skin, confined core

Define a procedure which generates a rectangular reinforced concrete section

with one layer of steel at the top & bottom, skin reinforcement and a

confined core.

by: Silvia Mazzoni, 2006

adapted from Michael H. Scott, 2003

#

Formal arguments

id – tag for the section that is generated by this procedure

Hsec – depth of section, along local-y axis

Bsec – width of section, along local-z axis

cH – distance from section boundary to neutral axis of reinforcement

cB – distance from section boundary to side of reinforcement

coreID – material tag for the core patch

coverID – material tag for the cover patches

steelID – material tag for the reinforcing steel

numBarsTop – number of reinforcing bars in the top layer

numBarsBot – number of reinforcing bars in the bottom layer

numBarsIntTot – TOTAL number of reinforcing bars on the intermediate layers, symmetric about z axis and 2 bars per layer–needs to be an even integer

barAreaTop – cross-sectional area of each reinforcing bar in top layer

barAreaBot – cross-sectional area of each reinforcing bar in bottom layer

\#   barAreaInt – cross-sectional area of each reinforcing bar in intermediate layer

\#   nfCoreY – number of fibers in the core patch in the y direction

\#   nfCoreZ – number of fibers in the core patch in the z direction

\#   nfCoverY – number of fibers in the cover patches with long sides in the y direction

\#   nfCoverZ – number of fibers in the cover patches with long sides in the z direction

\#

\# Notes

\#   The core concrete ends at the NA of the reinforcement

\#   The center of the section is at (0,0) in the local axis system

set coverY [expr $Hsec/2.0];   # The distance from the section z-axis to the edge of the cover concrete – outer edge of cover concrete

set coverZ [expr $Bsec/2.0];   # The distance from the section y-axis to the edge of the cover concrete – outer edge of cover concrete

set coreY [expr $coverY-$coverH];   # The distance from the section z-axis to the edge of the core concrete -- edge of the core concrete/inner edge of cover concrete

set coreZ [expr $coverZ-$coverB];   # The distance from the section y-axis to the edge of the core concrete -- edge of the core concrete/inner edge of cover concrete

set numBarsInt [expr $numBarsIntTot/2];   # number of intermediate bars per side

\# Define the fiber section

section Fiber $id -GJ 1000000000 {

\# Define the core patch

patch quadr $coreID $nfCoreZ $nfCoreY -$coreY $coreZ -$coreY -$coreZ $coreY -$coreZ $coreY $coreZ

\# Define the four cover patches

patch quadr $coverID 2 $nfCoverY -$coverY $coverZ -$coreY $coreZ $coreY $coreZ $coverY $coverZ

patch quadr $coverID 2 $nfCoverY -$coreY -$coreZ -$coverY -$coverZ $coverY -$coverZ $coreY -$coreZ

patch quadr $coverID $nfCoverZ 2 -$coverY $coverZ -$coverY -$coverZ -$coreY -$coreZ -$coreY $coreZ

patch quadr $coverID $nfCoverZ 2 $coreY $coreZ $coreY -$coreZ $coverY -$coverZ $coverY $coverZ

define reinforcing layers

#layer straight $steelID $numBarsInt $barAreaInt -$coreY $coreZ $coreY $coreZ;
        # intermediate skin reinf. +z

#layer straight $steelID $numBarsInt $barAreaInt -$coreY -$coreZ $coreY -$coreZ;
        # intermediate skin reinf. -z

layer straight $steelID $numBarsTop $barAreaTop $coreY $coreZ $coreY -$coreZ;
        # top layer 298einforcement

layer straight $steelID $numBarsBot $barAreaBot -$coreY $coreZ -$coreY -$coreZ;
        # bottom layer reinforcement

        };   # end of fibersection definition

};   # end of procedure

Procedure *SIunits*

```
# define UNITS ----------------------------------------------------------------
set m 1.0;                          # output units
set kN 1.0;                 # output units
set sec 1.0;               # output units
set LunitTXT "m";                  # text for output
set FunitTXT "kN";                 # text for output
set TunitTXT "sec";                # text for output
set cm [expr $m/100];       # input units
set mm [expr $m/1000];             # input units
set N [expr $kN/1000];             # output units
set MPa [expr $N/pow($mm,2)]
set pi [expr 2*asin(1.0)];         # define constants
set g 9.81;      # gravitational acceleration
set Ubig 1.e10;                    # a really large number
set Usmall [expr 1/$Ubig];         # a really small number
```

Procedure *LibGeneratePeaks*

proc GeneratePeaks {Dmax {DincrStatic 0.00001} {CycleType "Full"} {Fact $LCol} } {;   # generate incremental disps for Dmax

##
############

GeneratePeaks $Dmax $DincrStatic $CycleType $Fact

##
############

generate incremental disps for Dmax

this proc creates a file which defines a vector then executes the file to return the vector of disp. increments

by Silvia Mazzoni, 2006

input variables

$Dmax : peak displacement (can be + or negative)

$DincrStatic   : displacement increment (optional, default=0.01, independently of units)

$CycleType   : Full (0->+peak), Half (0->+peak->0), Full (0->+peak->0->-peak->0)   (optional, def=Full)

$Fact   : scaling factor (optional, default=1)

$iDstepFileName   : file name where displacement history is stored temporarily, until next disp. peak

output variable

$iDstep   : vector of displacement increments

file mkdir data

set outFileID [open data/tmpDsteps.tcl w]

set Disp 0.

puts $outFileID "set iDstep { ";puts $outFileID $Disp;puts $outFileID $Disp; # open vector definition and some 0

set Dmax [expr $Dmax*$Fact];   # scale value

if {$Dmax<0} {; # avoid the divide by zero

        set dx [expr -$DincrStatic]

} else {

```
        set dx $DincrStatic;

}
set NstepsPeak [expr int(abs($Dmax)/$DincrStatic)]
for {set i 1} {$i <= $NstepsPeak} {incr i 1} {;              # zero to one
        set Disp [expr $Disp + $dx]
        puts $outFileID $Disp;                              # write to file
}
if {$CycleType !="Push"} {
        for {set i 1} {$i <= $NstepsPeak} {incr i 1} {;        # one to
zero
                set Disp [expr $Disp - $dx]
                puts $outFileID $Disp;                      # write to file
        }
        if {$CycleType !="Half"} {
                for {set i 1} {$i <= $NstepsPeak} {incr i 1} {;        #
zero to minus one
                        set Disp [expr $Disp - $dx]
                        puts $outFileID $Disp;              # write to
file
                }
                for {set i 1} {$i <= $NstepsPeak} {incr i 1} {;        #
minus one to zero
                        set Disp [expr $Disp + $dx]
                        puts $outFileID $Disp;              # write to
file
                }
        }
}
puts $outFileID " }";         # close vector definition
close $outFileID
source data/tmpDsteps.tcl;              # source tcl file to define entire vector
```

```
        return $iDstep

}
```

Procedure *LibAnalysisStaticParameters*

--

static analysis parameters

I am setting all these variables as global variables (using variable rather than set command)

so that these variables can be uploaded by a procedure

Silvia Mazzoni & Frank McKenna, 2006

CONSTRAINTS handler -- Determines how the constraint equations are enforced in the analysis (http://opensees.berkeley.edu/OpenSees/manuals/usermanual/617.htm)

Plain Constraints -- Removes constrained degrees of freedom from the system of equations (only for homogeneous equations)

Lagrange Multipliers -- Uses the method of Lagrange multipliers to enforce constraints

Penalty Method -- Uses penalty numbers to enforce constraints --good for static analysis with non-homogeneous eqns (rigidDiaphragm)

Transformation Method -- Performs a condensation of constrained degrees of freedom

variable constraintsTypeStatic Plain;   # default;

if { [info exists RigidDiaphragm] == 1} {

        if {$RigidDiaphragm=="ON"} {

                variable constraintsTypeStatic Lagrange;   #   for large model, try Transformation

        };   # if rigid diaphragm is on

};   # if rigid diaphragm exists

constraints $constraintsTypeStatic

\# DOF NUMBERER (number the degrees of freedom in the domain): (http://opensees.berkeley.edu/OpenSees/manuals/usermanual/366.htm)

\# determines the mapping between equation numbers and degrees-of-freedom

\#   Plain -- Uses the numbering provided by the user

\#   RCM -- Renumbers the DOF to minimize the matrix band-width using the Reverse Cuthill-McKee algorithm

set numbererTypeStatic RCM

numberer $numbererTypeStatic

\# SYSTEM (http://opensees.berkeley.edu/OpenSees/manuals/usermanual/371.htm)

\#   Linear Equation Solvers (how to store and solve the system of equations in the analysis)

\#   -- provide the solution of the linear system of equations Ku = P. Each solver is tailored to a specific matrix topology.

\#   ProfileSPD -- Direct profile solver for symmetric positive definite matrices

\#   BandGeneral -- Direct solver for banded unsymmetric matrices

\#   BandSPD -- Direct solver for banded symmetric positive definite matrices

\#   SparseGeneral -- Direct solver for unsymmetric sparse matrices

\#   SparseSPD -- Direct solver for symmetric sparse matrices

\#   UmfPack -- Direct UmfPack solver for unsymmetric matrices

set systemTypeStatic BandGeneral;   \# try UmfPack for large model

system $systemTypeStatic

\# TEST: \# convergence test to

\#   Convergence   TEST (http://opensees.berkeley.edu/OpenSees/manuals/usermanual/360.htm)

\# -- Accept the current state of the domain as being on the converged solution path

\# -- determine if convergence has been achieved at the end of an iteration step

\#   NormUnbalance -- Specifies a tolerance on the norm of the unbalanced load at the current iteration

\#   NormDispIncr -- Specifies a tolerance on the norm of the displacement increments at the current iteration

\#   EnergyIncr-- Specifies a tolerance on the inner product of the unbalanced load and displacement increments at the current iteration

\#   RelativeNormUnbalance --

\#   RelativeNormDispIncr --

\#   RelativeEnergyIncr --

variable TolStatic 1.e-3;   \# Convergence Test: tolerance

variable maxNumIterStatic 1000;   \# Convergence Test: maximum number of iterations that will be performed before "failure to converge" is returned

variable printFlagStatic 0;   \# Convergence Test: flag used to print information on convergence (optional)   \# 1: print information on each step;

variable testTypeStatic EnergyIncr ; \# Convergence-test type

test \$testTypeStatic \$TolStatic \$maxNumIterStatic \$printFlagStatic;

\# for improved-convergence procedure:

    variable maxNumIterConvergeStatic 2000;

    variable printFlagConvergeStatic 0;

\# Solution ALGORITHM: -- Iterate from the last time step to the current (http://opensees.berkeley.edu/OpenSees/manuals/usermanual/682.htm)

\#   Linear -- Uses the solution at the first iteration and continues

\#   Newton -- Uses the tangent at the current iteration to iterate to convergence

\#   ModifiedNewton -- Uses the tangent at the first iteration to iterate to convergence

\#   NewtonLineSearch --

\#   KrylovNewton --

\#   BFGS --

\#   Broyden --

variable algorithmTypeStatic Newton

algorithm $algorithmTypeStatic;

\# Static INTEGRATOR: -- determine the next time step for an analysis (http://opensees.berkeley.edu/OpenSees/manuals/usermanual/689.htm)

\#   LoadControl -- Specifies the incremental load factor to be applied to the loads in the domain

\#   DisplacementControl -- Specifies the incremental displacement at a specified DOF in the domain

\#   Minimum Unbalanced Displacement Norm -- Specifies the incremental load factor such that the residual displacement norm in minimized

\#   Arc Length -- Specifies the incremental arc-length of the load-displacement path

\# Transient INTEGRATOR: -- determine the next time step for an analysis including inertial effects

\#   Newmark -- The two parameter time-stepping method developed by Newmark

\#   HHT -- The three parameter Hilbert-Hughes-Taylor time-stepping method

\#   Central Difference -- Approximates velocity and acceleration by centered finite differences of displacement

integrator DisplacementControl $IDctrlNode $IDctrlDOF $Dincr

\# ANALYSIS -- defines what type of analysis is to be performed (http://opensees.berkeley.edu/OpenSees/manuals/usermanual/324.htm)

\# Static Analysis -- solves the KU=R problem, without the mass or damping matrices.

\# Transient Analysis -- solves the time-dependent analysis. The time step in this type of analysis is constant. The time step in the output is also constant.

\# variableTransient Analysis -- performs the same analysis type as the Transient Analysis object. The time step, however, is variable. This method is used when

\# there are convergence problems with the Transient Analysis object at a peak or when the time step is too small. The time step in the output is also variable.

set analysisTypeStatic Static

analysis $analysisTypeStatic

VITA

NAME   Ali Ejaz

DATE OF BIRTH   20 August 1995

PLACE OF BIRTH   Attock, Pakistan

INSTITUTIONS ATTENDED   B.Sc in Civil Engineering from University of Engineering & Technology (UET) Taxila, Pakistan
M.Eng in Civil Engineering from Saitama University, Japan

HOME ADDRESS   Adjacent to Muslim Cambridge Public School Mohallah Noora Baba Sheenbagh Attock 43600